Broadband radio jet emission and variability of γ–ray Blazars

INAUGURAL-DISSERTATION

zur
Erlangung des Doktorgrades
der Mathematisch-Naturwissenschaftlichen Fakultät
der Universität zu Köln

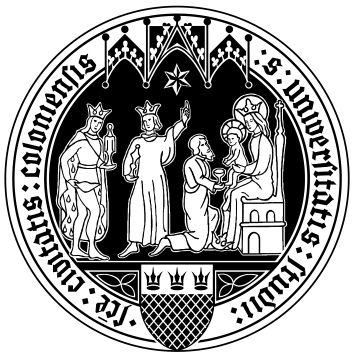

vorgelegt von

Ioannis Nestoras
aus Larissa, Griechenland
Köln 2015

Berichterstatter: Prof. Dr. Andreas Eckart
Prof. Dr. J. Anton Zensus

Tag der letzten mündlichen Prüfung: 22/06/2015

Abstract

AGN (Active Galactic Nuclei) and in particular their subclass blazars, are among the most energetic objects observed in the universe, featuring extreme phenomenological characteristics such as rapid broadband flux density and polarization variability, fast super–luminal motion, high degree of polarization and a broadband, double-humped spectral energy distribution (SED). The details of the emission processes and violent variability of blazars are still poorly understood. Variability studies give important clues about the size, structure, physics and dynamics of the emitting region making AGN/blazar monitoring programs of uttermost importance in providing the necessary constraints for understanding the origin of energy production.

In this framework the F-GAMMA program was initiated, monitoring monthly ∼60 *Fermi*-GST detected AGN/blazars at 12 frequencies between 2.6 and 345 GHz since 2007. For the thesis in hand observations and data analysis were performed within the realms of the F-GAMMA program, using the Effelsberg (EB) 100 m and Pico Veleta (PV) 30 m telescopes at 10 frequency bands ranging from 2.64 to 142 GHz. The cm to short-–mm variability/spectral characteristics are monitored for a sample of 59 sources for a period of five years enabling for the first time a detailed study of the observed flaring activity in both the light curve and spectral domains for such a large number of sources and such high cadence. Also the observing systems and methods are introduced as well as the data reduction techniques. The thesis at hand is structured as follows:

Chapter 3 presents the reduction methods and post measurement corrections applied to the data such as pointing offsets, gain–elevation and sensitivity corrections as well as specific corrections applied for each of the EB and PV observing systems respectively.

Chapter 4 presents the analysis tools and methods that were used such as: variability characteristics, flare amplitudes with a new method for estimating the intrinsic standard deviation, flare time scales using Structure Function analysis, spectral indices and spectral peak estimations.

Chapter 5 presents the results of the analysis performed upon the five year light curves. The significance of variability through a χ^2 test is estimated as well as the flare amplitudes using the intrinsic variability of the light curves along with a new proposed k–index. The introduction of the k–index enables the characterization of the observed variability amplitudes across frequency, thus permitting us to limit the parameter space of various physical models. Also flare time scales, brightness temperatures and Doppler factors are reported.

Chapter 6 presents the corresponding analysis in the spectral domain, including results for spectral indices and an $S_{max} - \nu_{max}$ analysis. By determining the spectral peak of every spectra for a selected number of sources, it is possible to track the evolution of the flaring activity in the $S_{max} - \nu_{max}$ plane, enabling us to discriminate between different underlying physical mechanisms that are in action. Finally ***Chapter 7*** includes the overall discussion and a summary of results obtained.

Zusammenfassung

Aktive Galaxienkerne (engl. AGN), insbesondere die Unterklasse der Blazare, zählen zu den energetischsten Objekten des beobachtbaren Universums. Sie zeigen extreme phänomenologische Charakteristika wie rapide Variation der Flussdichte und der Polarisation über den gesamten Spektralbereich, Bewegung mit scheinbarer Überlichtgeschwindigkeit, hohe Polarisation und eine spektrale Energieverteilung, die das gesamte Spektrum abdeckt, mit einem typischem Verlauf , der zwei Maxima im niedrigen und hohen Energiebereich zeigt. Die Details der Emissionsprozesse und der drastischen Variabilität sind bislang nicht vollständig verstanden. Untersuchungen der Variabilität geben Hinweise auf die Größe, Struktur, Physik und Dynamik der strahlungsemittierenden Region. Daher sind kontinuierliche AGN/Blazar-Beobachtungskampagnen von höchster Bedeutung, um den Ursprung der Energieproduktion zu verstehen.

In diesem Rahmen wurde das F-GAMMA Programm initialisiert, in welchem seit 2007 monatlich etwa 60 von *Fermi*-GST identifizierte AGNs/Blazare in 12 Frequenzen zwischen 2.6 und 345 GHz beobachtet werden. Für diese Doktorarbeit wurden Beobachtungen am Effelsberg-100 m-Teleskop (EB) und am Pico Valeta-30 m-Teleskop (PV) in 10 Frequenzbändern von 2.64 bis 142 GHz durchgeführt sowie die zugehörige Datenanalyse. Die Beobachtung von 59 Objekten in verschiedenen Frequenzen über einen Zeitraum von fünf Jahren erlaubt zum ersten Mal das detaillierte Untersuchen von Intensitätsausbrüchen (Flares) sowohl in den Lichtkurven als auch in den Spektren für eine große Anzahl von Objekten bei so hoher Zeitauflösung. Die Beobachtungssysteme und -methoden werden in dieser Arbeit vorgestellt, ebenso wie die Methoden der Datenreduktion. Die Arbeit ist in nachfolgende Kapitel unterteilt.

In Kapitel 3 werden die Methoden der Datenreduktion vorgestellt, die nach der Beobachtung angewendeten Korrekturen, darunter Offsets der Teleskopausrichtung, Signalverstärkung, Sensitivitäts und spezifische weitere Korrekturen, die auf die Daten der EB und PV Systeme angewendet wurden.

In Kapitel 4 werden die Methoden der Datenanalyse dargestellt, darunter die Charakterisierung der Variabilität, der Flare–Amplituden mit einer neuen Methode zur Einschätzung der intrinsischen Standardabweichung, der typischen Flare–Zeitskalen mittels Anwendung der Strkturfunktion sowie Abschätzung der spektralen Indizes und der Maxima der spektralen Energieverteilung.

In Kapitel 5 werden die Ergebnisse präsentiert, die auf der Untersuchung der 5-Jahres-Lichtkurven basieren. Die Signifikanz der Variabilität wird mittels eines χ^2–Testes abgeschätzt sowie die Amplituden der Flares unter Verwendung der intrinsischen Variabilität der Lichtkurven und dem hier neu eingeführtem k–Index. Der k–Index erlaubt die Charakterisierung der beobachteten Variabilitätsamplituden über den gesamten Frequenzbereich und ermöglicht es somit Schranken für die Parameter verschiedener physikalischer Modelle zu finden. Des Weiteren werden Flare-Zeitskalen, Strahlungstemperatur und Doppler-Faktoren diskutiert.

In Kapitel 6 werden entsprechend die Ergebnisse der Spektralanalyse dargestellt, daru-

nter die Spektral-Indizes und die $S_{max} - \nu_{max}$ Analyse. Indem das Maximum jeder spektralen Energiedichte verschiedener Objekte ermittelt wird, ist es möglich die Entwicklung eines Intensitätsausbruches in der $S_{max} - \nu_{max}$ Ebene zu verfolgen. Dies erlaubt verschiedene physikalische Prozesse zu unterscheiden, die Ursache für dieses Verhalten sind.

In Kapitel 7 werden die Ergebnisse dieser Doktorarbeit und deren Interpretation zusammengefasst.

Acknowledgements

When I started writing the acknowledgements, I realized that the difference in choosing the proper words to express myself, from the somewhat proper words is similar to the difference between night and day. In that sense if I forgot someone or if someone feels not properly acknowledged please have in mind that I did my best to express my feelings and thoughts but certainly not succeeded completely.

First of all I would like to thank my family, my mother Elpiniki my brothers Alekos and Petros my uncle Petros and my grandmother Kiki. Without them I would not be the man I am now and certainly without their help I would not have been able to accomplish anything. The security I felt throughout the years being able to pursue my dreams, is something you can not buy, but only be given and only if you are lucky enough to be blessed with a family supporting you like mine. I don't simply thank them but owe them everything. This thesis is devoted to all of them that are still here beside me and to those that have left from this life.

Secondly I would like to thank my friends, that stood beside me in good and bad moments. Specifically I would like to thank my dear friends A. Tsitali and V. Karamanavis. I owe them a lot, without them I wouldn't be able to finish this quest. Their help is far beyond the simple and practical things and lies in true friendship that never dies or is forgotten. My dear friends I. Antoniadis, L. Tremou, I. Miserlis, K. Markakis, K. Papadopoulou, K. Metallinos, X. Milea, V. Oikonomou, K. Lazarides, H. Kalantarova, O. Vantzos, E. Katsikogiani and S. Lopez for being there when I needed them, I shall never forget the amazing times we had together all those years. Living abroad without them would have been a torture. Also I could not have forgotten X. Spilioti for the long conversations by the Rhine and for her true friendship in bad times, I honestly thank her for that.

My gratitude to V. Papaioanou, it was an honour for me being my friend all those years, teaching me even until his last moments on how to truly live life and for playing a key role to experiences that can not easily be explained. Some memories are never forgotten and will always remain.

A special place in my heart has Prof. J. Seiradakis. Because of him I started my journey into astronomy, because of him I have so many more experiences that I wouldn't be able to have in any other way. He was the beginning and thus I am infinitely grateful for all the knowledge and support he gave me in my humble beginnings.

Many people played a key role for the completion of the thesis in hand. I would like to thank my supervising professor Dr. A. Zensus, for the trust, resources, patience and overall support over the years. My advisor Dr. L. Fuhrmann, his guidance and comments all these years, in good and in bad times, played a key role to the success of this endeavour. Special thanks goes to Dr. E. Angelakis for his help and support.

I truly thank Dr. V. Pavlidou, Dr. N. Marchili and Dr. T. Krichbaum for their significant help and contribution to several key scientific aspects of this work. Their contribution was of uttermost importance. I also thank all the people in the VLBI group for accepting me as one of their own. My office mates and colleagues Dr. F. Schinzel, Dr. M. Karouzos, Dr. M.

Mezcua and Dr. C. Fromm I thank them all for their friendship and patience with me. Also I would like to thank S. Kielhlmann for the quick translation of the abstract to the German language. Special thanks goes also to Kostas Markakis and Nadeen Sabha for their real help with the practicalities at the last moments. I can not forget also K. Gotzman for her help with all the trivial but important papers of the University. The secretaries of the MPI and IMPRS for their help all these years, Dr. Simone Pott and Beate Naunheim.

Also I would like to thank all the operators in both Effelsberg and Pico Veleta telescopes. All the countless nights and days of observing would have been far more difficult without their technical support and friendly company.

Last but not least, I would really like to thank all those that stood in my way trying to make my life difficult. Without them I could not have obtained the cast of mind and mental strength that is required to successfully accomplish anything in life. All of you, I thank you from the deepest part of my heart !!

"Words have no power to impress the mind without the exquisite horror of their reality"

Edgar Alan Poe

Contents

1 Introduction

With the opening of the radio window in the 60's many great discoveries were made. The discovery of the microwave background, pulsars and quasars are among the most important. The term "quasar" originally stood for "quasi–stellar radio source", and refers to the fact that these type of objects are point like and appear very similar to stars when are observed in the optical. These sources belong to a class of objects called AGN, which stands for "Active Galactic Nuclei". In the following a brief introduction to this type of objects and to their different observed flavours is given.

1.1 Historical background

In the beginning of the twentieth century, Fath (1909) made the first observations in order to clarify the nature of the "spiral nebulae". The question back then was if these nebulae are similar to other well known objects as the Orion nebulae or a collection of unresolved stars. Seyfert (1943) began observations systematically of galaxies with emission lines. He obtained spectrograms of 6 galaxies with nearly stellar nuclei showing emission lines superimposed on a normal G-type star spectrum. These type of galaxies today are called Seyfert galaxies in honour of the work of Carl Seyfert. The next leap came with the development of radio astronomy in the 60's. In 1963 the first quasars where discovered by Schmidt (1963) with the observations of 3C 273. These first results were also published in papers by Hazard et al. (1963); Schmidt (1963); Oke (1963); Greenstein and Matthews (1963) and their most reasonable explanation was that these objects were extragalactic in nature with redshifts that according to Hubble expansion where placing them far beyond our own galaxy. In particular 3C 48 was identified also in the optical as a variable source (Matthews and Sandage 1963), with strong emission lines in its spectrum. An example of

a quasar imaged in different wavelengths is shown in Fig. 1.1.

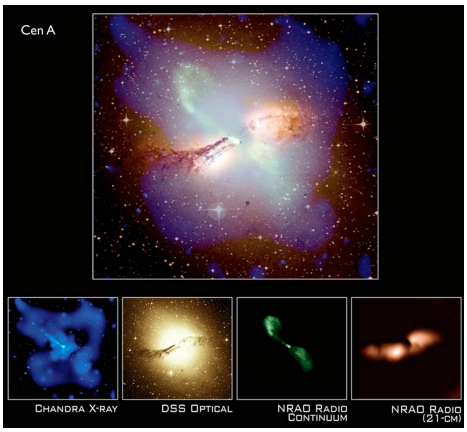

Figure 1.1: A typical case of a quasar. Cen A at different wavelengths demonstrating the different morphologies observed in AGN.

Today we know that these objects exhibit a compact core at the center and extended radio structures and are the largest single known astronomical sources in the universe. Their energy content is very large up to 10^{43} erg/s. The origin of this energy and the way it is converted into relativistic particles and magnetic fields is one of the most challenging problems of modern astrophysics. Several properties of this new class of objects emerged:

- star like objects identified with radio sources
- time variable flux density
- large UV flux
- broad emission lines
- large redshifts
- compact nucleus and jet structures in the radio bands

Today these galaxies are part of what we call an AGN. So, at a basic level, AGN are simply the cores of galaxies that are in contrast to "normal galaxies" active. Not all AGN share all of the above properties.

One of the defining characteristics of quasars and AGN is their broad spectral energy distribution (SED). An example of an SED of the powerful blazar 3C 454.3 can be seen in Fig. 1.2. Typically AGN are among the brightest objects in the sky at every observable frequency. AGN spectra can not be described simply in terms of black body emission like in the case of stars. Non-thermal processes are needed to explain the observed shape of their spectra. The primary process is incoherent synchrotron radiation for the low SED bump (see Sect. 1.4).

The radio morphology of AGN is described by extended structures that are resolved by modern imaging techniques. VLBI radio images show a very compact feature which is thought to be close to the "central engine" of the AGN producing the energy needed. The

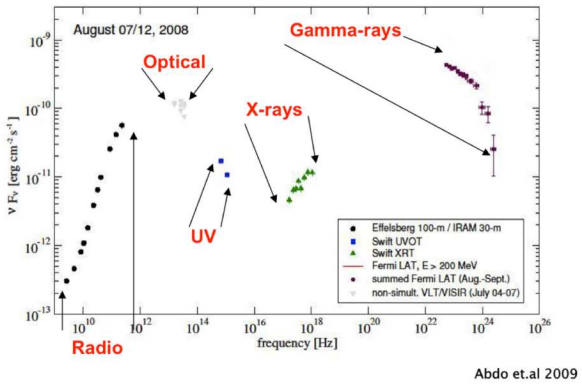

Figure 1.2: Example of the Spectral Energy distribution of 3C 454.3 Two distinct peaks are clearly visible.

resolved features include long thin jets that extend away from the central core towards the outer radio lobes and transfers energy from the central engine to the outer lobes in a highly collimated beam of relativistic particles. Example of these features are seen in Fig. 1.1.

1.2 AGN structure

The amount of energy that is produced by the central source is enormous usually exceeding the amount of energy output of its host galaxy. Several theories tried to explain this energy production. Hoyle and Fowler (1963b) discussed the idea of a super massive star of up to $\sim 10^8\,M_o$ as an energy source. Hoyle and Fowler (1963b) suggested that a magnetic field could store a large amount of energy, leading to explosions and jets. Hoyle and Fowler (1963a) suggested that the observed energies can only be observed by the the contraction of a mass of 10^7 - 10^8 M_o to the relativistic limit. The process that powers the stars though , thermonuclear reactions, is not enough to power quasars. This was realized quite soon with the work of Salpeter (1964); Lynden-Bell (1969); Shakura and Sunyaev (1973).

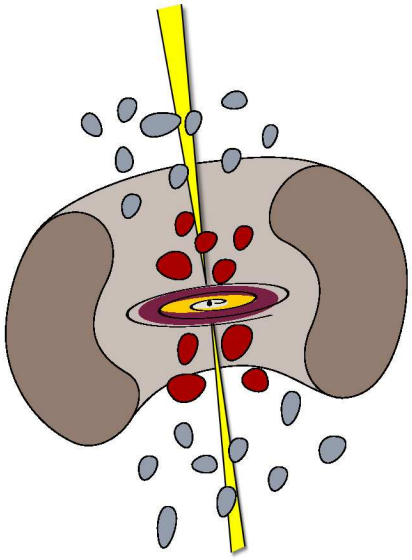

Figure 1.3: Artistic representation of an AGN. Jets are depicted with yellow, acretion disk is the inner yellow disk and a dust torus in purple around the central engine. (Image courtesy of V. Karamanavis)

Salpeter (1964) and Zel'dovich (1964) proposed the idea of accretion onto a supermassive black hole (SMBH). The black hole model received limited attention until Lynden-Bell (1969) argued that black holes should be common in galactic nuclei.

Our current understanding of the AGN phenomenon includes as the central energy

production region a black hole fed by an accretion disk of falling material and launching relativistic jets alongside magnetic field lines. This AGN paradigm is graphically illustrated in Fig. 1.3. Broad emission lines are produced in clouds orbiting near the black hole. A thick dusty torus obscures the broad-line region from transverse lines of sight. A hot corona above the accretion disk plays a role in producing the X-ray continuum. Narrow lines are produced in clouds farther away from the central engine. In summary the basic structure of an AGN includes:

- *A black hole*, acting as the central engine of the AGN, with a mass range of $10^6\,M_o < M < 10^{10}\,M_o$.
- *An accretion disk*, matter with angular momentum, spirals into the black hole and forms a disk.
- *An X–ray corona*, surrounding the accretion disk. The X-ray emission is variable on short time scales implying a very compact region. Its luminosity is is linked to optical/UV emission from the accretion disk.
- *An obscuring torus*, surrounding the black hole and accretion disk on parsec scales, absorbing some part of the radiation and re-emitting it in the infrared.
- *Broad Line Region* (BLR), a region of small fast moving clouds close to the black hole at a distance of $\sim 10^{17}$–10^{18} cm and displaying spectral lines with large velocity widths. They absorb ∼10% of radiation of the accretion disk, and re emit it in the form of lines.
- *Narrow Line Region* (NLR), similar to the BLR region but at larger distances of the order of 100 pc with less dense clouds that are moving with smaller speeds.
- *Jets*, about 10% of AGN exhibits two oppositely directed jets. The material inside the jets is moving at relativistic speeds causing relativistic effects. As it will be discussed later jets are the key ingredient for the range of phenomena observed.

1.3 AGN Classification & Unification

AGN exhibit a wide variety of different observational signatures. Some AGN produce powerful radio jets while others do not, some produce powerful X-ray and γ–ray emission as well as broad optical emission lines and are highly optical polarized and others are not, some are strongly variable while others are not. The main host galaxies of radio-quiet AGN seem to be spirals in contrast to powerful radio loud AGNs that are usually found only in ellipticals. Complicated at first glance a classification of all this phenomenology exists, as shown at Fig. 1.4. The causes of these diverse characteristics can be traced down to the combination of the AGN structure and the angle of the jet towards earth i.e. the line of sight.

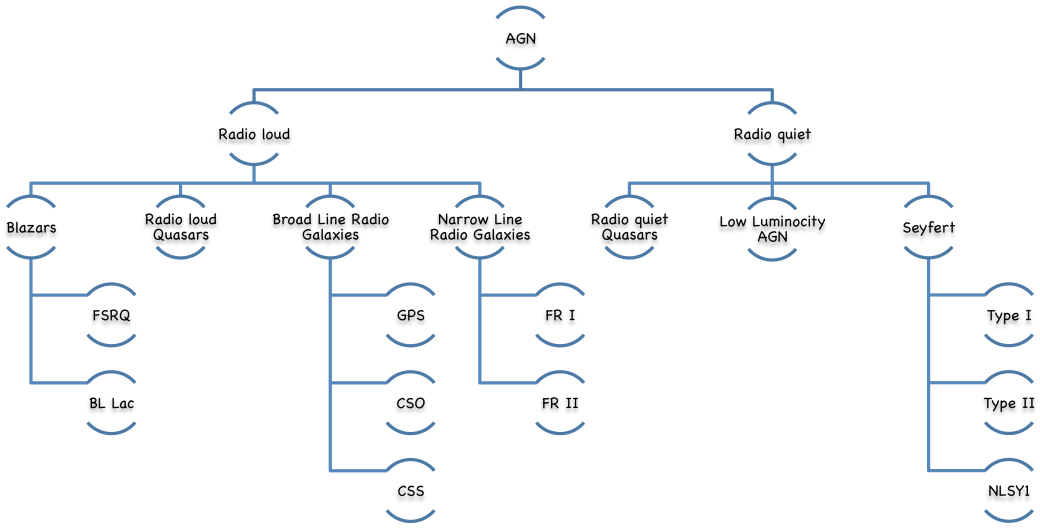

Figure 1.4: Schematic view of the AGN classification with different types and sub-types according to our current understanding.

Two major sub-divisions exist, radio-loud and radio quiet AGN. The first quasars ever discovered were radio loud, but we now know that the majority is radio quiet and that radio loud AGN are only ∼10% of all AGN population. The separation in terms of radio loud and radio quiet is based on the flux density ratio at 5 GHz to optical flux in the B–band, with radio loud AGN having ratios of $F_{radio}/F_{optical} > 10$ (Kellermann 1989). Radio loud AGN are further sub-divided into the classes of blazars, Broad Line Radio Galaxies (BLRG) and Narrow Line Radio Galaxies (NLRG). Radio-quiet AGN are sub-divided into radio quiet quasars, Low luminocity AGN (LLAGN) and Seyfert galaxies.

These classifications are based upon the observed characteristics that include spectral properties, structure at radio and other wavelengths. Blazars are furthermore divided into Flat Spectrum Radio Quasars (FSRQ) and BL Lac objects, NLRG are divided to FR I and II types, BLRG into GPS (GHz Peaked Sources), CSO (Compact Symmetric Objects) and CSS (Compact Steep Source) sources. Seyfert galaxies are further sub-divided into Type I and II and NLSY1 sources. The vast array of different phenomena and types can be unified under a relative simple model. This unified scheme is graphically demonstrated in Fig. 1.5. The main idea is that the type and thus the phenomena we observe from an AGN largely depend on the line of sight towards the observer. In principle all AGN have the same basic structure but their appearance changes with the angle that we look upon them. Below a brief explanation of the most important AGN sub-types is given :

- **Blazars**

  An AGN is called a blazar in the case that the line of sight is aligned with the jet and thus the observer looks directly into the jet. This type of objects are the most variable and belong to the radio loud category of AGN. Relativistic boosting of the radiation along the direction of motion takes place in blazars and leads to the extreme apparent luminosity at all wavelengths. Other characteristics of blazars include powerful γ–ray emission, high and rapid optical polarization. Two main type of blazars exist,

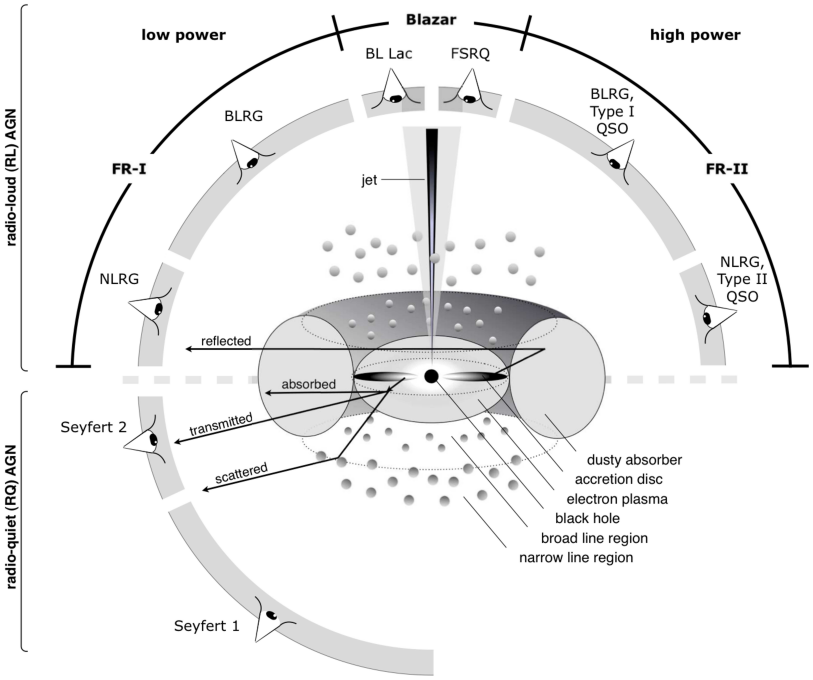

Figure 1.5: Schematic representing our current understanding of the the AGN phenomenon according to the unified scheme. The type of object we observe depends on the viewing angle to the AGN. (graphic from Beckmann and Shrader 2013)

namely FSRQs and BL Lacs. These two classes have many common features but also some differences that are summarized in Table 1.1. The main differences are their optical features, the integrated power and spectral energies.

Table 1.1: Main differences between the FSRQ and BL Lac radio-loud AGN classes.

	FSRQs	BL lacs
Optical features	Em. Lines & Th. Bump	NO Em. Lines & NO Th. Bump
Top energy	$L \sim 10^{48}$	$L \sim 10^{46}$
Integrated power	10 GeV	10 TeV

Unlike other AGNs, they do not emit much power in the broad emission lines. There are two general classes of BL Lacs: High-Frequency Peaked BL Lacs (HBL) and Low-Frequency Peaked BL Lacs (LBL). The LBL class have their low frequency SED peak in the IR/optical, while the HBLs have their spectral break at UV/X-ray. Blazars and their sub-types are the focus of the current thesis.

- **BLRG**

  Broad line region galaxies are divided into GPS, CSO and CSS sources. GPS sources emit in radio and have convex spectra peaking at GHz frequencies. The current view for these sources is that they are young, compact, and powerful AGN that have a large amount of gas in their central cores (Fanti et al. 1995). CSS source are quite similar to GPS sources, but with a spectral peak turnover at a few hundred GHz. CSO sources are practically a GPS source but with a two-sided morphology. Also they are not so compact as CSS sources.

- **NRLG**

  NLRG class is sub-divided into FR I and FR II type of objects. FR I sources are best known for their distorted jets. Originally, the FR classification is based on the ratio between the distance from the core of the highest radio surface brightness to the distance of the low-power radio width. Sources are classified as a FR I if the ratio is < 0.5. FR II galaxies are those radio galaxies with large extended radio lobes farther away from the central core. They typically have jets that appear undistorted.

- **Seyfert galaxies**

  Different types of Seyfert galaxies were recognised by Khachikyan and Weedman (1971), based on the widths of their emission lines. Both types show powerful narrow forbidden lines from high excitation species. Some Seyfert galaxies also show broad ($\sim$ 10000 km·s^{-1}) Balmer lines, while in others these lines are much more narrow (250 to 1000 km·s^{-1})

- **NLSy1**

  Narrow-line Seyfert 1 (NLSy1) share the same properties as Seyfert type 1 galaxies but with narrower Balmer lines (FWHM $<$ 2000 km·s^{-1}) and strong optical emission. They are peculiar because of their soft X-ray excess and rapid X-ray variability. Recently it was also found that the are strong γ-rays emitters.

1.4 Physical processes in Blazars

Several processes are actively producing the diversity of the observed phenomena in AGN and particularly in blazars. In this section these processes are presented in more detail, always from the perspective of the blazar subclass.

1.4.1 Relativistic beaming & Superluminal motion

One of the basic observational characteristics of blazars is relativistic beaming and superluminal motion. Relativistic beaming is referred to the process of modifying the emission characteristics of emitting matter that is moving close to our line of sight at high relativistic speeds. It can be shown (see Ghisellini 2012) that for instance the intensity of an emitting region is modified due to relativistic effects according to $I_o = \delta^{3+a} \cdot I$, where I_o is the apparent intensity as received by the observer, I is the intensity actually emitted and δ is the relativistic Doppler factor:

$$\delta = \frac{1}{\Gamma\,(1 - \beta \cdot \cos\theta)} \tag{1.1}$$

where:

Γ : is the Lorentz factor
θ : is the angle between the line of sight and the direction of movement
β : equals v/c where v is the intrinsic linear velocity and c the speed of light.

Another effect for an emission element moving near the speed of light and close to the line of sight, is the illusion of apparent transverse motion which is greater than that of the speed of light i.e. superluminal motion. Relativistic beaming (Blandford et al. 1977; Blandford and Königl 1979) is widely accepted as the simplest way in explaining the observed phenomena. This effect occurs for emitting regions moving at actual speeds lower than the speed of light and with small angles to the line of sight (Rees 1966). Lets assume that a radiating feature is ejected from an AGN, with a velocity v and an angle θ with respect to the line of sight. After time t, the feature has moved a distance $v \cdot t$. This motion is projected along the line of sight and is $vt\dot{\cos}\theta$ and perpendicularly $vt \cdot \sin\theta$. An observer in earth sees this emission delayed by Δt when compared to the time the feature was at the AGN source, according to:

$$\Delta t = ct\,(1 - \cos\theta) \tag{1.2}$$

Then the apparent transverse velocity seen by the observer is :

$$v_a = \frac{v \sin\theta}{1 - \beta\cos\theta} \tag{1.3}$$

Typical proper motions observed with Very Long Baseline Interferometry (VLBI) are in the range of 0.1 to 1 milliarcsecond per year. These motions are corresponding to apparent velocities of up to ~ 30 times the light speed (e.g. Vermeulen and Cohen 1994). Relativistic effects are of profound importance for our understanding of quasars and AGNs.

1.4.2 Synchrotron emission & absorption

The electromagnetic radiation emitted when charged relativistic particles are accelerated radially is called synchrotron radiation. Usually the Lorentz force is responsible for the resulting radiation by means of gyrating particles around magnetic field lines. Our goal and what we need to know is the shape and characteristics of an ensemble of electrons that emit synchrotron radiation.

Two processes take place, synchrotron emission and absorption. What makes synchrotron radiation special is the fact that relativistic particles are the source of the radiation and that their energy distribution is not Maxwellian. Considering the emission part first, it is shown that the synchrotron flux received from a homogeneous and thin source of volume $V \propto R^3$ and at a luminosity distance d_L, is given by :

$$F_s = \epsilon_s(\nu) \cdot \frac{V}{d_L^2} \tag{1.4}$$

and if we replace the emissivity then we have :

$$F_s = \theta_s^2 \cdot R \cdot K \cdot B^{1+\alpha} \cdot \nu^{-\alpha} \tag{1.5}$$

where:

$\epsilon_s(\nu)$: is the frequency depended emissivity
α : is the spectral index
B : is the magnetic field

Considering the absorption part as well, for an absorbed source the brightness temperature, that is defined by Eq. 5.1, must be equal to the kinetic energy of the electrons. It can be proven that for the absorption from photons, the following relation holds :

$$I(\nu) \propto \frac{\nu^{5/2}}{B^{1/2}} \tag{1.6}$$

To have the final expression for the flux we must integrate over θ_s. We obtain :

$$F(\nu) \propto \theta_s^2 \frac{\nu^{5/2}}{B^{1/2}} \tag{1.7}$$

The final spectrum emitted by a collection of electrons is shown in Fig. 1.6

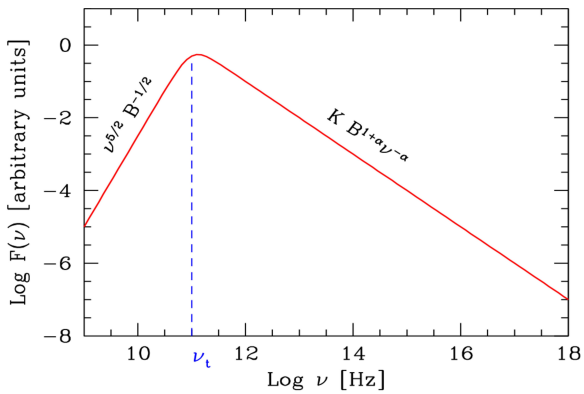

Figure 1.6: Spectrum of an ensemble of electrons from a partially self absorbed source. (Ghisellini 2012)

A very important point is the transition between the self-absorbed part to the optically thin part. This transition happens at the self-absorption frequency ν_t. It can be shown that this frequency is given by:

$$\nu_t \propto \left[R \cdot K \cdot B^{(p+2)/2} \right]^{2/(p+4)} \tag{1.8}$$

the quantity p is one of the indices of the original power law distribution : $(p = 2 \cdot \alpha + 1)$. The self-absorption frequency is a crucial quantity for studying astronomical sources exhibiting synchrotron radiation because the synchrotron spectrum peaks very close at the frequency of ν_t. For a more detailed derivation see Ghisellini (2012).

1.4.3 Inverse Compton Scattering: SSC & EC

The mechanisms producing the high energy γ–ray peak in blazar SED is believed to be: (i) inverse Compton up-scattering of photons to high energies or (ii) proton induced cascades in hadronic models (Mannheim 1993). Inverse Compton scattering involves the scattering of photons from low to high energies by ultra–relativistic electrons whereas the photons gain and the electrons lose energy. In the framework these leptonic models target photon fields for inverse Compton up-scattering are required(e.g Böttcher 2007; Krawczynski 2004; Sikora and Madejski 2001). There are three main sources of target photons namely: (a) the synchrotron photons themselves (Synchrotron Self-Compton, SSC), (b) external photons from the accretion disk (External Comptonization of Disk photons, ECD) (Sikora et al. 1994; Dermer and Schlickeiser 1993), (c) external photons from the BLR (Sikora et al. 1994) or the dusty torus (Błażejowski et al. 2000).

1.5 Variability of Blazars

Up to now we have seen the various types of AGN observed and the various processes that produce the observed spectra in a specific time. Variability though have been observed from the early observations of AGNs with observed time scales of months, years or even minutes are frequently observed. The rapid blazar variability, probes spatial scales inaccessible even to interferometric imaging and has been explained in terms of e.g. relativistic shock-in-jet models (e.g Marscher and Gear 1985; Valtaoja et al. 1992a,b; Stevens et al. 1994; Türler 2011) or colliding relativistic plasma shells (e.g. Spada et al. 2001; Guetta et al. 2004). Quasi–periodicities seen in the long term variability curves on time scales of months to years, may indicate systematic changes in the beam orientation (Camenzind and Krockenberger 1992), possibly related to binary black hole systems, MHD instabilities in the accretion disks and/or helical/precessing jets (e.g. Begelman et al. 1980; Villata and Raiteri 1999; Chen et al. 2013). Bellow a short description of the shock in jet model is presented.

1.5.1 Shock–in–Jet model

The classical shock in a jet model of Marscher and Gear (1985); Valtaoja et al. (1992a,b); Stevens et al. (1994); Türler (2011) assumes a shock wave propagating through a conical

jet accelerating relativistic particles at the shock front (Fig. 1.7), while travelling behind the shock front these particles loose energy due to different mechanisms i.e. Compton synchrotron and adiabatic losses. The three distinct evolutionary stages can be described as follows:

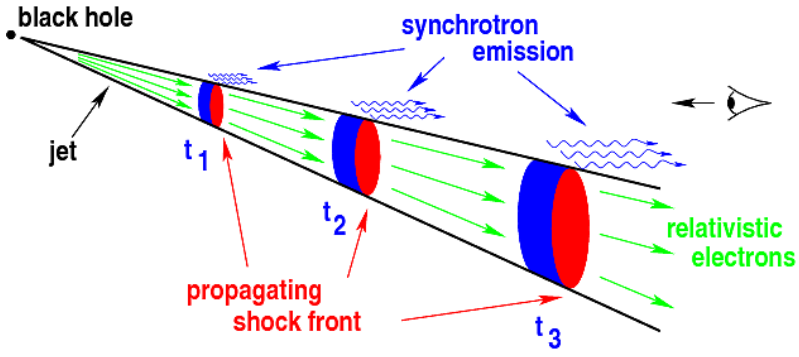

Figure 1.7: Representation of a the shock in jet model. (image from: Türler (2011))

the growth stage: The first is called the Compton stage due the dominant energy losses by Compton scattering. It is characterised by the increase of the observed turnover flux density and the decrease of the turnover frequency. This stage can be described by the following relations :

$$S_{\mathrm{m}} \propto \nu_{\mathrm{m}}^{-(11-\alpha)/[2(\alpha+1)]} \tag{1.8a}$$

$$\nu_{\mathrm{m}} \propto R^{-(\alpha+1)/4} \tag{1.8b}$$

where:

S_{m} : is the flux density at the turnover frequency
ν_{m} : is the self absorbed turnover frequency
α : is the spectral index
R : is the distance from the vertex of the cone

the plateau stage: The second is called the synchrotron stage were energy losses are dominated by synchrotron losses of the electrons. It is characterized by and almost constant value of the turnover flux density and the decay of the turnover frequency. The behaviour of the turnover flux density and frequency can then be described by :

$$S_{\mathrm{m}} \propto \nu_{\mathrm{m}}^{[(2s-5)\cdot(2+3\alpha)]/[4(s+2)+3\alpha(s-1)]} \tag{1.8c}$$

$$\nu_{\mathrm{m}} \propto R^{-[4(s+2)+3\alpha(s-1)]/[3(s+5)]} \tag{1.8d}$$

where s is the slope of the spectral energy distribution.

the decay stage: The third and last is called the adiabatic stage and refers to energy losses due to adiabatic expansion. It is characterized by the decrease of both the turnover frequency and flux. In that case the above relations become :

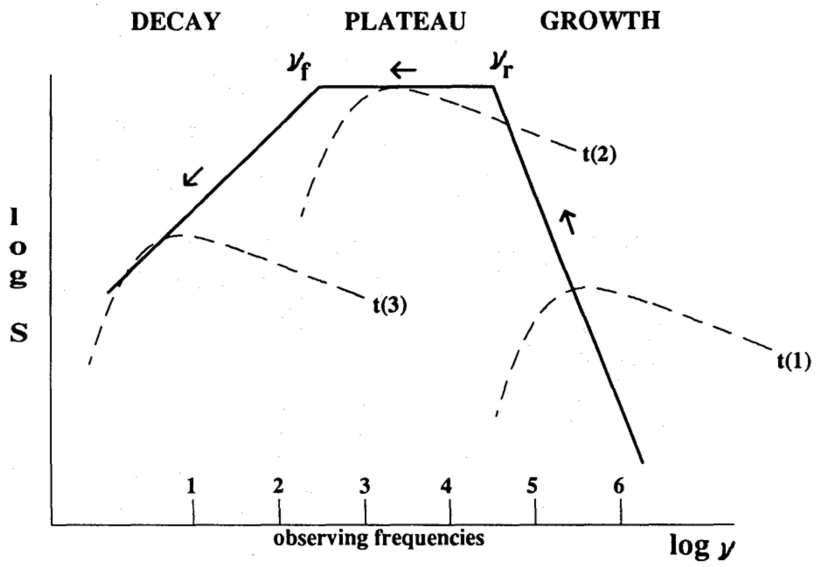

Figure 1.8: Prototype behaviour according to the generalized shock–in jet model of Valtaoja et al. (1992b)

$$S_m \propto \nu_m^{10(s-1)/(7s+8)} \tag{1.8e}$$

$$\nu_m \propto R^{-(7s+8)/[3(s+4)]} \tag{1.8f}$$

These three stages are demonstrated in Fig. 1.8, tracing the self-absorbed turnover frequency of the shock spectrum as it evolves in the frequency-flux space. The standard Marscher and Gear (1985) model assumes a constant Doppler factor whereas the latter can strongly influence the slopes of the different evolution stages in the $S_{max} - \nu_{max}$ plane. This model is the basis that the generalized shock in jet model of Valtaoja et al. (1992b) is based upon.

1.5.2 Geometrical models

Apart from shock in jet model described above also geometrical effects can modulate the observed emission and can introduce variations in flux density on different long term time scales. One possible explanation is the emission regions moving alongside bend radio structures. Such bend jets are frequently found (e.g Agudo et al. 2012; Lobanov and Zensus 2001; Ly et al. 2007; Piner et al. 2009; Camenzind and Krockenberger 1992). Several theoretical models exist i.e. oscillating bent jets, helical modes in hydrodynamic jets (Hardee

1987) or in magnetized jets (Konigl and Choudhuri 1985). The basic idea is that whenever an emission feature moves along alongside the helical or bend structures differential Doppler boosting occurs producing the observed variability.

1.6 F-GAMMA Program description

F-GAMMA stands for **F**ermi **G**amma-ray Space Telescope **A**GN **M**ulti-frequency **M**onitoring **A**lliance and comprises the coordinated efforts of a broad consortium of scientific groups and observatories with the aim to collect (quasi-) simultaneous and high–precision broadband monitoring data (total intensity and polarization) for a large number of γ–ray sources in the ''low-energy'' synchrotron part of blazar SEDs. Monthly monitoring observations are performed for about 60 sources at frequencies between 2.6 and 345 GHz with the Effelsberg 100–m (EB), Pico Veleta 30–m (PV) and APEX 12–m telescopes including polarization at several bands.

Scientific motivation and goals of the program

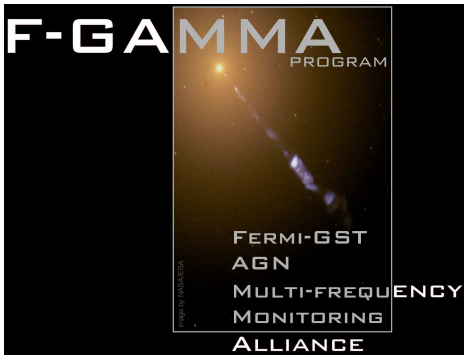

Figure 1.9: The F-GAMMA program logo.

As already mentioned Blazars (FSRQs and BL Lacs) as AGN sub–class exhibit extreme phenomenological characteristics such as rapid broadband flux density and polarization variability, high degree of polarization and a broadband, double–humped spectral energy distribution (SED) (e.g. Urry 1999). The recent discovery of blazars as a group of bright and highly variable high energy γ–ray sources (Hartman et al. 1992) expanded our knowledge but many questions remain unanswered. Is the jet composition leptonic or hadronic and which are the emission processes? What is the origin of their often violent broadband variability? Where in the jet are the high energy γ–ray photons produced? Is the production region located at the jet–foot point close to the SMBH or at several parsecs downstream?

The launch of the *Fermi Gamma-ray Space Telescope* ((*Fermi–GST Michelson 2008)* in June 2008, along with the Large Area Telescope detector (LAT, Atwood et al. 2009) on board *Fermi* and its dramatically improved capabilities compared to its predecessor EGRET, is providing spectacular γ–ray light curves and spectra resolved at a variety of time scales for a large number of AGN during the first years of operation (Abdo et al. 2009a, 2010b; Ackermann et al. 2011).

The new era in AGN astrophysics introduced by *Fermi*-GST will help answer still open questions, in particular the production and location of the γ–ray emission as well as the origin of the rapid (time scales of days to months/years) variability of the synchrotron and IC branch. The observed rapid blazar variability as already mentioned is

attributed to either intrinsic variability or geometrical models. Variability studies give important clues about the size, structure, physics and dynamics of the emitting region making AGN/blazar monitoring programs of uttermost importance in providing the necessary constraints for understanding the origin of energy production.

Detailed long term monitoring data sets of large source samples are rare at cm and short–mm bands. In this framework, and in order to fully explore the opportunities opened up by *Fermi*–LAT, the F-GAMMA monitoring program (Fuhrmann et al. 2007; Angelakis et al. 2010b; Fuhrmann et al. 2014; Angelakis et al. 2015) was initiated in 2007, monitoring the variability and spectral evolution of $\sim$60 *Fermi* bright sources at frequencies between 2.6 and 345 GHz. It is the first AGN radio monitoring program that covers such a large frequency range in a highly homogeneous and coordinated manner.

Participating facilities and groups

The core facilities of the F-GAMMA program are the EB and the PV telescopes. A full and detailed description of the observations performed in these two telescopes is given in Sect. 2, Sect. 3.1.1 and Sect. 3.3.1.

The F-GAMMA program is closely collaborating with a large number of other observatories, programs and teams in the AGN community. A summary of all the participating facilities is shown at Table 1.2. More specifically :

- *the APEX 12-m telescope*

  Since 2008, the bolometer array LABOCA (Siringo et al. 2008) of the APEX 12-m telescope to obtain complementary observations at a frequency of 345 GHz. Quasi-regular flux density measurements are performed during several dedicated APEX LABOCA time-blocks per year. These, however, are not coordinated with the EB and PV measurements and instead depend on the scheduling of the regular LABOCA sessions. At APEX, a sub-sample of 25 γ-ray blazars of the F-GAMMA sample are observed together with a sample of 14 southern hemisphere γ-ray AGN. Details including the first five years of data will be presented in Fuhrmann et al. (in prep). (see also Larsson et al. 2012).

- *the Caltech/OVRO 40-m monitoring program*

  In 2007 a program complementary to F-GAMMA was commenced at the OVRO 40-m telescope. It is monitoring a statistically complete sample of about 1200 blazars. This sample also includes all the sources that are monitored by the F-GAMMA program. The observations are performed at least twice a week making it a perfect companion to the monthly observations of the F-GAMMA program. For more details see also Richards et al. (2011)

- *Abastomani Observatory optical monitoring program*

  Abastomani Observatory observes a large sample of AGN since 1997 at the optical R band using the 70-cm and 125-cm telescopes (Kurtanidze et al. 2009). There is a large

overlap in monitored sources with the F-GAMMA sources.

- *Korea Astronomy and Space Science Institute: monitoring program with the KVN*

  An F-GAMMA collaboration has been established with the Korean VLBI Network (KVN) team using the KVN antennas for single-dish monitoring of γ-ray loud blazars at 22 and 42 GHz in total intensity and polarisation. The program started in 2010 and is performed monthly including most of the F-GAMMA sources.

Table 1.2: List of participating telescopes and projects in the F-GAMMA program.

Telescope	Band	Frequencies [GHz]	Diameter [m]	Remarks
EB	cm/mm	2.64, 4.85, 8.35, 10.45, 14.6, 14.6, 23.02, 32.0, 43.0	100	Total int. & polarization
PV	mm	86.24, 142.33, 228.24	30	Total int. & polarization
APEX	sub-mm	345	12	Quasi regular since 2007
OVRO	cm	15	40	bi-weekly
KVN	cm/mm	21.7 & 42.4	21	monthly since 2010
Abastomani	optical	R band	0.4	–

1.7 Scope of current thesis

The lack of continuous observations at a wide range of spectral bands and the lack of sufficiently dense sampled and long–term monitoring data prevented the detailed study of the broadband jet emission in the past. The analysis performed for the thesis in hand is accomplished within the framework of the F-GAMMA program, analysing the variability of light curves and quasi-simultaneous spectra of the first five years of F-GAMMA observations, allowing a detailed study of the broadband emission characteristics and variability scenarios.

While cm variability is believed to originate mainly at the outer parsec scales of jets, at higher frequencies the lower source intrinsic opacity allows a deeper and less obscured look into the central engine. Consequently, the variability in the mm bands probes the processes in the ultimate vicinity of the core and allows a far more direct study of the physics of the central engine than possible at cm bands. In the current thesis cm and short–mm variability is studied as a whole allowing for the first time to study the evolutionary paths of flares from frequencies as high as 142 GHz down to 2.6 GHz for such a large number of sources. Variability characteristics (amplitudes and time scales) and spectral characteristics (spectral indices, $S_{max} - \nu_{max}$ flare peak analysis) are presented along with estimations of brightness temperatures and Doppler factors. The thesis is organized as follows:

Chapter 2 provides general information of the source sample characteristics and the dataset that is used for the analysis. The observing methods utilized for observations performed at EB and PV , as well as a cross calibration study of the two aforementioned telescopes. Finally information the observing logistics is provided.

Chapter 3 presents the data reduction methods and post measurement corrections applied to the data acquired with EB and PV alongside with a detailed error budget analysis and a detailed study of the PV telescope system.

Chapter 4 describes the analysis tools and methods that are applied to the light curves and broadband spectra to obtain information such as: variability characteristics, flare amplitudes, flare time scales, spectral indices and spectral peak estimations.

Chapter 5 presents the results in the time domain of the analysis performed upon the five year of EB and PV combined light curves. The significance of variability through a χ^2 test is estimated as well as the flare amplitudes using a new analysis method for the estimation of the intrinsic variability of the light curves along with a new proposed k–index to quantify the variability across frequency. Finally flare time scales, brightness temperatures and Doppler factors are reported.

Chapter 6 presents the corresponding analysis in the spectral domain, including results for spectral indices and an $S_{max} - \nu_{max}$ analysis.

Finally *Chapter 7* provides the overall discussion and summary of the obtained results and the contribution of the thesis at hand. Finally a short description of future studies that can be based on the results obtained here is provided.

2 Observations

2.1 The Source sample

Since January 2007 the F-GAMMA program has been monitoring about 60 sources on a monthly basis, consisting of the most prominent, famous, frequently active, and usually strong blazars. In June 2009 a revision of the sample took place making the total number of sources that were ever observed within the program ∼90. The source sample that is used for the analysis presented here consists of the 59 sources of the revised F-GAMMA sample. The selection criteria of the original and the revised samples can be summarized as follows:

The original F-GAMMA sample: The F-GAMMA source sample observed between January 2007 and June 2009 consisted of 69 sources with a declination limit of $\delta > -30°$. A large fraction of these sources were selected on the basis of their previous γ–ray detection with the EGRET detector on board the Compton Gamma Ray Observatory (CGRO) and their presence in the "high priority" AGN/blazar list announced by the *Fermi*-LAT AGN group (Fuhrmann et al. 2007). Furthermore, the source selection was done so that a maximum overlap with existing cm and mm VLBI and other programs of similar kind is achieved. Of the 61 original sources monitored at PV , 35 sources were also part of the more general monitoring conducted by IRAM.

The revised F-GAMMA sample: After the launch and the first year of *Fermi*-GST operations a revision of the original sample was performed in June 2009 to exclusively include *Fermi*-GST detected sources. Specifically, 38 sources of the revised sample have already been in the original sample, while 31 have been replaced by new *Fermi* γ-ray sources. 34 sources are part of the more general monitoring conducted by IRAM. Furthermore, some of the new sources have data prior to June 2009, thanks to the IRAM program. The original

and revised samples are presented in Tables A.1 and A.2 along with some basic information.

It must be noted that the described F-GAMMA samples are not constructed according to strict selection criteria and are thus statistically incomplete. Generalizations of any findings must be made with caution. To address the incompleteness of the source sample and to enable statistically robust population studies of the variability properties of blazars, a statistically complete parent sample is needed. For this purpose sources located at $\delta > -20°$ where selected from CGRaBS (Healey et al. 2008) and are observed about twice each week at 15 GHz within the OVRO 40 m monitoring program (Richards et al. 2009).

2.1.1 Redshift distribution of F-GAMMA Blazars

For several studies that follow (Chapters 6 and 5) the knowledge of redshift (z) for monitored sources is important. The distribution of z for the revised sample for the FSRQs and BL Lacs is presented in Fig. 2.1. It is clear that FSRQs are systematically farther away compared to BL Lacs as expected. The mean value of z for all the sources in the sample is 0.77 with a median of 0.66 , while FSRQs exhibit a mean value of 1.18 and median of 1.14 and BL Lacs a mean value of 0.29 and median of 0.19.

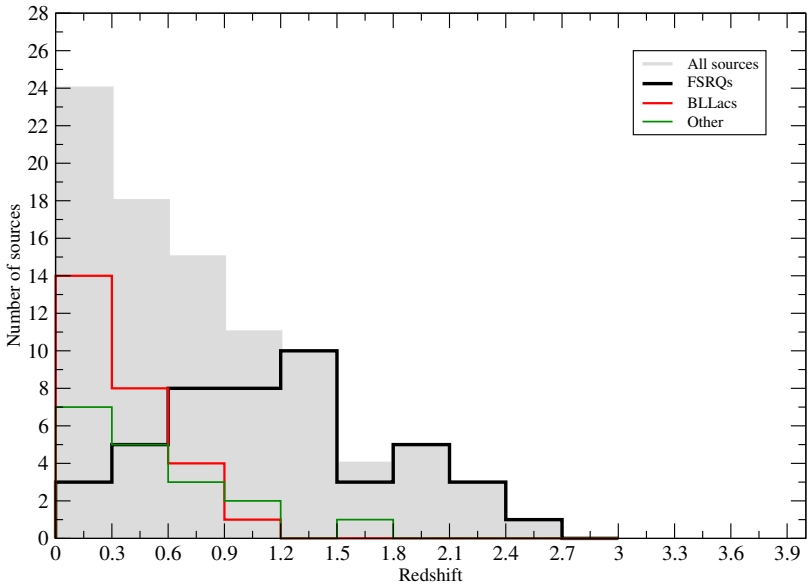

Figure 2.1: Redshift distribution of F-GAMMA blazars. All sources in Grey, BL Lacs in Red, FSRQs in Black and other types in Green.

For any physical quantities that are estimated from the analysis done for the current thesis (e.g brightness temperatures, Doppler factors, k-index), the redshift distribution is taken into account.

2.1.2 The Dataset

The dataset used for the following analysis covers the period from January 2007 to January 2012 i.e. the first five years of F-GAMMA observations. All sources in the revised sample

are utilized and given the limited sampling and time coverage of APEX, the analysed dataset is based on 10 different bands provided by EB and PV (i.e. 2.64, 4.85, 8.35, 10.45, 14.6, 23.05, 32, 42, 86 and 142 GHz, Table 1.2). Details for each source including J2000 coordinates, number of observations, redshift and source class are given in Table A.2.

Based on the BZCAT catalogue (Massaro et al. 2009) the optical classification of the revised sample is presented in Table 2.1 demonstrating that about 54 % of the sources are FSRQs and about 25 % are BL Lac objects. 7 sources, however, lack a detailed classification and are denoted simply as "Blazars".

Table 2.1: Summary of the optical classifications for the sources in the original and revised F-GAMMA samples.

–	FSRQs	BL Lacs	Blazar	Other
Orig. :	30 (49.1%)	23 (37.7%)	4 (6.6%)	4 (6.6%)
Curr. :	32 (54.2%)	15 (25.4%)	7 (11.9%)	5 (8.5%)

The number of sources of the original sample detected by *Fermi*-GST after the first 11 months of operation (Abdo et al. 2010b) is given in Table 2.2 demonstrating the high γ-ray detection rate for the original sample (81 %). Table 2.2 shows that BL Lac objects of the F-GAMMA sample have a higher detection rate than FSRQs. However the Large Area

Table 2.2: *Fermi*-GST detections for the different source classes of the original sample with respect to the 11–month source list (Abdo et al. 2010b).

Class	Sample fraction (%)	*Fermi*-GST detected	*Fermi*-GST non-detected
FSRQs	32 (51.6%)	26 (81.3%)	6 (18.7%)
BL Lacs	23 (37.0%)	21 (91.3%)	2 (8.7%)
Blazar	3 (4.8%)	1 (33.3%)	2 (66.6%)
Other	4 (6.5%)	2 (50.0%)	2 (50.0%)
Total	62 (100%)	50 (80.6%)	12 (19.4%)

Telescope (LAT) aboard *Fermi*-GST is a pair conversion telescope and source detection is biased towards the detection of "hard" spectrum sources owing to the strong energy dependence of the Point Spread Function (PSF) of the telescope (Abdo et al. 2009b). The detected BL Lac objects amount to half of the total detected sources by *Fermi*-GST . This explains the higher relative number of detected BL Lac objects compared to FSRQs in the F-GAMMA sample considering the selection criteria.

2.2 Observing methods

F-GAMMA as a monitoring program covers many years of observations. It is essential to conduct observations and reduce the acquired data continuously in a self–consistent way. This enables comparison of the results over the entire length of the program. The reduction techniques are described in Sections 3.3.3 and 3.1.2, for EB and PV data, respectively.

Inevitably throughout the years some changes occurred as for instance with the upgrade to the new EMIR receivers (see Sect. 3.1.1) or the change of the secondary mirror

at EB . In any case continuity and backwards compatibility was always insured with any previous status. In the case of the new EMIR receivers, possible cross–calibration differences between the two different receiver systems was investigated as well as other details of the EMIR receivers (see Sect. 3.1.3). All other details concerning the actual observations remained the same for both EB and PV during the F-GAMMA observations.

2.2.1 Observing modes

The notion 'observing mode' refers here to the method used to obtain an estimate of the flux density of a source (see also Wilson et al. 2009, for more details). There are two observing modes that can be combined with a switching mode (Sect. 2.2.2) to realize the observing method.

On–Off method

A 'On–Off' scan is defined by two distinct states of the telescope. The first one with the telescope pointing *on* the source for the required integration time and the second one with the telescope pointing *off* the source in a preferably empty portion of the sky for the subtraction of atmospheric effects. This method is highly time efficient and suitable for the detection of weak sources. For reasons that will be apparent bellow it was not chosen as the standard observing method for observations within the F-GAMMA program.

Cross–scans method

A 'cross–scan' is defined by the slew (scan) of the telescope over the target position (observed source) with a length of about 3-4 times the telescope beam width, producing a Gaussian profile as the result of the convolution of the source brightness distribution on the sky with the response pattern of the telescope. Examples of cross–scans are shown in Figs. 2.3 and 2.2 for PV and EB respectively. A typical cross scan made with EB consists of four sub–scans[1] as shown, two in each driving direction (Azimuth/Elevation). In Fig. 2.3 a typical example of a cross–scan with at PV is presented. Here again the scan is composed of four sub–scans two in each driving direction. whereas the azimuthal sub–scans are utilized with the double–beam technique.

There are several advantages of the cross–scans method: (a) it provides a very good estimate of the baseline, enabling us to easily subtract it, (b) it provides an excellent estimate of the instantaneous pointing error of the telescope (see Fig. 3.2). By having two consecutive cross–scans we can minimize the pointing offset of the second cross–scan by measuring the first one[2], (c) provides immediate information of confusing sources in the field near the studied source by examining the profile of the cross–scan, (d) provides immediate information if the source is point like or extended with respect to the telescope beam size. Confusion is especially important for lower frequencies where the telescope

[1] Every sub–scan is a cross–scan in a specific direction.
[2] See section 3.1.3 on how a pointing correction is done.

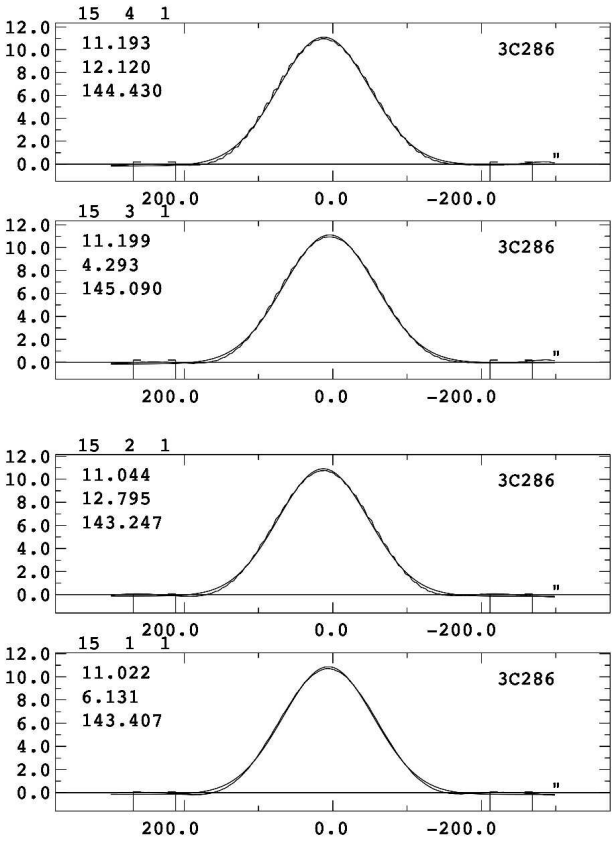

Figure 2.2: Example of a cross scan as it is taken with the EB 100 m telescope. This particular scan has four individual sub-scans. Two in each driving direction (AZI, ELV)

beam becomes large and thus the probability of having two or more sources in the field of view increases. For all the above reasons the cross–scan method is widely used at the EB for flux density measurements.

There are also some disadvantages of the method that should be taken into account: (a) cross–scans are less suitable for very weak sources. A considerable amount of integration time is spent slewing over the source, thus the actual time on source is small. (b) In consequence with the previous, in order to reach a usable flux density limit a cross-scan requires more observing time compared to the 'on–off' method. Thus when very low flux density levels are required the 'on–off' method is more suitable. For the F-GAMMA program all the sources were bright enough ($\geqslant 0.3$ Jy) and the aforementioned advantages of the cross scans method enabled a high accuracy in the determination of the flux density.

Measuring the flux density from cross scans As it can be seen in Fig. 2.2 the resulting response pattern of a cross–scan has a Gaussian shape. It is the convolution of the beam pattern and the brightness distribution of the source at the sky. The general method to calculate the flux density of a source observed with a cross–scan, is to calculate the area bellow the Gaussian profile which is represented by the integral of the Gaussian. Assuming that the source is point like and thus not resolved by the telescope, it can be proven

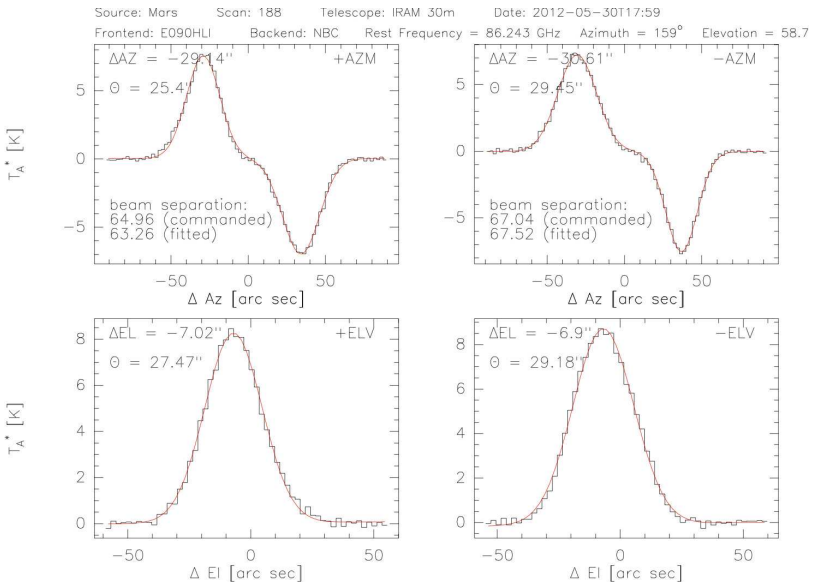

Figure 2.3: Example of a cross scan as it is taken with the PV 30 m telescope. This particular scan has four individual sub–scans, two in Azimuth and two in Elevation. The azimuthal sub–scans are with the double–beam technique.

that the integral is equivalent to the height of the peak of the Gaussian profile. The antenna temperature of a source is given by the peak of the Gaussian after the subtraction of it's baseline (see also Sect. 3.1.2).

2.2.2 Switching Modes

The notion 'switching mode' refers to the method used at a radio telescope to obtain an estimate of the observing system instabilities and noise. By 'observing system' the contribution of the telescope and the atmosphere is inferred. The goal of any switching method is to remove these effects and also the tropospheric perturbations that highly affect the quality of the data.

Beam Switching

Beam switching or else multi-beam observation, is a general method in which the signals from two different areas on the sky are subtracted from each other to remove atmospheric effects. For the PV 30 m telescope beam switching is realized through a rotating chopper wheel in the receiver cabin or by using the wobbler technique (see bellow). The use of chopper wheel dictates that in each rotation two reflecting blades are moved into the beam path for a total of four phases: (1) direct beam path to the source, (2) beam path offset by first blade, (3) direct beam path, (4) beam path offset by the second blade of the chopper wheel. The source signal is calculated as the difference between direct and offset phases. This 'chopper wheel' method should not be confused with the 'chopper wheel calibration' which is a different concept (see Sect. 3.1.1 for details on the latter).

For EB the beam switching method is utilized with physically different feeds placed at adjacent positions in the (primary or secondary) focus. One feed is pointing the source and

at the same time the other on an adjacent and empty position of the sky. This capability is not present for all the secondary focus receivers that are used by the F-GAMMA observations (see also Sect. 3.3.1). Software beam switching is the preferred method during the observations of the F-GAMMA program with the EB telescope.

Frequency Switching

Frequency Switching is usually used for observations of spectral lines. This mode switches the observing frequency between the desired frequency and one that is very different. So there are two phases, the final signal is calculated as the difference between these two phases. This method requires careful calibration as it requires that the receiver characteristics do not change over the phases.

Wobbler Switching

During wobbler switching the secondary mirror changes its position relative to the optical axis and thus changing the path of the beam and equivalently the position that the telescope is pointing on the sky is changing. The wobbling secondary mirror is switched between two positions, which are offset by a fixed amount. The first position being the 'source' and the second being the 'sky', thus there are two phases, and the signal is calculated as the difference between these two phases. Wobbler switching was used with the new *EMIR* system using a Wobbler throw of 240″and a frequency of 0.25 Hz. This 'wobbling' procedure offers several advantages for observations, in particular improved baseline quality. Currently the Wobbler only works in the azimuth direction for the PV 30 m telescope. Wobbling capability does not exist for the EB 100 m telescope.

In particular for the PV telescope if wobbler switching and the on–off method are combined, the effectively data are collected at three positions: (1) the source position, (2) the source position plus the throw from the wobbler, (3) the source position minus the wobbler throw. Data taken from the first phase are treated as source signal, data from phase two and three as the off–source reference signal.

2.2.3 Focus & Calibration

"Focus" refers to the procedure of maximizing the response of the telescope to the incoming radiation. This is done by moving the receiver to the focal point of the telescope or equivalently the focal point to the receiver. The latter can be achieved by changing the distance of the secondary mirror to the primary mirror. This technique is implemented in EB for practical reasons.

A typical F-GAMMA observing session lasts several hours. During this time, temperature changes periodically from day to night and also randomly due to fast changing weather conditions. Temperature can lead to expansion and contraction of the telescope structure which affects the position of the focal point thus it is of uttermost importance to

focus regularly. The strategy that is implemented for a typical F-GAMMA observing run is the following:

- focus the telescope when the observing session starts
- focus always after a large change in temperature and always when the temperature is stabilized. This usually is the case during day–night changes
- focus the telescope again, always when there are large gaps during the observing session

"Calibration" refers to the procedure of observing a source with known flux density that is stable over time. The goal is during the reduction of data to relate the system temperature of the telescope to the physical value of Jy (Sect. 3.3.4). It is important to calibrate as often as possible and with different calibrator sources, in order to detect and later correct any systematic deviations of focus or any other problems that could occur.

Using several calibrators sources (Table 3.8), the calibration strategy that is followed during observations is the following:

- calibrate at the beginning of the observing session before the first target source is observed
- calibrate every 3–4 hours
- when there is a large gap of time between sessions then always start with a calibration
- calibrate always at the end of the observing session

Usually focus and calibration is performed at the same time using the same calibrator for both procedures. This tactic saves time and increases the number of calibration measurements taken. In the case a calibrator is not high in the sky to perform a focus, then a target source is used that has high flux density and is unresolved by the telescope in all the frequencies that the focus is performed.

2.3 EB - PV cross calibration

In this section the accuracy of the relative calibration between the EB and PV stations is discussed. Because the two telescopes observe at very different frequencies (EB: $\nu \leqslant 43\,\mathrm{GHz}$ and PV: $\nu \geqslant 86\,\mathrm{GHz}$), one must rely on the spectral properties of a calibrator source.

NGC 7027 has a well defined as well as stable spectrum and is being observed by both telescopes. Its spectrum is mildly convex and follows a power law of the form $S = k \cdot \nu^{-0.1}$ at frequencies above 10 GHz. In Fig. 2.4 is shown: (a) the observed mean spectrum (yellow curve), (b) the theoretical spectrum (Zijlstra et al. 2008) (green curve). In black is shown

the power law $S = k \cdot \nu^{-0.1}$ as determined by the theoretical spectrum in the range 15 to 43 GHz and extrapolated to the PV frequencies.

It is apparent that the observed EB spectrum agrees well with the theoretically expected one. These divergences are calculated for every frequency and the results are presented at Table 2.3. It is clear that the mean divergence for most of the frequencies is better than $\sim$ 2%. The highest divergence is observed at 228 GHz. This is not due to the influence of weather, which would cause only a scatter and not a systematic divergence but mainly due to an imperfect beam correction factor at this frequency. NGC 7027 at these high frequencies is not point like and furthermore is expanding with time (Zijlstra et al. 2008) making it more difficult to estimate a proper correction. It should be noted though that this affects nothing in terms of analysis and conclusions in this thesis, since 228 GHz data are note used.

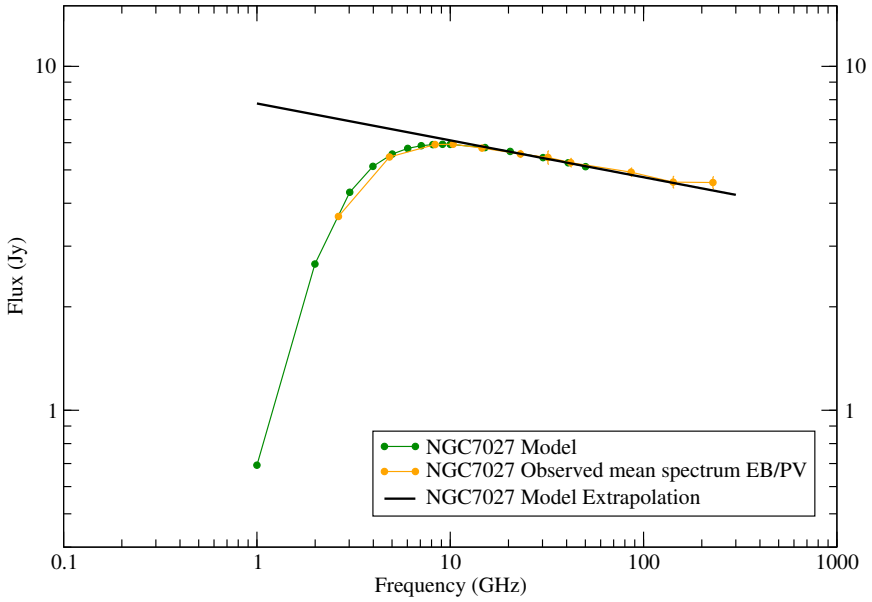

Figure 2.4: The radio spectrum of NGC 7027 as observed with EB at 2 to 43 GHz and with PV at 86 to 230 GHz. A very good agreement with the theoretical spectrum is indicative of the good cross-calibration between both telescopes.

Table 2.3: Observed and theoretical spectrum divergence of NGC 7027. For every frequency in the first row the percentage divergence is given in the second row.

Freq (GHz)	2.64	4.85	8.36	10.45	14.6	23.05	32.0	42.0	86.24	142.33	228.24
Percentage (%)	3.0	1.47	0.1	0.12	1.18	0.12	1.22	0.38	1.96	0.61	5.6

2.4 Observing logistics

2.4.1 Time allocation

Since June 2007, the monthly F-GAMMA EB observations are complemented by PV observations at 3, 2 and 1 mm wavelength (86–270 GHz) in order to increase the spectral coverage from the longer cm/mm bands observed at EB to the important short-mm bands.

Similar to EB, the flux density monitoring at PV is performed in monthly scheduled observing blocks. Given the demand for quasi-simultaneity of the flux measurements at EB and PV due to the extreme inherent variability of the observed source sample, a high degree of synchronization (typically days up to about one week) between the EB/PV observing blocks is achieved with a mean coherence time of 2.26 days during the first five years of observations (see Table 2.4).

Furthermore, the PV monitoring is performed in close collaboration and coordination with the existing 'classical' flux density monitoring program at PV (Steppe et al. 1988, 1992, 1993; Reuter et al. 1997; Ungerechts et al. 1998) due to a large overlap of monitored sources. As a result, (i) the overall sampling for many sources could be improved and any observing time losses (e.g. due to weather) during the regular blocks could be significantly compensated through the adjacent observing blocks of the 'classical' monitoring program, (ii) common observing, data reduction and analysis procedures have been implemented as well as an optimization of the observing strategy and data archiving could be achieved, (iii) the available F-GAMMA data sets could be extended to January 2007 for overlapping sources of the two programs.

2.4.2 Coherence time and Sampling

The sampling of an observing session is defined as the number of measurements[3] divided by the time span of this session. The effective sampling achieved in real observing conditions is always lower than the ideal sampling, which is the sampling that theoretically can be achieved according to the observing time allocated at each telescope. The effective sampling is lower because of (a) sometimes poor weather conditions resulting to bad data that are eventually flagged (b) telescope and general hardware problems resulting in telescope down times.

Due to the design of the observing system and receivers used at PV (see Sect. 3.1.1), the obtained flux densities are truly simultaneous for each source and epoch, in contrast to EB , where practically a full cm/mm spectrum requires about 35–40 minutes. The reason being that a successive scanning through all secondary focus receivers is required. In order to finally obtain broadband cm/mm spectra demanding the best possible quasi-simultaneity, the individual EB/PV data sets are combined allowing a maximum coherency time of ± 10 days as a compromise between minimum simultaneity and maximum number of combined EB/PV spectra. Consequently, the mean effective coherency time of a full broadband spectrum is 2.26 days for the first five years of observations. Table 2.4 summarizes the effective spectral coherency times obtained individually at EB and PV, as well as the combination of both.

The effective sampling reached at PV is lower compared to the nominal of one measurement per month per source due to uncontrollable effects. Periods of bad weather conditions, in particular high wind speeds and snow during the winter periods, as well as (minor) technical issues cause telescope downtime, influencing the overall observing

[3]One measurement is defined by a coherent spectrum.

Table 2.4: Mean spectrum coherency and mean effective sampling for PV and for the combination of the PV and EB .

	Eff. Sampling (Months)	σ	Spect. Coher. (Days)	σ
PV	1.41	0.61	0	0
EFF	1.45	0.58	0.11	0.15
EFF+PV	1.21	0.39	2.26	1.41

efficiency and therewith the sampling of each individual source. In the latter case, for example, the PV receiver upgrades in 2009 (see Sect. 3.1.1) and the secondary mirror change in EB resulted in a telescope downtime. Higher wind speeds $> 10\,\mathrm{m\,s^{-1}}$ cause tracking errors and dish deformations and consequently, increasing pointing errors (see Sect. 3.1.3 and Table 3.1) which limits telescope operation. The resulting mean effective sampling rate is 1.41 months for the first five years of observations at PV. At EB effectively due to the reasons mentioned above this value is a bit larger at 1.45 months. The combination of the two though results in a mean sampling of 1.21 months.

3

Pico Veleta & Effelsberg data

3.1 The IRAM 30–m telescope

One of the largest and most sensitive single dish telescopes at short–mm bands is the IRAM 30 m, equipped with heterodyne receivers operating at 3, 2, 1, and 0.9 mm wavelengths. It is located on Pico Veleta in the Spanish Sierra Nevada, at an altitude of 2850 m. The telescope design is a single dish antenna with a parabolic surface adjusted to a precision of 55 micrometers, corresponding to the width of a human hair. In this section a description of the receivers, the overall observing system and the reduction methods used within the F-GAMMA program is given.

Figure 3.1: The PV 30 m radio telescope.

3.1.1 PV System Description

The ABCD & EMIR receivers

Until mid–March 2009, the observations were conducted using the 'ABCD' SIS heterodyne receivers mounted in the receiver cabin of the 30-m telescope (Baars et al. 1987). Nasmyth mirrors, a splitter box and a set of Martin-Publett Interferometers fed the signal from the subreflector into the eight single pixel, dual (V/H) polarization receivers (A/B 100, C/D 150, A/B 230, C/D 270). Only four out of the eight channels could be used simultaneously, resulting in a truly instantaneous spectrum. The 'BC' combination was used as the standard configuration providing single polarization channels B 100, B230,

C 150, C 270 (each with a bandwidth of 1 GHz) tuned to 86.2, 142.3, 228.9 and 261.0 GHz, respectively, and with a continuum backend attached. The latter provides a bandwidth of 0.5 GHz for the B 100 and 1 GHz for the rest of the receivers.

During a major receiver upgrade in March 2009, the old 'ABCD' system was replaced by the Eight MIxer Receiver (EMIR, Carter et al. 2012) and after its commissioning at the end of April 2009 is used as the new standard system for continuum measurements within the F-GAMMA program and the monitoring by IRAM. EMIR offers four bands that cover four atmospheric windows around 3, 2, 1.3, and 0.9 mm wavelength, each in 2 linear polarizations (horizontal and vertical); however, only two bands can be used simultaneously. For the observations undertaken for this thesis within the F-GAMMA program, only 3 mm and 2 mm bands tuned to the same frequencies as previously the 'B' and 'C' receivers were used. For the current analysis data from the narrow band continuum backends (NBC) were used, which limit the bandwidth to 1 GHz. With these backends the data are also restricted to a single sideband.

Table 3.1: System characteristics of the ABCD and EMIR receivers including bandwidth (BW) and typical values of receiver temperature ($T_{\rm rec}$), Jy/Kelvin conversion factor (Γ), Full Width Half Maximum (FWHM) and pointing offset.

Receiver	Freq. (GHz)	BW (GHz)	Polarization	$T_{\rm rec}$ (K)	Γ factor (Jy · K^{-1})	FWHM (″)	Pointing offset (″)
B 100	86.24	0.5	Linear	$\sim$ 75	$\sim$ 6.2	29.0	$\sim$ 0.5
C 150	142.33	1.0	Linear	$\sim$ 100	$\sim$ 7.8	16.0	$\sim$ 1.0
B 230	228.93	1.0	Linear	$\sim$ 220	$\sim$ 8.9	10.5	$\sim$ 0.8
*C*270	261.0	1	Linear	$\sim$ 250	—	9.5	—
E 090	86.24	8	H/V	$\sim$ 65	$\sim$ 5.9	29	$\sim$ 0.7
E 150	142.33	4	H/V	$\sim$ 65	$\sim$ 7.0	16	$\sim$ 0.5

As it will be discussed in Sect. 3.2, a significant improvement in data quality is evident after the change to the EMIR receivers. In Fig. 3.5 the secondary calibrator NGC 7027 and the target source J0238+1636 are shown demonstrating this effect, which is mainly due to better receiver temperature. Table 3.1 provides a summary of the main *EMIR* system parameters, whereas Table 3.4 provides the mean fractional errors before and after the change of the receivers.

The 'Chopper wheel calibration'

The traditional calibration method applied at the PV telescope is called *"chopper wheel method"* (Ulich 1980; Mauersberger et al. 1989) and a short overview is given bellow. The goal of the calibration method is to relate backend counts to antenna temperatures. This method should not be confused with the physical 'chopper wheel' used during beam switching (see Sect. 2.2.2) In order to relate these two quantities two sources with known temperature are needed.

The receiver temperature ($T_{\rm rec}$) The first of these sources is the *"chopper"* which is the hot load at approximately room temperature. The second source is called the cold load

and it is at the temperature of liquid nitrogen. In both of these two sources, the counts that a specific channel and backend is getting, are measured and averaged. Assuming a linear detector the counts that are measured are proportional to the temperature of the source. In this way we can measure in a general way the receiver temperature. Thus is given by:

$$T_{rec} = \frac{T_{chop} - Y \cdot T_{cold}}{Y - 1} \tag{3.1}$$

where Y is given by:

$$Y = \frac{\langle C_{chop} \rangle - \langle c_{off} \rangle}{\langle C_{cold} \rangle - \langle c_{off} \rangle} \tag{3.2}$$

In the above equations (3.1) and (3.2) the symbols T_{xx} and C_{xx} denote temperature and counts respectively. In eq. (3.2) the $\langle c_{off} \rangle$ term is called *"Dark counts"* and it is a constant that must be subtracted. It represents the counts that arise in a backend even if no signal is coming from the frontend. $\langle C_{chop} \rangle$ and $\langle C_{cold} \rangle$ are defined by:

$$\langle C_{chop} \rangle = \langle c_{off} \rangle + \left(T_{chop} + T_{rec} \right) \cdot \mathrm{g}$$
$$\langle C_{cold} \rangle = \langle c_{off} \rangle + \left(T_{cold} + T_{rec} \right) \cdot \mathrm{g}$$

where g is the varying gain factor to be calibrated out.

The receiver temperature given by Eq. 3.1 can be used to evaluate the performance of the receiver including the optics and the backend but with the advantage that we don't have to consider atmospheric fluctuations.

The system temperature (T_{sys}) Our final goal is to evaluate the receiver noise temperature plus the contribution of the atmosphere, i.e. the system temperature (T_{sys}) . This is the value that later all the corrections will be made upon. In order to calculate this we need to find the relation that gives us the temperature of the calibration signal (T_{cal}). Essentially what it is done is to relate the difference of counts between the source and the blank sky $\langle C_{\mathrm{source}} \rangle - \langle C_{\mathrm{atm}} \rangle$ to the difference of counts between the hot load and the blank sky $\langle C_{\mathrm{source}} \rangle - \langle C_{\mathrm{atm}} \rangle$. It can be proven that the calibration signal is given by:

$$T_{cal} = \frac{\Delta C_{cal}}{\Delta C_{source}} \cdot T_A^* \tag{3.3}$$

where T_A^* is the antenna temperature corrected for the attenuation of the atmosphere. Finally the system temperature it will be given by:

$$T_{sys} = T_{cal} \cdot \frac{\langle C_{atm} \rangle}{\langle C_{chop} \rangle - \langle C_{atm} \rangle} \tag{3.4}$$

Table (3.1) and (3.1) shows typical values of system temperature for the various receivers used during the F-GAMMA program.

The above calibration procedure has some assumptions that should be taken into account.

- All of the above loads are considered to be black bodies with their physical temperature being equivalent to their Rayleigh–Jeans radiation temperatures (i.e. $h\nu \ll kt$)
- The temperature conductance of the external cold load is high enough, that the cold load has a physical temperature at its entire radiating surface
- The ambient temperature measured within the receiver cabin is the same as that of the hot load
- Counts are directly proportional to the incoming power
- The amplification of the system does not change on time scales smaller than the time required for the calibration procedure to finish.

Observing technique

Since all target sources are point like for PV and sufficiently bright at mm-bands, the monitoring observations at PV are performed with "pointing" scans across the source in azimuth and elevation direction (cross-scans), using a larger number of sub–scans for weaker sources. For the given flux density range covered by the monitored sources ($\sim$0.3–19 Jy), typically 2 to 4 sub-scans per direction (each of about 30 to 45 seconds) provide sufficiently high Signal-to-Noise (SNR). The pointing off-sets are typically less than 2″(see Table 3.4).

The cross-scans are usually preceded by a calibration scan to obtain instantaneous opacity information and to relate the backend counts to the antenna temperature scale $T_{\rm A}^{*}$ corrected for atmospheric attenuation (see below). Furthermore, with the 'BC' receivers beam switching is used with a frequency of about 5 Hz. Since the change to EMIR, wobbler switching is used for the pointing scans, during which the secondary (sub-reflector) is switched by $\pm$33″along azimuth with a frequency near 2 Hz. This change of switching mode contributes to an improvement of the data quality, particularly during not ideal weather conditions.

3.1.2 Data reduction

In this section the details of the data reduction process, are described. In summary, the necessary steps for extracting finally calibrated flux densities from raw measurements, are:

- Measuring the antenna temperature from the telescope response pattern for every sub-scan (Sect. 3.1.2).
- Data quality control and consequent filtering out of bad measurements. This "flagging" is done on a sub-scan level (Sect. 3.1.2).
- Averaging the remaining sub-scans in each scanning direction(Azimuth/Elevation) separately and measuring the resulted antenna temperature (Sect. 3.1.2)

- Remove possible residuals by filtering out bad measurements using the same criteria as before (Sect. 3.1.2)
- Applying post-measurement corrections (Sect. 3.1.3) to account for: pointing offsets, gain variations caused by the elevation dependence of the telescope
- Perform absolute calibration to obtain final values in Jy, or as usually called "sensitivity" correction (Sect. 3.1.3).

For all these steps the standard installation of Mira at Pico Veleta has been used along with IDL routines developed at MPIfR.

Reduction of cross-scans with Mira

This is the first step of the reduction and its objective is to measure the observed *antenna temperature* from the telescope response pattern. Specifically, the parameters of the Gaussian profile fitted to the observed response pattern for each sub-scan, are: (a) the *amplitude*, which corresponds to the measured *antenna temperature*, (b) the *Full Width at Half Maximum (FWHM)*, corresponding to the telescope's *beam size* and (c) the *offset*, corresponding to the true, as opposed to the assumed position of the targeted source, thus giving the *pointing offset*.

This step is processed entirely by the default reduction software of the PV 30 m telescope, called *Mira*, which also performs atmospheric opacity corrections. The result is the raw determination of:

- $T_{\rm obs}$: measured antenna temperature (equal to the amplitude of the fitted Gaussian)
- Δp: the measured pointing offset (the distance of the ideal telescope position compared with the measured one)
- $FWHM$: the full width at half maximum of the telescope beam (assuming a point-like source)

Data quality checks and sub-scan flagging

In order to ensure the quality of the final dataset, the measurements (on the sub-scan level) must fulfil some minimum quality criteria in the same manner as followed with EB data (see Sect. 3.3.3). Sub-scans that fail to pass those are flagged out of the consequent data reduction procedure. With the following set of criteria it is found that high data quality with minimum data loss can be obtained:

1. *Non-converging fits:* Bad weather conditions characterized by non linear tropospheric fluctuations lead to poor data quality (e.g. low signal-to-noise ratios, SNR). Here, often the fluctuations in the telescope response pattern are so large that the Gaussian fitting algorithm does not converge. Clearly, such sub-scans are excluded i.e. flagged out. An exception to this procedure is applied for the weakest sources in the

monitored sample, i.e. sources with flux densities $\lesssim 0.3$ Jy. In order to increase their SNR no sub-scan flagging is performed and the method described in Sect. 3.1.2 is followed.

2. *FWHM criterion:* Bad weather conditions also affect the fitted $FWHM$. The result is an either overestimated or underestimated measurement. For that matter, the observed $FWHM$, at any given frequency ν [GHz], is required to agree with the known value of the $FWHM$ of the main telescope beam, given by $2390''/\nu$ [GHz] within 45 %. For calibrator sources that are not point-like with respect to the telescope beam size (e.g. NGC 7027), this criterion is not applied (see also Sect. 3.1.3).

3. *Pointing offset criterion:* A number of factors such as low SNR, imperfect pointing model, temperature gradients in the telescope structure, induce high pointing offsets resulting in a power loss which may be significant. In cases of relatively small offsets the "real" antenna temperature (which should be recorded if the telescope was exactly on source) can be recovered as described in Sect. 3.1.3. In extreme cases however the measurement is irrecoverable. To avoid such cases the pointing offset Δp is required to be less than 35 % of the $FWHM_\nu$.

Averaging over sub-scans

At this step, all the sub-scans that have passed the quality checks mentioned (Sect. 3.1.2) earlier are averaged to extract a reliable estimate of the measured antenna temperature. The averaging is done for the sub-scans in each direction separately thus producing one average sub-scan per scanning direction (AZI/ELV). After fitting a final Gaussian to extract the observables as already discussed, the same flagging criteria described in Sect. 3.1.2 are applied to the two (AZI/ELV) scan directions. This ensures that only those scans are further processed which show good agreement between AZI and ELV results. The calculated parameters are then further corrected as it is described in Sect. 3.1.3.

The procedure of first calculating the average in a specific direction and then fitting a Gaussian, is chosen over the reverse operation of fitting the sub-scans with a Gaussian and then averaging the resulting parameters. The result is an increase in the SNR (signal to noise ratio) which greatly helps the fitting algorithms to determine the various parameters.

Primary & Secondary calibrators

Frequent observations of the primary calibrators, Mars and Uranus, or the secondary calibrators, W3(OH), K3-50A and NGC 7027 (HII regions/planetary nebulae), provide for each session conversion factors that relate the antenna temperature to the standard flux density scale (see Sect. 3.1.3). For the calibrators the same observing modes are used as for the targets. Their flux densities are summarized in Table 3.2.

Mars measurements indicate that is approximately a black body in the frequencies observed at PV because of its solid and tenuous atmosphere (Griffin et al. 1986). Is very bright making it very useful for focusing and calibrating under bad weather conditions.

Table 3.2: Calibrators at the PV -30 m telescope.

Calibrator	86 GHz (Jy)	142 GHz (Jy)	228 GHz (Jy)
NGC7027[1]	4.84	4.58	4.35
K3-50A[2]	6.28	6.20	6.91
W3OH[2]	3.95	4.30	6.31

Values are taken from : [1] Zijlstra et al. (2008)
[2] Reuter et al. (1997)

Uranus on the other hand is much weaker than Mars its brightness temperature is also well known. Also due to its larger distance from the sun its brightness varies much slower. This fact makes it easier to predict its brightness temperature and thus making Uranus also a good calibrator.

3.1.3 Post-measurement corrections

Pointing offsets correction

Due to residual errors of the pointing model, the telescope is not pointed exactly on source resulting in pointing offsets in one or both directions (ELV/AZI). For observations performed with the PV telescope, the strategy followed is the minimization of the slewing distance by observing sources consecutive that are close to each other in the sky. In this way the pointing corrections of the first source are used as input for the next one. The

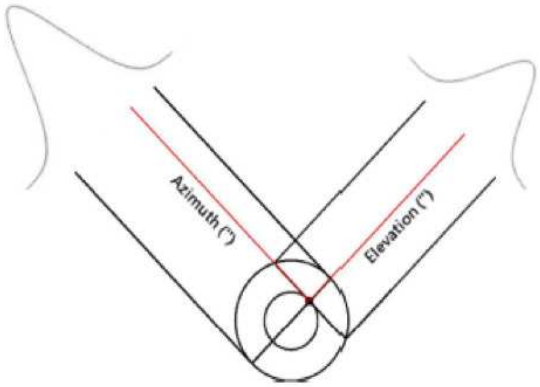

Figure 3.2: Representation of the principal behind the pointing error and it's correction. Source is on axis for the direction of elevation but is of axis for the Azimuth (Figure: Nicola Marchili).

mean pointing offset achieved within the F-GAMMA observations, for every receiver can be seen in Table 3.1. As it can be seen in Fig. 3.2 a large offset in the Azimuth axis will cause an underestimation of the flux density in the Elevation axis and vice versa. From the residual pointing offsets the result is an underestimation of the received flux density. After averaging the sub-scans in each direction, the parameters of the fitted Gaussian profiles allow correcting for these pointing offsets. Assuming that the telescope beam pattern is approximated sufficiently well by a circular Gaussian, the pointing offset in one scanning direction is used for correcting the power measured in the other direction. On the

basis of this assumption, the pointing-offset corrected antenna temperature in direction i, $T_{i,\mathrm{poi}}$ will be a function of the pointing offset measured in the direction j and vice versa:

$$T_{i,\mathrm{poi}} = T_{i,\mathrm{obs}} \cdot \exp\left(4 \cdot \ln 2 \cdot \left(\frac{\Delta p_j}{FWHM_\nu}\right)^2\right) \tag{3.5}$$

where :

i, j	the scanning direction indices with i : ELV, AZI and j : AZI, ELV
$T_{i,\mathrm{poi}}$	the antenna temperature in the direction i after the pointing correction
$T_{i,\mathrm{obs}}$	the observed antenna temperature in the direction i before the pointing correction
Δp_j	the pointing offset, calculated from Gaussian fitting, in j direction
$FWHM_\nu$	the reference FWHM for the observing frequency ν.

Assuming that the uncertainty $e_{i,\mathrm{poi}}$ in $T_{i,\mathrm{poi}}$, is depended on (a) the scatter of the power received in the corresponding sub-scans (see also Sect. 3.1.4) and (b) the uncertainty in the computation of the pointing offset, the formal error in a specific direction will be given by:

$$e^2_{i,\mathrm{poi}} = \left[\exp\left(4 \cdot \ln 2 \cdot \frac{\Delta p_j^2}{FWHM_\nu^2}\right) \cdot e_{T_{i,\mathrm{obs}}}\right]^2 + \left[\frac{T_{i,\mathrm{obs}} \cdot \exp\left(4 \cdot \ln 2 \cdot \frac{\Delta p_j^2}{FWHM_\nu^2}\right) \cdot 8 \cdot \ln 2 \cdot \Delta p_j \cdot e_{\Delta p_j}}{FWHM_\nu^2}\right]^2 \tag{3.6}$$

where :

$e_{T_{i,\mathrm{obs}}}$	is the error in the determination of the antenna temperature by the fitting algorithm in the i direction. It is the scatter of the power received from the averaged sub-scans
$e_{\Delta p_j}$	is the error in the calculation of the pointing offset by the fitting algorithm in the j direction.

The derivation of Eq. 3.6 is described in section (3.1.4).

In the case that the method of first fitting the sub-scans and then averaging the resulted parameters (Sect. 3.1.2) is chosen, then the error $e_{T_{i,\mathrm{obs}}}$ will be replaced by the scatter σ (i.e. *rms*) of the averaging parameters and Eq. 3.6 will have an approximate rather than a definite form. The reason to use σ rather than the error in the mean, is because the scatter is a more conservative estimate.

Gain–elevation correction

The next correction that must be applied to the data is meant to correct for elevation-dependent gain variations. For the estimation of the gain curve of the telescope, archival data were used (Greve et al. 1998). There, the On-axis gain-elevation dependence ($G_0(\varepsilon, \varepsilon_0)$)[1] was measured in 10 degree steps of elevation angle. Taking these values and performing a second order polynomial fit the detailed behaviour of the telescope across all the usable elevation angles is obtained (Eq. 3.7). In Fig. 3.3 a graphical depiction of this behaviour is shown.

$$\mathrm{G}(x) = \mathrm{a2} + \mathrm{a1} \cdot x + \mathrm{a0} \cdot x^2 \tag{3.7}$$

were x is elevation and a0, a1, a2 are the parameters of the polynomial. The fitted values can be seen in Table 3.3 for the frequencies utilized at the PV telescope.

Table 3.3: Fitted gain curve values for 86, 142 and 228 GHz.

Freq. (GHz)	a_0	a_1	a_2
86	$-2.67 \cdot 10^{-5}$	0.0023	0.948
142	$-5.91 \cdot 10^{-5}$	0.0053	0.876
228	$-1.19 \cdot 10^{-4}$	0.0103	0.766

According to the elevation of every scan during the observations, the following formula is used for correction along with the corresponding error:

$$T_{\mathrm{gain}} = \frac{T_{\mathrm{poi}}}{G} \tag{3.7a}$$

$$e_{\mathrm{gain}} = \frac{e_{\mathrm{poi}}}{G} \tag{3.7b}$$

where :

- T_{poi} the antenna temperature (K) after the pointing correction, to be corrected for elevation-dependent gain losses
- T_{gain} the antenna temperature (K) after the elevation-dependent gain correction
- e_{poi} the error in T_{obs} as derived from Eq. 3.6
- e_{gain} the formal error in T_{gain}
- G the fractional gain loss normalized at unity as given by Eq. 3.7

[1] where ε is the elevation angle and ε_0 is the angle at which the reflector is free of gravity deformations. This angle for the PV 30 m telescope is $\varepsilon_0 = 43°$ (Greve et al. 1998)

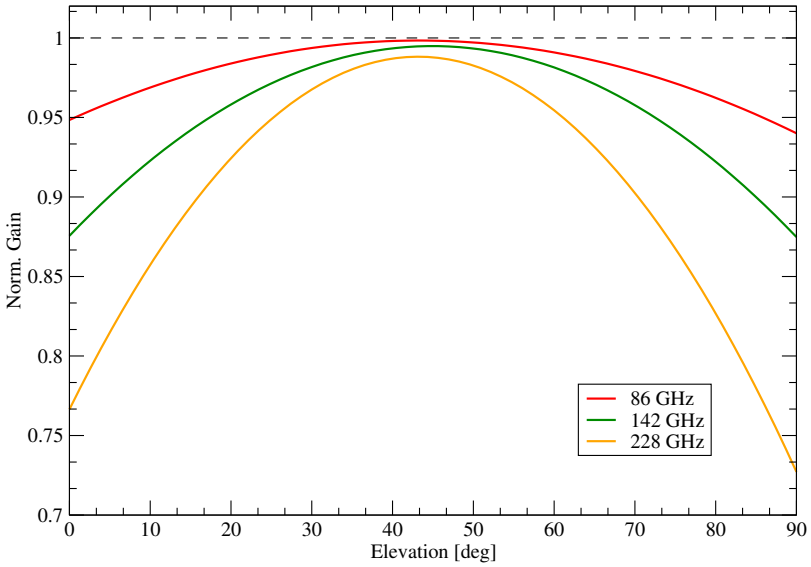

Figure 3.3: Normalized gain curves for 86, 142 and 228 GHz (see also Table 3.3)

Absolute Calibration

Throughout the previous discussion the observable has been the antenna temperature in units of K. Its conversion to flux density S in units of Jy, is the last step of the data reduction (sensitivity correction). It is done by comparing the antenna temperature of sources with their flux density known (calibrators). The used calibrators along with their assumed flux density can be seen in Table 3.2. The values of NGC 7027 are the extrapolated values of a theoretical model as discussed in Sect. 2.3. For the planets on the other hand a semi-analytical model is used to calculate the expected flux density as a function of epoch. The uncertainty in this model is better than 5 % (Reuter and Kramer 1998; Ulich 1981; Ulich et al. 1980) For every scan of a calibrator a calibration factor Γ has been calculated. Consequently an average value $\langle\Gamma\rangle$ for the whole observing session has been computed. The flux density and the associated error of a scan, is then:

$$S_{\mathrm{sens}} = \langle\Gamma\rangle \cdot T_{\mathrm{gain}} \tag{3.7c}$$

$$e^2_{\mathrm{sens}} = \left(\langle\Gamma\rangle \cdot e_{\mathrm{gain}}\right)^2 + \left(T_{\mathrm{gain}} \cdot e_{\langle\Gamma\rangle}\right)^2 \tag{3.7d}$$

where :

T_{gain}	the antenna temperature to be converted to flux density, after all other corrections are applied
$\langle\Gamma\rangle$	the mean calibration factor in Jy/K
e_{gain}	the error in T_{gain} (Eq. 3.8)
$e_{\langle\Gamma\rangle}$	the formal error in the derivation of $\langle\Gamma\rangle$

Mean values of Γ factors are shown in Table 3.1.

EMIR related corrections

The steps described in Sect. 3.1.3 are applied to all observed data independently of the receiver used. However, the two polarization channels of the new EMIR receivers, are two independent systems with same characteristics but non-identical behaviour and thus the receiver gain differs mildly between the two polarizations. By examining all available data from calibrators acquired with the EMIR receivers, it has been found that this difference is of the order of $\sim 2\%$.

The gain ratio between the two polarizations, was found to be $H/V = 0.98$[2] at 86 GHz. To correct for this, the Vertical channel was taken as a reference and the Horizontal was scaled accordingly. After this correction the final flux densities are calculated by averaging the two polarizations (Horizontal and Vertical). As seen from Fig. 3.4 no significant difference is found at 142 GHz.

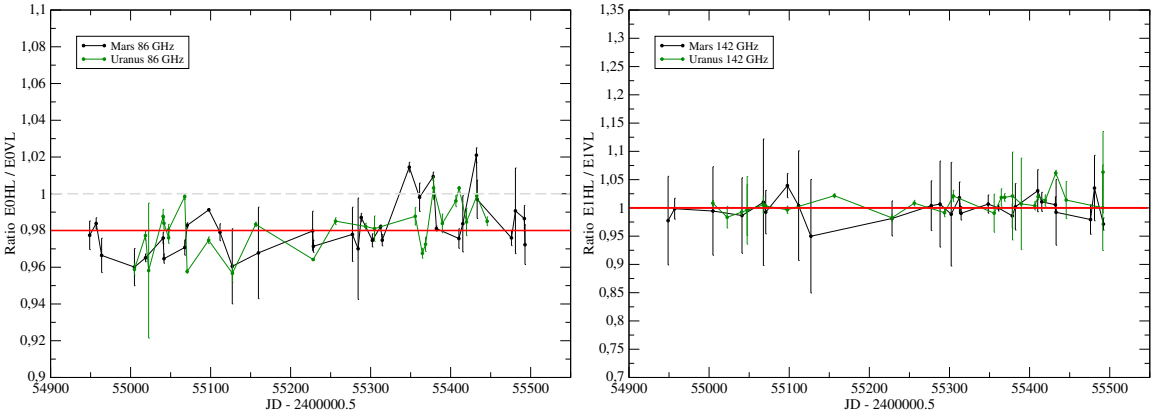

Figure 3.4: Gain ratio between the Horizontal and Vertical polarization channels of the EMIR receivers at 86 GHz (left panel) and 142 GHz (right panel). Data for the main calibrators Mars and Uranus are shown. Red lines represent the mean ratio at each frequency. The grey dashed line on the left panel represents the expected ratio. While both calibrators behave similarly, a significant offset from unity is evident only at 86 GHz.

3.1.4 Error estimates

The uncertainty in any of the observables discussed here is the result of several factors. In order to realistically estimate the errors on every step of the data reduction, two general rules have been applied:

1. For every operation that is performed to any observable, the formally propagated error that the particular operation is introducing to the observable, is computed. The general Eq. 3.8 is applied:

$$e_x^2 = \left(\frac{\partial x}{\partial a} \cdot e_a^2\right)^2 + \left(\frac{\partial x}{\partial b} \cdot e_b^2\right)^2 + \dots \tag{3.8}$$

[2](V) for Vertical and (H) for Horizontal polarization.

where :

e_x	is the propagated error of an observable
$x(a, b, \ldots)$	is the observable that is depended on the quantities a,b,...
e_a, e_b	are the coresponding errors of the quantities a,b,...

2. In any averaging operation apart from the formally propagated error, also the scatter of the elements over which the averaging is performed is taken into account. Eq. 3.9 is applied in this case:

$$e_x^2 = \left(\frac{\sqrt{\sum e_i^2}}{N_i} \right)^2 + \sigma^2 \tag{3.9}$$

where :

e_x	is the error in the average
e_i	are the individual errors of the elements that are being averaged
σ	is the standard deviation of those elements.

Equations 3.6, 3.8 and 3.8 are worked out on the basis of these rules.

Pre–correction error estimates

Bellow there will be a description of the error estimates before all the corrections (described bellow) are applied to the data. As described at Sect. 3.1.2 the products of the fitting procedure with MIRA are:

$T_{\rm obs}$	the observed antenna temperature
$e_{T_{\rm obs}}$	the error in the determination of that temperature.
Δp	the pointing offset calculated from the fitted Gaussian
$e_{\Delta p}$	the error in that offset.

For the example here, the data are assumed to be in the sub-scan level. If not then the step of averaging over the sub-scans (Eq. 3.10) is skipped. The above initial values can be thus either in the scan or sub–scan level.

Averaging over sub-scan parameters In the case that the method of first fitting the sub–scans and then averaging the resulted parameters is chosen then the corresponding errors must be taken into account in the chain of propagation. The operations for each direction are:

$$\left\langle T_{obs}^{azi} \right\rangle = \sum_{N=1}^{N} \frac{T_{j,obs}^{azi}}{N_{azi}} \tag{3.9a}$$

$$\left\langle T_{obs}^{elv} \right\rangle = \sum_{N=1}^{N} \frac{T_{j,obs}^{elv}}{N_{elv}} \tag{3.9b}$$

where:

$T_{j,obs}$	is the antenna temperature of every sub-scan and direction respectively
N	is the number of sub-scans in the two directions respectively.

The error per direction after the averaging of the sub-scans parameters and taking into account (Eq. 3.8 & 3.9) will be :

$$e^2_{T_{i,obs}} = \left(\frac{\sqrt{\sum e^2_{T_{j,obs}}}}{N} \right)^2 + \sigma^2 \tag{3.10}$$

where (i) denotes the different direction and (j) denotes the different sub–scans. The values of $\langle T_{obs} \rangle$ and $e_{T_{i,obs}}$ are the ones used in Eq. 3.5 & 3.6. The same procedure is followed for the parameter of pointing offset Δp and the corresponding error $e_{\Delta p}$.

The EMIR case

Since the EMIR system records separately two orthogonal linear components, the total power will come as the average of H and V. In terms of flux density the Stokes-I will be:

$$\langle S_{\mathrm{I}} \rangle = \frac{\langle S_{\mathrm{H}} \rangle + \langle S_{\mathrm{V}} \rangle}{2} \tag{3.11}$$

where $\langle S_{\mathrm{H}} \rangle$ and $\langle S_{\mathrm{V}} \rangle$ are the averages of the available scans for a specific source for H and V polarizations, respectively. The corresponding error will be:

$$e^2_{\mathrm{I}} = \left(\frac{\sqrt{e^2_{\mathrm{H}} + e^2_{\mathrm{V}}}}{2} \right)^2 + \sigma^2 \tag{3.12}$$

Where e_{H} and e_{V} are the formal errors of the averages for every polarization respectively and σ is the scatter of the scans used. This will be the final error in the case data from the EMIR receiver system are used.

Calibration error

In Eq. 3.8 the terms $\langle \Gamma \rangle$ and $e_{\langle \Gamma \rangle}$ appear. The first is the calibration factor applied to the data and the second is its error. These values are computed with the same principal technique

but with the addition of an error in the computation of the reference flux used for the main calibrators as well as the scatter of the calibration factors obtained from a unique observing session. The calibration factor is defined as:

$$\Gamma = \frac{S_{\rm ref}}{T_{\rm cal}} \tag{3.13}$$

where:

- $S_{\rm ref}$ is the reference flux density (Jy) of the calibrator.
- $T_{\rm cal}$ is the measured antenna temperature (K) for the same calibrator.

The error $e_{\rm cal}$ in the antenna temperature of the calibrators is described by Eq. 3.6. So the error in the calibration factor Γ is given by:

$$e_\Gamma^2 = \left(\frac{S_{\rm ref}}{T_{\rm cal}^2}\cdot e_{\rm cal}\right)^2 + \left(\frac{1}{T_{\rm cal}}\cdot e_{\rm ref}\right)^2 \tag{3.14}$$

where:

- $e_{\rm ref}$ is the error in the reference flux used for the derivation of the calibration factor.
- $e_{\rm cal}$ is the observational error in the derivation of the antenna temperature as described by Eq. 3.6

The final calibration factor $\langle\Gamma\rangle$ is the average of all the calibration factors observed in a specific session. The corresponding final error $e_{\langle\Gamma\rangle}$ as used also in Eq. 3.8 will be:

$$e_{\langle\Gamma\rangle}^2 = \left(\frac{\sqrt{\sum e_{\Gamma_i}^2}}{N}\right)^2 + \sigma_\Gamma^2 \tag{3.15}$$

where:

- σ_Γ is the standard deviation of the calibration factors.
- N is the number of calibration factors used.
- e_{Γ_i} are the errors of the individual Γ-factors as computed in Eq. 3.14

The error $e_{\rm ref}$ as already mentioned is the error in the reference flux of a calibrator. In the case that a secondary calibrator is used then it is taken every time from the literature (Table 3.2). For the main calibrators a planetary model is used for the calculation of $S_{\rm ref}$, in that case $e_{\rm ref}$ is representing the uncertainty in the used model.

3.2 PV system studies

Many factors contribute to the final measurement uncertainties. Equation 3.8 gives the uncertainty of a measurement e_{sens}, which results from the formal error propagation over all reduction steps, assuming a Gaussian error distribution. One source of uncertainty in the calculated absolute flux densities, is the uncertainty in the flux density values assumed for the calibrators (e_{ref} in Eq. 3.14). For the main calibrators used in the current analysis, namely the planets Mars and Uranus, this uncertainty is of the order of 5 % (Reuter and Kramer 1998; Ulich 1981; Ulich et al. 1980). For the secondary calibrators the corresponding uncertainties can be seen in Table 3.2 (See also Sect. 3.1.3). It should be noted that these uncertainties only add an overall offset to the absolute flux density scale and do not affect the observed relative flux density variations in a given light curve. In Table 3.4 the mean

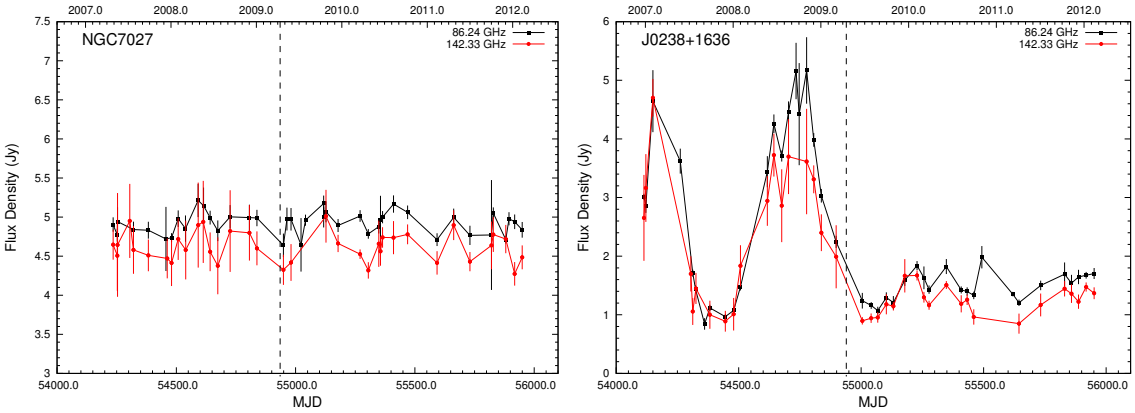

Figure 3.5: Comparison of the data quality before and after the change to the new *EMIR* receivers. The light curves of the secondary calibrator NGC 7027 (left) and the target source J0238+1636 (right) at 86 and 142 GHz are shown. The dashed line in each plot represents the time of the change to the new *EMIR* receiver system. The mean fractional error was reduced from 16.7 % to 11.2 % for 2 mm data (see also Sect. 3.2).

fractional flux density errors and mean pointing offsets for all frequencies and receivers are given. Those have been calculated using all available measurements of the 5 year observing period. At 142 GHz a significant decrease of the fractional flux density error is noticed after the change to the EMIR system in 2009 (see also Fig. 3.5). This demonstrates the gain in overall performance which is due to lower receiver temperatures, bandwidth improvements and, most importantly, the use of whobbler switching. At 86 GHz no significant difference is seen. The mean pointing errors are small and comparable for both systems. One way to quantify the repeatability of an observing system is by means of the modulation index m ($m = \sigma/S$, see also Sect. 4.1) calculated over an extended period of time. The calculated values of m over the 5 year observing period are shown in Table 3.5 using the secondary calibrators. It can easily be seen that weather has a much larger effect at higher observing frequencies.

To further quantify the performance of the observing system the errors for each individual flux density measurement (with typical integration times of 2–4 minutes) obtained at a given time and after all post-measurement corrections of systematics have been ap-

Table 3.4: Mean fractional flux density errors, pointing offsets and the corresponding errors in the mean for all frequencies of the old ABCD and new EMIR receivers.

	ABCD		EMIR	
Freq. (GHz)	Frac. Err. (%)	Poi. Offset (″)	Frac. Err. (%)	Poi. Offset (″)
86.24	8.64 ± 0.29	1.82 ± 0.02	8.53 ± 0.15	1.90 ± 0.01
142.33	16.74 ± 0.43	1.81 ± 0.02	11.18 ± 0.21	1.68 ± 0.01
228.24	19.86 ± 0.52	1.44 ± 0.02	–	–

Table 3.5: Modulation indices per frequency for the secondary calibrators and mean value over all these calibrators.

	Secondary Calibrators			Mean
Freq. (GHz)	NGC 7027	K3-50A (%)	W3OH	(%)
86.24	2.92	3.23	2.19	2.78
142.33	4.16	3.85	4.32	4.11
228.24	7.91	7.52	11.96	9.13

plied are investigated. As shown in Fig. 3.6 an inherent dependence of the fractional error of a measurement and its flux density at each frequency is evident. Empirically this dependence can be described by:

$$P_{\mathrm{err}}(S) = \sigma_0 + \mathrm{m} \cdot S^{-\alpha} \tag{3.16}$$

where:

- S is the flux density of a measurment
- σ_0 is the constant offset in the equation, defining the plateau in Fig. 3.6
- m is the parameter for the flux depended part of the plot.
- α is a unitless parameter defining the slope of the flux depented part.

The solid lines in Fig. 3.6 represent fits of lower envelopes to the data using Eq. 3.16. The fit parameters can be seen in Table 3.6. All plots are characterized by a plateau at higher flux density levels and a flux dependent part at lower levels. The relative large scatter of the data points in the Y–axis is due to weather effects. The continuous distribution of data points in the X–axis is due to the intrinsic variability of the sources. For the secondary calibrators that have a non–variable flux density, they cover only a stripe in these plots and only the effect of weather is clearly seen as the scatter in the Y–axis. The lower envelope is only telescope dependent and represents the error in ideal weather conditions and thus this is what is used for the fit. As frequency increases, the influence of weather gets crucial making the flux density dependent part of Eq. 3.16 difficult to discern (e.g. 228 GHz).

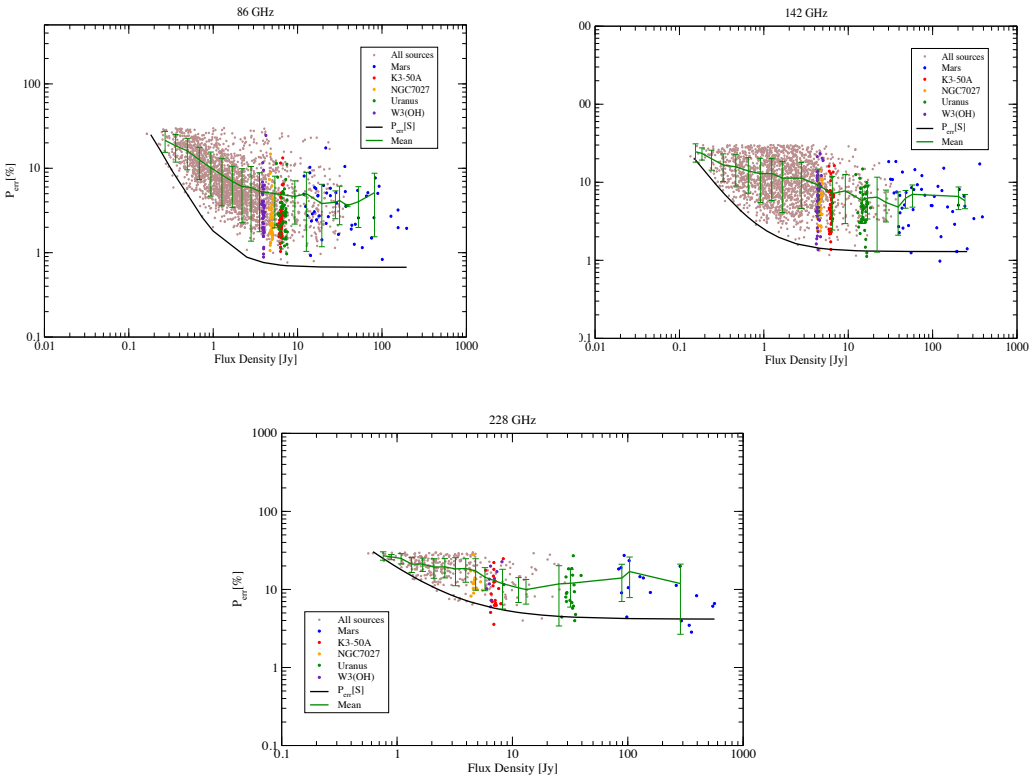

Figure 3.6: Dependency of the fractional error of each single measurement on flux density for 86 GHz (top left), 142 GHz (top right) and 228 GHz (bottom). The solid lines represent the fitted lower envelope for each frequency whereas as green lines are shown averages binned in flux density together with their 1 sigma scatter (see text).

Table 3.6: Fitted values for the lower envelope at 86, 142 and 228 GHz of Eq. 3.16 to the data of Fig. 3.6.

Freq. (GHz)	σ_0 (%)	m	α
86	0.67 ± 0.25	1.13 ± 0.10	1.82 ± 0.16
142	1.29 ± 0.27	1.21 ± 0.16	1.44 ± 0.15
228	4.15 ± 0.80	15.05 ± 0.04	1.15 ± 0.16

The two distinct parts in Fig. 3.6 can be interpreted in a similar way as in Angelakis et al. (2009): (a) the constant part σ_0 can be attributed to the inherent thermal noise of the system and the absorption of the atmosphere, (b) the flux depended part (m) can be attributed to pointing errors and the emission of the atmosphere that becomes more evident at low flux density levels. The lower envelope of these plots represents the minimum error one can expect, for a specific flux density level during good weather conditions. The position of a measurement in one of these plots is a direct measure of the performance of the observing system, at the specific time of observation.

The performance of the system in real life conditions can be characterised by the mean dependence of the fractional error with flux density and is shown by the green curve in

each plot of Fig. 3.6. The fractional error drops from a value of $\sim 20\,\%$ to $\sim 5\,\%$ for 86 GHz and $\sim 24\,\%$ to $\sim 7\,\%$ for 142 GHz. The error bar represents the 1σ scatter around the mean value. Unfortunately due to small number statistics this value is over estimated at higher flux density levels. It is worthwhile noting that 90 % of the sources at 86 GHz and 142 GHz have a fractional error of 15 % and 20 % respectively.

3.3 The Effelsberg 100–m telescope

3.3.1 System Description

The 100–m radio telescope of the Max-Planck-Institut für Radioastronomie (MPIfR) in Effelsberg is located in a valley near Bad Münstereifel, Germany. It is one of the largest fully steerable radio telescopes in the world. It is used for various observations of celestial objects at frequencies ranging from 300 MHz to 90 GHz. The telescope is of Gregorian design with a 100 m primary and 6.5 m secondary mirror. The primary mirror is constructed according to the homology principle, meaning that the shape of the dish closely retains a parabolic shape independent of the elevation an observation is performed. Holographic measurements showed a mean deviation from the ideal parabolic form in the order of 0.55 mm. The secondary mirror which was replaced in 2006, has a surface error of only 60 μm. This new secondary is equipped with 96 actuators and compensates incomplete homologous structures of the main dish.

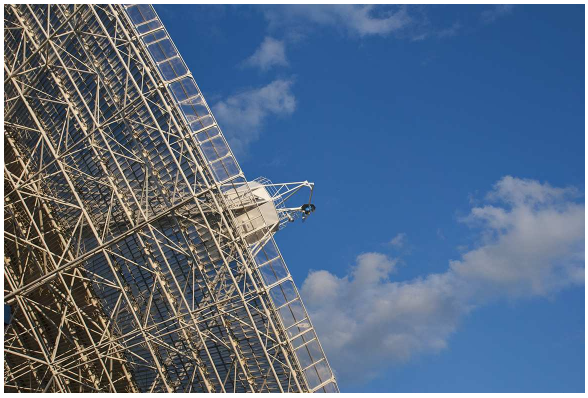

Figure 3.7: The EB 100 m radio telescope.

The mechanical elevation limit of the telescope is $\sim 8°$. The telescope is located in a valley, limiting real visibility to $\sim 20°$ depending on Azimuth. The horizon as seen from the lower edge of the telescope can be seen at Fig. 3.8 The combination of all these advan-

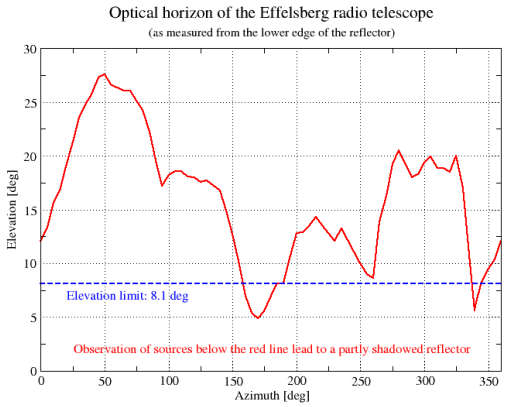

Figure 3.8: EB visibility as seen from the lower edge of the telescope.

tages, enables EB to conduct very sensitive observations at all the operating frequencies, making it ideal for the F-GAMMA program.

3.3.2 The receivers

Various receivers are mounted in both the secondary and primary cabins of EB ranging from 300 MHz to 86 GHz. For the observations of the F-GAMMA program receivers of the

secondary cabin were utilized ranging from 2.64 GHz up to 42 GHz. Table 3.7 presents the main characteristics of the used receivers. The main reasons for the choice of the secondary cabin receivers is the large variety of different frequency bands and the fast ($\sim$ 30 sec) switching time from one receiver to another. This allows spectrum coherency time to be of the order of $\sim$ 40 min (see also Sect 2.4.2). All the receivers that have been used are of heterodyne type, mixing the incoming signal with a pure, monochromatic frequency tone, known as a Local Oscillator (or LO). Fig. 3.9 depicts the signal path of a prototype heterodyne receiver including several steps of amplification, mixing, signal integration and finally recording. All the used recievers are capable of recording polarization information as seen in Table 3.7. The receivers at 4.85, 10.45 and 32 GHz are equipped with multiple feeds for the subtraction of atmospheric effects.

Table 3.7: EB secondary focus receiver characteristics.

Freq. [GHz]	BW [GHz]	Pol. –	T_{sys} [K]	Γ [K/Jy]	FWHM ($''$)	Poi. Off. ($''$)	No. Feeds –	Aperture efficiency (%)
2.64	0.1	LCP,RCP	$\sim$ 17	$\sim$ 1.5	260	13.6	1	53
4.85	0.5	LCP,RCP	$\sim$ 27	$\sim$ 1.55	146	7.2	2	53
8.35	1.2	LCP,RCP	$\sim$ 22	$\sim$ 1.35	82	2.3	1	45
10.45	0.3	LCP,RCP	$\sim$ 52	$\sim$ 1.35	68	1.8	4	50
14.6	2.0	LCP,RCP	$\sim$ 50	$\sim$ 1.14	50	2.5	1	43
23.05	2.7	LCP,RCP	$\sim$ 77	$\sim$ 0.9	36	1.6	1	30
32.0	4.0	LCP,H/V	$\sim$ 64	$\sim$ 0.75	25	1.3	7	32
42.0	2.8	LCP,RCP	$\sim$ 120	$\sim$ 0.53	20	1.0	1	19

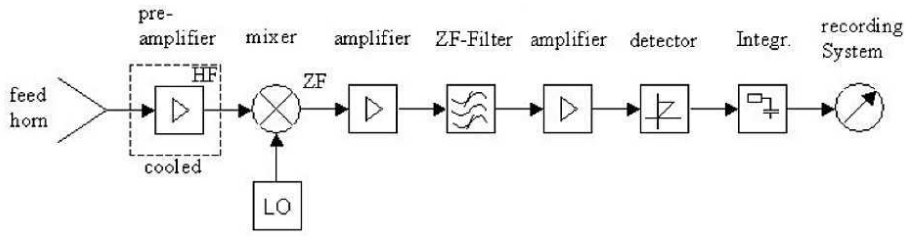

Figure 3.9: Block diagram of a prototype heterodyne receiver (image thanks to Hans-Rainer Klöckner).

The 2.64 GHz receiver This is the lowest frequency observed by the F-GAMMA program. The receiver is cooled with typical noise temperature in the order of $\sim$ 4 K and has two channels. It can be tuned in the range of 2599.5 MHz – 2679.5 MHz and it's calibration is accomplished with a noise diode. The frequencies utilized are quite often contaminated by interference of various sources, mainly mobile telecommunications and wireless networks that work in this frequency range.

The 4.85 GHz receiver The 6 cm receiver is a four channel system with cooled HEMT pre–amplifiers, with typical noise temperatures of $\sim$ 9 K. The calibration is done via a noise diode.

The 8.35 GHz receiver This system is a secondary focus receiver with cooled HEMT amplifiers and a cooled polarization transducer. The calibration signal is injected with a noise diode also. Typical noise temperatures for this receiver are $\sim$ 4 K.

The 10.45 GHz receiver This system has 4 feeds, 8 channels and 4 Broadband Polarimeters. In total 16 data channels exist and 2 total power and 2 polarization signals per feed are recorded. This receiver is being used in a software beam–switching mode and has typical noise temperatures of ~ 50 K. The calibration is done with a noise diode. The feeds are mounted in a row in azimuth direction, having distances of 3, 9 and 5 arcmin.

The 14.6, 23.05 and 42.0 GHz receivers This system comprises 3 dual channel frontends at the frequencies of 14.6, 23.05 and 42.0 GHz. The three feeds are placed in a row at the elevation axes, but offset in azimuth. The 14.6 and 23.05 GHz frontends share a common dewar in contrast to the 42.0 GHz frontend that is contained in a separate one. Observations are possible only at one frequency at a time due to common use of parts of the IF and Oscillator Systems. Switching between these frequencies is however possible within seconds. The calibration is accomplished with noise diodes and the receiver noise temperature is ~ 30 K for the 14.6 anf 23.05 GHz receivers and ~ 73 K for the 42.0 GHz.

The 32.0 GHz receiver This receiver is a pseudo–correlation design. Seven corrugated horns exist, with beam switching implemented in hardware with horns 3 and 4 differenced by means of a wave–guide magic tee. Calibration is performed with a noise diode transmitter that is optically coupled. The receiver noise temperature performance is 18 K – 24 K.

3.3.3 Data reduction and calibration

Overview

All post–measurement reduction steps and corrections applied to EB data of all the observing sessions are described in the following. The reduction steps were performed by semi–automated python routines (Angelakis et al. 2015) that allowed the data to be reduced and calibrated in a matter of a few hours after each observing session. The reduction process for EB data includes: (a) Gauss fitting of raw data to estimate the antenna temperature, (b) data quality checks and flagging of bad data, (c) post–measurements corrections involving opacity, pointing, gain–elevation and sensitivity corrections, described in more detail bellow. The data products of this process are stored in a database for later reference. The combination of all the different sessions as well as the combination with data acquired with the PV telescope is subsequently performed by another python routine included in the same software package.

Data quality checks

To ensure the quality of the final data products, every scan must fulfil some criteria. Not passing one of these criteria or a combination of them, means that the corresponding scan is flagged and not taken into account in the following reduction and analysis. The criteria are similar to the criteria used for the reduction of PV data (Sect. 3.1.2).

- *Non–converging fits.* The algorithm that performs the Gaussian fitting fails to converge and produces no physical parameter values for the profile. In this case the

corresponding scans and sub–scans are flagged.

- *Pointing offsets.* In EB the pointing to a target source is performed through a pointing model. This model of course is not perfect especially if the weather conditions are not ideal and for higher frequencies, leading to poor pointing. For this reason during the F-GAMMA observations for higher frequencies a second scan is performed to validate and ensure the pointing of the telescope. If the resulting scan has a pointing offset that is larger than 20 % of the beam size (FWHM) at the observed frequency, then this scan will be flagged.

- *FWHM criterion.* For a specific observing session if the FWHM of a scan is larger by 30 % of the mean FWHM of that session, then it is flagged. Special care must be taken for sources that are extended and thus inherently have larger FWHM.

- *Amplitude criterion.* Due to the aforementioned effects the relative amplitude of the Gaussian profiles between two scanning directions (AZI/ELV) is changed. In the case that the difference is larger than 20 % of the mean amplitude of the observing session then the scan is flagged. Care must be taken in cases that the weather is highly variable within the observing session, resulting in non–natural mean values of the amplitude. In such cases this criterion is not applied and a manual check is performed.

Calibrators

The various calibrators used for final flux density calibration at the EB telescope are shown in Table 3.8 along with their main characteristics. All source are point-like for the beam size of the EB dish in all of the observed frequencies. The specific characteristics for each calibrator are described in the following. Table 3.9 presents the modulation indices of all the used calibrators and its mean values per frequency over the five years of F-GAMMA observations, demonstrating their low scatter. The light curves and spectra of the calibrators can be seen in Appendix A.3 and A.2.1 respectively.

Table 3.8: Flux Densities of the calibrators used at the Effelsberg 100 m telescope.

Frequency [GHz]	Calibrator [Jy][1]				
	3C 48	3C 161	3C 286	3C 295	NGC 7027[2]
2.64	9.51	11.35	10.69	12.46	3.75
4.85	5.48	6.62	7.48	6.56	5.48
8.35	3.25	3.88	5.22	3.47	5.92
10.45	2.60	3.06	4.45	2.62	5.92
14.60	1.85	2.12	3.47	1.69	5.85
23.05	1.14	1.25	2.40	0.89	5.65
32.0	0.80	0.83	1.82	0.55	5.49
42.0	0.57	0.57	1.4	0.35	5.34

[1] Flux densities of the calibrators were taken from Ott et al. (1994) and Baars et al. (1977).
[2] The flux density of NGC 7027 is corrected for beam extension above 10.45 GHz.

Table 3.9: Modulation indices (m_0) for the calibrators at each observing frequency together with their mean values.

Frequency	Calibrator – modulation index [%]							
[GHz]	3C 48	3C 161	3C 286	3C 295	NGC 7027	K3–50A	W3(OH)	Mean
2.64	0.61	0.80	0.78	0.95	0.94	–	–	0.82
4.85	0.60	0.63	0.47	0.88	0.41	–	–	0.60
8.35	0.88	1.08	0.73	1.48	0.84	–	–	1.00
10.45	1.14	1.32	1.14	1.16	1.19	–	–	1.19
14.60	1.63	2.18	1.69	1.50	1.14	–	–	1.63
23.05	2.46	2.29	1.99	2.03	1.62	–	–	2.08
32.00	2.94	2.99	2.22	3.54	3.07	–	–	2.95
42.00	3.39	1.91	2.68	–	2.61	–	–	2.65
86.24	–	–	–	–	2.92	3.23	2.19	2.78
142.33	–	–	–	–	4.16	3.85	4.32	4.11

- *3C 48:* Is a steep–spectrum quasar at redshift z = 0.367. Its radio structure is quite compact making it a good source to focus the telescope for frequencies bellow 10 GHz. 3C 48 is not entirely stable and undergoes slow variations in flux density over the past 30 years (Perley and Butler 2012). From the light curves and spectra (see Appendix A.3 and A.2.1) is shown that for the time scales the F-GAMMA program is active 3C 48 can be considered as a constant source and used safely as a calibrator. Its mean m_0 ranges from 0.61 % at 2.64 GHz to 3.4 % at 42 GHz.

- *3C 161:* Is a compact radio source with observed structure on arc-second scale(Goss et al. 2008). Is very stable within the F-GAMMA time scales and can be even be used for focusing in higher frequencies if the weather is good enough. Its mean m_0 ranges from 0.8 % at 2.64 GHz to 1.9 % at 42 GHz.

- *3C 286:* Is a compact steep–spectrum quasar at redshift z = 0.846. Without optically thick central nuclear emission, VLBA imaging shows that it is uniformly polarized (Perley and Butler 2012). This makes 3C 286 an extraordinarily stable and useful calibrator. It is one of the most frequently observed calibrators within the F-GAMMA program. From the light curves and spectra (see Appendix A.3 and A.2.1), apart from some small outliers, the lack of variations is apparent. Its mean m_0 ranges from 0.78 % at 2.64 GHz to 2.7 % at 42 GHz.

- *3C 295:* Is a radio galaxy at a redshift z = 0.464, and exhibits a very weak central nucleus that contributes to less than 1% in the total flux density at 15 GHz (Taylor and Perley 1992). This fact implies that the source could have constant flux density over time and thus be a good calibrator. Light curves and spectra (see Appendix A.3 and A.2.1) are shown demonstrating it's stable character. Its mean m_0 ranges from 0.95 % at 2.64 GHz to 3.5 % at 32 GHz.

- *NGC 7027:* Is a bright nearby planetary nebula. Its spectrum is mildly convex and follows a power law of the form $S = k \cdot \nu^{-0.1}$ at frequencies above 10 GHz. It is known that its flux density is increasing with time, at frequencies where it is optically thick and to be decreasing in frequencies that is optically thin (Zijlstra et al. 2008).

For time scales the F-GAMMA program is active, these variations are negligible. It has a relative high angular size making it not suitable for focus operations. A beam correction due to it's size is needed especially at higher frequencies (Sect. 3.3.4). NGC 7027 is also very important because it is used as a cross calibration source for the EB and PV telescopes (see Sect. 2.3). Its mean m_0 ranges from 0.94 % at 2.64 GHz to 2.6 % at 42 GHz.

It should be noted that on average the scatter of the calibrators is very low overall ranging from 0.8% at 2.64 GHz to 2.65% at 42 GHz.

3.3.4 Post–measurement corrections

What is actually measured from the receivers is counts. To convert the measured signal from counts into temperatures the value of the noise diode in k is required. This is done automatically by the used software (Toolbox) and it is done by multiplying a given value (T_{cal}) to the data. The measured product of the astronomical observations after the conversion to kelvins is the system temperature T_{sys}. In general is given by:

$$T_{sys} = T_r + T_s + T_{atm} + T_g \tag{3.17}$$

where :

T_r	is the receiver temperature
T_s	is the source brightness temperature
T_{atm}	is the atmospheric temperature
T_g	is the ground spillover temperature

The ground, atmospheric and source temperatures constitute the antenna temperature T_A. The final goal of every observation is to estimate the source brightness temperature, thus all other contributions must be accounted for. The receiver and ground temperatures are usually small and especially for the former also stable, leaving as the main contributor the atmosphere.

Opacity

The atmosphere influences the incoming radio signal not only by means of absorption but also by introducing noise with atmospheric emission. The latter can be removed by performing differential observations (Sect. 2.2.1), but the attenuation of the signal must be corrected with a process called "opacity correction". The atmospheric temperature depends on the total column of water vapour that the beam of the telescope "sees" and thus depends on the elevation the observation is made. The attenuation of the observed signal because of the atmosphere is by a factor $e^{\tau \cdot AM}$. The correction that must be applied to the

data is:

$$T_A^* = T_A \cdot e^{\tau \cdot AM} \tag{3.18}$$

where :

T_A^*	is the antenna temperature after the correction
AM	is the airmass, given by AM $= 1/\sin(\text{Elv})$, where Elv is the elevation
τ	is the zenith opacity

The zenith opacity is depended on the observed frequency. For this reason this correction must be applied to all the different frequencies separately. In order to derive the instantaneous opacity at the given time of observation the relation :

$$T_{sys} = T_0 + T_{atm} \cdot \tau \cdot AM \tag{3.19}$$

can be used. T_{sys} can be easily determined with the methods described in Sect. 2.2.1 for every individual measurement, also the airmass is known. The atmospheric temperature can be approximated by :

$$T_{atm} = 1.12 \cdot T_g - 50\,K \tag{3.20}$$

For each session usually there is a significant number of T_{sys} measurements enabling the estimation of T_0 and τ by a least–square fit, as shown in Fig. 3.10.

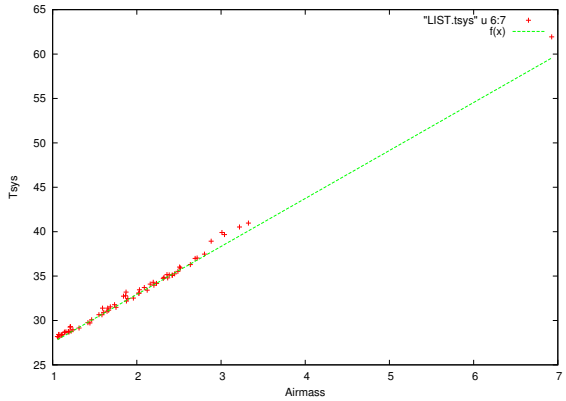

Figure 3.10: Example of airmass versus system temperature for a typical observing session. The green dotted line is the lower envelope least–square fit to the data.

Because weather is a dynamical phenomenon and atmosphere is not only absorbing radiation but also emits, the system temperature is exhibiting variations as seen from Fig. 3.10. The best way to derive the desired quantities, is to fit the lower envelope of the data, enabling to accurately determine T_0 as the point where the fit crosses the Y–axis. The zenith opacity τ is given by the slope of the resulting fit. For each individual observation

the corresponding opacity can then be calculated as:

$$\tau = -\frac{1}{\mathrm{AM}} \cdot \ln\left(1 - \frac{T_{\mathrm{sys}} - T_0}{T_{\mathrm{atm}}}\right) \tag{3.21}$$

An example of a least–square fit, is presented in Fig. 3.10.

NGC 7027 beam correction

NGC 7027 is a regularly used calibrator during the F-GAMMA observations. It has a relatively flat spectrum (see Fig. 2.4) making it an important calibrator at the higher frequencies. Moreover as described in Sect. 2.3 it is a very important source for cross calibration studies between EB and PV telescopes.

The angular size of NGC 7027 on the sky is comparable to the beam size of the EB telescope, especially at frequencies above 10.45 GHz. Consequently the flux density of NGC 7027 is underestimated and thus also the conversion factor Γ (see also Sect. 3.3.4), which eventually affects the whole dataset of a given observing session. A correction factor *bm* is applied only to NGC 7027 data to compensate, according to Eq. 3.22. The correction factors applied at each frequency are shown in Table 3.10.

$$T_{\mathrm{bm}} = T_{\mathrm{A}} \cdot bm \tag{3.22}$$

where T_{bm} is the system temperature of NGC 7027 data after the correction and *bm* is the correction factor. This effect is important for frequencies higher than 10.45 GHz and thus a correction is applied only to those.

Table 3.10: NGC 7027 beam size correction factors. (E. Angelakis, priv. comm.)

Freq (GHz)	2.64	4.85	8.36	10.45	14.6	23.05	32.0	42.0
bm	1.0	1.0	1.0	1.0082	1.0145	1.0287	1.0551	1.089

Pointing correction

The process of pointing correction is described in Sect. 3.1.3 and as a generic procedure is the same for both EB and PV telescopes. The mean values of pointing offsets achieved with the EB telescope as seen in Table 3.7 are small comparable to the beam size at each frequency, ranging from 13.6″at 2.64 GHz to 1″at 42 GHz.

Gain–elevation correction

Because of the homology principle that the construction of the telescope is based upon, most of the effects are corrected. Some residual deviations from a flat curve in the gain that are depended on the elevation of the observation are left. The gain-curve correction

is applied in the same manner as done in Sect. 3.1.3 for PV The obtained parameters used for each observing frequency are given in Table 3.11 whereas the gain-elevation curves are shown in Fig. 3.11 and 3.12.

Table 3.11: Normalized gain curve parameters for frequencies used at EB , according to Eq. 3.7

Freq. (GHz)	A_2	A_1	A_0	Date
2.64	1.0	0.0	0.0	Feb. 2007
4.85	0.99	$5.20 \cdot 10^{-4}$	$-1.28 \cdot 10^{-5}$	Feb. 2008
8.35	0.99	$4.34 \cdot 10^{-4}$	$-1.06 \cdot 10^{-5}$	Feb. 2007
10.45	0.99	$8.25 \cdot 10^{-4}$	$-1.74 \cdot 10^{-5}$	Feb. 2007
14.6	0.97	$1.83 \cdot 10^{-3}$	$-2.87 \cdot 10^{-5}$	Feb. 2007
23.05	0.91	$4.76 \cdot 10^{-3}$	$-6.29 \cdot 10^{-5}$	Feb. 2007
32.0	0.92	$4.95 \cdot 10^{-3}$	$-7.13 \cdot 10^{-5}$	Feb. 2007
42.0	0.88	$5.87 \cdot 10^{-3}$	$-7.12 \cdot 10^{-5}$	Dec. 2007

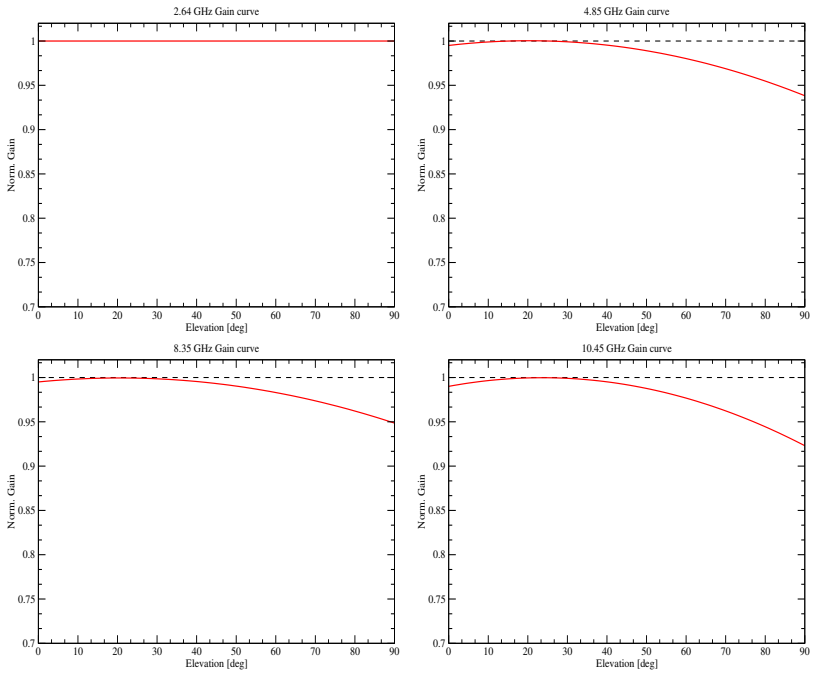

Figure 3.11: Gain–Elevation curves for the low frequencies. Clockwise are shown 2.64, 4.85, 8.35 and 10.45 GHz respectively (see also Table 3.11). For 2.64 GHz no significant deviation from a flat curve exists.

The correction applied to the data is :

$$T_G = \frac{T_{poi}}{G} \tag{3.23}$$

where :

T_{poi} is the antenna temperature after the pointing correction
T_G is the corrected antenna temperature for the gain–elevation effect

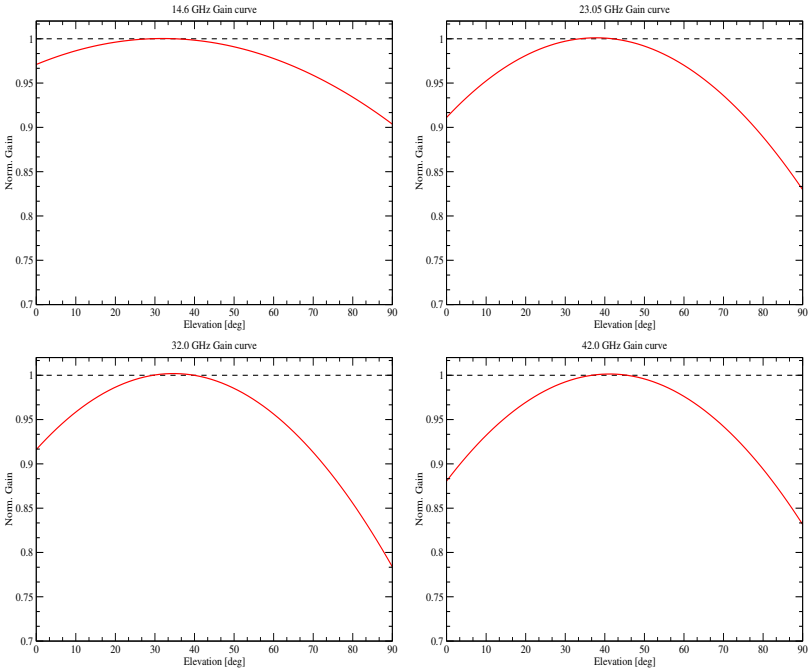

Figure 3.12: Gain–Elevation curves for the high frequencies. Clockwise are shown 14.6, 23.05, 32.0 and 42.0 GHz respectively (see also Table 3.11).

Sensitivity correction

Throughout the previous steps antenna temperatures where given in units of K. Its conversion to flux density S in units of Jy is done by comparing the antenna temperature of the calibrators with their known flux densities (Table 3.8). For every observation of a calibrator a calibration factor Γ is calculated. Then an average value $\langle\Gamma\rangle$ for the whole observing session can be computed using all the available calibrators measurements. The final sensitivity correction is the applied according to:

$$S_{\text{sens}} = \langle\Gamma\rangle \cdot T_{\text{G}} \tag{3.24}$$

where :

T_{G} the antenna temperature after all other corrections are applied
$\langle\Gamma\rangle$ the mean calibration factor in Jy/K

3.3.5 Error estimates

The final errors reported for every observation is the result of the cumulative factors already discussed in previous sections. For a more realistic estimation of the uncertainties, several different errors have been calculated and the error with the largest value is used as the most conservative uncertainty. In more detail:

The scatter of $\langle S \rangle$**.** In a particular observing session it is common that not only one measurement is obtained per source. Ideally every measurement should have the same value, but because of reasons like the weather or hardware imperfections this is not true. The scatter of these measurements over the mean is an indication of how well the system[3] repeats a measurement. This scatter is denoted as sigma (σ).

Error in the mean. Whenever an averaging operation is performed the respective error can be defined in the mean as $e_{\mathrm{mean}} = \sigma/\sqrt{\mathrm{N}}$ where N is the number of measurements. This error is always equal or smaller than the aforementioned σ.

Formal Gaussian error. If several measurements S_i exists with an error of e_i in each one of them, then we can define the formal Gaussian error as:

$$S_e = \frac{\sqrt{\sum e_i^2}}{N} \tag{3.25}$$

where:

- S is the mean value of the measurements, $S = \langle S_i \rangle$
- N the number of measurements

Repeatability error. The previous error estimations are relatively straightforward. A more sophisticated estimation of the system behaviour can be obtained using the 'repeatability' curves. For the construction of those all the calibrator measurements over the five years of observations have been used. Plotting the uncertainty in the determination of the flux density versus the flux density a clear dependence is observed. This dependence can be modelled by the following equation:

$$e_{\mathrm{S}} = \sqrt{\sigma_0^2 + (m \cdot \mathrm{S})^2} \tag{3.26}$$

where :

- S is the flux density of the measurements
- e_{S} is the uncertainty in a measurement
- m is the modulation index due to the calibration errors
- σ_0 is the offset in the equation

This error can be thus divided into two distinctive parts. The first part is flux density independent (σ_0^2) and the second part is flux density depended ($(m \cdot \mathrm{S})^2$). The constant part can be attributed to the following:

[3] the notion system refers to the combination of the weather and the telescope as a whole.

- *thermal noise.* Is derived from the radiometer formula and it is the lowest limit in the detection of a flux density level.
- *confusion error.* Is the error in the determination of the flux density of the target source due to the cumulative contribution of background sources.
- *atmospheric emission error.* Ideally by performing differential observations we can completely subtract the contribution of the atmosphere to our signal. This error is any residuals left from imperfect subtraction of this term.

The flux depended part can be attributed to:

- *pointing errors.* The pointing errors are already discussed (Sect. 3.3.4).
- *noise diode error.* This error is introduced by the instability of the noise diode that is used for the calibration of the receiver signal.
- *atmospheric absorption error.* This error is introduced by the variable atmosphere, causing changes in the opacity. See also Sect. 3.3.4 for opacity corrections.

Table 3.12: Repeatability curve parameters

Freq. (GHz)	σ_0	m
2.64	0.001	0.0080
4.85	0.001	0.0077
8.35	0.001	0.0112
10.45	0.001	0.0125
14.60	0.001	0.0187
23.05	0.001	0.0281
32.00	0.001	0.0306
42.00	0.001	0.0346

The values of σ_0 and m that have been calculated for all the different frequencies are shown in Table 3.12. From all the different error estimations described above, as the final error of a given measurement the maximum error is used as the most conservative approach. This work was first done by E. Angelakis in his PhD thesis, but the numbers here are updated to the current values. For the actual plots and more details please refer to that thesis.

4

Analysis tools and methods

The following chapter presents an introduction to the analysis tools and methods that are applied to the F-GAMMA datasets. The period of focus for all the subsequent analysis is January 2007 to January 2012 i.e. the first five years of F-GAMMA observations of the revised source sample (see also Sect. 2.1). The aim is to characterize the extreme variability and spectral properties of blazars. The used tools and methods are :

- *Variability characterization χ^2– Analysis*

  To test the existence and significance of variability in the observed light curves a χ^2–test is performed. Sect. 4.1 presents the details of this method.

- Variability / flare amplitudes – Intrinsic standard deviation (σ_{int})

  The strength of the observed flares in the light curves can be quantified by the variability amplitudes. A likelihood method estimating the σ_{int} of a given light curve (i.e. amplitude) is used. Sect. 4.2 presents this method.

- *Flare time scales*

  Very important is to quantify the time scales of the occurring flares. The estimated values were computed by means of a structure function (SF) and wavelet analysis. Sect. 4.3 presents these methods.

- *Spectral indices*

  A way to quantify the spectral behaviour of an observed source is by means of the spectral index at various frequency bands. Sect. 4.4 presents the details of the used method.

- Spectral peak estimation

  A more detailed approach to characterize the behaviour in the spectral domain is by means of estimating and studying the properties of the spectral peak (peak frequency and peak flux density) of the observed broadband spectra. Sect. 4.5 presents the details of the used method.

4.1 Significance of variability: the χ^2–test

The χ^2–test is a statistical method applied to the data in order to evaluate the possibility that any observed difference between the dataset in question and an expected dataset is random or not, i.e. if the sampling distribution is a χ^2 distribution when the null hypothesis is true. In particular for the current analysis, the dataset is tested against the hypothesis of a constant function i.e. a non–variable source. This means that the χ^2 statistic is a way to quantify if an observed variation is statistically important or not (Bevington and Robinson 1992).

The χ^2 statistic is given by :

$$\chi^2 = \sum_{i=1}^{N} \left(\frac{S_i - \langle S \rangle}{\sigma_i} \right)^2 \tag{4.1}$$

where :

S_i	is the observed flux density
$\langle S \rangle$	is the average flux density of the light curve
σ_i	is the uncertainty of the S_i measurement
N	is the number of observations in the light curve

and the reduced χ^2 statistic is simply Eq. 4.1 divided by the degrees of freedom (df $= N-1$):

$$\chi^2_{red} = \frac{\chi^2}{N-1}$$

The value of the reduced χ^2 statistic is then compared to the χ^2 distribution according to the degrees of freedom and evaluated to calculate the probability P that the observed variation in the light curve is significant or not. A source is considered to be variable only if the probability of constant flux density is $\leqslant 0.1\,\%$ (99.9 % significance level for variability).

There are some assumptions for the above calculations of the χ^2 statistic to be applicable, namely:

- *Random sample*
- *Large sample size*
- *Independent data points*

All these requirements are met in the current study, making the χ^2–test a very good method to quantify the variability behaviour of the observed source sample. The results of this study are presented in Sect. 5.2.

Due to the fact that the measurement errors are taken into account by the χ^2–test algorithm, means that for sources that are weak or for any reason have high errors then the characterization of variability is compromised. This means that sources that are flagged as non–variables in the current study could be variables if observed under different conditions (e.g different telescopes) and or with different time spans. This is an important consequence of the use of the χ^2–test leading to the conclusion that the acceptance of the null hypothesis can not be proven, meaning that with this test we can not conclude for the actual variability or not for sources that are marked as non–variables. On the other hand for sources that are marked as variables is a proof of their actual variable character. For the aforementioned reasons only those sources with light curves which showed significant variability according to the χ^2–test are considered in the analysis presented in this thesis.

To further quantify the observed variability, the modulation index m can be used. It is defined as the percentage ratio of the rms- variations σ_0 of the light curve and the average flux density $\langle S \rangle$:

$$m[\%] = 100 \cdot \frac{\sigma_0}{\langle S \rangle}$$

It provides a measure of the strength of the observed variations and it is also used in the subsequent analysis of σ_{int} (Sect. 4.2).

4.2 Intrinsic standard deviation

Many different approaches can be followed to quantify the variability amplitudes of the observed flares e.g. Ciaramella et al. (2004) makes a probability distribution of $\log(S/\bar{S})$ (where S is the instantaneous flux density at a specific frequency and $\bar{S}$ is its average). To study the variability amplitude and it's dependence on frequency, possible biases must be taken into account such as (a) redshift and (b) measurement uncertainties of the traditional determination of the variability amplitude.

To address the effects of redshift all calculations are done in the rest frame of every source. To address the second effect of measurement uncertainties in the determination of variability amplitudes a new method is applied. In particular, the intrinsic values for the standard deviation of the fluxes for each light curve using a maximum likelihood analysis are computed. In this computation the different measurement uncertainties σ_j at each flux density measurement S_j and the different number of flux density measurements for different light curves are taken into account, making this way of quantifying the variability amplitudes more robust. This method was introduced by V. Pavlidou (Pavlidou et al. 2012; Richards et al. 2011) and is applied here. The results from the application of this method are presented in Sect. 5.3 whereas a summary of the method is provided bellow.

The goal of the method is to compute the intrinsic standard deviation σ_0 and thus

characterize the intrinsic variability amplitude of the observed flares. For the analysis that follows a source is assumed to have some intrinsic variability. Moreover the true flux densities under consideration (S_t) due to the intrinsic variability are assumed that are normally distributed with a mean value of S_0, a standard deviation of σ_0 and a modulation index of $m = \sigma_0/S_0$. Due to observational uncertainties the measured flux is not S_t but S_j with an uncertainty of σ_j. Also N measurements of S_j each with its own uncertainty σ_j are assumed. This method has some inherent disadvantages because of these assumptions.

Model dependence For the derivation of the intrinsic standard deviation a functional form of the distribution of flux densities must be assumed. In this case it is assumed that this distribution is Gaussian. This leads to a loss of generality. Three different methods can be used to test the effect of this assumption :

- (a) The first method is to compare the maximum–likelihood (max–$\mathcal{L}$) intrinsic flux distribution with the distribution of the measured fluxes. In this way the assumed model can be evaluated if it is a reasonable fit to the real data.

- (b) The second method is to compare the max–$\mathcal{L}$ value of σ_0 and the value of σ_0 obtained from the sample of S_0 and m. If these two differ significantly then the used model probably does not describe properly the distribution of fluxes. The latter value of m is contaminated by uncertainties but is model independent and thus it allows this comparison. This test can be done only for well sampled objects with relative small observational uncertainties.

- (c) The third test is to compare max–$\mathcal{L}$ values derived from different models. This allows to see how large the effect of the model is compared to the values of σ_0.

Assumption of unbiased sampling Compared to ideal light curves with infinite sampling, real world light curves have finite sampling. Thus it is assumed that the sampling is uniform and that we have sampled all the variability of the observed source. In cases that lengthy gaps exist in the data or increased sampling in a single epoch then this assumption is poor and Monte–Carlo simulations are needed to quantify how much the max–$\mathcal{L}$ value of m is affected.

Leakage of power There is leakage to the non–physical domain of negative true fluxes because of integrations starting from $-\infty$. This is expected to be a problem only for very dim or very variable AGN. In the latter case, the problem is usually the bi–modality of the flux distribution. This is discussed in Sect. 4.2.2. Thus two cases for the flux distribution of an AGN are taken into account, a Gaussian and a bi–modal, with the latter constituted by the sum of two Gaussian. It should be noted that the simpler Gaussian flux distribution method is applied to the data for the study of the current thesis.

4.2.1 Gaussian flux distribution

At the moment of observation a source has a true flux density of S_t. If the observational uncertainty is σ_j, the probability of the observed flux density S_j is:

$$p\left(S_t, S_j, \sigma_j\right) = \frac{1}{\sigma_j\sqrt{2\pi}} \exp\left[-\frac{\left(S_t - S_j\right)^2}{2\sigma_j^2}\right]. \tag{4.2}$$

If the true fluxes of the source due to intrinsic variability are distributed normally with a mean of S_0 and standard deviation of σ_0, the probability that the source at the moment of observation has a true flux density of S_t is:

$$p\left(S_t, S_0, \sigma_0\right) = \frac{1}{\sigma_0\sqrt{2\pi}} \exp\left[-\frac{\left(S_t - S_0\right)^2}{2\sigma_0^2}\right]. \tag{4.3}$$

Hence the likelihood of observing a flux density S_j with an uncertainty σ_j from the source is:

$$\ell_j = \int_{-\infty}^{\infty} \frac{1}{\sigma_j\sqrt{2\pi}} \exp\left[-\frac{\left(S_t - S_j\right)^2}{2\sigma_j^2}\right] \cdot \frac{1}{\sigma_0\sqrt{2\pi}} \exp\left[-\frac{\left(S_t - S_0\right)^2}{2\sigma_0^2}\right] \mathrm{d}S_t \tag{4.4}$$

ℓ_j represents the probability to observe S_j through any possible true flux S_t. Eq. 4.4 has an analytical solution:

$$\ell_j = \frac{1}{\sqrt{2\pi\left(\sigma_0^2 + \sigma_j^2\right)}} \cdot \exp\left[-\frac{\left(S_j - S_0\right)^2}{2\left(\sigma_j^2 + \sigma_0^2\right)}\right]. \tag{4.5}$$

Consequently for N observations of S_j, σ_j with $j = 1, \ldots N$ the likelihood will be:

$$\mathcal{L}(S_0, \sigma_0) = \prod_{j=1}^{N} \ell_j \Rightarrow$$

$$\mathcal{L}(S_0, \sigma_0) = \left(\prod_{j=1}^{N} \frac{1}{\sqrt{2\pi(\sigma_0^2 + \sigma_j^2)}}\right) \times \exp\left[-\frac{1}{2}\sum_{j=1}^{N} \frac{(S_j - S_0)^2}{\sigma_j^2 + \sigma_0^2}\right]. \tag{4.6}$$

It is apparent that the likelihood is symmetric about $\sigma_0 = 0$, leading to the conclusion that for the calculations of the uncertainties the lower limit for the integration can be zero without any loss of information or introduction of biases. With this formalism negative intrinsic standard deviation values are not possible.

By maximizing Eq. 4.6 an estimation of the maximum–likelihood values for S_0 and σ_0 can be made. For the purposes of this thesis the intrinsic standard deviation σ_0 and the associated uncertainties are only needed, without the true value of S_0. To do that we marginalize Eq. 4.6 taking out the mean and then obtain the marginalized likelihood as a

function of only σ_0:

$$\mathcal{L}(\sigma_0) = \int_0^\infty \left(\prod_{j=1}^{N} \frac{1}{\sqrt{2\pi(\sigma_0^2 + \sigma_j^2)}} \right) \times \exp\left[-\frac{1}{2} \sum_{j=1}^{N} \frac{(S_j - S_0)^2}{\sigma_j^2 + \sigma_0^2} \right] \mathrm{d}S_0 \tag{4.7}$$

The value of σ_0 that maximizes Eq. 4.7 is the best guess for the intrinsic standard deviation (hereafter σ_{int}) and is used as a measure of the variability amplitude in the following analysis of this thesis. The 1–sigma uncertainty of σ_0 can be found by locating the iso–likelihood σ_0–values σ_1 and σ_2 ($\mathcal{L}(\sigma_1) = \mathcal{L}(\sigma_2)$) for which:

$$\frac{\int_{\sigma_1}^{\sigma_2} \mathcal{L}(\sigma_0)\mathrm{d}\sigma_0}{\int_{-\infty}^{\infty} \mathcal{L}(\sigma_0)\mathrm{d}\sigma_0} = 0.68$$

4.2.2 Bi–modal flux distribution

The initial approach of assuming a single Gaussian distribution for the intrinsic fluxes (Sect. 4.2.1) of a source is not always true in general. A more appropriate model would be then the sum of two Gaussian weighted by a duty cycle f. The two Gaussian represent two different states of the source i.e. 'on' and 'off' state, where their fluxes are normally distributed with a mean value of $S_{\rm on}$ and $S_{\rm off}$ and standard deviation of $\sigma_{\rm on}$ and $\sigma_{\rm off}$ respectively. The duty cycle is defined as the time spent in the on–state.

Following the same logic as in the case of a single Gaussian distribution, the likelihood of a single observation for a bi–modal distribution is:

$$\begin{aligned} \ell_j = &\int_{-\infty}^{\infty} \frac{f}{\sigma_j\sqrt{2\pi}} \exp\left[-\frac{(S_t - S_j)^2}{2\sigma_j^2} \right] \cdot \frac{1}{\sigma_{\rm on}\sqrt{2\pi}} \exp\left[-\frac{(S_t - S_{\rm on})^2}{2\sigma_{\rm on}^2} \right] \mathrm{d}S_t \\ &+ \int_{-\infty}^{\infty} \frac{1-f}{\sigma_j\sqrt{2\pi}} \exp\left[-\frac{(S_t - S_j)^2}{2\sigma_j^2} \right] \cdot \frac{1}{\sigma_{\rm off}\sqrt{2\pi}} \exp\left[-\frac{(S_t - S_{\rm off})^2}{2\sigma_{\rm off}^2} \right] \mathrm{d}S_t \end{aligned} \tag{4.8}$$

Eq. 4.8 in the same manner as Eq. 4.4, represents the probability of observing S_j through any possible true flux S_t. The analytic solution to this equation is:

$$\ell_j = \frac{f}{\sqrt{2\pi\left(\sigma_{\rm on}^2 + \sigma_j^2\right)}} \cdot \exp\left[-\frac{(S_j - S_{\rm on})^2}{2\left(\sigma_j^2 + \sigma_{\rm on}^2\right)} \right] + \frac{1-f}{\sqrt{2\pi\left(\sigma_{\rm off}^2 + \sigma_j^2\right)}} \cdot \exp\left[-\frac{(S_j - S_{\rm off})^2}{2\left(\sigma_j^2 + \sigma_{\rm off}^2\right)} \right] \tag{4.9}$$

The likelihood then of N observations will be:

$$\mathcal{L}(S_{\rm on}, S_{\rm off}, \sigma_{\rm on}, \sigma_{\rm off}, f) = \prod_{j=1}^{N} \ell_j(S_{\rm on}, S_{\rm off}, \sigma_{\rm on}, \sigma_{\rm off}, f) \tag{4.10}$$

4.3 Flare time scales

In order to estimate the duration of the observed flares in the light curves, time scales have been estimated by means of two independent methods of time series analysis, a first-order

structure function (Simonetti et al. 1985) and a wavelet analysis, based on the Ricker ('Mexican hat') mother wavelet (Marchili et al. 2012). The wavelet method works by associating a variability amplitude to each time scale, in this way the dominant time scale is selected unambiguously. It is defined by :

$$\Psi(t) = C\left(1 - t^2\right) \exp\left(-\frac{t^2}{2}\right) \tag{4.11}$$

where C is the normalization factor and t is the time parameter.

The structure function instead is calculated for a time series $\{f_i\}_i$ according to :

$$SF\left(\tau\right) = \frac{1}{N} \sum_{ij} \left[f\left(t_i\right) - f\left(t_j\right)\right]^2 \tag{4.12}$$

where the sum is extended to the N pairs (t_i, t_j) for which $t_i \neq t_j$ and $\tau - \frac{\Delta\tau}{2} \leqslant \| t_i - t_j \| \leqslant \tau + \frac{\Delta\tau}{2}$. $\Delta\tau$ is generally of the order of the data sampling; the SF is calculated over a discrete set of τ values, multiples of $\Delta\tau$.

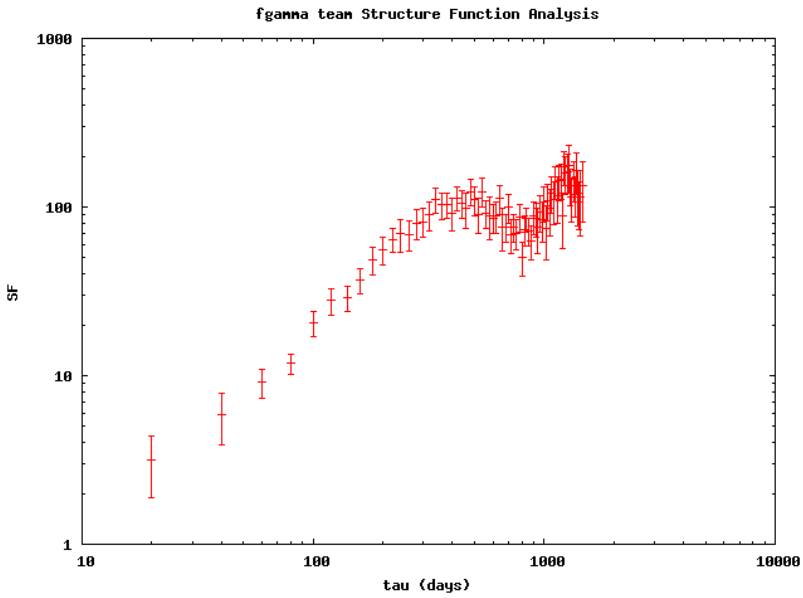

Figure 4.1: Example of the Structure function analysis output for source J2253+1608. The existence of two bumps is a signature of two distinct variability components in the dataset.

When a structure function is applied to a red-noise signal, the result is a monotonic increase that can be described by a power law. At a specific time lag the structure function shows a plateau, corresponding to the maximum coherency time of the signal. The time scale is identified then by the τ value for which the structure function shows this plateau. An example of the results of a structure function is depicted in Fig. 4.1 for J2253+1608. The existence of two bumps is a signature of two distinct variability components in the dataset and it nicely depicts that there is some degree of arbitrariness to the results of SF analysis. In this case more than one plateaus can detected, for instance at time-lags τ_1, τ_2, ..., τ_n, and

can not easily identify the most significant. In order to overcome this problem, the time scale is then defined as the τ_k for which $SF(\tau_k) \simeq \overline{SF_{high}}$, where $\overline{SF_{high}}$ is the average value of the structure function calculated for $\tau > \tau_k$. The advantage of such a definition is that it allows the automation of the calculations given the large number of light curves for the F-GAMMA sample that need to be analysed.

The comparison of the values that are returned by the SF analysis and the independent wavelet method (Marchili et al. 2012), indicates the consistence of each value. A linear regression of the structure function time scales versus the wavelet ones for the whole sample, returns a correlation coefficient of 0.83, with a slope of 1.0, showing that the definitions of the time scales are consistent among each other. More details of the methods described here are given in Marchili et al. (2012). For the analysis performed in the current thesis values of the SF method are actually used.

4.4 Spectral indices

The spectral index α of a source can provide information about the nature of the observed emission and behaviour. Spectral index depicts the dependence of flux density on frequency and is defined by $S = \mathrm{k} \cdot \nu^{\alpha}$, where ν is the frequency S is the flux density and k is a constant. To calculate the spectral index of a spectrum a least square fit using the Levenberg–Marquant numerical method is made according to equation :

$$\alpha = \frac{\log(S) - \log(\mathrm{k})}{\log(\nu)} \tag{4.13}$$

where S is flux density, ν is frequency and k is a fitting parameter. S is a straight line when depicted in a log–log space and α is the slope of that line. Three point spectral indices are calculated based on every spectrum of each source for two different set of wavelengths, namely α_{low} (60, 36, 20 mm) and α_{high} (9, 3, 2 mm). Instead of using one single spectral index for the full spectrum the approach of using two sub–band spectral indices was chosen to also study the shape and evolution of the observed spectra in greater detail. The results for the sources of the revised sample for both the calculated spectral indices are presented in Sect. 6.2.

We can discern three different cases of spectra depending on the value of the calculated α :

- Flat spectra with $\alpha = 0$
- Inverted spectra with $\alpha > 0$
- Steep spectra with $\alpha < 0$

An example of the the aforementioned α definitions are shown in Fig. 4.2. As it is shown in Sect. 6.2, all of these three cases can be seen for the computed spectral indices of α_{low} and α_{high} for the observed spectra. Traditionally in AGN studies a spectral index is assumed flat when it is smaller than ~ 0.5.

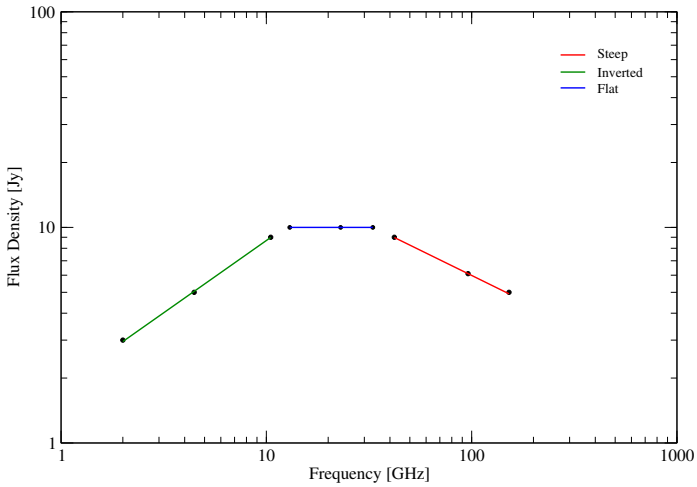

Figure 4.2: Example of three different spectral indices i.e. flat (blue), inverted (green) and steep (red) slopes.

4.5 Spectral peak analysis

The goal of the spectral analysis is to characterize the spectral behaviour of the observed sources and discriminate between possible different behaviours. For this purpose an analysis of isolated flares is performed aiming to characterize the temporal evolution and behaviour of selected flares in the S_{max}–ν_{max} plane. To find the S_{max} and ν_{max}, for every spectrum that was chosen for this analysis (see also Table 6.2), a power law with a break in the log space was used and least square fit using the numerical method of Levenberg–Marquardt. The broken power law is of the form :

$$\log(S) = k - \sqrt{l^2 + (m \cdot \log(\nu) - n)^2} \tag{4.14}$$

where S is the flux density in Jy, ν is the frequency in GHz and k, l, m, n are the fitted parameters. The corresponding frequency of the peak is given by:

$$\nu_{max} = 10^{(n/m)} \tag{4.15}$$

and the flux density at this frequency is given by:

$$S_{max} = 10^{(k-l)} \tag{4.16}$$

where S_{max} and ν_{max} are the flux density and frequency at the spectral peak respectively. As it can be seen for the spectra of the observed sources, the flaring activity is often superimposed to a steady optically thin quiescent spectrum. For the current analysis this quiescent spectrum is first subtracted before any fitting is done using Eq. 4.14. The steep quiescent spectrum can be modelled in the same manner as in Sect. 4.4, by a power law of the form :

$$S = \mathrm{k} \cdot \nu^{\alpha} \tag{4.17}$$

where ν is the frequency and S is the flux density and k is a normalization parameter that is calculated using the lowest frequency of the studied spectrum.

Ideally a source specific value of α should be used but it is not always possible to calculate such a value. The activity of the observed sources prohibits this, since flaring activity reaches the lowest observed frequencies at EB and thus is obscuring the steady and underlying quiescent spectrum. Thus for uniformity a universal and fixed value of $\alpha = -0.7$ was used as a reference for the spectral analysis performed in this thesis. Results from the spectral peak analysis are presented in Sect. 6.3.

5 Light Curve analysis

In this chapter the analysis and results of the combined 5–year F-GAMMA light curves obtained at EB and PV are presented using the tools and methods described in Chapter 4. The analysis here covers a frequency range of 2.6 GHz up to 142 GHz. In order to study the variability characteristics of the monitored sources in the time domain, a detailed light curve analysis is performed. The analysis is based on the following steps:

- Test for the existence and significance of variability (χ^2-test) (Sect. 4.1)
- Determination of the variability/flare amplitudes (see Sect. 4.2) and k–index
- Estimation of the observed flare time scales (see Sect. 4.3)
- Estimation of variability brightness temperatures and Doppler factors (see Sect. 5.5)

5.1 Observed light curves

Examples of light curves of prominent and particularly active γ–ray sources are shown in Fig. 5.1 demonstrating the extreme variability seen at all bands. The full set of light curves for the revised sample are presented in Appendix A.3.

All sources show extreme variability at all of the observed wavelengths. Dramatic flux density changes of up to a factor of 5 or more during the observed period are observed. The large outbursts and extended activity periods often last for years, however, considerable sub–structure is seen with smaller amplitude and more rapid (weeks to months) "sub-flares" are often superimposed. As it is seen from Fig. 5.1, variability at higher frequencies is often observed to be faster when compared to lower frequencies for most of

the cases. Delays are also evident for many cases, often variability first appears at mm-bands and then subsequently at cm–bands. The delay between mm and cm–bands is not always apparent with several sources showing simultaneous variability at all observed frequencies. This behaviour is fundamentally different from sources that show delays across frequencies.

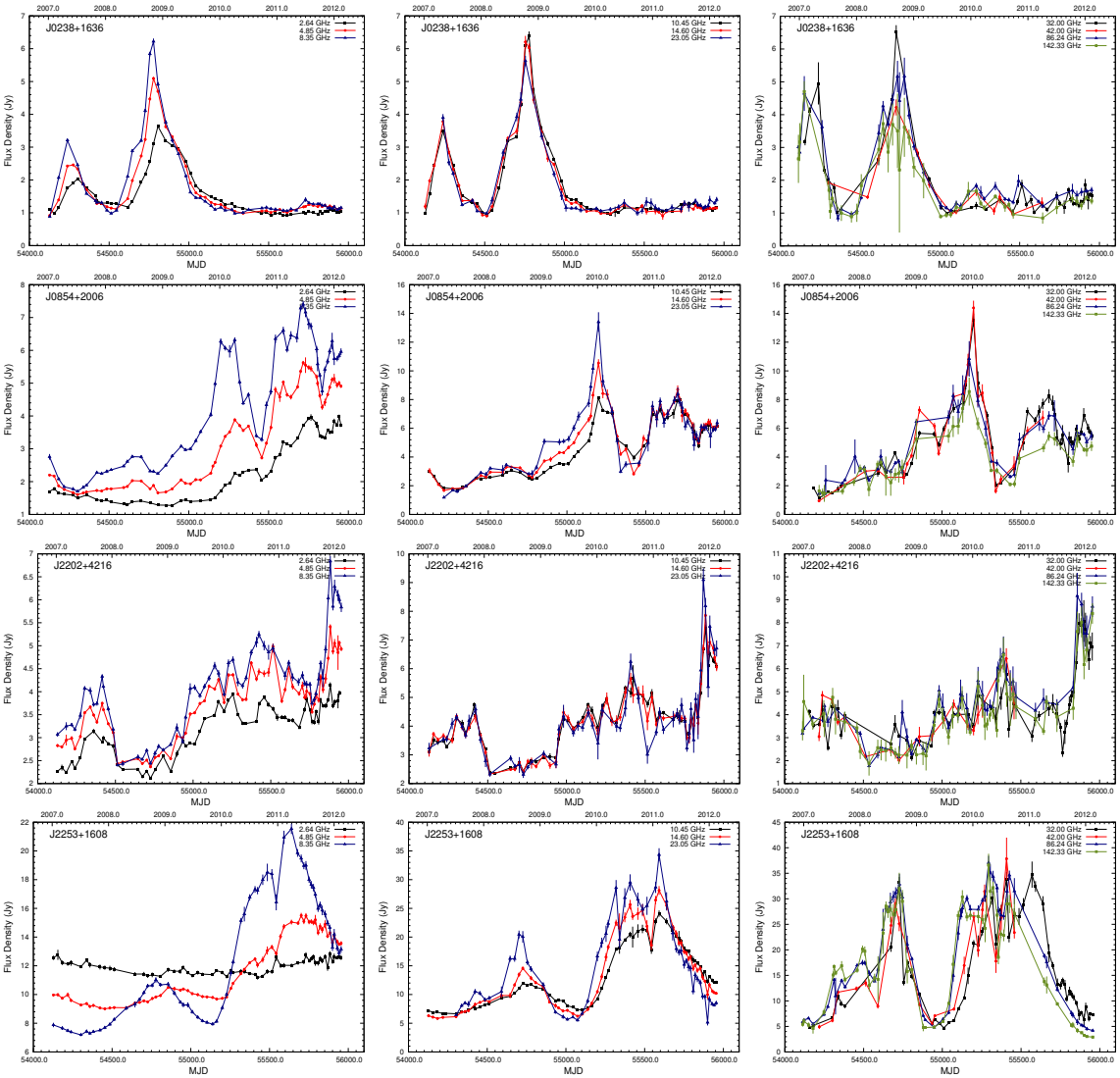

Figure 5.1: Example of light curves for selected, active γ-ray sources demonstrating the extreme variability observed at cm to short-mm wavelengths. From top to bottom are shown: J0238+1636, J0854+2006, J2202+4216 and J2253+1608. From left to right column are: Low (2, 4, 8 GHz), Medium (10, 14, 23 GHz) and High (32, 42, 86, 142 GHz) frequencies.

5.2 Variability test

The presence of significant variability in the light curves of a certain source has been evaluated through a χ^2–test as presented in detail in Sect. 4.1. A source is considered to have significant variability if the probability of constant flux density is $\leqslant 0.1\%$ (99.9% significance level). As expected, the χ^2–test results show that the calibrators used within the

F-GAMMA program are non–variable. Table 3.9 presents the calculated modulation indices of all the calibrators at all the observed frequencies.

The accuracy of determining the absolute flux density of a source is limited by the observational uncertainty the calibrators exhibit. From Table 3.9 is apparent that this uncertainty increases with frequency due to increased influence of weather at higher frequencies. Nevertheless the mean accuracy is always better than 5% reaching less than 1% at lower frequencies, demonstrating the high quality of the F-GAMMA data.

Table 5.1 presents the percentages of variable/non–variable sources in the original and revised samples for all observed frequencies. The percentage of variable sources for the revised sample is high at all frequencies with a minimum of about 90 % at 86 GHz and a maximum of 100% at many other frequencies. This shows the highly variable character of the observed source sample at all frequencies within the 5–year monitoring period.

Table 5.1: Variability as a function of observing frequency for both the original and the revised source samples and for frequencies of 2.64, 4.85, 8.35, 10.45, 14.6, 23.05, 32, 42, 86 and 142 GHz.

	2.64 GHz		4.85 GHz		8.35 GHz		10.45 GHz	
	Orig.	Cur.	Orig.	Cur.	Orig.	Cur.	Orig.	Cur.
Variable	59 (96.7%)	58 (98.3%)	59 (96.7%)	59 (100%)	58 (95.1%)	59 (100%)	57 (93.4%)	59 (100%)
non-Var.	2 (3.3%)	1 (1.7%)	2 (3.3%)	0 (0%)	3 (4.9%)	0 (0%)	4 (6.5%)	0 (0%)
	14.6 GHz		23.05 GHz		32 GHz		42 GHz	
	Orig.	Cur.	Orig.	Cur.	Orig.	Cur.	Orig.	Cur.
Variable	57 (98.3%)	59 (100%)	53 (98.1%)	54 (91.5%)	54 (98.1%)	58 (98.3%)	49 (94.2%)	47 (96.0%)
non-Var.	1 (1.7%)	0 (0%)	1 (1.9%)	4 (8.5%)	1 (1.8%)	1 (1.7%)	3 (5.8%)	3 (4.0%)
	86 GHz		142 GHz					
	Orig.	Cur.	Orig.	Cur.				
Variable	47 (77.1%)	53 (89.8%)	49 (80.3%)	55 (93.2%)				
non-Var.	14 (22.9%)	6 (10.2%)	12 (19.7%)	4 (6.8%)				

Table 5.2: Object classes of variable sources in the sample divided per frequency for both the original and the revised samples and for frequencies of 2.64, 4.85, 8.35, 10.45, 14.6, 23.05, 32, 42, 86 and 142 GHz. Reported percentages refer to variable sources only.

	2.64 GHz		4.85 GHz		8.35 GHz		10.45 GHz	
	Orig.	Cur.	Orig.	Cur.	Orig.	Cur.	Orig.	Cur.
FSRQs	30 (50.8%)	32 (55.2%)	30 (50.8%)	32 (54.2%)	30 (51.7%)	32 (54.2%)	30 (52.6%)	32 (54.2%)
BL Lacs	22 (37.3%)	15 (25.9%)	22 (37.3%)	15 (25.4%)	21 (36.2%)	15 (25.4%)	20 (35.1%)	15 (25.4%)
Blazar	4 (6.8%)	6 (10.3%)	4 (6.8%)	7 (11.9%)	4 (6.9%)	7 (11.9%)	4 (7.0%)	7 (11.9%)
Other	3 (5.1%)	5 (8.6%)	3 (5.1%)	5 (8.5%)	3 (5.2%)	5 (8.5%)	3 (5.3%)	5 (8.5%)
	14.6 GHz		23.05 GHz		32 GHz		42 GHz	
	Orig.	Cur.	Orig.	Cur.	Orig.	Cur.	Orig.	Cur.
FSRQs	30 (52.3%)	32 (55.2%)	30 (56.6%)	31 (57.4%)	27 (50.0%)	31 (53.4%)	29 (59.2%)	27 (56.3%)
BL Lacs	20 (35.1%)	15 (25.4%)	16 (30.2%)	14 (25.9%)	20 (37.0%)	15 (25.9%)	13 (26.5%)	12 (25.0%)
Blazar	4 (7.0%)	7 (11.9%)	4 (7.6%)	5 (9.3%)	4 (7.4%)	7 (12.1%)	4 (8.2%)	4 (8.3%)
Other	3 (8.5%)	5 (8.5%)	3 (5.7%)	4 (7.4%)	3 (5.6%)	5 (8.6%)	3 (6.1%)	4 (8.3%)
	86 GHz		142 GHz					
	Orig.	Cur.	Orig.	Cur.				
FSRQs	26 (55.4%)	30 (56.6%)	22 (44.9%)	31 (56.4%)				
BL Lacs	13 (27.6%)	13 (24.5%)	19 (38.8%)	14 (25.4%)				
Blazar	4 (8.5%)	6 (11.4%)	4 (8.2%)	6 (10.9%)				
Other	4 (8.5%)	4 (7.5%)	4 (8.2%)	4 (7.3%)				

An observed effect is the apparent decrease of variable sources from a value of 100%

at lower frequencies to a value of 93% at 142 GHz. This is attributed to the combined effect of weather influence, that is increasing the measurement errors (Table 3.9) at higher frequencies and the use the χ^2–test as already explained in Sect. 4.1.

The percentages of variable sources separated by source class of both the revised and original samples are presented in Table 5.2. For the revised sample the number of FSRQs is about 55% of the overall variable sources and 25% for BL Lac objects. This fraction remains constant throughout all the observed frequencies. This result is important as it allows to perform statistical comparisons across frequencies between FSRQs and BL Lac's in later analysis.

5.3 Variability amplitudes & k–index

One aspect of the encoded information in the light curves is the amplitude of the observed flares/variability. A measure of this is the intrinsic standard deviation ($\sigma_{\rm int}$) as described in Sect. 4.2. In this section the results of the computed $\sigma_{\rm int}$ values are presented. A study of $\sigma_{\rm int}$ versus rest frame frequency is also performed.

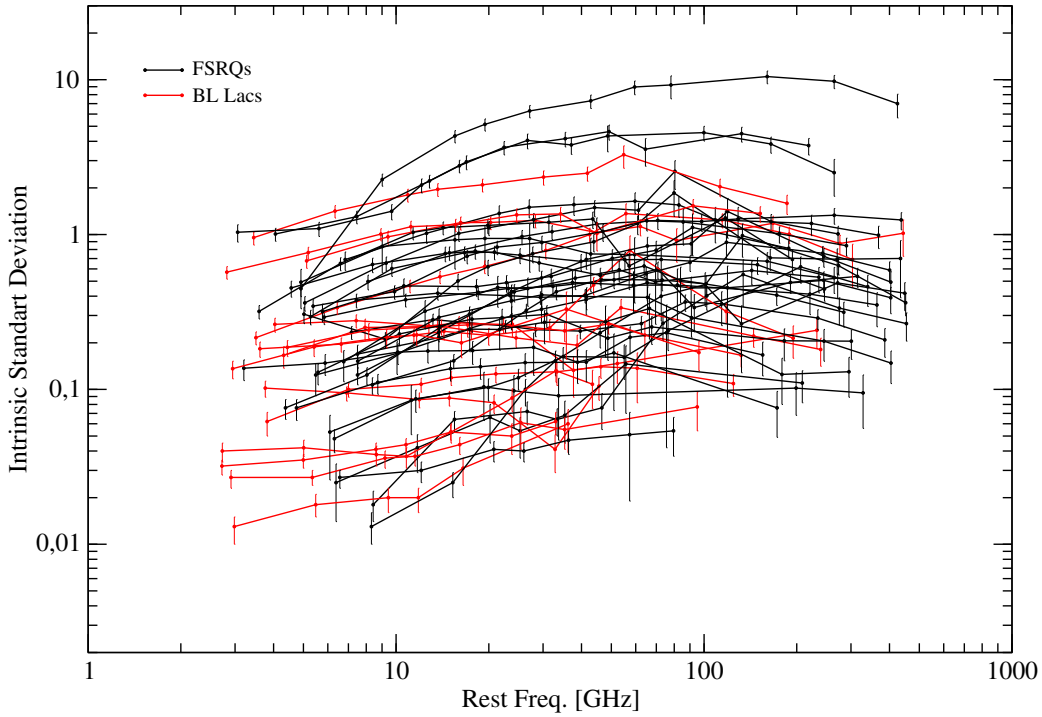

Figure 5.2: $\sigma_{\rm int}$ versus rest frequency for χ^2 variable sources. Each line represents one source, black lines are for FSRQs, red lines for BL Lac objects. BL Lac objects seem to be less variable compared to FSRQ's.

It should be noted that because the analysis is performed in the rest frequency domain, the x–axis of Figs. 5.2 and 5.3 have a range far larger than the actual observing bandpass. The dependence of $\sigma_{\rm int}$ with rest frequency for each source is presented in Fig. 5.2. A general trend is apparent with the $\sigma_{\rm int}$ for most of the sources increasing monotonously from lower towards higher frequencies reaching a maximum and then dropping again. The av-

erage $\sigma_{\rm int}$ after binning in frequency is presented in Fig. 5.3. The aforementioned trend is better seen now, with the maximum $\sigma_{\rm int}$ occurring at a rest frequency of ~ 70 GHz. Some sources though do not show this behaviour. A relative constant value of $\sigma_{\rm int}$ is observed across all frequencies for these cases. This behaviour is indicative of a source that changes its flux density in the same relative amount across all frequencies. The observed spectra of such sources are expected to change in a self–similar manner, retaining their shape as indeed observed (see also Chapter 6).

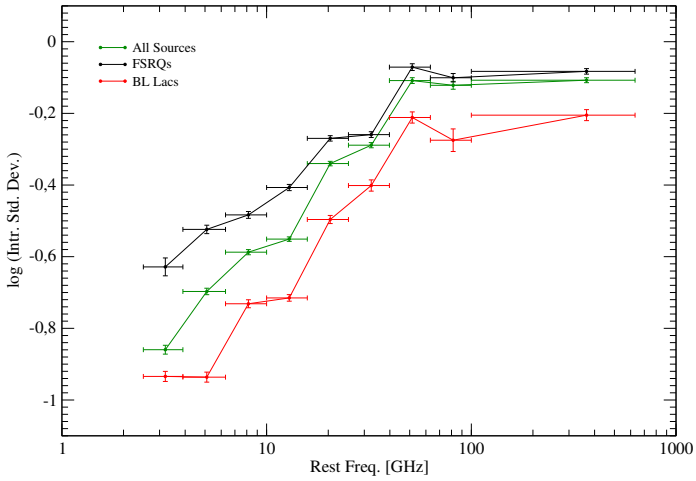

Figure 5.3: Logarithm of average $\sigma_{\rm int}$ versus rest frequency for χ^2 variable sources. Black line is for FSRQs and red line for BL Lac objects. The average is done in frequency bins, the width of each bin is represented by the bar lines in the x–axis.

The overall trend is also evident for the populations of FSRQs and BL Lacs. FSRQs exhibit much higher $\sigma_{\rm int}$ (by a factor of 2) across all frequencies when compared to BL Lac objects. An interesting feature is prominent for BL Lacs at the lowest end of the frequency range, a plateau emerges from 5 GHz to 3 GHz. This is not observed for FSRQs indicating that flare variability of BL Lacs barely reaches the lower end of the sampled frequencies, in contrast to FSRQs that the opposite behaviour is evident.

It should be noted that the decreasing trend of $\sigma_{\rm int}$variability amplitudes at frequencies higher than ∼70 GHz is not clearly seen in Fig. 5.3. This is due to a significantly lower number of sources in the particular frequency bin smearing out possible trend. The histogram of all the available measurements of the $\sigma_{\rm int}$ is presented in Fig. 5.4. BL Lacs show a clear trend towards lower values of intrinsic variability. Also a much wider distribution is evident with 95% of the sources having a range of 2.8, compared to a range of 1.8 for FSRQs. A Kolmogorov–Smirnov (K–S) test (Smirnov 1948; Press et al. 1992)[1] performed on the populations of FSRQs and BL Lacs gives a significance level of P = 99.9% for the two populations to have intrinsically different statistical characteristics in producing the observed variability, indicating that BL Lacs are intrinsically less variable compared to FSRQs.

To visualize and quantify the results of $\sigma_{\rm int}$, a new index is proposed i.e. the k–index. A power law of the form $\sigma_0 \sim \nu_{\rm rest}^k$ has been fitted to the $\sigma_{\rm int}$ data of each source in four

[1] Appendix A.5 provides information on the K–S test

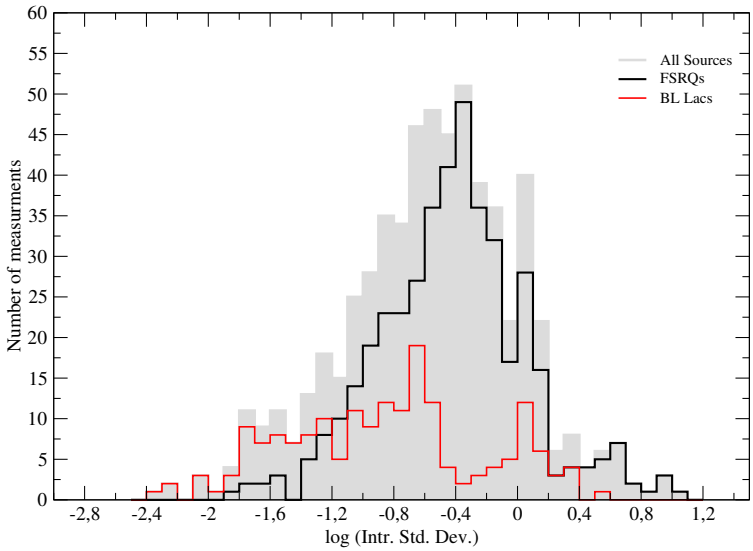

Figure 5.4: Histogram of all intrinsic variability amplitude measurements of χ^2 variable sources, black is for FSRQs and red for BL Lac objects. K–S test indicates a clear statistical difference between the aforementioned classes. Variability of BL lac objects is less powerful and with a wider distribution compared to FSRQs.

different rest frequency bands, *low* (2.64, 4.85, 8.35 GHz), *medium* (10.45, 14.6, 23.05 GHz), *high* (32, 42, 86 GHz) and *super high* (86, 142 GHz), with the k–index being the slope of the corresponding segments in Fig. 5.2.

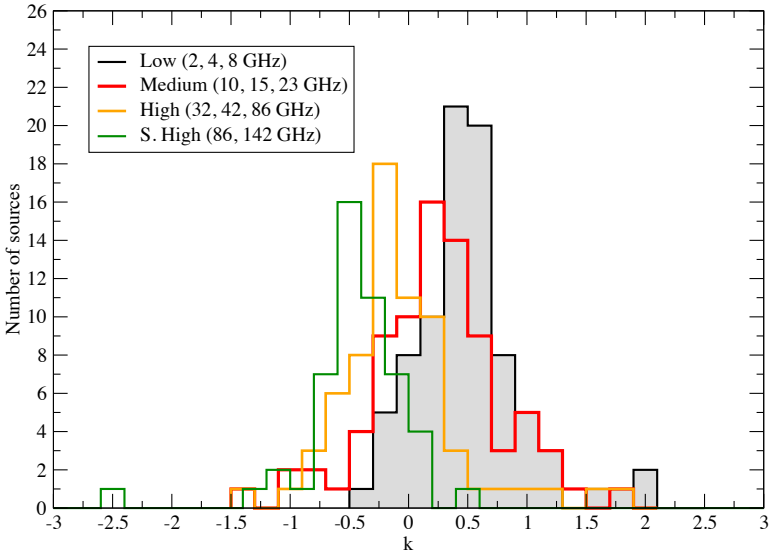

Figure 5.5: Histogram of the computed k–index ($\sigma \sim \nu^k_{\rm rest}$) for all the four frequency bands. A clear trend towards steep slopes is seen as the frequency increases. K–S test for the all the different bands, gives a significance level of $P = 99.9\,\%$ of having different statistical properties.

The distribution of the computed k–indices for all the four different bands is shown at Fig. 5.5 clearly reflecting the aforementioned behaviour and overall convex shape of the σ_{int} curves. The average values of k-index from *low* to *S. high* are initially inverted with a value of 0.51 then becomes flat (i.e. close to zero) with a value of −0.08 and finally becomes steep with a value of −0.44 (see Table 5.3). This is expected from the overall trend seen at Fig. 5.2 and Fig. 5.3. The overall convex shape of the $\sigma_{\rm int}$ curves as seen in Fig. 5.2 with a peak value at $\sim$ 70 GHz, indicates that many flares evolve towards lower frequencies within the observed bandpass. The different values of k–index at various frequencies for a specific source characterizes the evolution of a flare in the $S_{\rm max} - \nu_{\rm max}$ space as it will be shown in Chapter 6.

Table 5.3: Average values of the computed k–index for different object class.

k–index	all sources	FSRQs	BL Lacs
Low	0.51	0.62	0.22
Medium	0.25	0.30	0.14
High	−0.08	−0.01	−0.33
S. High	−0.44	−0.39	−0.32

A K–S test of all the different distributions i.e. *low* to *S.high* of k–indices, give a significance level of $P = 99.9\,\%$ of having different statistical properties indicating the different variability amplitudes that are observed throughout the frequency band.

It should be also mentioned that sources having a flat k–index across all frequencies do exist, suggesting a bi–modal nature of the observed sources, with one type of sources showing dynamically changing variability that has different strength at different parts of the spectrum and another type showing variability that changes their flux density in the same amount across all frequencies. As it will be discussed in Chapter 6 there are some exceptions to the above scheme, i.e. sources with flat k–index but with evolving spectral characteristics.

5.4 Observed time scales

As described in detail in Sect. 4.3 an SF method was employed to estimate the observed flare time scales of sources that were considered as variable by the χ^2–test. Tables 5.4 and 5.5 present the mean and median values of the estimated time scales. A trend is visible as observing frequency increases the estimated time scales are decreasing with mean values of 590 days (median 480 days) at 2.64 GHz to values of 320 days (median 300 days) at 142 GHz.

Table 5.4: Estimated mean and median variability time scales per frequency, for the revised sample and for frequencies of 2.64, 4.85, 8.36, 10.45 and 14.6 GHz.

2.64 GHz		4.85 GHz		8.36 GHz		10.45 GHz		14.6 GHz	
mean	median	mean	median	mean	median	mean	median	mean	median
592	480	555	540	494	420	475	420	480	377

Table 5.5: Estimated mean and median variability time scales per frequency, for the revised sample and for frequencies of 23.05, 32, 42, 86 and 142 GHz.

23.05 GHz		32 GHz		42 GHz		86 GHz		142 GHz	
mean	median	mean	median	mean	median	mean	median	mean	median
472	450	458	375	505	495	317	280	326	300

The estimated flare time scales range from $\sim$60–80 to a maximum of $\sim$1400 days whereas it is worth noting that 85 % of the sources at 86 GHz and 81 % at 142 GHz exhibit observed time scales shorter than 450 days. These findings are consistent with previous studies and results. For instance Hovatta et al. (2008, 2007) report variability time scales of 2.5 years and Trippe et al. (2011) deduced time scales ranging between 2 and 8 years at 90 GHz for a sample of 6 sources.

5.5 Brightness temperatures & Doppler factors

The brightness temperature of a celestial object observed at a frequency ν, is defined as the equivalent temperature of a black body in thermal equilibrium with its surroundings It is given by:

$$T_B = \frac{\lambda \cdot F(\lambda)}{2 \cdot \pi \cdot k \cdot \theta^2} \tag{5.1}$$

assuming that the received flux density is $F(\lambda)$ and that the apparent angular source size is θ. There are two main ways of measuring the source size and hence estimate the brightness temperature:

- VLBI observations
- from variability and causality arguments. The brightness temperature that is estimated with this method is called variability brightness temperature.

With VLBI observations a direct measurement of the source size and the flux density of the emitting region is possible and hence directly estimate its brightness temperature. By observing flux density variations in a specific time period δt the source size of the emitting region can be inferred using causality arguments i.e. requiring that the size of the emitting region R can not be larger than the distance light can travel within the given time δt:

$$R \leqslant c \cdot \delta t = c \cdot \frac{\delta t}{1+z} \tag{5.2}$$

where

δt : is the time scale of the observed flux density variations
z : is the redshift

Assuming that the emitting feature is moving with some velocity in the co-moving frame of the observed source and with an angle to our line of sight, then the rest frame variability brightness temperature is given by the relation :

$$T_B = 4.5 \cdot 10^{10} \cdot \Delta S_\lambda \left(\frac{\lambda \cdot \mathrm{D_L}}{\delta t_\lambda \cdot (1+z)^2} \right)^2 \tag{5.3}$$

where:

ΔS_λ : is the observed variability amplitude at λ
$\mathrm{D_L}$: is the Luminosity distance in Mpc.

Kellermann and Pauliny-Toth (1969) suggested that there is an upper limit on the brightness temperatures of compact self-absorbed radio sources. At a brightness temperature of $\sim 10^{12}$ K the energy losses imposed by inverse Compton processes of radiating electrons, become so large that rapid cooling of the system takes place, bringing the synchrotron brightness temperature below this limit. Readhead (1994) showed that for the inverse Compton catastrophe to occur, a very large divergence from the equipartition and minimum energy condition is required. Assuming equipartition between the particles radiating and the magnetic field (Scott and Readhead 1977) and combing this with an upper limit to the magnetic field, an equipartition brightness temperature limit of $5 \cdot 10^{10}$K can be defined. For the estimations performed in the following, an equipartition brightness temperature limit of $5 \cdot 10^{10}$K is assumed.

It is very common to observe brightness temperatures in excess of the equipartition limit. This excessive and over the theoretical limits temperatures can be explained in terms of relativistic boosting of the emission region allowing to obtain estimates of the Doppler boosting factors. The equation relating the brightness temperature to the Doppler factor is:

$$\delta_{var,IC} = (1+z) \sqrt[3+\alpha]{T_B / 5 \cdot 10^{10}} \tag{5.4}$$

where z is the redshift. It should be reminded that a value of $\alpha = -0.7$ is used for the current analysis.

Having estimated the observed flare amplitudes (Sect. 5.3) and time scales (Sect. 5.4) the observed flare brightness temperatures and Doppler factors can now be estimated for each source and frequency. This enables us to quantify and probe the physical conditions of the observed variable emitting regions of the monitored sources across the whole frequency band. Fig. 5.6, 5.7 and 5.8 present the histograms of the computed brightness temperature values from Eq. 5.3 for all frequencies. The mean brightness temperature is decreasing towards higher frequencies ranging between a value of $6.9 \cdot 10^{12}$ K at 2.6 GHz to $7.5 \cdot 10^{10}$ K at 142 GHz.

A similar trend is also observed when the populations of FSRQ and BL Lacs are inspected separately with values of $1.7 \cdot 10^{13}$ K at 2.6 GHz to $9.6 \cdot 10^{10}$ K at 142 GHz for FSRQs and values of $2.7 \cdot 10^{12}$ K at 2.6 GHz to $5.3 \cdot 10^{10}$ K at 142 GHz for BL Lacs. The obtained mean and median values for every frequency are given in Table 5.6.

Table 5.6: Mean and median values of estimated brightness temperatures (in K) of Eq. 5.3 for the various classes of sources and frequencies. See also Figs. 5.6, 5.7 and 5.8.

Freq.	all sources		FSRQs		BL Lacs	
(GHz)	mean [k]	median [k]	mean [k]	median [k]	mean [k]	median [k]
2.64	$6.9 \cdot 10^{12}$	$1.3 \cdot 10^{13}$	$1.7 \cdot 10^{13}$	$1.5 \cdot 10^{13}$	$2.7 \cdot 10^{12}$	$2.3 \cdot 10^{12}$
4.85	$4.0 \cdot 10^{12}$	$6.2 \cdot 10^{12}$	$1.1 \cdot 10^{13}$	$1.3 \cdot 10^{13}$	$1.2 \cdot 10^{12}$	$7.2 \cdot 10^{11}$
8.35	$2.7 \cdot 10^{12}$	$5.1 \cdot 10^{12}$	$7.2 \cdot 10^{12}$	$6.5 \cdot 10^{12}$	$9.8 \cdot 10^{11}$	$1.7 \cdot 10^{12}$
10.45	$2.0 \cdot 10^{12}$	$3.9 \cdot 10^{12}$	$5.6 \cdot 10^{12}$	$5.5 \cdot 10^{12}$	$5.0 \cdot 10^{11}$	$5.9 \cdot 10^{11}$
14.6	$1.1 \cdot 10^{12}$	$2.4 \cdot 10^{12}$	$3.3 \cdot 10^{12}$	$3.8 \cdot 10^{12}$	$3.1 \cdot 10^{11}$	$3.4 \cdot 10^{11}$
23.05	$6.8 \cdot 10^{11}$	$1.2 \cdot 10^{12}$	$2.0 \cdot 10^{12}$	$2.3 \cdot 10^{12}$	$1.6 \cdot 10^{11}$	$3.3 \cdot 10^{11}$
32.0	$3.5 \cdot 10^{11}$	$5.2 \cdot 10^{11}$	$1.1 \cdot 10^{12}$	$1.2 \cdot 10^{12}$	$7.8 \cdot 10^{10}$	$1.3 \cdot 10^{11}$
42.0	$3.0 \cdot 10^{11}$	$3.1 \cdot 10^{11}$	$7.9 \cdot 10^{11}$	$1.0 \cdot 10^{12}$	$6.9 \cdot 10^{10}$	$7.7 \cdot 10^{10}$
86.24	$2.4 \cdot 10^{11}$	$6.6 \cdot 10^{10}$	$3.0 \cdot 10^{11}$	$8.0 \cdot 10^{10}$	$1.9 \cdot 10^{11}$	$2.3 \cdot 10^{10}$
142.33	$7.5 \cdot 10^{10}$	$2.9 \cdot 10^{10}$	$9.6 \cdot 10^{10}$	$4.0 \cdot 10^{10}$	$5.3 \cdot 10^{10}$	$4.8 \cdot 10^{9}$

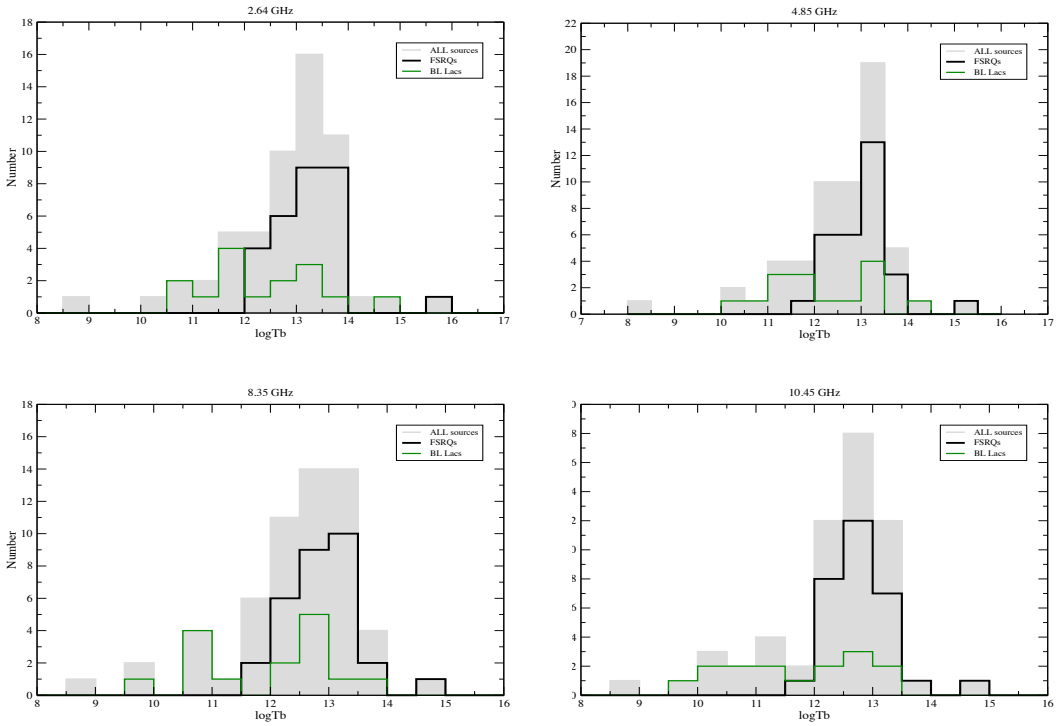

Figure 5.6: Distributions of estimated brightness temperatures at 2.64, 4.85, 8.35 and 10.45 GHz. All sources (grey) are shown with FSRQs (black) and BL Lacs (green) superimposed.

Figs. 5.6, 5.7 and 5.8 present the histograms for the distributions of FSRQs and BL Lacs for all the observed frequencies. A K–S statistical test was performed on the distributions of FSRQ and BL Lac populations, to investigate the possibility of significant differences between the two samples. The K–S tests indicate that there is a statistical difference at a significance level of $P = 99.5\%$ between FSRQs and BL Lacs population in the observed sample for all frequencies except 86 GHz. At 86 GHz the significance level for the samples to have different statistical properties is $P = 92.7\,\%$

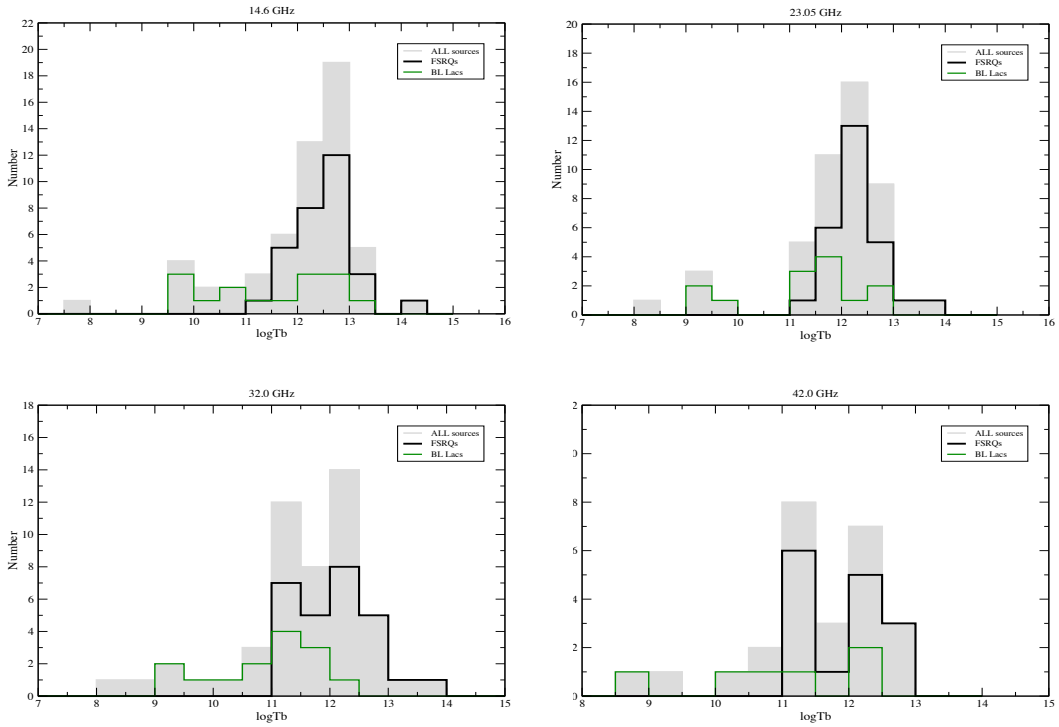

Figure 5.7: Distributions of estimated brightness temperatures at 14.6, 23.05, 32 and 42 GHz. All sources (grey) are shown with FSRQs (black) and BL Lacs (green) superimposed.

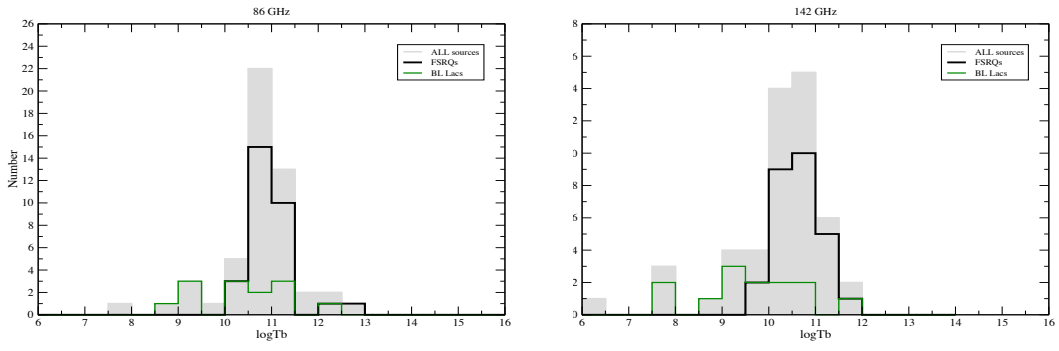

Figure 5.8: Distributions of estimated brightness temperatures at 86 and 142 GHz. All sources (grey) are shown with FSRQs (black) and BL Lacs (green) superimposed.

From the previous results it is obvious that in most of the cases estimated values of variability brightness temperatures are in excess of $5 \cdot 10^{10}$K. This excess can be attributed to relativistic Doppler boosting of the emitting region. Fig. 5.9, 5.10 and 5.11 present the histograms of the estimated Doppler factors for all the observed frequencies in the same manner as it was done with for variability brightness temperatures.

Table 5.7: Mean and median values of Doppler factors for the various classes of sources and frequencies. Doppler factors were calculated from eq. 5.4 and for a maximum T_B of $5 \cdot 10^{10}$.

Freq.	all sources		FSRQs		BL Lacs	
(GHz)	mean	median	mean	median	mean	median
2.64	9.6	8.11	13.0	10.7	5.5	3.2
4.85	8.0	7.0	10.6	9.8	4.5	2.5
8.64	6.9	6.3	9.4	8.0	4.1	3.8
10.5	6.4	6.1	8.7	7.4	3.4	2.1
14.6	5.7	5.1	7.6	6.7	3.1	2.6
23.05	4.9	4.5	6.5	6.5	2.5	2.4
32.00	4.1	3.8	5.7	5.6	1.8	1.7
42.00	3.6	3.2	4.7	4.5	2.0	2.1
86.24	2.3	2.1	2.9	2.6	1.4	1.2
142.33	1.7	1.7	2.2	2.0	0.9	0.7

As expected from the behaviour of T_b, the Doppler factors decrease towards higher frequencies. The corresponding average and median values are presented in Table 5.7. The Doppler factors are observed to decrease from values of ∼9.6 at 2.64 GHz to values of ∼1.7 at 142 GHz. The same behaviour is also evident for the populations of FSRQs and BL Lac in the sample with values ranging from ∼13 at 2.64 GHz to values of ∼2.2 at 142 GHz for FSRQs and ∼5.5 at 2.64 GHz to values of ∼0.9 at 142 GHz for BL Lacs. It should be noted that FSRQs show on average higher values of Doppler factors than BL Lacs at all frequencies.

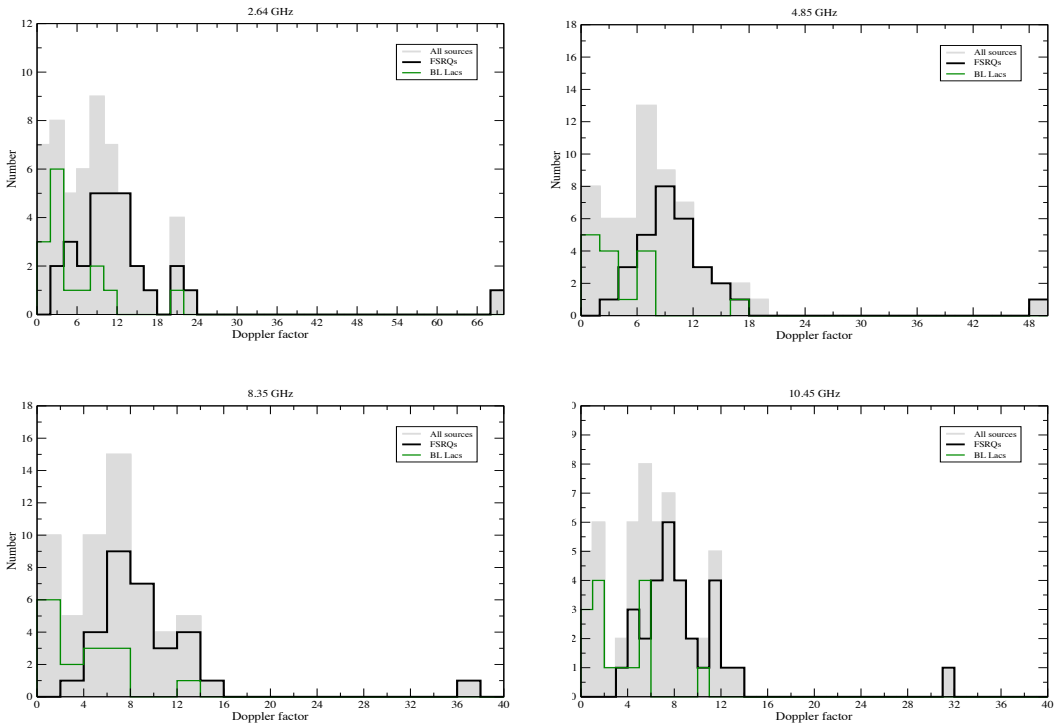

Figure 5.9: Distributions of estimated variability Doppler factors at 2.64, 4.85, 8.35 and 10.45 GHz. All sources (grey) are shown with FSRQs (black) and BL Lacs (green) superimposed. A brightness temperature limit of $5 \cdot 10^{10}$K was assumed.

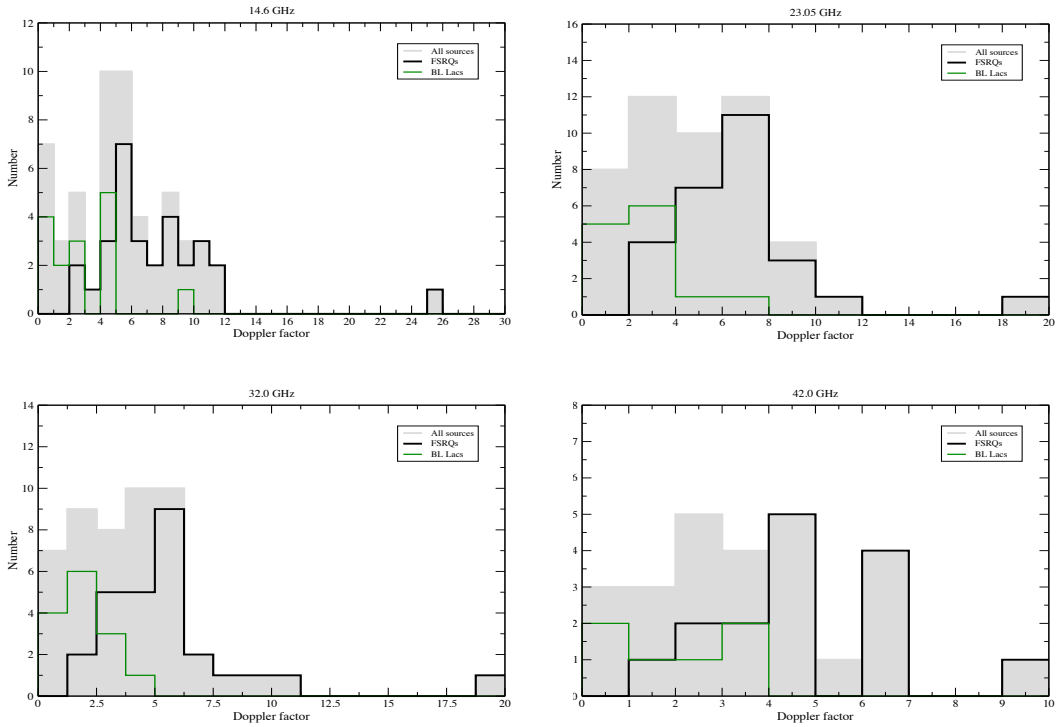

Figure 5.10: Distributions of estimated variability Doppler factors at 14.6, 23.05, 32 and 42 GHz. All sources (grey) are shown with FSRQs (black) and BL Lacs (green) superimposed. A brightness temperature limit of $5 \cdot 10^{10}$K was assumed.

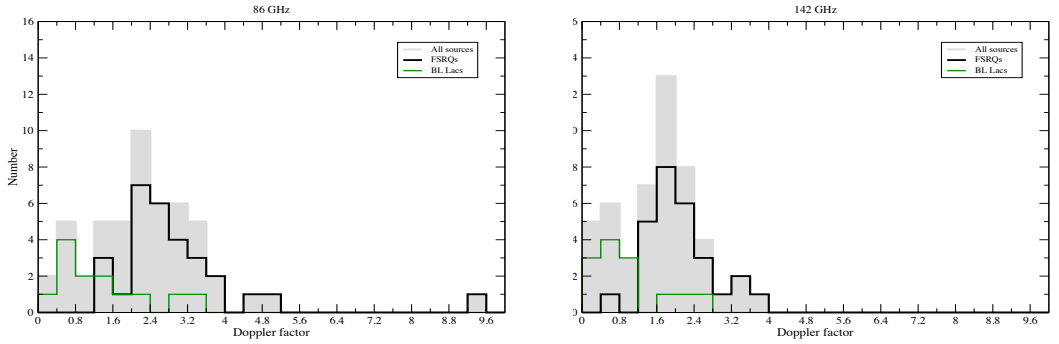

Figure 5.11: Distributions of estimated variability Doppler factors at 86 and 142 GHz. All sources (grey) are shown with FSRQs (black) and BL Lacs (green) superimposed. A brightness temperature limit of $5 \cdot 10^{10}$K was assumed.

A K–S test was performed and indeed demonstrated that there is significant statistical difference between the populations of FSRQs and BL Lacs at a significance level of $P = 99.8\%$ for all the observed frequencies. Furthermore as seen from Table 5.7 FSRQs show on average higher values of Doppler factors than BL Lacs at all frequencies. This difference is larger at lower frequencies, in accordance with the findings of the k–index and σ_{int} presented in Sect. 5.3.

6 Spectral analysis

In this chapter spectra are combined using multi–frequency data gathered at EB and PV with the techniques described in previous chapters. The resulting broadband spectra are presented and analysed aiming at a qualitative description of the observed phenomenological characteristics. A detailed study of the spectral properties of the revised sample is performed with longer data trains than previous studies. Also the evolution of flares in the $S_{max} - \nu_{max}$ plane is investigated enabling the qualitative comparison of the different variability mechanisms that are observed. The methods used for this analysis have been presented in Sect. 4.5.

6.1 Observed spectra

Typical examples of spectra observed within the F-GAMMA program are presented in Fig 6.1. Each curve depicts a quasi–simultaneous spectrum these plots is a spectrum of a specific observing epoch with measurements of up to 10 different frequencies and a coherency time of $\sim$ 2.26 days. Several characteristics of the observed spectra are evident. The overall spectral shape of the vast majority of sources is a convex one. More specifically a steep quiescent spectrum is seen at lower frequencies with superimposing and evolving flares having the shape of an SSA spectrum (e.g J2253+1608). In other cases only flares are evident showing no apparent quiescent spectrum (QS–spectrum) (e.g J0238+1608) or cases where the QS–spectrum is dominating (e.g J0418+3801) especially at lower frequencies.

The temporal behaviour of the observed spectra show extreme variability at all frequencies in accordance with the findings of the light curve analysis. As expected from findings of the k–index, most of the sources show more extreme variability towards higher frequencies. Most of the observed flares evolve from higher to lower frequencies pro-

ducing the observed delays of variability seen across frequencies (e.g J2253+1608). Other sources show variability that is correlated across the bandpass with a convex spectrum changing in a self–similar way with no apparent evolution of their flares (e.g J0730-1141 and J0750+1231).

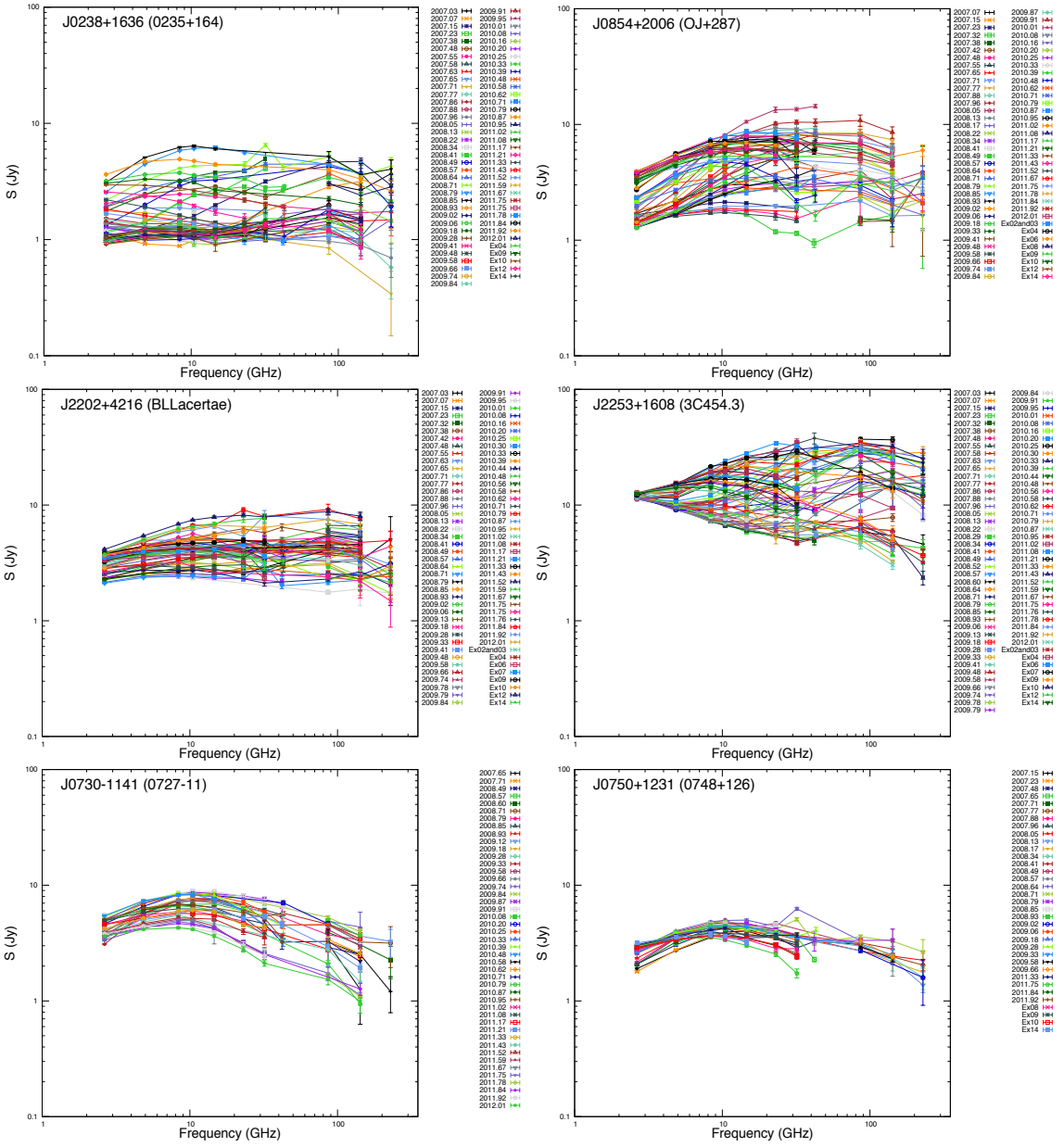

Figure 6.1: Example of spectral variability for selected, active γ-ray sources demonstrating the extreme behaviours observed at cm to short-mm wavelengths. From top to bottom are shown: J0238+1636, J0854+2006, J2202+4216, J2253+1608, J0730-1141, J0750+1231. Each curve represents a spectrum of a specific observing epoch combining quasi–simultaneous and multi–frequency data obtained at EB and PV .

All of the aforementioned characteristics confirm the large multitude of phenomenological behaviours that are seen in the observed sample. Closer inspection of the observed phenomenology reveals two major categories of behaviours that differ in a fundamental way: (a) sources that exhibit flaring events that evolve from higher to lower

frequencies (hereafter Type I sources) significantly changing the peak position of the convex SSA spectrum across frequency and (b) sources that change their convex spectrum in an "up/down" manner without changing largely their overall spectral shape and peak position (hereafter Type II sources). These fundamental differences indicate intrinsically different underlying physical mechanisms producing the observed behaviours. For a more limited data set Angelakis et al. (2012a) showed that Type I sources can be even further categorized in four phenomenological types of observed spectral behaviours with their own sub–categories. According to the analysis performed here and to the above definitions of Type I and II, of the 59 sources of the revised sample, 37 are categorized as Type I, 16 as Type II and 6 are not defined at all due to lack of data. The Type of each source as defined above and for the revised sample is presented in Table A.2.

As shown in Sect. 5.3 several sources exhibit a flat k–index in all bands. Now it becomes clear that this fact can be attributed to two different spectral behaviours of the observed sources: (a) sources that are of Type II and (b) sources that are of Type I but show continuously extreme variability at all frequencies thus producing a flat k–index (e.g. J0238+1636 at Fig. 6.1). It is interesting to note that all Type II sources have a flat k–index but not all sources with flat k–index are of Type II. Thus the k–index alone is not enough to discriminate between Type I and II sources and should only be used to point out Type II sources.

The examples presented in Fig 6.1 show typical cases of the two aforementioned type of sources. The top four sources represent typical examples of Type I behaviour and the lower two represent Type II behaviour. All observed spectra for the sources of the revised sample are presented in Appendix A.3.

6.2 Spectral indices

As already introduced in Sect. 4.4, F-GAMMA broadband spectra are analysed by calculating spectral indices in two different spectral bands: *low*, (α_{low}) (60, 36, 20 mm) and *high*, (α_{high}) (9, 3, 2 mm). This approach is followed in order to better sample the wide bandpass of the observations.

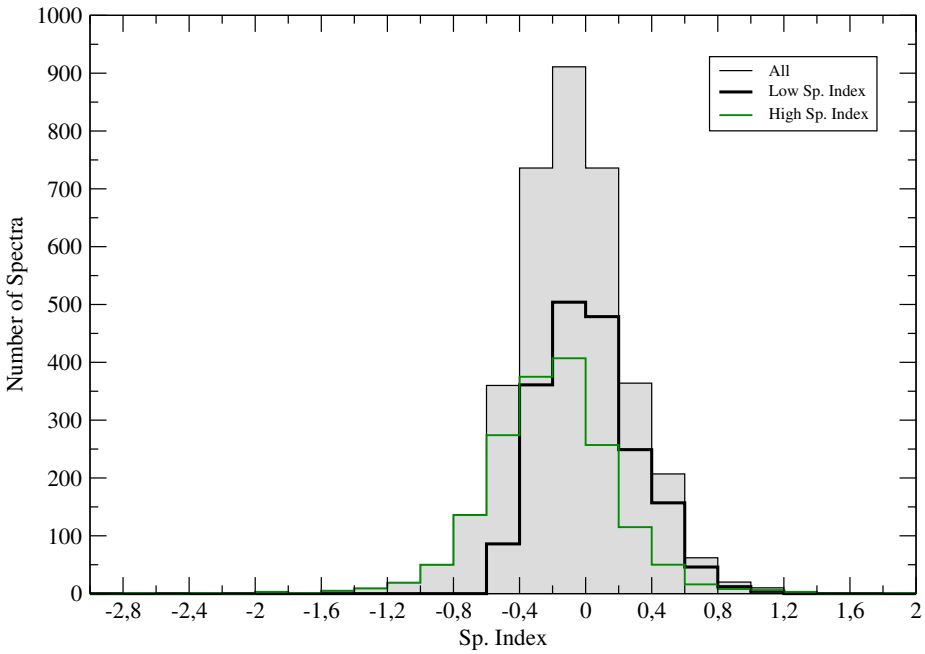

Figure 6.2: Histogram of all individual spectral indices α_{low} and α_{high} of the revised sample. The α_{high} spectral index shows a tendency of having steeper characteristics that α_{low} (see also Table 6.1 & A.3).

These spectral indices are calculated for every spectrum of a source for the revised sample allowing the study of spectral changes over five years of observations (Fig. 6.4). Fig. 6.2 presents the histogram of all the computed spectral indices. Table 6.1 presents the average values of α_{low} and α_{high}.

Table 6.1: Average values of spectral indices α_{low} and α_{high} for the various types of sources in the F-GAMMA revised sample (see also Fig. 6.2 and 6.3).

Sp. Index	all sources		FSRQs		BL Lacs	
	mean	median	mean	median	mean	median
α_{low}	0.02	0.0	0.05	0.0	0.0	−0.04
α_{high}	−0.20	−0.20	−0.25	−0.25	−0.12	−0.12

A tendency is revealed in Fig. 6.2, the α_{high} spectral index has a mean value of −0.2 and median of −0.2, steeper than α_{low} with a mean value of 0.02 and median of 0.0. A K–S test gives a significance level of $P = 99.9\,\%$ for the two distributions of spectral indices to have different statistical properties. This is in accordance to the aforementioned scheme of flares evolving from higher to the lowest observed frequencies, i.e. as a flare enters the bandpass the observer first detects the inverted leading part of the flare and then the steep part, thus an excess of steep spectra in the α_{high} band exist in contrast to the α_{low} band producing

the difference in the distributions. In addition it must be noted that the differences seen between the overall $\alpha_{\rm low}$ and $\alpha_{\rm high}$ distributions would be larger if all the observed sources exhibited flares in the same evolutionary phase and thus not averaging out the observed behaviours. Consequently Fig. 6.2 is a direct representation of the overall convex spectral shape in conjunction to evolving flares, over the five years of observations of the observed sample. The individual spectral indices for all sources of the revised sample are presented in Table A.3.

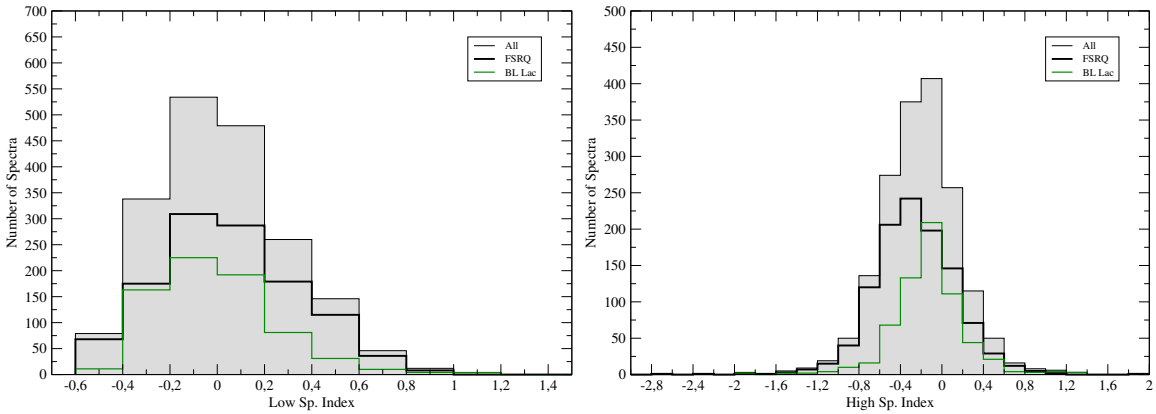

Figure 6.3: Histogram of all individual spectral indices $\alpha_{\rm low}$ and $\alpha_{\rm high}$ for FSRQs (black), BL Lacs (green) and all sources (grey) for the revised sample. It is obvious that FSRQs on average have steeper spectra than BL Lacs for the $\alpha_{\rm high}$ spectral index (see also Table 6.1 & A.3).

The histograms of $\alpha_{\rm low}$ and $\alpha_{\rm high}$ for the populations of FSRQs and BL Lacs are presented respectively in Fig. 6.3 with differences evident for the individual populations of each spectral index. $\alpha_{\rm low}$ spectral index of FSRQs and BL Lacs have similar values with a mean of 0.05 (median 0.0) and 0 (median -0.04) respectively (Table 6.1). A K–S test reports a significance level of $P = 99.9\,\%$ of the two datasets to statistically differ indicating that BL Lacs have a tendency to show on average a steeper $\alpha_{\rm low}$ index. In contrast and for the $\alpha_{\rm high}$ spectral index a K–S test reports that the significance level for the distributions of FSRQs and BL Lacs to have different statistical properties is also $P = 99.9\,\%$ but with different mean values of -0.25 (median -0.25) and -0.12 (median -0.12) respectively, confirming the visual seen difference. Therefore FSRQs on average have steeper spectra than BL Lac objects for the $\alpha_{\rm high}$ spectral index and BL Lacs tend to be steeper for the $\alpha_{\rm low}$ index. According to the aforementioned scheme of flare evolution, the observed differences between FSRQs and BL Lacs, lead to the conclusion that flares occurring in FSRQs reach lower frequencies as compared to those occurring in BL Lac objects.

Examples of the $\alpha_{\rm low}$ and $\alpha_{\rm high}$ spectral indices in comparison with multi–frequency flux density co-evolution are presented in Fig. 6.4. The corresponding evolution plots of all sources are presented in Appendix A.2. The two spectral indices are often observed to be anti–correlated, meaning that in the existence of a convex spectrum $\alpha_{\rm high}$ will be negative (steep) and $\alpha_{\rm low}$ will be positive (inverted). As seen in Fig. 6.4 the activity in the light curve of a source always relates to changes of the $\alpha_{\rm low}$ and $\alpha_{\rm high}$ spectral indices in two distinct ways corresponding to Type I and II sources. For Type I sources as a flare enters

the observed bandpass (e.g J2253+1608 in Fig. 6.4) $\alpha_{\rm high}$ becomes flatter or even inverted and then again steeper as the flare progresses to lower frequencies. $\alpha_{\rm low}$ exhibits similar behaviour but with a delay that corresponds to the individual characteristics of the flare. The two indices are observed to match and cross each other many times due to this effect. This behaviour is expected for Type I sources that produce evolving flares from higher to lower frequencies.

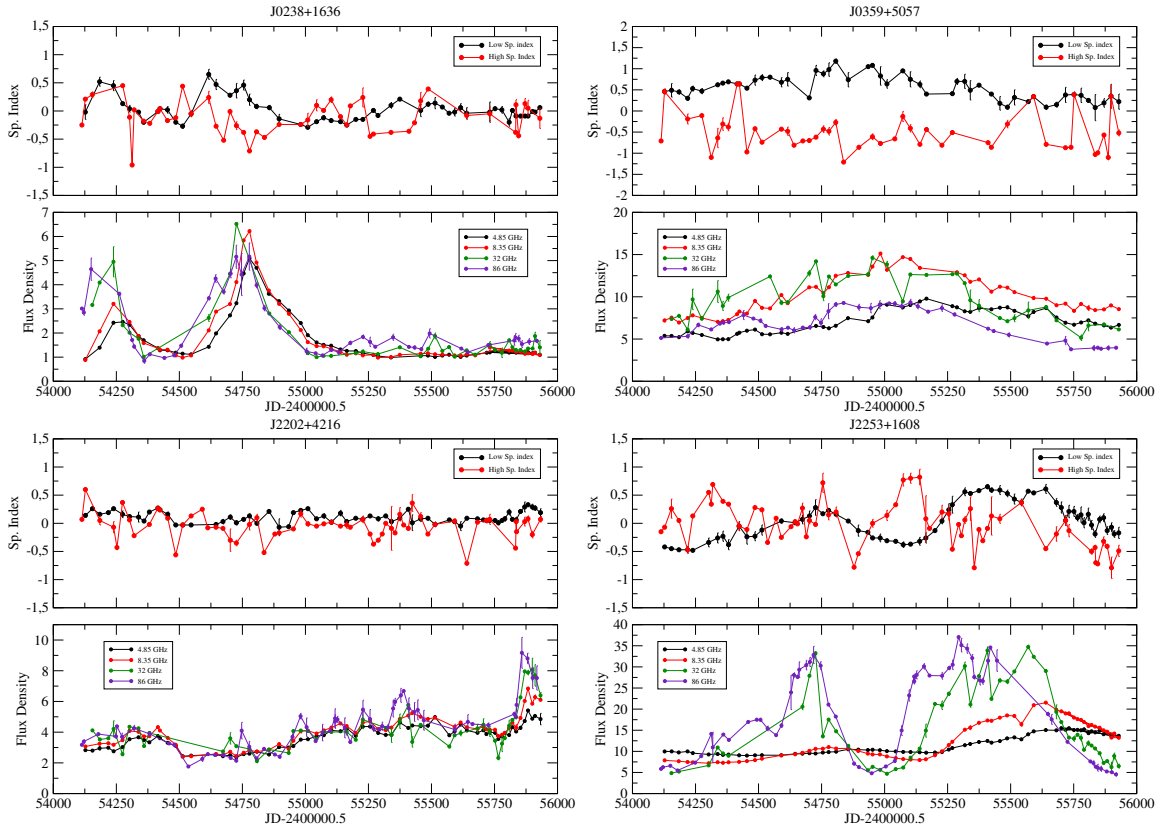

Figure 6.4: Examples of spectral index evolution. From top left and clockwise are shown J0238+1636, J0359+5059, J2202+4216 and J2253+1608. For each source the top panel presents the $\alpha_{\rm low}$ and $\alpha_{\rm high}$. The lower panel presents the light curves for the same time period for 4.85, 8.35, 32 and 86 GHz. It is clear that there is a correlation of the behaviour of the spectral indices with the observed flares in the light curves.

In contrast flaring activity in Type II sources (e.g J0359+5057 in Fig. 6.4) produces a different behaviour of the spectral indices. As the flare evolves $\alpha_{\rm low}$ and $\alpha_{\rm high}$ remain anti-correlated with the former always being flat or inverted and the latter always being flat or steep. In some cases also $\alpha_{\rm high}$ is observed to become more steep and $\alpha_{\rm low}$ to become more inverted. This is expected for Type II sources that have self–similar changing spectra and thus the spectral index values of high and low bands always sample the constant shape of a convex spectrum.

As it will be discussed in Chapter 7, this complex phenomenology of Type I sources as observed in Fig. 6.4, can be attributed to the same underlying physical mechanism as proposed in Angelakis et al. (2012a) with the modulus of redshift and observing bandpass playing a significant role.

6.3 S_{max}– ν_{max} analysis

As shown two fundamentally different types of spectral behaviour are observed, i.e. Type I and Type II sources. To quantify and characterize the individual spectral characteristics of each type an $S_{max} - \nu_{max}$ analysis is performed. Individual flare evolution and characteristics are studied according to the methods presented in Sect. 4.5. The spectral peak for each spectrum of the studied flares is estimated allowing to trace the evolution of the flare in the S_{max}– ν_{max} plane.

6.3.1 Flare sample

The observations of the F-GAMMA program provide a large number of spectra for all the sources of the revised sample. Some strict criteria though have to be applied in order to isolate simple flares and events that are suitable for the current analysis. The applied criteria for constructing the flare sample are as follows:

- *Well defined start and end time of a flare*

  The *Start Time* of a flare is defined as the time of the flux density local minimum before the flare starts at the highest observed frequency.

  The *End Time* of a flare defined as the time of the flux density local minimum after the flare decayed at the lowest observed frequency. With these definitions a flare can be observed throughout all its evolutionary phases.

- *No superimposing flares or part of a larger flare*

  Any flare should not be a superimposition of other several minor flares. From a physical point of view the case of a flare that is a composite of two or more sub–flares, indicates the superimposition of several independent events not correlated to each other. In order to avoid any influence of the resulting spectral peak path in the S_{max}– ν_{max} plane only flares showing no secondary activity are selected.

- *Sufficient spectral coverage and data*

  The fitting algorithm requires a minimum number of data points to estimate the spectral peak correctly. The minimum number of points is four and ideally equally spaced around the spectral peak. To sufficiently trace the evolutionary path of a spectral peak in the S_{max}– ν_{max} plane a minimum number of 6 spectra is required.

Table 6.2: Basic information for the 24 flares that fulfilled the criteria and were used for the analysis. Each line presents information for a separate flare.

No.	Source	MJD Start	MJD End	Duration [days]	# Epochs	Sampl. [mon/spec]	z	ΔS [Jy]	$\Delta\nu$ [GHz]	Class	Type
1	J0102+5824	54500	55200	700	21	1.07	0.644	2.6	96.8	Blazar	I
2	J0217+0144	54300	54950	650	24	0.87	1.715	0.8	30.1	FSRQ	II
3	””	55100	55550	450	20	0.72	1.715	1.5	21.2	FSRQ	II
4	J0237+2848	54300	55200	900	33	0.88	1.213	1.3	20.2	FSRQ	II

Table 6.2: continued.

No.	Source	MJD Start	MJD End	Duration [days]	# Epochs	Sampl. month/spec.	z	ΔS [Jy]	$\Delta\nu$ [GHz]	Class	Type
5	J0238+1636	54100	54500	400	16	0.80	0.940	3.9	102.9	BL Lac	I
6	″″	54500	55100	600	19	1.02	″″	5.1	136.0	″″	I
7	J0359+5057	54200	55800	1600	56	0.92	1.520	10.4	17.3	Blazar	II
8	J0418+3801	54100	54800	700	24	0.94	0.049	8.8	66.2	RG	I
9	J0423-0120	54750	55600	850	32	0.85	0.914	5.0	45.0	FSRQ	I
10	J0730-1141	54600	56000	1400	43	1.05	1.589	6.0	8.3	FSRQ	II
11	J0818+4222	54750	55600	850	28	0.98	0.530	1.0	15.0	BL Lac	II
12	J0854+2006	54700	55450	750	26	0.93	0.306	11.63	33.9	BL Lac	I
13	J1130-1449	54800	55650	850	25	1.10	1.184	2.9	70.9	FSRQ	I
14	J1159+2914	54300	55100	800	27	0.95	0.729	3.6	126.4	FSRQ	I
15	″″	55150	56000	850	27	1.01	″″	2.4	41.5	″″	I
16	J1256-0547	54300	55100	800	31	0.83	0.536	11.7	38.7	FSRQ	I
17	J1504+1029	54600	55400	800	32	0.80	1.839	3.8	28.1	FSRQ	II
18	J1512-0905	54400	54900	500	21	0.77	0.360	1.7	42.2	FSRQ	I
19	J1642+3948	54550	55600	1050	36	0.94	0.593	4.6	28.0	Blazar	I
20	J1751+0939	55400	56000	600	23	0.84	0.322	5.1	65.5	Blazar	I
21	J2025-0735	55250	55700	450	14	1.03	1.388	1.5	89.8	FSRQ	I
22	J2232+1143	54850	55400	550	20	0.88	1.037	4.2	77.4	FSRQ	I
23	J2253+1608	54400	55000	600	24	0.80	0.859	23.6	111.1	FSRQ	I
24	″″	55000	56000	1000	48	0.67	″″	30.1	135.9	″″	I

Even with the large F-GAMMA database in hand, after the application of the above criteria only 24 flares could be isolated for further analysis. This is indicative of blazars, being highly active at all wavelengths and time scales with flares frequently blending with each other. Table 6.2 presents these 24 flares that are finally selected along with their individual characteristics, in Appendix A.4 all the obtained $S_{max} - \nu_{max}$ plots for all the studied flares.

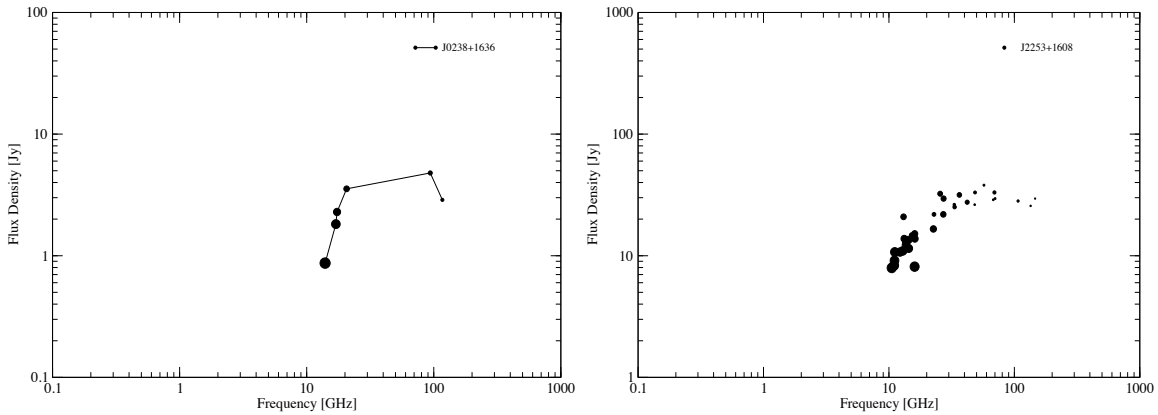

Figure 6.5: Evolution of the spectral peak in the S_{max}– ν_{max} plane for Type I flares. Left panel is J0238+1636, right panel is J2253+1608. The size of the symbols represents the time evolution. Time flows forward from smaller to larger points.

Typical examples of the observed behaviour for the selected flares in the $S_{max} - \nu_{max}$ plane are presented in Fig. 6.5 for J0238+1636 and J2253+1608 and in Fig. 6.6 for J0730-1141 and J0359+5057. Two categories of evolutionary paths are evident: (a) 17 flares show a systematic evolutionary path starting at higher frequencies with low flux density, a plateau at high flux density levels and subsequently a decay towards lower frequencies. This be-

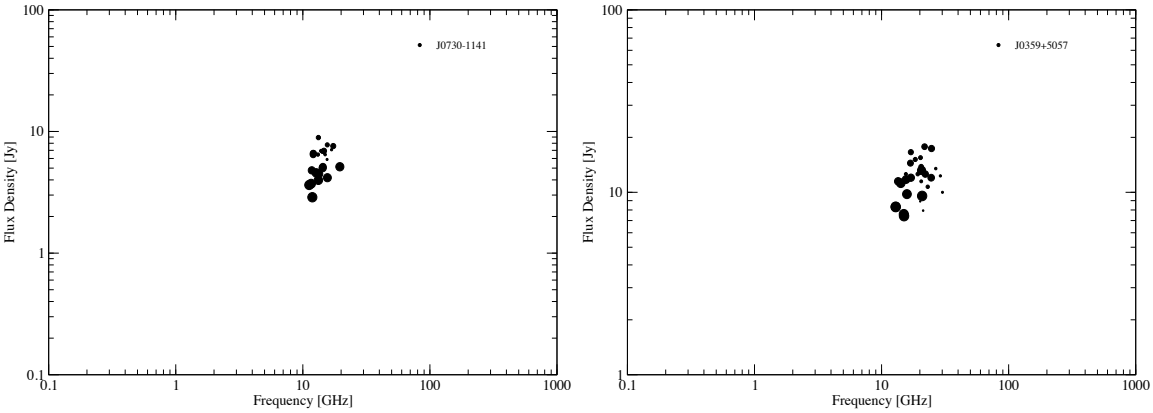

Figure 6.6: Evolution of the spectral peak in the S_{max}– ν_{max} plane for Type I flares. Left panel is J0730+1141, right panel is J0359+5057. The size of the symbols represents the time evolution. Time flows forward from smaller to larger points.

haviour is in accordance with the spectral evolution of Type I sources. The observed path closely resembles the three evolutionary stages of shocks (Valtaoja et al. 1992b) as seen in Fig. 1.8 and discussed in Sect. 7.1 (b) 7 flares show a more chaotic and much less systematic path of evolution with flux density mostly changing only in an "up/down manner" in accordance with behaviour observed to Type II sources and in disagreement with the standard shock in jet models.

As seen in Table 6.2, is interesting that both FSRQs and BL Lacs show Type I and II characteristics indicating that both are capable of producing variability with intrinsically different physical mechanisms. It is worthwhile noting that from the 7 flares corresponding to Type II sources only one source is of the BL Lac class. No conclusions can be made for the parent populations due to low number statistics and biases inherent to the flare selection process performed here.

The number of FSRQ flares is much larger than BL Lac flares is such a bias. The selection of flares reaching much lower frequencies is favoured over flares that their whole evolution is not visible within the observed frequency bandpass due to the fact that they do not reach low enough frequencies. Since FSRQ flares reach lower frequencies it is more probable to observe their flares in contrast to BL Lac flares.

In summary in order to discriminate between Type I and II sources only three basic factors are needed:

- *Flux density range* – $\Delta\,(S_{max})$

  The range of values in the y–axis, defined as the difference between maximum and minimum observed S_{max} values.

- *Frequency range* – $\Delta\,(\nu_{max})$

  The range of values in the x–axis, defined as the difference between the highest and lowest ν_{max} values a spectral peak is observed.

- *Evolutionary path*

The existence or not of a systematic evolutionary path in the S_{max} – ν_{max} plane. Time evolution in the S_{max} – ν_{max} plots is indicated by the size of the points. Time flows forward from smaller to larger symbol size, indicating the path that is followed by the spectral peak.

In order to further quantify the observed characteristics of the selected flare sample in the S_{max}– ν_{max} plane, the calculated values of $\Delta(S_{max})$ and $\Delta(\nu_{max})$ for each flare are plotted against each other in Fig. 6.7, the individual calculated values are shown in Table 6.2.

Flares that correspond to Type I sources show a large scatter in both frequency and flux density, with mean values of $\Delta(S_{max}) = 7.5\,\mathrm{Jy}$ and $\Delta(\nu_{max}) = 76.9\,\mathrm{GHz}$ respectively (e.g Fig. 6.5. Often not all phases are seen and no plateau is visible. This indicates that all Type I sources have similar phenomenology but the detailed behaviour of a particular source is governed by it's individual physical parameters. Flares corresponding to Type II sources show in contrast much smaller scatter in both frequency and flux density with a mean value of $\Delta(\nu_{max}) = 20.0\,\mathrm{GHz}$ and a mean value of $\Delta(S_{max}) = 3.5\,\mathrm{Jy}$ (e.g Fig. 6.6). The key element that differentiates Type I and II flares apart from the different scatter in frequency is the distinct evolutionary path that the former follow in the S_{max}– ν_{max} plane. It is interesting to note that a source exhibiting a particular type of flare never exhibited flares of the other type. This indicates that the underlying physical mechanism in a given source remained the same over the whole 5 years period of F-GAMMA observations.

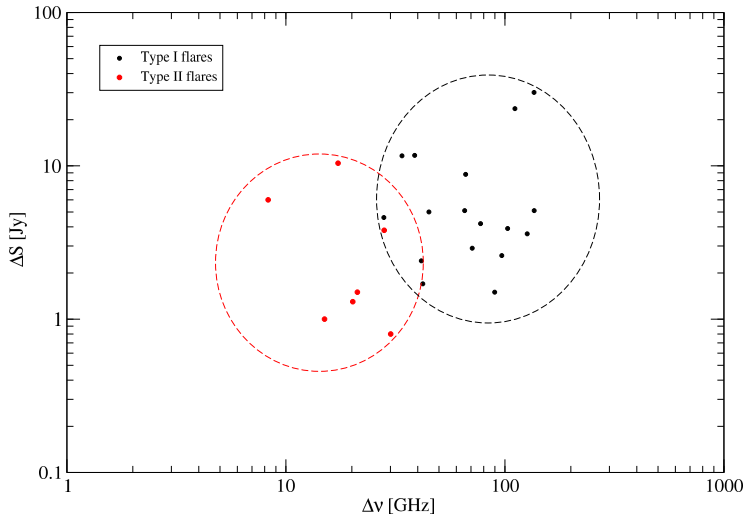

Figure 6.7: Type I and Type II flares in a $\Delta(S_{max})$–$\Delta(\nu_{max})$ plane, showing a clear distinction between them.

The difference between Type I and II flares is graphically depicted in Fig.6.7, with the two populations occupying a distinct space in the $\Delta(S_{max})$ – $\Delta(\nu_{max})$ plane. Type I flares shown in black are located in the upper right corner in contrast to the Type II flares that occupy the lower left area of the plot. As it will be discussed in Chapter 7, these two sepa-

rate populations support a scenario of two intrinsically different mechanisms that governs their behaviour.

7

Discussion and Summary

7.1 Discussion

For the first time a large sample of blazars is systematically monitored at cm to short-mm bands during an extended period of 5 years and at a mean cadence of 1.2 months and spectral coherency of 2.2 days. In order to study and establish the detailed cm to mm-variability and spectral characteristics of the monitored sources, precise flux density measurements are required including a detailed understanding of the inherent measurement uncertainties. A rigorous error analysis has been developed which accounts for all possible uncertainties of the observables for data acquired with the Pico Veleta 30 m telescope. For this reason new semi-automated routines in IDL were written that accommodate all of the above. A careful system study has been carried out in order to estimate the contribution of each element and reduction step to the final error propagation.

As shown in Sect. 5, the observed sources have mean total flux densities in the range of $\sim 0.3 - 40$ Jy at all observed frequencies and overall fractional flux density uncertainties of $\sim$ 1 % at 2.64 GHz and $\sim$ 12 % at 142 GHz. However these numbers are mean values over 5 years, i.e. averaged over all possible system and weather conditions. For instance, during excellent atmospheric conditions the single flux density uncertainty values are significantly lower. Furthermore, the system repeatability and overall calibration/gain stability is demonstrated by the small residual mean scatter (m_0) in the calibrator light curves with values ranging between $\sim$ 0.6 % at 4.85 GHz and $\sim$ 4 % at 142 GHz (Table 3.9).

The overall system behaviour of the PV telescope is summarized in Fig. 3.6 and allows the estimation of the expected uncertainty at a certain flux density level, given the typical integration times used in the current monitoring program (2 – 4 minutes). Those uncertainties which are dominated by the telescope characteristics (rather than atmospheric

conditions) can be described by fitting lower envelopes like presented in Fig. 3.6. At flux density levels between $\gtrsim$ 100 mJy to about 4 Jy the maximum fractional error ($\sim$25 %) drops and reaches a plateau. Here, at flux density values $\gtrsim$4 Jy, the minimum fractional error is $\sim$ 0.7 % at 86 GHz and $\sim$ 1.3 % at 142 GHz. The averaged behaviour (green curve in Fig. 3.6) represents the typical performance at average atmospheric conditions. Here, the fractional error at 86 GHz drops with increasing flux density from a value of $\sim$ 20 % (at $\sim$0.3 Jy) to $\sim$ 5 % towards larger flux densities. At 142 GHz the corresponding values drop from $\sim$ 24 % to $\sim$ 7 % (see also Sect. 3.2). Finally it is found that the relative gain between the two orthogonal polarizations of the EMIR system at 86 GHz is of the order of 2 % and that the achieved cross-calibration between the EB and PV telescopes is better than 2 % up to 142 GHz.

Based on a χ^2 test and for a 99.9 % significance level it is found that a minimum of about 90 % of the 59 target sources at 86 GHz of the revised F-GAMMA sample are variable. For lower frequencies this percentage is 100% showing the highly variable character of the observed sample. An observed effect is the apparent decrease of variable sources from a value of 100% at lower frequencies to a value of 90% at 86 GHz. This is attributed to the combined effect of weather influence, that increases the measurement errors (Table 3.9) at higher frequencies and the use of the χ^2–test that is not sensitive enough under those conditions, as explained in Sect. 4.1. For the revised sample the number of FSRQs sources is about 55% of the overall variable sources and 25% for BL Lac objects. This fraction remains constant throughout all the observed frequencies enabling statistical comparisons between the populations of FSRQs and BL Lacs.

A visual inspection of the cm/mm band light curves often shows extended activity periods typically lasting for years whereas considerable sub-structure and more rapid (single) flares (weeks/months to $\leqslant$ 1-2 years) are observed. The estimated time scales of flares in the five year light curves using SF analysis range from $\sim$60–80 to a maximum of $\sim$1400 days whereas 85 % of the sources at 86 GHz and 81 % at 142 GHz exhibit observed time scales shorter than 450 days (Sect. 5.4). A trend is visible as observing frequency increases, the estimated time scales are decreasing with mean values of 590 days (median 480 days) at 2.64 GHz to values of 320 days (median 300 days) at 142 GHz. These findings are consistent with previous short–mm band studies and results, reporting variability time scales of $\sim$ years (long-term trends/activity) and (single) flares occurring on shorter time scales. Hovatta et al. (2008, 2007) report variability time scales in the order of 2.5 years for a sample of 55 sources and Trippe et al. (2011) found time scales ranging from 2 to 8 years at 90 GHz for a sample of 6 sources. At cm–bands the corresponding time scales are found to be of the order $\sim$ 500 days in accordance with previous findings. Hovatta et al. (2008, 2007) reports time scales of $\sim$ 3 years which are considerably longer. This difference can be explained by the stochastic nature of variability and the limited observing period of five years in the current analysis, limiting the sensitivity of detecting long-term variations and trends. Furthermore, the monthly cadence limits the detection of variability on time scales shorter than a few months.

The amplitudes of the observed flare activity has been estimated using a likelihood

analysis allowing for an accurate determination of the observed intrinsic light curve standard deviations ($\sigma_{\rm int}$). The vast majority of sources show an increasing intrinsic standard deviation as rest frequency increases (Fig. 5.3), reaching a plateau at $\sim$ 60–70 GHz. This shows that peak amplitudes occur at rest frequencies $\sim$ 70 GHz confirming previous studies (Valtaoja et al. 1992b; Stevens et al. 1994; Hovatta et al. 2008). FSRQ and BL Lac populations show a similar behaviour but with BL Lacs showing a clear trend with significant lower values of $\sigma_{\rm int}$ (Table 5.3 and Fig. 5.4). An interesting feature is evident for BL Lacs at the lowest end of the frequency range, a plateau emerges from 5 GHz to 3 GHz in contrast to FSRQs, indicating that flare variability for BL Lacs rarely reaches the lowest observed frequencies. The corresponding slope (k–index) of $\sigma_{\rm int}$ was calculated to quantify the behaviour across rest frame frequency (Fig. 5.2). The k–index was calculated at four different frequency bands namely *Low, Medium, High* and *S. High* with calculated values ranging from an inverted slope of 0.51 in the *Low* band to a steep slope of -0.44 in *S. High*, revealing a clear trend: the k–index shows steeper values as frequency increases. This is expected from the overall trend seen at Fig. 5.2 and Fig. 5.3. The overall convex shape of the $\sigma_{\rm int}$ curve as shown at Fig. 5.2 with a peak value of $\sim$ 70 GHz, indicating that many flares start evolving towards lower frequencies within the observed bandpass. Valtaoja et al. (1992b); Hovatta et al. (2008) typically obtain high frequency slopes of -0.2 to -0.3 using (single) flare amplitudes and frequencies scaled to the frequency where the maximum occurs, in very good agreement with currently reported values (Table 5.3). This behaviour is in accordance to physical models with the hypothesis of flares produced by shocks in jets (see bellow). Sources with flat k-index values across all the observed frequencies are also found to exist, showing inherently different behaviour from the previous described sources. This behaviour consists of sources that show similar values of $\sigma_{\rm int}$ across the spectrum indicating that a different physical mechanism is at work.

For the first time variability brightness temperatures are presented for a large number of sources at cm to short mm–bands. The estimated flare time scales and flare amplitudes correspond to mean variability brightness temperatures decreasing from $6.9 \cdot 10^{12}$ K at 2.64 GHz to $7.5 \cdot 10^{10}$ K at 142 GHz, which are above the theoretically allowed equipartition limit of $5 \cdot 10^{10}$ K (see also Sect 5.5) thus requiring Doppler boosting to account for the difference. It is also found that there is a statistically significant difference between the T_B distributions of FSRQs and BL Lacs. The corresponding Doppler factors (see Sect. 5.5) show a drop as frequency increases with FSRQs having higher Doppler factors when compared to BL Lacs. Mean values ranging form 9.6 to 1.7 for 2.64 and 142 GHz are obtained respectively. Hovatta et al. (2009) has calculated Doppler factors at 22 and 37 GHz using the same limit of $T_B = 5 \cdot 10^{10}$ K and reports that at 22 GHz the Doppler factors are slightly higher than at 37 GHz. This is in agreement with the current findings and with the trend of increasing Doppler factors towards lower frequencies suggesting that Doppler factors of blazars at cm and mm wavelengths are generally different. Looking deeper into the jet towards higher frequencies, decreasing Doppler boosting would then indicate either jet-acceleration (changes of the Lorenz factor along the jet) and/or jet bending (with changes in the viewing angle) for outward motion. An interpretation of these results as a geomet-

rical effect, however, is less likely given it's statistical nature. Consequently, these findings can be interpreted as evidence for jet-acceleration on pc-scales. The reported trend of FSRQs exhibiting stronger Doppler boosting compared to BL Lacs, is in good agreement with BL Lacs typically showing slower VLBI apparent jet speeds and Lorentz factors compared to FSRQs (e.g Piner et al. 2010). However the influence of effects due to specific shock in jet model parameters on the currently obtained results, can not be ruled out and needs further investigation in future studies.

A wealth of different spectral characteristics are observed for the source sample, that at a first glance seem diverse and uncorrelated to each other. A closer inspection reveals that all this behaviours can be reduced to two major categories: *Type I source:* corresponding to behaviour that exhibits spectra typically consisting of two components (a) a steep quiescent spectrum and (b) a Synchrotron Self–Absorbed (SSA) convex spectrum, with the latter evolving from higher to lower frequencies. Depending on the source–specific characteristics and redshift (see bellow) and also (Angelakis et al. 2012a) their flares are observed either throughout all of their evolution or only during a specific part. *Type II sources:* corresponding to behaviour that shows "achromatic" variability, meaning that their spectra change in a self–similar manner mostly retaining their shape in contrast to Type I sources. This type of sources also shows a flat k–index as already mentioned, showing relatively constant variability amplitudes across the observed spectrum.

Further analysis of the spectral characteristics included the estimation of spectral indices at two different bands i.e. $\alpha_{\rm low}$ and $\alpha_{\rm high}$. Estimated mean values of 0.02 for $\alpha_{\rm low}$ and -0.2 for $\alpha_{\rm high}$ (Fig. 6.2) show that at higher frequencies spectra are on average steeper. Mean values for FSRQs and BL Lacs (Table 6.1) reveal that at lower frequencies ($\alpha_{\rm low}$) both populations have flat spectra but BL Lac objects tend to have slightly steeper spectra with a mean value of 0.0 in comparison to FSRQs with mean values of 0.05 (Fig. 6.3). At higher frequencies ($\alpha_{\rm high}$) FSRQs are found to have steeper spectra with a mean value of -0.25 in comparison to BL Lacs with a mean value of -0.12. The overall spectral flatness that is observed, especially for $\alpha_{\rm low}$, is the result of averaging over different spectral components and states (optically thin, steep spectrum quiescent jet and evolving SSA components). Trippe et al. (2011) finds variable spectral indices ranging between -0.5 to -1 for their 6 sources studied at short-mm bands. These results are in good agreement with the 86/142 GHz spectral indices obtained for FSRQs in the current analysis. The observed difference between FSRQs and BL Lacs could be interpreted by assuming that BL Lacs show turnover frequencies at systematically higher frequencies and that their flares systematically do not reach the lowest frequencies when compared to FSRQs.

In order to quantify and characterise the phenomenological behaviour of Type I and II sources an analysis of 24 individually selected flares has been performed. The spectral peak position and evolution in the $S_{\rm max} - \nu_{\rm max}$ plane is studied (Sect. 6.3) showing that flares of Type I sources exhibit a clear evolutionary path in the $S_{\rm max} - \nu_{\rm max}$ plane with large scatter in both frequency ($\nu_{\rm max}$) and flux density ($S_{\rm max}$). Mean values of $\Delta\left(S_{\rm max}\right) = 7.5\,$Jy and $\Delta\left(\nu_{\rm max}\right) = 76.9\,$GHz are found for Type I flares. In contrast Type II sources exhibit flares that show no clear evolutionary path in the $S_{\rm max} - \nu_{\rm max}$ plane but rather show an

"up/down" pattern as expected from the self–similar changing spectrum of these sources. Here, mean values of $\Delta(S_{\max}) = 3.5\,\mathrm{Jy}$ and $\Delta(\nu_{\max}) = 20\,\mathrm{GHz}$ are found for Type II flares significantly different compared to Type I sources. It should also be noted that in the light curves of Type II sources mostly no time delays are evident between flares at different frequencies in complete contrast to the large time delays of Type I sources. These differences are clearly depicted in the $\Delta(S_{\max}) - \Delta(\nu_{\max})$ plane (Fig. 6.7) showing that the populations of Type I an II flares occupy a different and distinct space in the aforementioned plane. Type I flares occupy the upper right corner and Type II flares the lower left corner supporting the scenario of two intrinsically different physical mechanisms are in action for Type I and I sources respectively.

Throughout the current analysis it became clear that sources that exhibit a flat k–index across all frequencies are mainly of Type II. It should be noted though that cases of Type I sources exist (e.g J0238+1636) that have a flat k–index. These cases are similarly variable across the spectrum producing a flat k–index but exhibit all the typical characteristics of Type I sources. Thus the k–index can not be used ad-hoc to discriminate between Type I and II sources. All Type II sources exhibit flat k–indices but not all flat k-index sources are of Type II. Thus k–index can only be used to point out Type II sources. It should also be mentioned that a source exhibiting a particular type of flare (Type I or II) never exhibited flares of the other type within the time span of the five years of monitoring. This indicates that the underlying physical mechanism remained unchanged over the whole 5 years period of F-GAMMA observations for all the observed sources (Type I and II).

The observed phenomenological characteristics of Type I sources can qualitatively be explained by the modulation of the combined attributes of (a) redshift and (b) intrinsic source properties (Angelakis et al. 2012a). The source redshift constrains the part of the rest frame spectrum we can sample within our observing bandpass. The different intrinsic source characteristics change the observed spectra in terms of peak frequency and flux density as well as the observed time scales of these events producing the observed flares, making each event even in the same source unique. As shown in Angelakis et al. (2012a) Type I sources can be further sub–categorized into four types of sources. The key differences between these types are due to the combined modulus of redshift and source specific characteristics. Thus the observed phenomenological multitude of observed behaviours within the Type I sources can be reduced to a single physical mechanism. Type I sources and flares seem to be in accordance with expectations from models of shocks evolving in jets (Marscher and Gear 1985; Valtaoja et al. 1992b, see bellow).

In contrast Type II sources and flares show fundamentally different characteristics allowing us to assume that the underlying physical mechanism is different. Flux density variations and the observed amplitudes are modulated in a different way. One possible explanation is the moving emission regions alongside bend radio structures. Such bend jets (e.g Agudo et al. 2012; Lobanov and Zensus 2001; Ly et al. 2007; Piner et al. 2009) are not rare. Several models of oscillating bent jets exist. Helical modes in hydrodynamic jets (Hardee 1987) or in magnetized jets (Konigl and Choudhuri 1985) predict that whenever a shock moves alongside the helical structure, each time the shock meets the twist of the

helical structure that is closest to the line of sight towards earth then Doppler boosting occurs, producing variability in the observed flux density. Conical jets can produce a quasi-periodic oscillation (Camenzind and Krockenberger 1992) that is believed to be connected to perturbations of the relativistic flow. The observed phenomenology can be explained at least qualitatively in a better way by models introducing geometrical parameters (Villata and Raiteri 1999). Further analysis is required to compare the specific physical parameters of such models to the observed behaviour of Type II sources.

Comparison with shock–induced variability for Type I sources/flares. Shock-in-jet models (e.g. Marscher and Gear 1985; Valtaoja et al. 1992b; Stevens et al. 1994; Türler et al. 2000; Fromm et al. 2011) predict a certain spectral evolutionary path for flares in the $S_{max} - \nu_{max}$ domain according to their Compton, synchrotron and adiabatic dominated energy loss phases. While the turnover frequency ν_{max} of the synchrotron self–absorbed flare spectrum evolves continuously from higher to lower frequencies, the spectral peak S_{max} first raises at high frequencies (Compton phase), reaches a plateau (synchrotron phase) at ν_r and subsequently decays towards lower frequencies (adiabatic phase) at frequencies $> \nu_f$. As shown in the generalized shock model of Valtaoja et al. (1992b), this evolution implies a certain frequency dependence of light curve parameters, such as the amplitude of the observed flares. According to the different energy loss stages, the flare amplitude is expected to first increase at high frequencies ($\nu \geqslant \nu_r$) and subsequently decrease at frequencies $\leqslant \nu_f$. As already mentioned the observed variability amplitudes (σ_{int}) increase towards higher frequencies reaching a plateau at $\sim$70 GHz and then decreasing again towards even higher frequencies. The observed evolutionary path of Type I sources in the $S_{max} - \nu_{max}$ plane, fits well into this scheme for shocks being first in the Compton–dominated growth phase then in the synchrotron plateau phase and last at the decaying adiabatic phase (Fig. 1.8). Thus the transition between Compton and synchrotron stage, i.e. maximum flare amplitudes, occur at rest frame frequencies of $\sim$70 GHz. At higher frequencies the k–index will depend on the optically thin spectral index, whereas the model of Marscher and Gear (1985) requires $\alpha_{thin} < -0.5$ for shocks to persist non–radiative, the obtained distribution of k–indices at the S. High band are in agreement with a mean value of -0.44 (Table 5.3). However the latter values represent an average behaviour over 5 years and is not obtained for single spectral (flare) components. Similarly, the k-indices, as obtained here, represent the average behaviour of different flares likely being also at different evolutionary stages.

7.2 Summary of Results

A large sample of blazars is systematically monitored at cm to short-mm bands during a period of 5 years within the F-GAMMA program, using the Effelsberg 100 m and Pico Veleta 30 m radio telescopes. Details of the Effelsberg and Pico Veleta observing systems and schemes as well as the observations and data reduction process have been presented including: (i) light curves and spectra for all sources of the revised F-GAMMA sample at 2.64, 4.85, 8.35, 10.45, 14.6, 23.05, 32, 42, 86 and 142 GHz, (ii) a variability and spectral

analysis of 59 sources of the revised sample. The analysis and results presented in the current thesis can be summarized as follows:

1. A detailed system study for the Pico Veleta 30 m telescope has been carried out including an analysis of the inherent measurement uncertainties given the typical flux density levels ($\sim$ 0.3–19 Jy) and cross–scan integration times (2–4 minutes) of the program. At average atmospheric conditions, the fractional flux density error at 86 GHz is found to drop with increasing flux density from a value of $\sim$ 20 % (at $\sim$ 0.3 Jy) to $\sim$ 5 % towards larger flux densities. At 142 GHz the corresponding values drop from $\sim$ 24 % to $\sim$ 7 % (Sect. 3.2).

2. The relative calibration accuracy between Effelsberg and Pico Veleta as deduced from the spectral properties of the secondary calibrator NGC 7027 is shown to be better than 2 % for most of the observing frequencies (Sect. 2.3).

3. New semi–automated IDL software has been written for the reduction of Pico Veleta data at 86 and 142 GHz, including a comprehensive error analysis and data correction options (Sect. 3.1.2).

4. The relative gain between the two orthogonal polarizations of the new EMIR system at 86 GHz is found to be of the order of 2 %. At 142 GHz no significant difference is found (Sect. 3.1.3).

5. The overall system repeatability and calibration/gain stability for both Effelsberg and Pico Veleta is demonstrated by the small residual mean scatter (m_0) in the calibrator light curves with values ranging between $\sim$ 0.6 % at 4.85 GHz and $\sim$ 4 % at 142 GHz (Table 3.9).

6. Based on a χ^2 test criterion the percentage of variable sources is found to be high for all frequencies with a minimum of about 90 % at 86 GHz and a maximum of 100% at lower frequencies (Sect. 5.2).

7. Using a structure function analysis, the flare time scales in the light curves were estimated with values ranging from $\sim$ 60–80 to a maximum of $\sim$ 1400 days. Also 85 % of the sources at 86 GHz and 81 % at 142 GHz exhibit observed time scales shorter than 450 days (Sect. 5.4).

8. Mean variability brightness temperatures are calculated from the corresponding flare time scales and amplitudes with values decreasing from $6.9 \cdot 10^{12}$ K at 2.64 GHz to $7.5 \cdot 10^{10}$ K at 142 GHz, showing a continuous decrease as frequency increases. All calculated values are found to be above theoretical limits thus relativistic Doppler boosting is needed to explain the excess. Doppler factors are estimated revealing mean values ranging from 9.6 and 1.7 at 2.64 and 142 GHz respectively. The calculated values follow an increasing trend towards lower frequencies likely due to to jet acceleration, whereas other intrinsically and model depended effects can not be ruled out and need further study (Sect. 5.5).

9. A likelihood analysis to compute intrinsic light curve standard deviations, reveals that most of the observed sources show extreme and increasing variability towards higher frequencies reaching a plateau at a rest–frame frequency of ~ 70 GHz (Fig. 5.3) and a subsequent decreasing trend. k–index is calculated at four different frequency bands showing a decreasing slope from lower to higher frequencies (Table 5.3). A difference between flares observed for FSRQ and BL Lac sources is found, with flares of FSRQs reaching lower frequencies. FSRQs also show mean variability amplitudes higher than those of BL Lacs, in all observed frequencies. These results are consistent with model predictions for shocks in jets. The existence of sources with flat k-index across the observed frequencies is confirmed, indicating an intrinsically different physical mechanism producing the observed flares (Sect. 5.3).

10. Quasi–simultaneous spectra combined from multi–frequency data of Effelsberg and Pico Veleta show two distinct type of source variability, i.e. Type I and Type II sources. The former sources usually show a quiescent spectrum superimposed by an SSA spectrum that evolves from higher to lower frequencies. In contrast the latter shows variability characterized by a self–similar changing spectrum. Of the 59 sources in the revised sample , 37 sources are found to be Type I, 16 are Type II and 6 are undefined. These two fundamentally different phenomenological behaviours indicate an intrinsically different underlying physical mechanism (Sect. 6.1).

11. Spectral indices ($S \sim \nu^{\alpha}$) at two different bands ($\alpha_{\rm low}$ and $\alpha_{\rm high}$) are calculated, with mean values of 0.02 and -0.2 respectively (Fig. 6.2), showing that at higher frequencies observed spectra are slightly steeper. Mean values for FSRQs and BL Lac objects (Table 6.1) of $\alpha_{\rm low}$ and $\alpha_{\rm high}$ show that at lower frequencies BL Lac objects tend to have steeper spectra in contrast to FSRQs that have steeper spectra at higher frequencies. These results are in accordance with findings of the k–index and the observed spectral phenomenology, indicating flares evolving from higher to lower frequencies in many cases. finally FSRQ flares are found to reach lower frequencies compared to BL Lac flares (Sect. 6.2).

12. An $S_{\rm max}$– $\nu_{\rm max}$ analysis of 24 individual flares was performed to quantify and characterize the phenomenological behaviour of Type I and Type II sources. Corresponding Type I and II flares are found to exist. A clear evolutionary path is seen in the $S_{\rm max}$– $\nu_{\rm max}$ plane for Type I flares in contrast to Type II flares showing an "up/down" behaviour, as expected from the self-similar spectral changes observed for Type II sources. Calculated values of $\Delta\,(S_{\rm max})$ and $\Delta\,(\nu_{\rm max})$ characterizing the flares, showed that Type I and II flares occupy a different and distinct space in the $\Delta\,(S_{\rm max}) - \Delta\,(\nu_{\rm max})$ plane (Fig. 6.7) indicating different underlying physical mechanisms. Type I sources seem to be in agreement with evolving shocks in jets according to well established models, in contrast to Type II sources where geometrical models could likely explain the observed phenomenology (Sect. 6.3).

7.3 Future work

Here a short summary is presented with possible future studies that can be performed based on the work presented in the current thesis.

- Include all the available datasets of the F-GAMMA program spanning ∼8 years. This will allow the isolation of more individual flares increasing the statistical significance of all the conclusions made so far.
- Polarization information is recorded for most of the receivers mounted in the Effelsberg 100 m telescope. Reducing and analysing these information will give a new perspective on the intrinsic differences between Type I and II sources.
- Investigate if there are any other differences between Type I and II sources in brightness temperatures, Doppler factors and spectral indices in the same manner as it is done with FSRQ and BL Lac sources.
- Perform analytical simulations of geometrical models and constrain their parameter space by comparing them with the observed behaviour of Type II sources. This will allow us to clarify and conclude if and how these models describe Type II sources giving an better insight of the physical processes in action.
- Define the quiescent spectrum slope (α) for each source independently, allowing a better subtraction (see Sect. 4.5) of it and thus a better estimation of the spectral peak. The determination of the quiescent spectrum can be done by gathering data from frequencies lower than < 2 GHz, were it should be dominant and unaffected by the flaring activity in higher frequencies.
- Use an SSA model to fit the observed flares instead of a broken power law. A far better determination of the spectral peak in both frequency and flux density domains (S_{max} and ν_{max}) is possible in this way, allowing to track the evolution of the spectral peaks in more detail in the $S_{max} - \nu_{max}$ plane.
- There are several predictions from shock in jet models about behaviour of the flaring activity in Type I sources. A first theoretical study was made by Fromm et al. (2014) using synthetic light curves to reconstruct qualitatively the observed behaviour of flares in blazars. By comparing the findings of the current thesis of broadband light curves and spectra with simulations of these analytical models a constrain of their parameter space is possible allowing to constrain the physical properties of flares seen in Type I sources. In more detail exact comparisons for each source can be made about the dependence of σ_{int} to frequency as well as the observed slopes of each evolutionary phase in the $S_{max} - \nu_{max}$ plane .

A

Appendices

A.1 Data Tables

Table A.1: Basic information of the original F-GAMMA source sample. Columns are: (1) J2000.0 source name, (2) common source name, (3) & (4) J2000.0 observing coordinates, (5) Number of epochs the source is observed, (6) Effective Sampling of the available data see also Sect. 2.4.2, (7) Literature redshift, (8) Classification of the source : FSRQ(Flat Spectrum Radio Quasar), BL Lac, Blazars, RG(Radio Galaxy), NLSY(Narrow Line Seyfert), (9) *Fermi*-GST detection taken from the 11 month published catalog (Abdo et al. 2010b).

Name	Other name	RA (J2000)	DEC (J2000)	# Epochs	Sampl. [month/spectra]	Redshift	Class	*Fermi*-GST
J0006-0623	–	00h 06m 13.893s	−06d 23m 35.334s	13	1.80	0.347	FSRQ	N
J0102+5824	–	01h 02m 45.762s	+58d 24m 11.136s	38	1.48	0.644	Blazar	Y
J0217+0144	PKS0215+015	02h 17m 48.955s	+01d 44m 49.699s	32	1.76	1.715	FSRQ	Y
J0222+4302	3C66A	02h 22m 39.611s	+43d 02m 07.799s	38	1.48	0.444	BL Lac	Y
J0237+2848	4C28.07	02h 37m 52.406s	+28d 48m 08.990s	44	1.39	1.213	FSRQ	Y
J0238+1636	AO0235+16	02h 38m 38.930s	+16d 36m 59.275s	44	1.39	0.940	BL Lac	Y
J0241-0815	NGC1052	02h 41m 04.799s	−08d 15m 20.751s	33	1.71	0.005	Seyfert	N
J0319+1845	E0317.0+1835	03h 19m 51.800s	+18d 45m 34.200s	13	2.00	0.190	BL Lac	Y
J0319+4130	3C84	03h 19m 48.160s	+41d 30m 42.106s	51	1.20	0.018	RG	Y
J0336+3218	OE355	03h 36m 30.108s	+32d 18m 29.342s	29	1.95	1.258	FSRQ	Y
J0339-0146	PKS0336-01	03h 39m 30.938s	−01d 46m 35.803s	29	1.95	0.852	FSRQ	Y
J0359+5057	NRAO150	03h 59m 29.746s	+50d 57m 50.230s	44	1.39	1.520	Blazar	N
J0418+3801	3C111	04h 18m 21.277s	+38d 01m 35.800s	44	1.39	0.049	RG	Y
J0423-0120	PKS0420-01	04h 23m 15.801s	−01d 20m 33.064s	40	1.53	0.914	FSRQ	Y
J0433+0521	3C120	04h 33m 11.096s	+05d 21m 15.620s	32	1.92	0.033	Blazar	N
J0507+6737	1ES0502+675	05h 07m 56.250s	+67d 37m 24.400s	10	2.19	0.416	BL Lac	Y
J0530+1331	PKS0528+134	05h 30m 56.417s	+13d 31m 55.150s	44	1.39	2.070	FSRQ	Y
J0721+7120	S50716+71	07h 21m 53.448s	+71d 20m 36.363s	56	1.09	0.328	BL Lac	Y
J0738+1742	PKS0735+17	07h 38m 07.394s	+17d 42m 18.998s	34	1.65	0.424	BL Lac	Y
J0750+1231	–	07h 50m 52.046s	+12d 31m 04.829s	16	1.69	0.889	FSRQ	Y
J0818+4222	TXS0814+425	08h 18m 16.000s	+42d 22m 45.415s	37	1.56	0.530	BL Lac	Y
J0830+2410	OJ248	08h 30m 52.086s	+24d 10m 59.821s	19	2.08	0.941	FSRQ	Y
J0841+7053	S50836+71	08h 41m 24.365s	+70d 53m 42.173s	42	1.37	2.172	FSRQ	Y
J0854+2006	OJ287	08h 54m 48.875s	+20d 06m 30.641s	40	1.44	0.306	BL Lac	Y
J0958+6533	S40954+65	09h 58m 47.245s	+65d 33m 54.818s	39	1.48	0.368	BL Lac	Y
J1041+0610	PKS1038+064	10h 41m 17.163s	+06d 10m 16.924s	14	2.93	1.270	FSRQ	N

Table A.1: continued.

Name	Other name	RA (J2000)	DEC (J2000)	# Epochs	Sampl. [month/spectra]	Redshift	Class	*Fermi*-GST
J1104+3812	Mkn421	11h 04m 27.314s	+38d 12m 31.799s	43	1.39	0.030	BL Lac	Y
J1130-1449	PKS1127-14	11h 30m 07.053s	−14d 49m 27.387s	35	1.61	1.184	FSRQ	Y
J1136+7009	Mkn180	11h 36m 26.408s	+70d 09m 27.306s	11	2.36	0.045	BL Lac	Y
J1159+2914	TON599	11h 59m 31.834s	+29d 14m 43.827s	41	1.46	0.729	FSRQ	Y
J1221+2813	Wcom	12h 21m 31.691s	+28d 13m 58.500s	32	1.63	0.102	BL Lac	Y
J1224+2122	4C21.35	12h 24m 54.458s	+21d 22m 46.388s	14	2.93	0.435	FSRQ	Y
J1229+0203	3C273	12h 29m 06.700s	+02d 03m 08.598s	50	1.15	0.158	FSRQ	Y
J1230+1223	M87	12h 30m 49.423s	+12d 23m 28.043s	18	1.60	0.004	RG	Y
J1256-0547	3C279	12h 56m 11.167s	−05d 47m 21.523s	51	1.17	0.536	FSRQ	Y
J1310+3220	OP313	13h 10m 28.664s	+32d 20m 43.783s	40	1.49	0.997	FSRQ	Y
J1408-0752	PKS1406-076	14h 08m 56.481s	−07d 52m 26.665s	13	2.98	1.494	FSRQ	Y
J1428+4240	H1426+428	14h 28m 32.660s	+42d 40m 20.600s	07	3.68	0.129	BL Lac	Y
J1504+1029	PKS1502+016	15h 04m 25.000s	+10d 29m 39.000s	33	1.73	1.839	FSRQ	Y
J1512-0905	PKS1510-08	15h 12m 50.533s	−09d 05m 59.828s	40	1.44	0.360	FSRQ	Y
J1522+3144	–	15h 22m 09.992s	+31d 44m 14.382s	18	1.68	1.487	FSRQ	Y
J1540+8155	1ES1544+820	15h 40m 16.010s	+81d 55m 05.500s	10	4.92	0.690	BL Lac	N
J1613+3412	OS319	16h 13m 41.064s	+34d 12m 47.908s	30	1.91	1.397	FSRQ	Y
J1635+3808	4C38.41	16h 35m 15.493s	+38d 08m 04.500s	45	1.31	1.814	FSRQ	Y
J1642+3948	3C345	16h 42m 58.810s	+39d 48m 36.993s	44	1.34	0.593	Blazar	Y
J1653+3945	Mkn501	16h 53m 52.217s	+39d 45m 36.609s	47	1.26	0.033	BL Lac	Y
J1733-1304	PKS1730-13	17h 33m 02.706s	−13d 04m 49.547s	31	1.90	0.902	FSRQ	Y
J1800+7828	S51803+78	18h 00m 45.684s	+78d 28m 04.018s	44	1.36	0.680	BL Lac	Y
J1806+6949	3C371	18h 06m 50.681s	+69d 49m 28.108s	35	1.70	0.051	BL Lac	Y
J1824+5651	4C56.27	18h 24m 07.068s	+56d 51m 01.490s	35	1.63	0.664	BL Lac	Y
J1959+4044	CygA	19h 59m 28.357s	+40d 44m 02.096s	11	1.50	0.056	RG?	N
J1959+6508	1ES1959+650	19h 59m 59.852s	+65d 08m 54.652s	14	2.13	0.047	BL Lac	Y
J2158-1501	PKS2155-152	21h 58m 06.282s	−15d 01m 09.327s	11	2.00	0.672	FSRQ	Y
J2158-3013	PKS2155-304	21h 58m 52.000s	−30d 13m 32.000s	23	2.27	0.116	BL Lac	Y
J2202+4216	BL Lac	22h 02m 43.291s	+42d 16m 39.979s	59	1.04	0.069	BL Lac	Y

Table A.1: continued.

Name	Other name	RA (J2000)	DEC (J2000)	# Epochs	Sampl. [month/spectra]	Redshift	Class	*Fermi*-GST
J2203+3145	4C31.63	22h 03m 14.976s	+31d 45m 38.269s	35	1.69	0.295	FSRQ	N
J2225-0457	3C446	22h 25m 47.259s	−04d 57m 01.390s	28	2.12	1.404	FSRQ	Y
J2232+1143	OY150	22h 32m 36.409s	+11d 43m 50.904s	42	1.46	1.037	FSRQ	Y
J2253+1608	3C454.3	22h 53m 57.748s	+16d 08m 53.560s	62	0.99	0.859	FSRQ	Y
J2347+5142	1ES2344+514	23h 47m 04.838s	+51d 42m 17.877s	11	3.63	0.044	BL Lac	Y
J2348-1631	PKS2345-16	23h 48m 02.609s	−16d 31m 12.022s	13	1.93	0.600	FSRQ	Y

Table A.2: Basic information of the revised F-GAMMA source sample. Columns are: (1) J2000.0 source name, (2) common source name, (3) & (4) J2000.0 observing coordinates, (5) Number of epochs the source is observed, (6) Effective Sampling of the available data see also Sect. 2.4.2, (7) Literature redshift, (8) Classification of the source : FSRQ(Flat Spectrum Radio Quasar), BL Lac, Blazars, RG(Radio Galaxy), NLSY(Narrow Line Seyfert), (9) *Fermi*-GST detection taken from the 2FGL published catalog (Ackermann et al. 2011; Abdo et al. 2010b), (10) Phenomenological Type (see also Sect. 6.3)

Name	Other name	RA (J2000)	DEC (J2000)	# Epochs	Sampl. [month/spectra]	Redshift	Class	*Fermi*-GST	Type
J0050-0929	PKS0048-09	00h 50m 41.317s	−09d 29m 05.209s	25	2.21	0.634	BL Lac	Y	II
J0102+5824	–	01h 02m 45.762s	+58d 24m 11.136s	38	1.48	0.644	Blazar	Y	I
J0136+4751	–	01h 36m 58.610s	+47d 51m 29.100s	26	2.13	0.859	FSRQ	Y	–
J0217+0144	PKS0215+015	02h 17m 48.955s	+01d 44m 49.699s	32	1.76	1.715	FSRQ	Y	II
J0221+3556	–	02h 21m 05.500s	+35d 56m 13.900s	14	1.72	0.944	Blazar	Y	II
J0222+4302	3C66A	02h 22m 39.611s	+43d 02m 07.799s	38	1.48	0.444	BL Lac	Y	II
J0237+2848	4C28.07	02h 37m 52.406s	+28d 48m 08.990s	44	1.39	1.213	FSRQ	Y	II
J0238+1636	AO0235+16	02h 38m 38.930s	+16d 36m 59.275s	44	1.39	0.940	BL Lac	Y	I
J0241-0815	NGC1052	02h 41m 04.799s	−08d 15m 20.751s	33	1.71	0.005	Seyfert	Y	II
J0319+4130	3C84	03h 19m 48.160s	+41d 30m 42.106s	51	1.20	0.018	RG	Y	I
J0324+3410	–	03h 24m 41.200s	+34d 10m 45.100s	05	0.84	0.061	NLSY1	Y	–
J0359+5057	NRAO150	03h 59m 29.746s	+50d 57m 50.230s	44	1.39	1.520	Blazar	Y	II
J0418+3801	3C111	04h 18m 21.277s	+38d 01m 35.800s	44	1.39	0.049	RG	Y	I
J0423-0120	PKS0420-01	04h 23m 15.801s	−01d 20m 33.064s	40	1.53	0.914	FSRQ	Y	I
J0530+1331	PKS0528+134	05h 30m 56.417s	+13d 31m 55.150s	44	1.39	2.070	FSRQ	Y	I
J0654+4514	–	06h 54m 23.600s	+45d 14m 22.900s	22	1.38	0.933	Blazar	Y	I
J0719+3307	–	07h 19m 19.400s	+33d 07m 09.700s	19	1.27	0.779	Blazar	Y	–
J0721+7120	S50716+71	07h 21m 53.448s	+71d 20m 36.363s	56	1.09	0.328	BL Lac	Y	I
J0730-1141	–	07h 30m 19.000s	−11d 41m 13.000s	27	1.98	1.589	FSRQ	Y	II
J0738+1742	PKS0735+17	07h 38m 07.394s	+17d 42m 18.998s	34	1.65	0.424	BL Lac	Y	I
J0808-0751	–	08h 08m 15.536s	−07d 51m 09.885s	27	2.11	1.837	FSRQ	Y	I
J0818+4222	TXS0814+425	08h 18m 16.000s	+42d 22m 45.415s	37	1.56	0.530	BL Lac	Y	II
J0824+5552	–	08h 24m 47.200s	+55d 52m 42.700s	24	2.40	1.417	FSRQ	Y	–
J0841+7053	S50836+71	08h 41m 24.365s	+70d 53m 42.173s	42	1.37	2.172	FSRQ	Y	I
J0854+2006	OJ287	08h 54m 48.875s	+20d 06m 30.641s	40	1.44	0.306	BL Lac	Y	I
J0920+4441	–	09h 20m 58.458s	+44d 41m 53.985s	19	1.59	2.190	FSRQ	Y	II

Table A.2: continued.

Name	Other name	RA (J2000)	DEC (J2000)	# Epochs	Sampl. [month/spectra]	Redshift	Class	*Fermi*-GST	Type
J0948+0022	–	09h 48m 57.320s	+00d 22m 25.558s	22	1.68	0.585	NLSY1	Y	I
J0958+6533	S40954+65	09h 58m 47.245s	+65d 33m 54.818s	39	1.48	0.368	BL Lac	Y	I
J1104+3812	Mkn421	11h 04m 27.314s	+38d 12m 31.799s	43	1.39	0.030	BL Lac	Y	I
J1130-1449	PKS1127-14	11h 30m 07.053s	−14d 49m 27.387s	35	1.61	1.184	FSRQ	Y	I
J1159+2914	TON599	11h 59m 31.834s	+29d 14m 43.827s	41	1.46	0.729	FSRQ	Y	I
J1217+3007	ON325	12h 17m 52.082s	+30d 07m 00.636s	21	1.44	0.130	BL Lac	Y	–
J1221+2813	Wcom	12h 21m 31.691s	+28d 13m 58.500s	32	1.63	0.102	BL Lac	Y	I
J1229+0203	3C273	12h 29m 06.700s	+02d 03m 08.598s	50	1.15	0.158	FSRQ	Y	I
J1256-0547	3C279	12h 56m 11.167s	−05d 47m 21.523s	51	1.17	0.536	FSRQ	Y	I
J1310+3220	OP313	13h 10m 28.664s	+32d 20m 43.783s	40	1.49	0.997	FSRQ	Y	I
J1332-0509	–	13h 32m 04.300s	−05d 09m 42.900s	21	1.44	2.150	FSRQ	Y	I
J1504+1029	PKS1502+016	15h 04m 25.000s	+10d 29m 39.000s	33	1.73	1.839	FSRQ	Y	II
J1512-0905	PKS1510-08	15h 12m 50.533s	−09d 05m 59.828s	40	1.44	0.360	FSRQ	Y	I
J1522+3144	–	15h 22m 09.992s	+31d 44m 14.382s	18	1.68	1.487	FSRQ	Y	II
J1553+1256	–	15h 53m 32.690s	+12d 56m 51.700s	17	1.51	1.308	FSRQ	Y	–
J1635+3808	4C38.41	16h 35m 15.493s	+38d 08m 04.500s	45	1.31	1.814	FSRQ	Y	I
J1642+3948	3C345	16h 42m 58.810s	+39d 48m 36.993s	44	1.34	0.593	Blazar	Y	I
J1653+3945	Mkn501	16h 53m 52.217s	+39d 45m 36.609s	47	1.26	0.033	BL Lac	Y	II
J1733-1304	PKS1730-13	17h 33m 02.706s	−13d 04m 49.547s	31	1.90	0.902	FSRQ	Y	I
J1751+0939	–	17h 51m 32.819s	+09d 39m 00.728s	39	1.51	0.322	Blazar	Y	I
J1800+7828	S51803+78	18h 00m 45.684s	+78d 28m 04.018s	44	1.36	0.680	BL Lac	Y	II
J1848+3219	–	18h 48m 22.000s	+32d 19m 01.900s	18	1.68	0.798	FSRQ	Y	I
J1849+6705	S41849+67	18h 49m 16.072s	+67d 05m 41.679s	23	1.32	0.657	FSRQ	Y	I
J2025-0735	–	20h 25m 40.600s	−07d 35m 52.000s	18	1.69	1.388	FSRQ	Y	I
J2143+1743	–	21h 43m 35.500s	+17d 43m 48.000s	18	1.69	0.213	FSRQ	Y	I
J2147+0929	–	21h 47m 10.000s	+09d 29m 45.900s	18	1.69	1.113	FSRQ	Y	I
J2158-3013	PKS2155-304	21h 58m 52.000s	−30d 13m 32.000s	23	2.27	0.116	BL Lac	Y	II
J2202+4216	BL Lac	22h 02m 43.291s	+42d 16m 39.979s	59	1.04	0.069	BL Lac	Y	I
J2203+1725	–	22h 03m 27.000s	+17d 25m 48.200s	14	1.72	1.076	FSRQ	Y	II

Table A.2: continued.

Name	Other name	RA (J2000)	DEC (J2000)	# Epochs	Sampl. [month/spectra]	Redshift	Class	*Fermi*-GST	Type
J2229-0832	–	22h 29m 40.084s	−08d 32m 54.434s	14	1.72	1.560	FSRQ	Y	I
J2232+1143	OY150	22h 32m 36.409s	+11d 43m 50.904s	42	1.46	1.037	FSRQ	Y	I
J2253+1608	3C454.3	22h 53m 57.748s	+16d 08m 53.560s	62	0.99	0.859	FSRQ	Y	I
J2327+0940	–	23h 27m 33.400s	+09d 40m 09.000s	16	1.90	1.843	FSRQ	Y	I

Table A.3: Average α_{low} and α_{high} spectral indices over the five year observing period for the sources of the revised sample. See also Sect. 4.4 and 6.2

Source Name	α_{low}	α_{high}	Source name	α_{low}	α_{high}	Source name	α_{low}	α_{high}
J0050-0929	−0.03	−0.09	J0808-0751	+0.12	−0.36	J1553+1256	−0.09	−0.37
J0102+5824	+0.26	−0.16	J0818+4222	−0.01	−0.25	J1635+3808	−0.00	−0.12
J0136+4751	+0.19	−0.30	J0824+5552	−0.31	−0.49	J1642+3948	−0.06	−0.30
J0217+0144	+0.15	−0.10	J0841+7053	−0.08	−0.39	J1653+3945	−0.20	−0.23
J0221+3556	−0.19	−0.41	J0854+2006	+0.42	−0.08	J1733-1304	−0.05	−0.22
J0222+4302	−0.32	−0.15	J0920+4441	+0.48	−0.33	J1751+0939	+0.23	−0.34
J0237+2848	−0.03	−0.30	J0948+0022	+0.49	+0.06	J1800+7828	+0.11	−0.22
J0238+1636	+0.02	−0.11	J0958+6533	+0.10	−0.11	J1848+3219	−0.00	−0.10
J0241-0815	+0.17	−0.13	J1104+3812	−0.28	−0.13	J1849+6705	+0.50	−0.17
J0319+4130	+0.35	−0.50	J1130-1449	−0.32	−0.35	J2025-0735	+0.00	−0.12
J0324+3410	−0.12	−0.16	J1159+2914	−0.03	−0.18	J2143+1743	−0.06	−0.40
J0359+5057	+0.55	−0.50	J1217+3007	−0.16	−0.22	J2147+0929	−0.05	−0.31
J0418+3801	−0.38	−0.31	J1221+2813	−0.14	−0.09	J2158-3013	−0.14	−0.19
J0423-0120	+0.30	−0.30	J1229+0203	−0.30	−0.43	J2202+4216	+0.11	−0.05
J0530+1331	−0.24	−0.25	J1256-0547	+0.33	−0.21	J2203+1725	+0.14	−0.34
J0654+4514	+0.09	−0.15	J1310+3220	+0.31	−0.06	J2229-0832	+0.09	−0.31
J0719+3307	+0.06	−0.20	J1332-0509	+0.64	−0.08	J2232+1143	−0.21	−0.37
J0721+7120	+0.31	+0.04	J1504+1029	+0.17	−0.21	J2253+1608	+0.03	−0.02
J0730-1141	+0.18	−0.50	J1512-0905	+0.18	−0.13	J2327+0940	+0.10	−0.28
J0738+1742	−0.20	−0.14	J1522+3144	−0.14	−0.30			

A.2 Spectra

A.2.1 Spectral plots

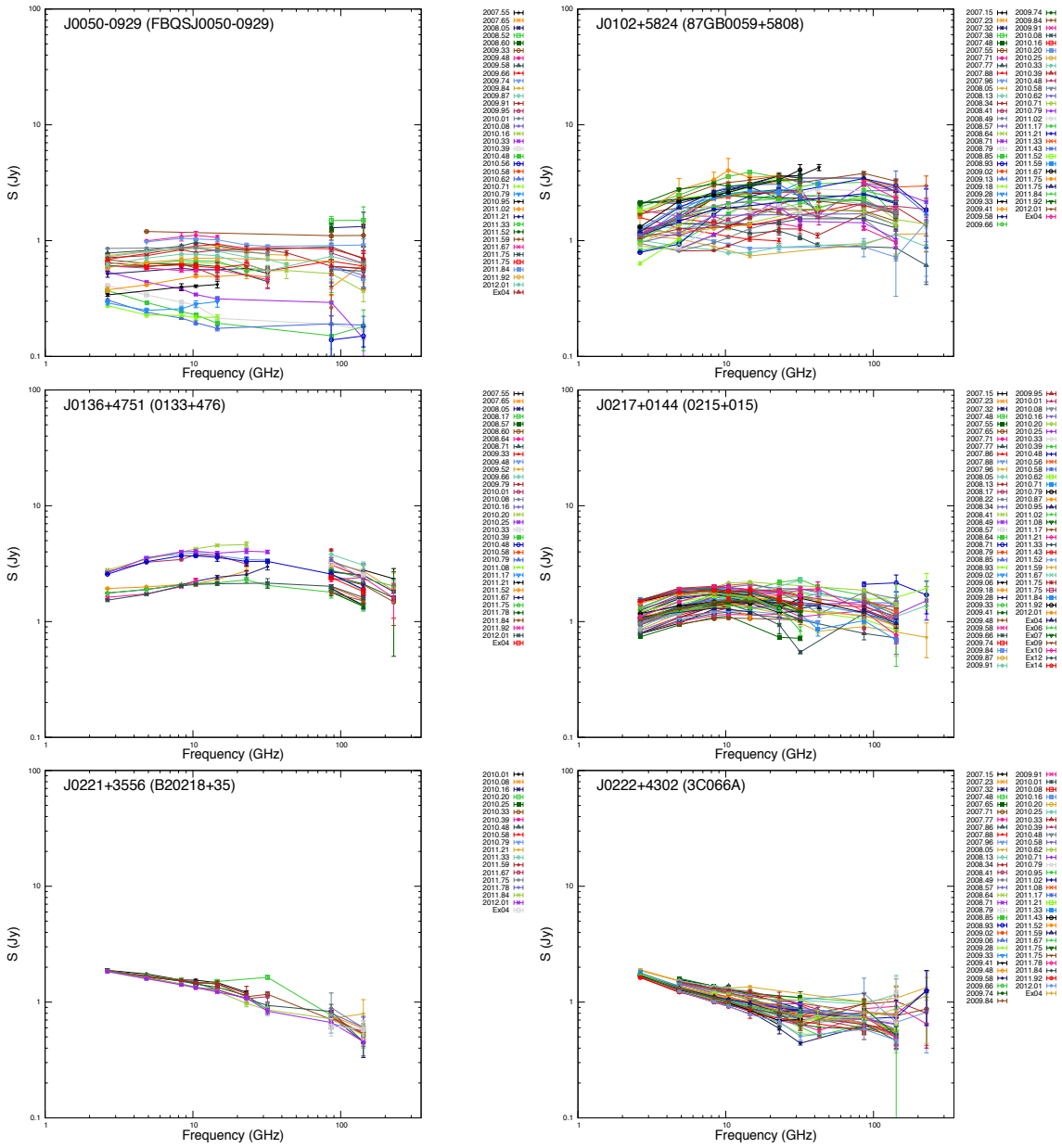

Figure A.1: From top to bottom are shown: J0050-0929, J0102+5824, J0136+4751, J0217+0144, J0221+3556, J0222+4302. Each curve is a spectra of a specific observing epoch combining quasi–simultaneous multi–frequency data obtained at Effelsberg and Pico Veleta.

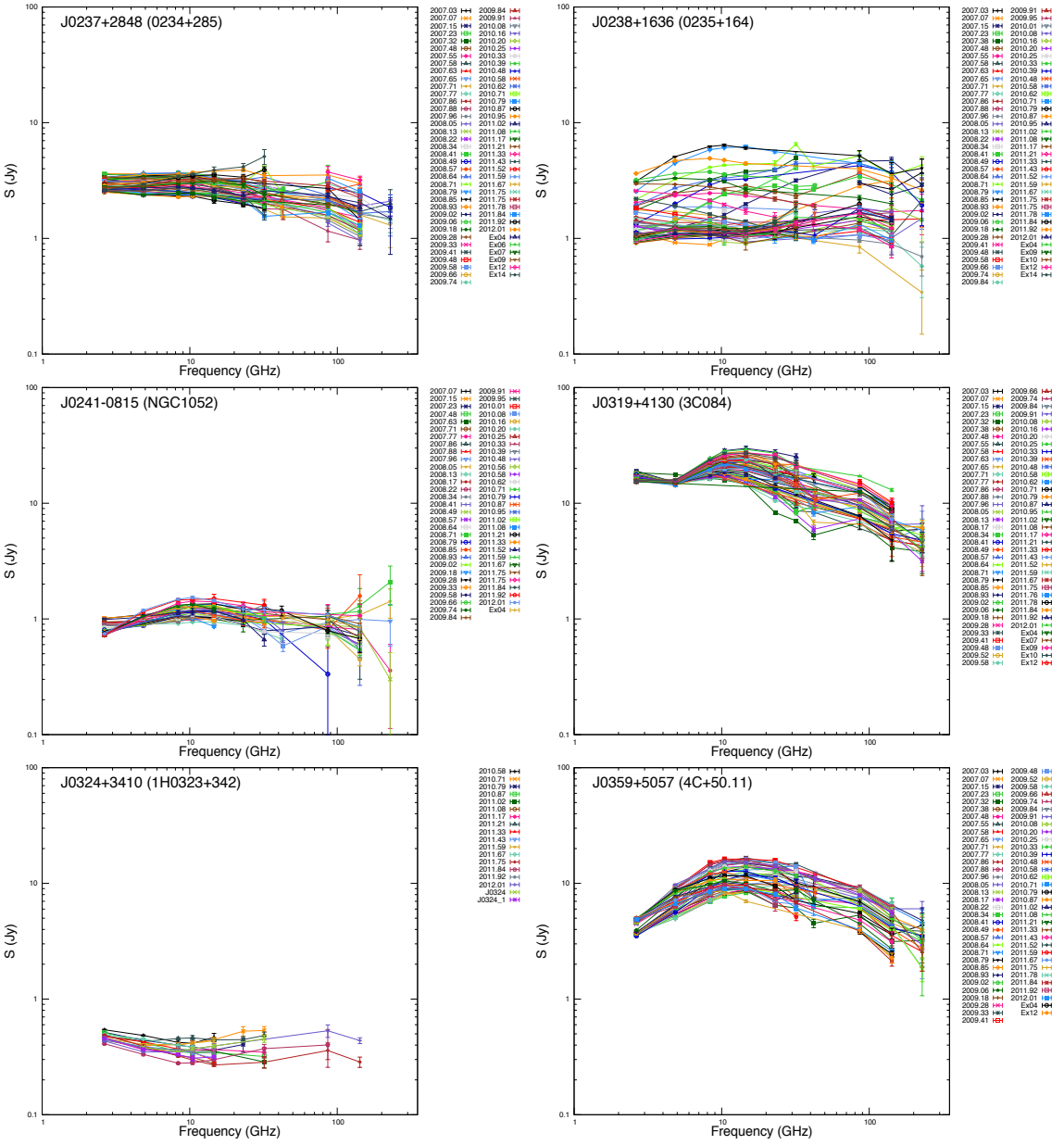

Figure A.2: From top to bottom are shown: J0237+2848, J0238+1636, J0241-0815, J0319+4130, J0324+3410, J0359+5057. Each curve is a spectra of a specific observing epoch combining quasi–simultaneous multi–frequency data obtained at Effelsberg and Pico Veleta.

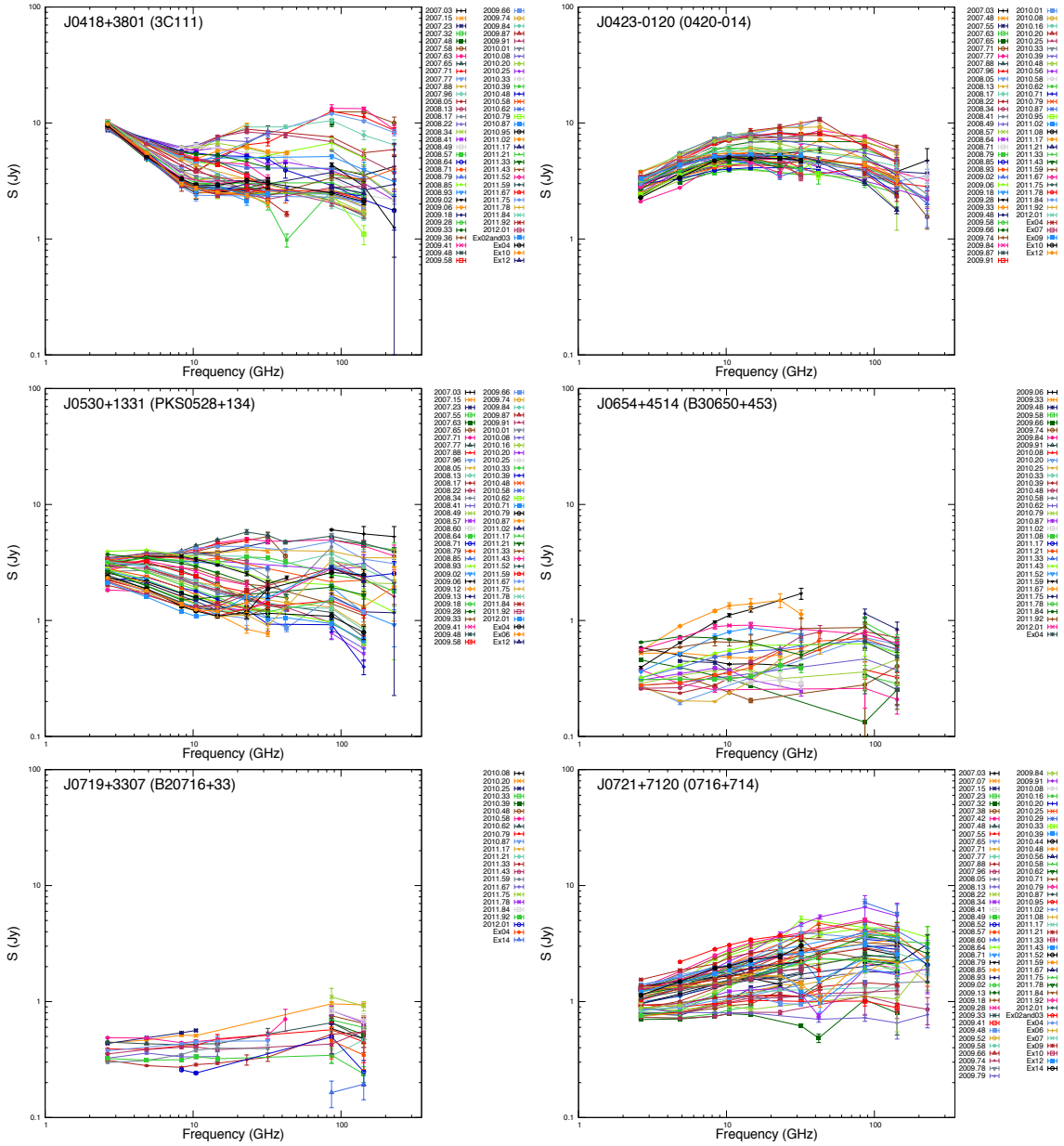

Figure A.3: From top to bottom are shown: J0418+3801, J0423-0120, J0530+1331, J0654+4514, J0719+3307, J0721+7120. Each curve is a spectra of a specific observing epoch combining quasi–simultaneous multi–frequency data obtained at Effelsberg and Pico Veleta.

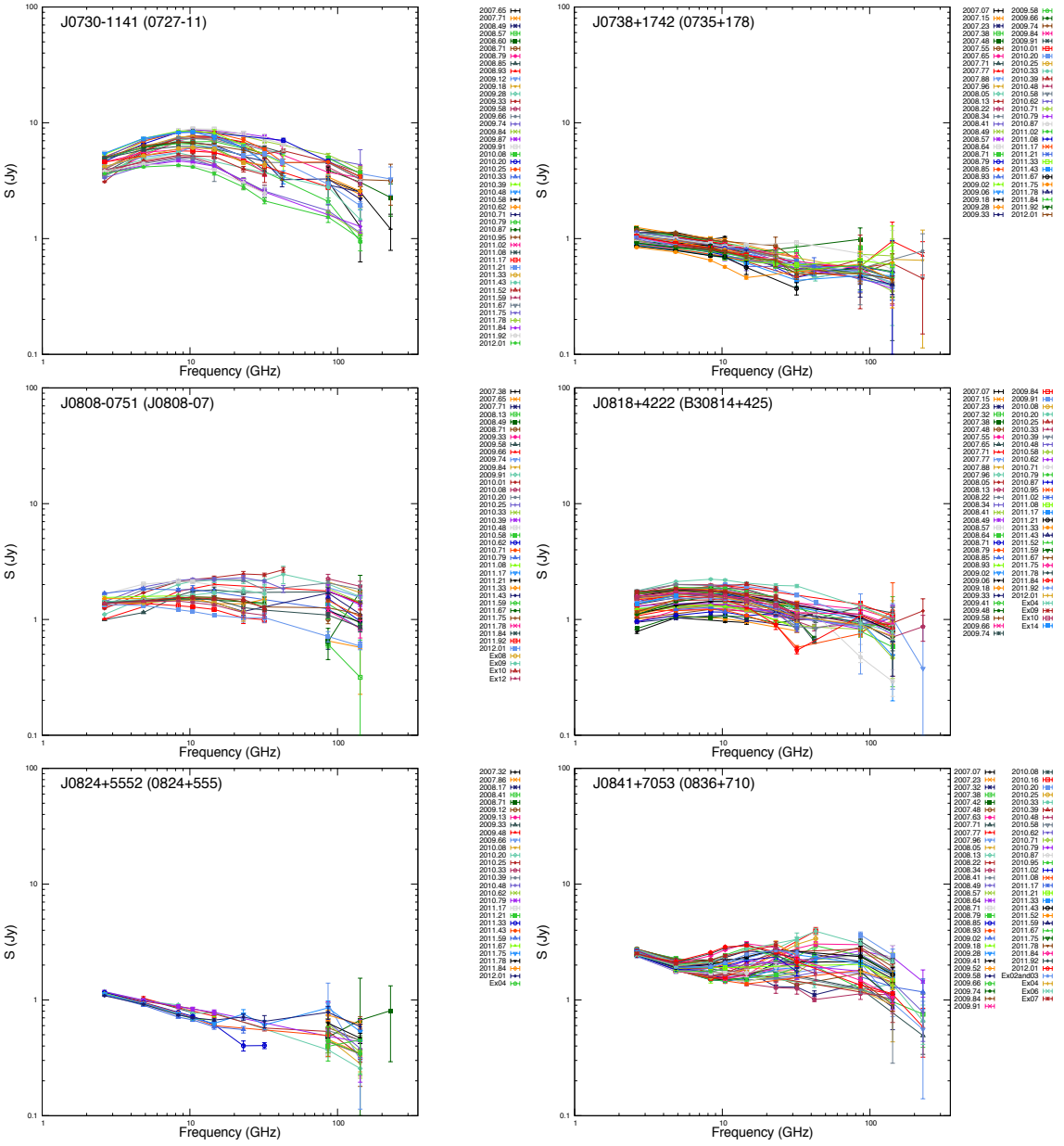

Figure A.4: From top to bottom are shown: J0730-1141, J0738+1742, J0808-0751, J0818+4222, J0824+5552, J0841+7053. Each curve is a spectra of a specific observing epoch combining quasi–simultaneous multi–frequency data obtained at Effelsberg and Pico Veleta.

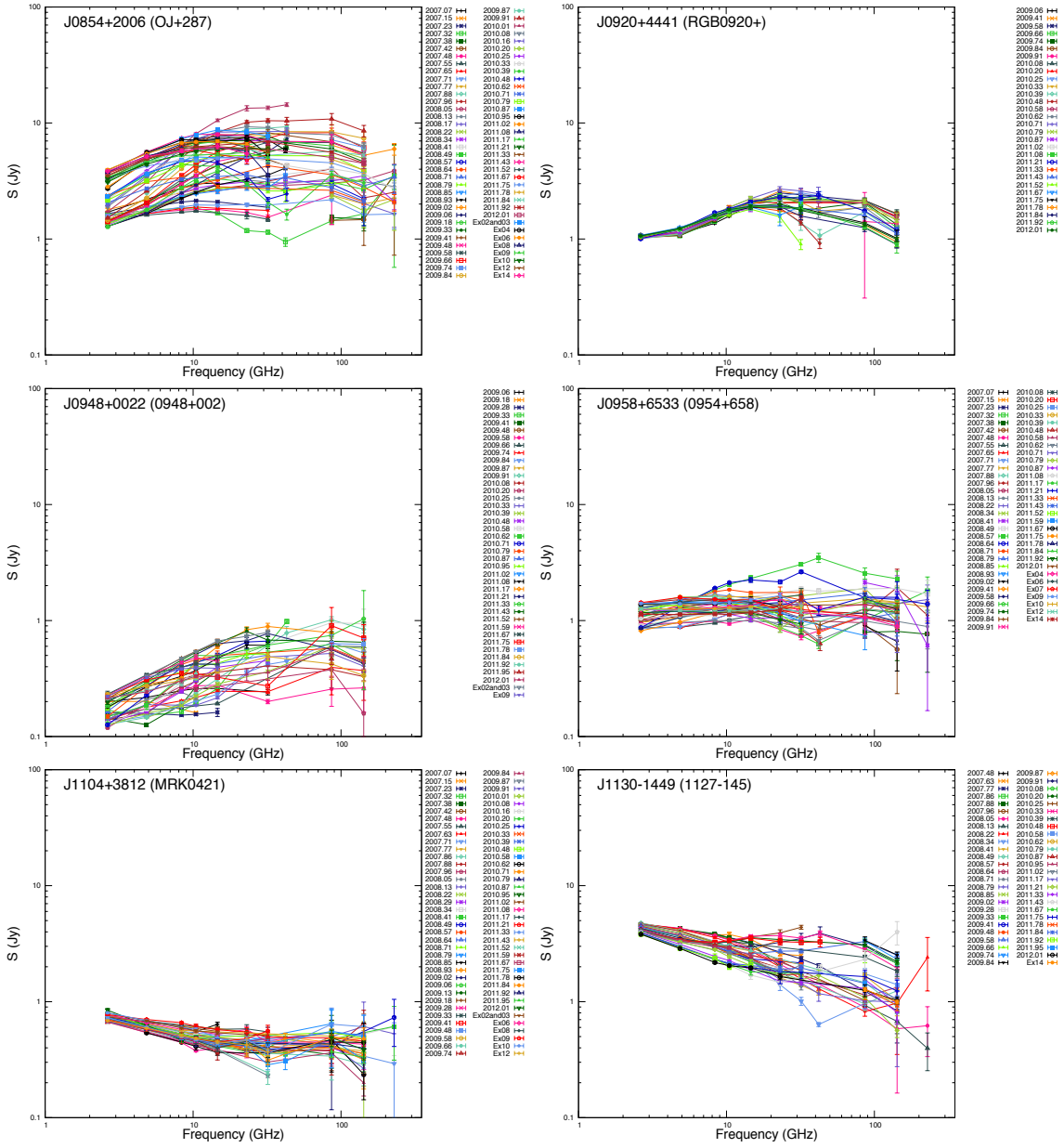

Figure A.5: From top to bottom are shown: J0854+2006, J0920+4441, J0948+0022, J0958+6533, J1104+3812, J1130-1449. Each curve is a spectra of a specific observing epoch combining quasi–simultaneous multi–frequency data obtained at Effelsberg and Pico Veleta.

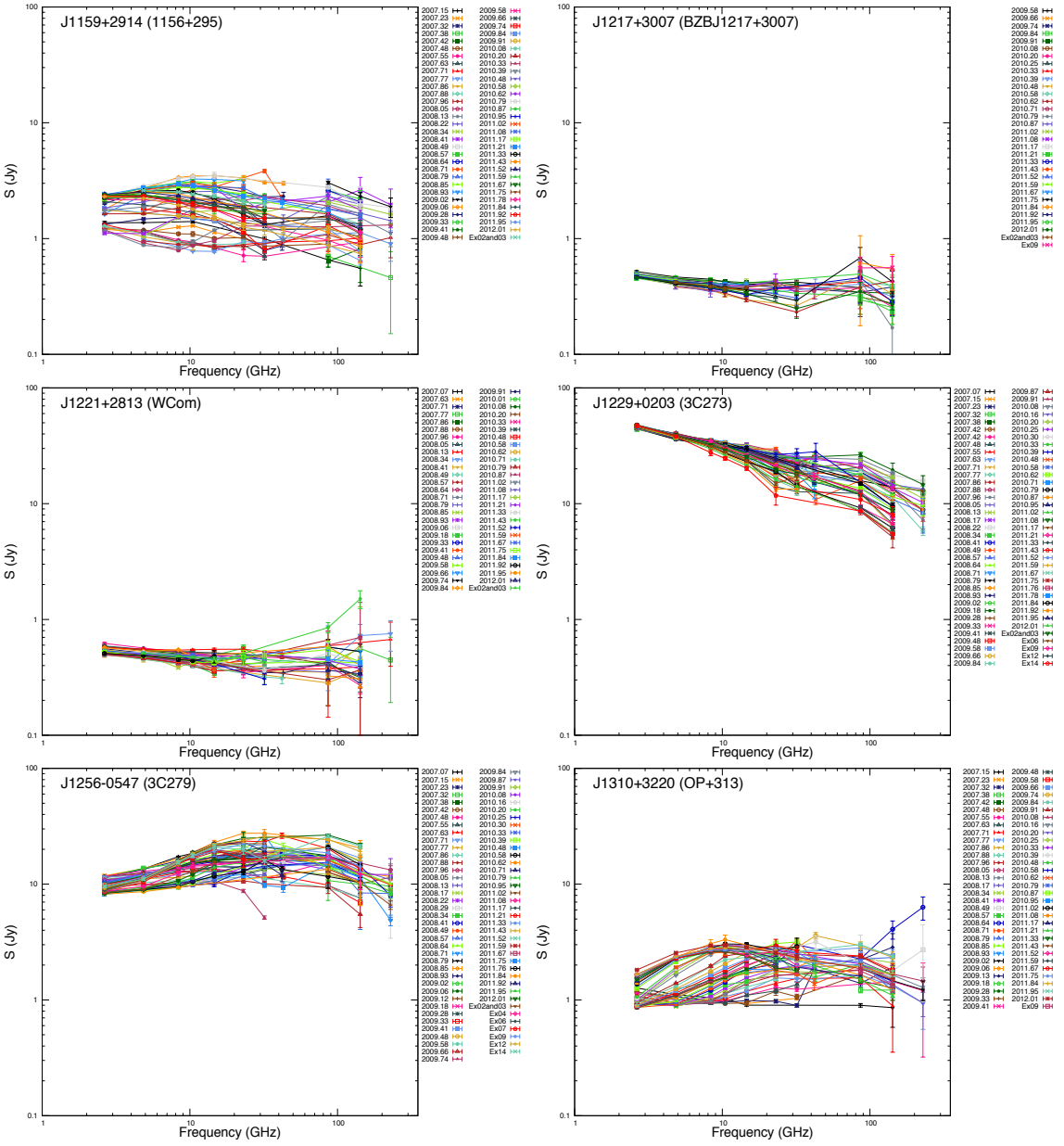

Figure A.6: From top to bottom are shown: J1159+2914, J1217+3007, J1221+2813, J1229+0203, J1256-0547, J1310+3220. Each curve is a spectra of a specific observing epoch combining quasi–simultaneous multi–frequency data obtained at Effelsberg and Pico Veleta.

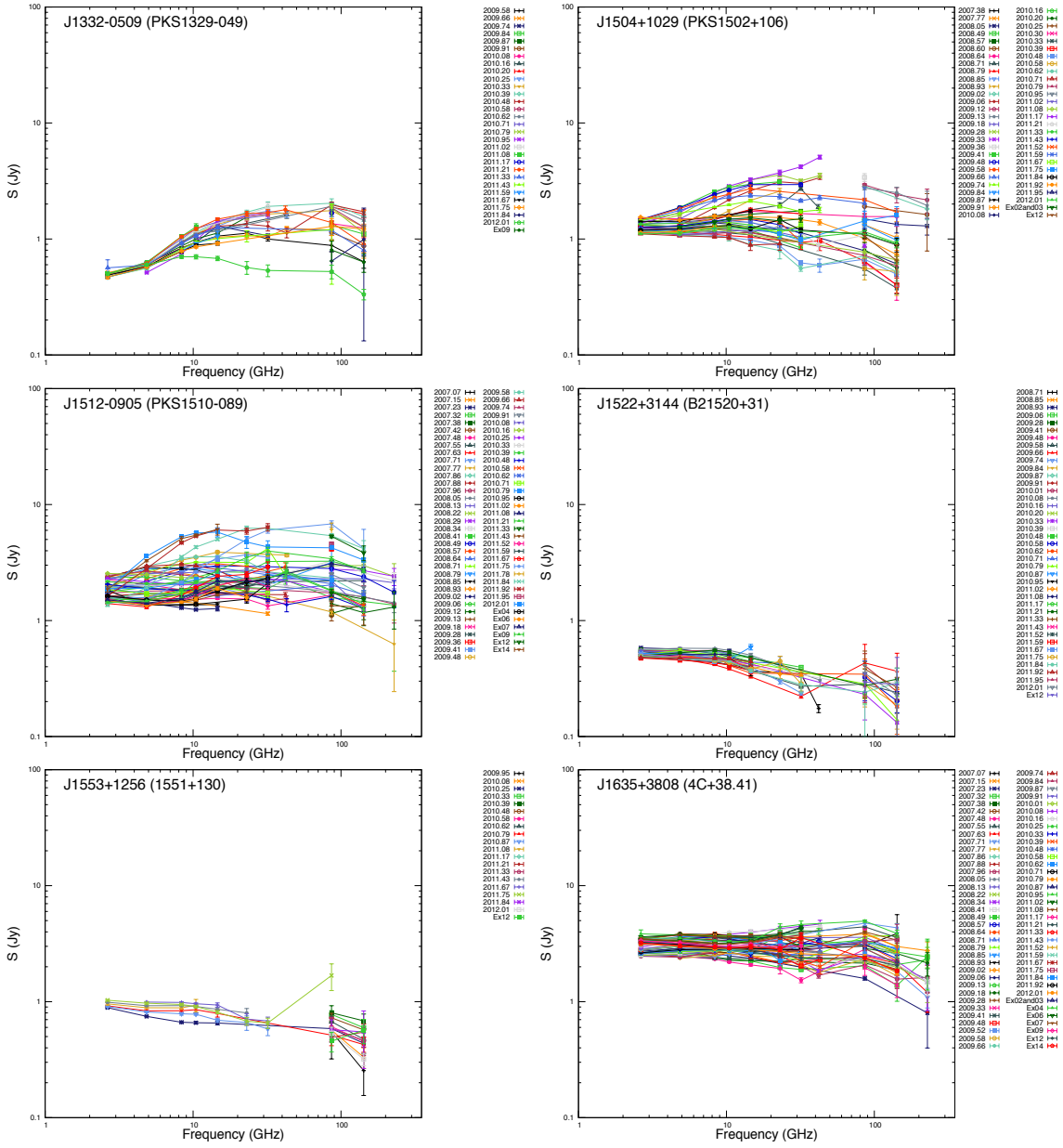

Figure A.7: From top to bottom are shown: J1332-0509, J1504+1029, J1512-0905, J1522+3144, J1553+1256, J1635+3808. Each curve is a spectra of a specific observing epoch combining quasi–simultaneous multi–frequency data obtained at Effelsberg and Pico Veleta.

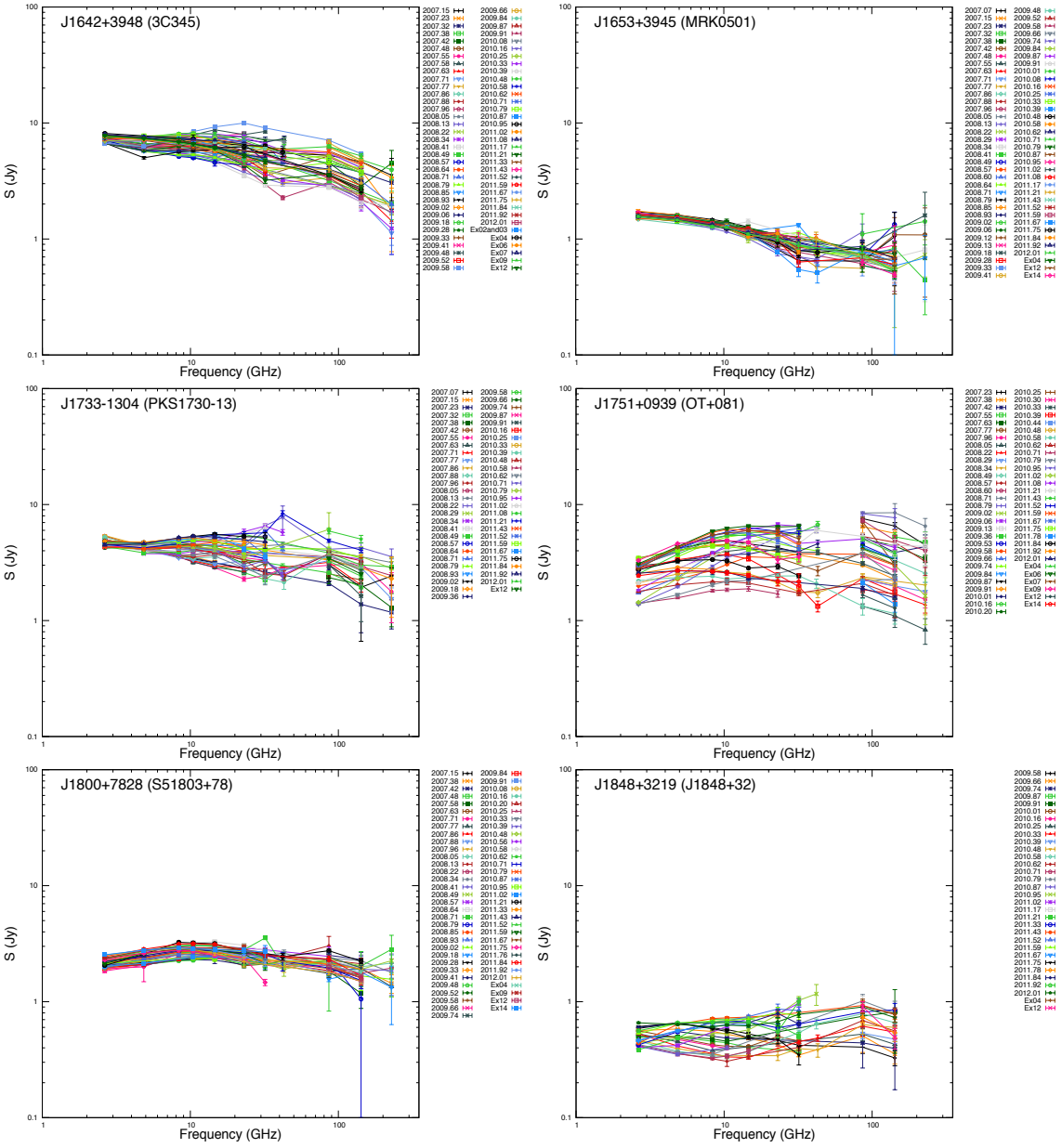

Figure A.8: From top to bottom are shown: J1642+3948, J1653+3945, J1733-1304, J1751+0939, J1800+7828, J1848+3219. Each curve is a spectra of a specific observing epoch combining quasi–simultaneous multi–frequency data obtained at Effelsberg and Pico Veleta.

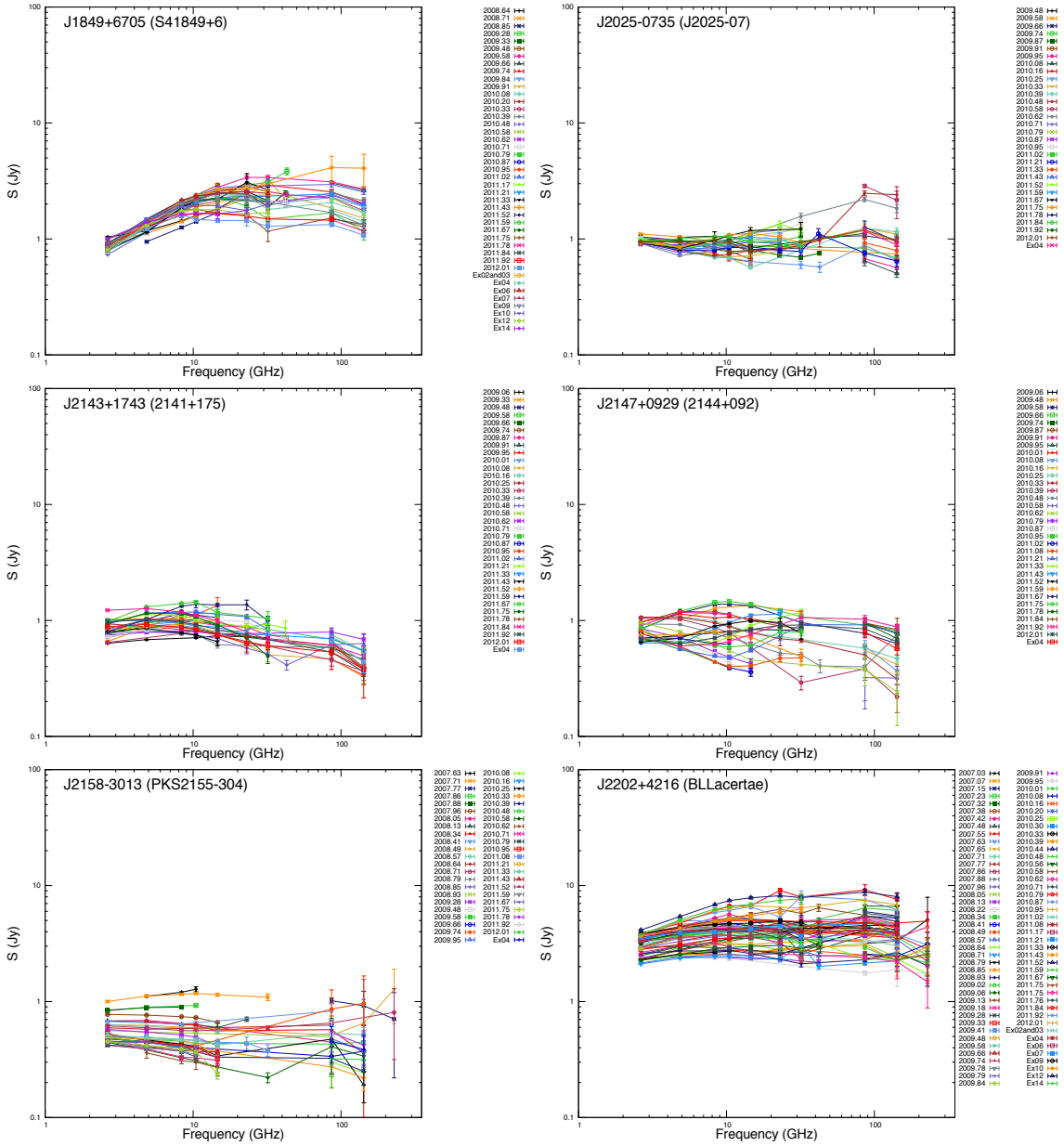

Figure A.9: From top to bottom are shown: J1849+6705, J2025-0735, J2143+1743, J2147+0929, J2158-3013, J2202+4216. Each curve is a spectra of a specific observing epoch combining quasi–simultaneous multi–frequency data obtained at Effelsberg and Pico Veleta.

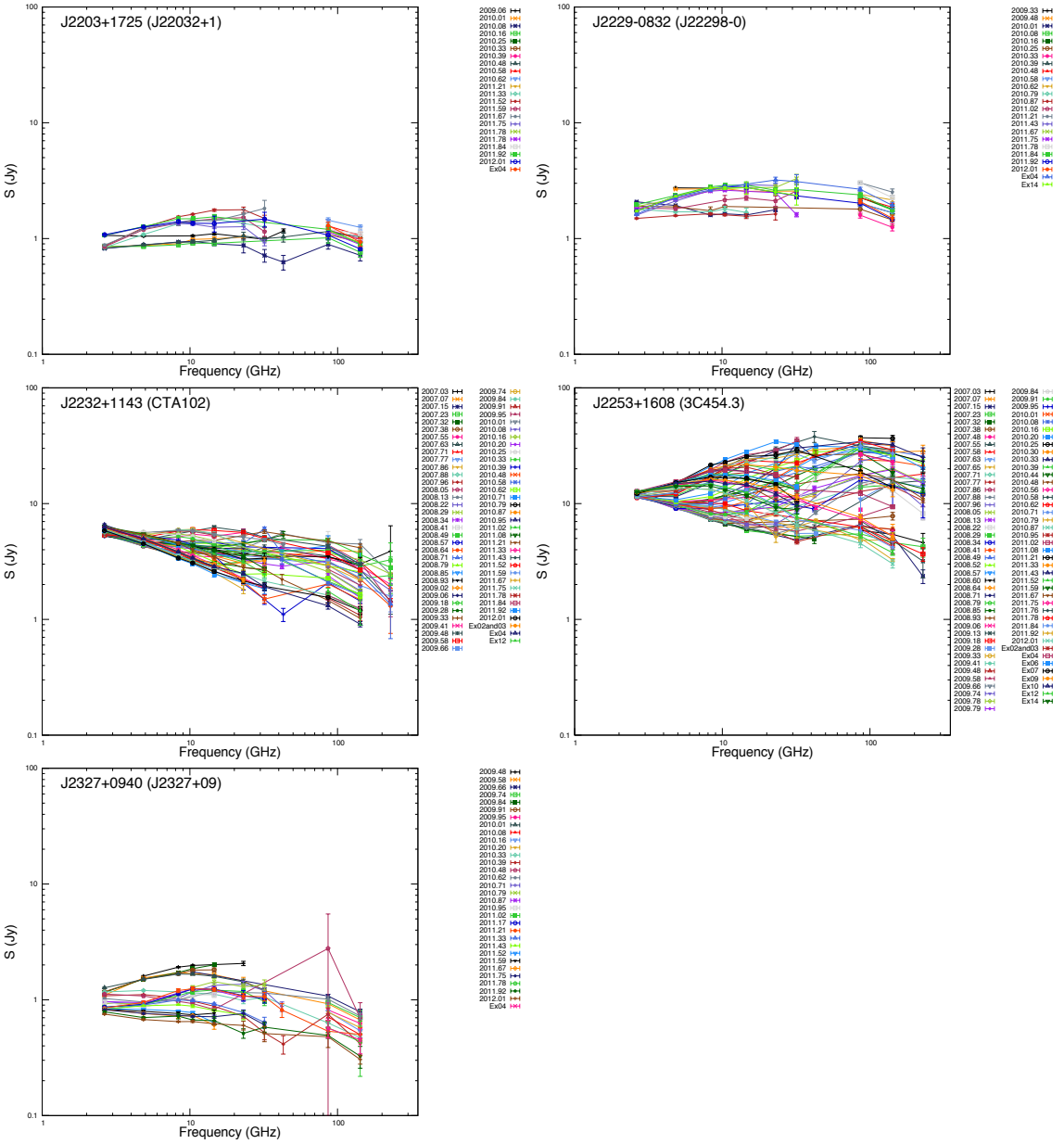

Figure A.10: From top to bottom are shown: J2203+1725, J2229-0832, J2232+1143, J2253+1608, J2327+0940. Each curve is a spectra of a specific observing epoch combining quasi–simultaneous multi–frequency data obtained at Effelsberg and Pico Veleta.

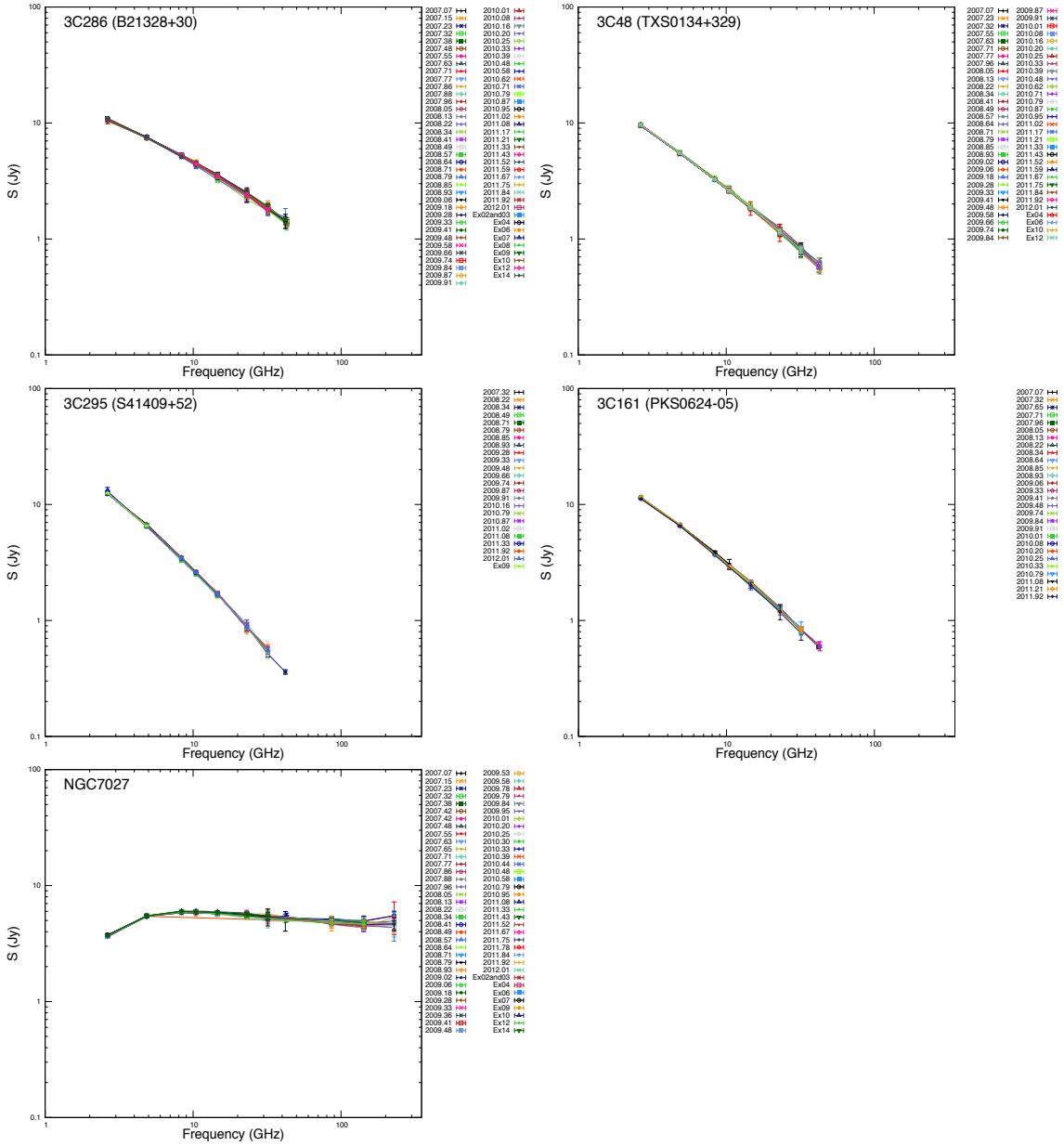

Figure A.11: Calibrator sources. From top to bottom are shown: 3C286, 3C48, 3C295, 3C161, NGC 7027. Each curve is a spectra of a specific observing epoch combining quasi–simultaneous multi–frequency data obtained at Effelsberg and Pico Veleta.

A.2.2 Spectral indices plots

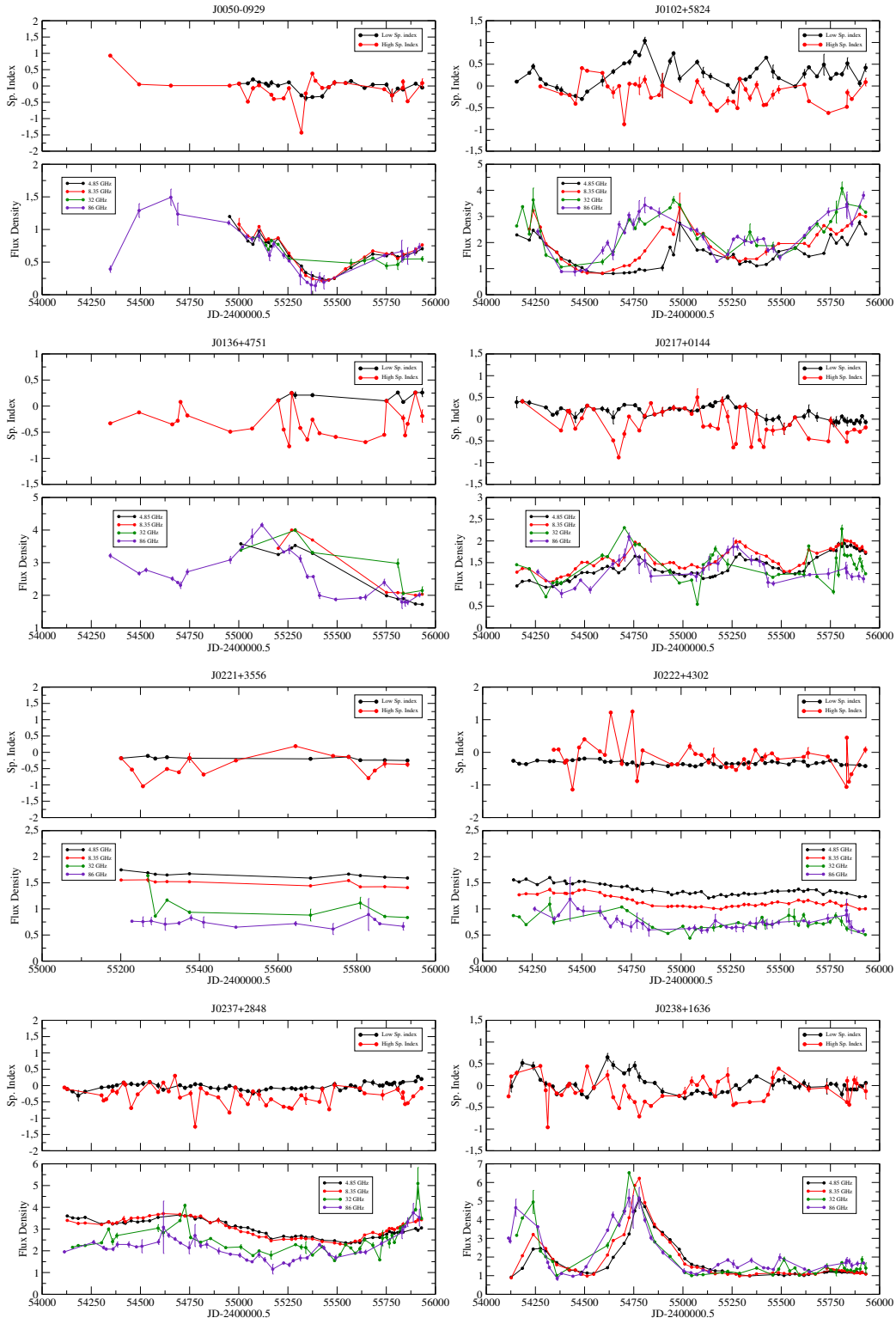

Figure A.12: Spectral indices plots (upper) Light curves for 4.85, 8.35, 32, 86 GHZ (lower). Sources from top to bottom: J0050-0929, J0102+5824, J0136+4751, J0217+0144, J0221+3556, J0222+4302, J0237+2848, J0238+1636

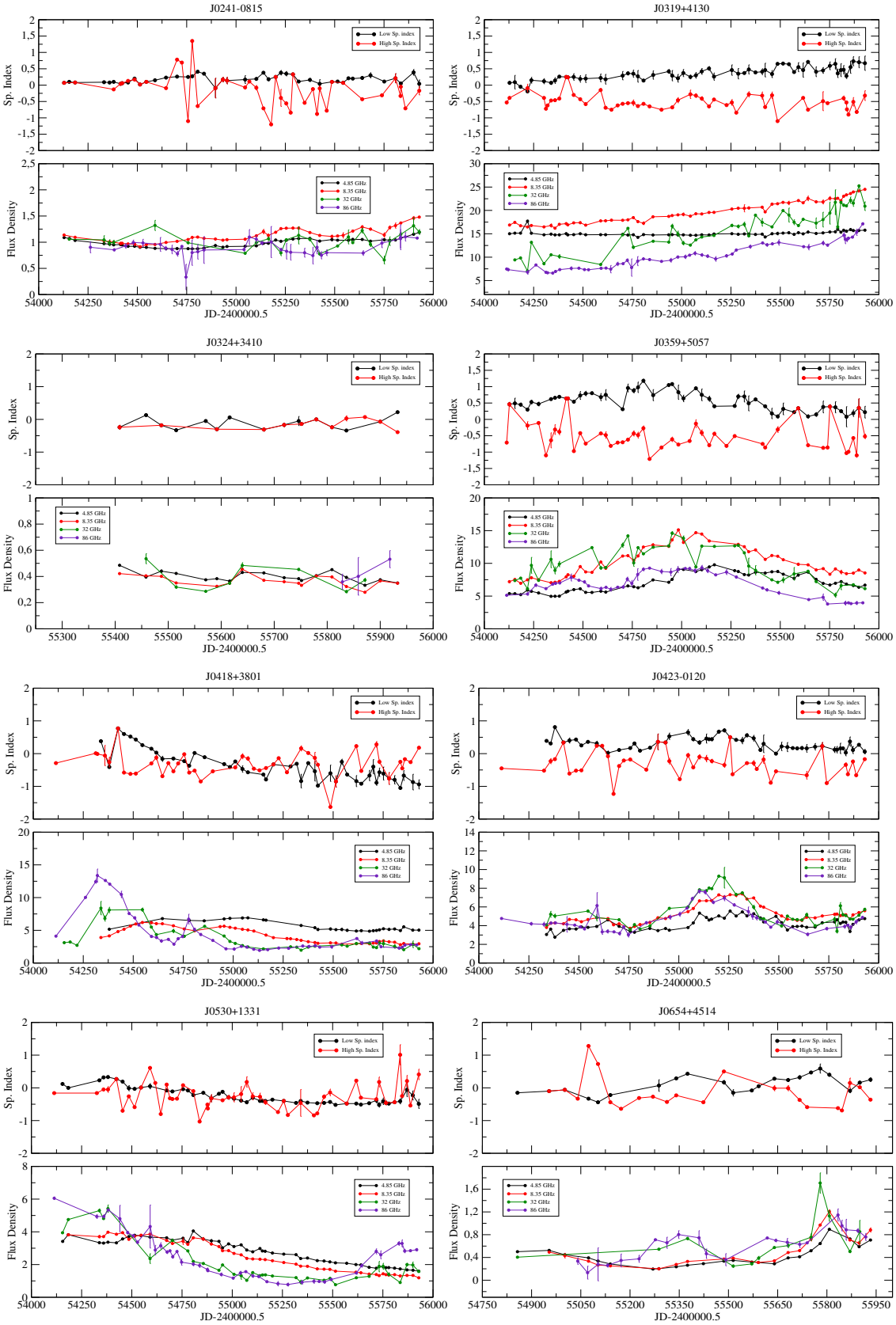

Figure A.13: Spectral indices plots (upper) Light curves for 4.85, 8.35, 32, 86 GHZ (lower). Sources from top to bottom: J0241-0815, J0319+4130, J0324+3410, J0359+5057, J0418+1801, J0423-0120, J0530+1331, J0654+4514

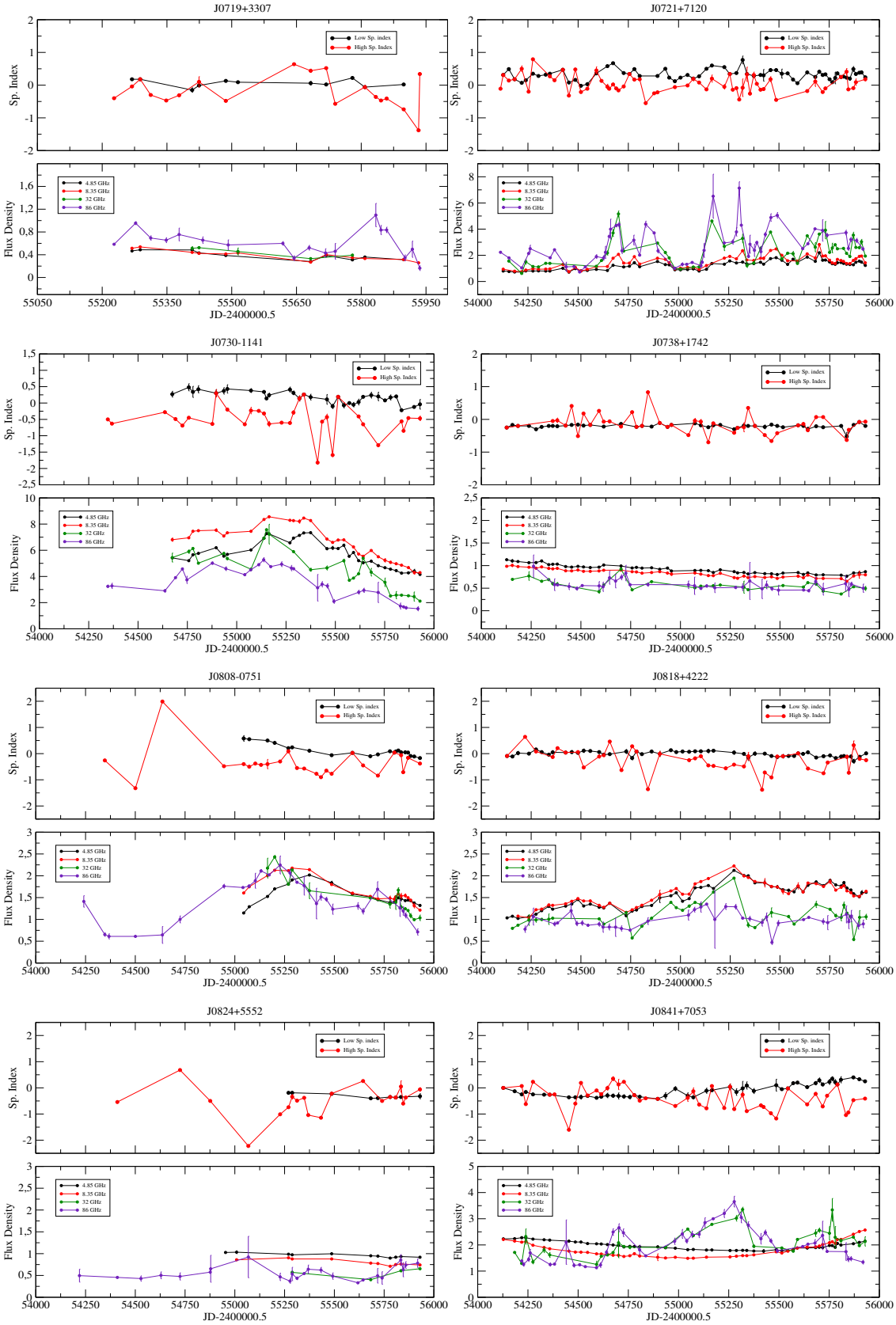

Figure A.14: Spectral indices plots (upper) Light curves for 4.85, 8.35, 32, 86 GHZ (lower). Sources from top to bottom: J0719+3307, J0721+7120, J0730-1141, J0738+1742, J0808-0751, J0818+4222, J0824+5552, J0841+7053

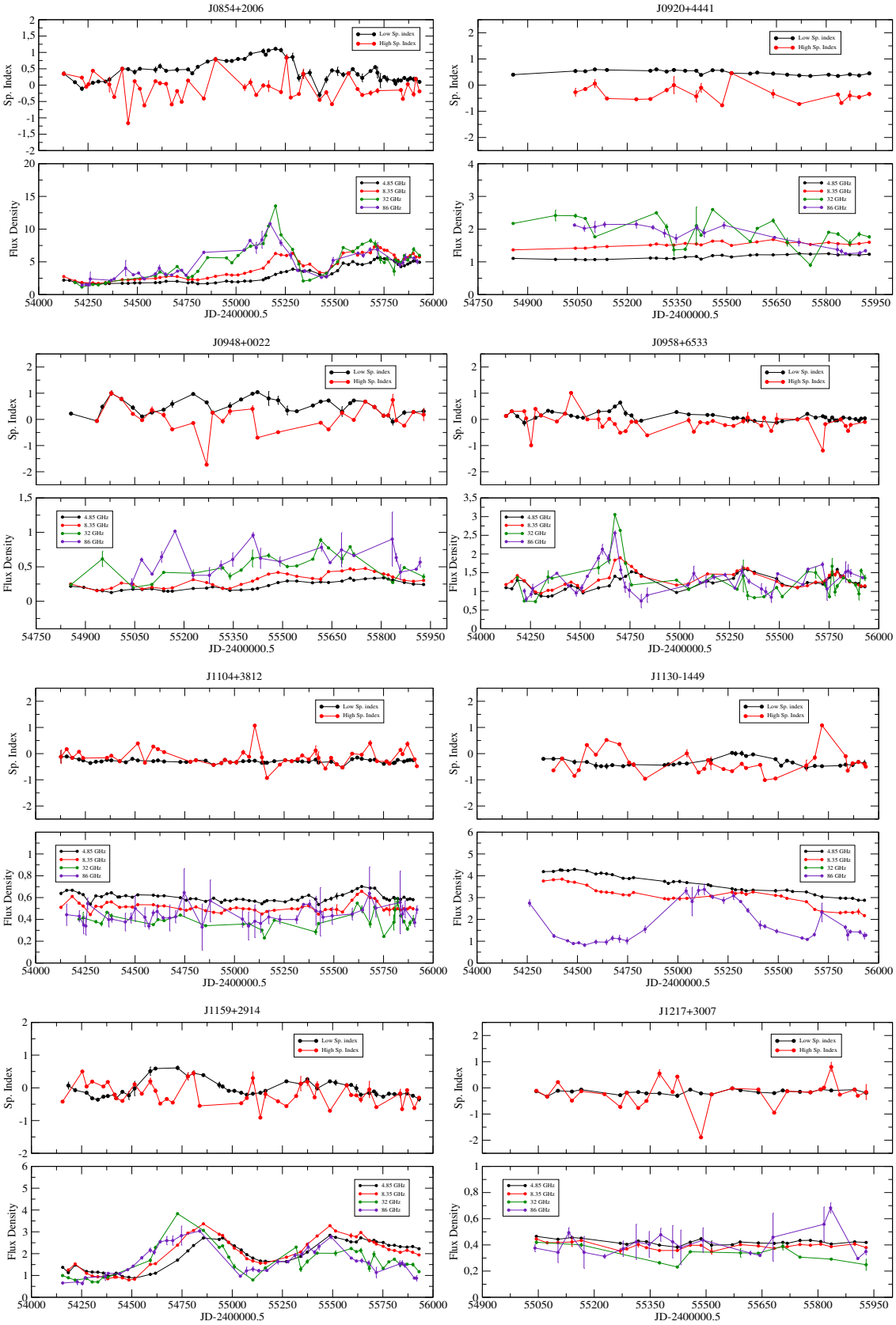

Figure A.15: Spectral indices plots (upper) Light curves for 4.85, 8.35, 32, 86 GHZ (lower). Sources from top to bottom: J0854+2006, J0920+4441, J0948+0022, J0958+6533, J1104+3812, J1130-1449, J1159+2914, J1217+3007

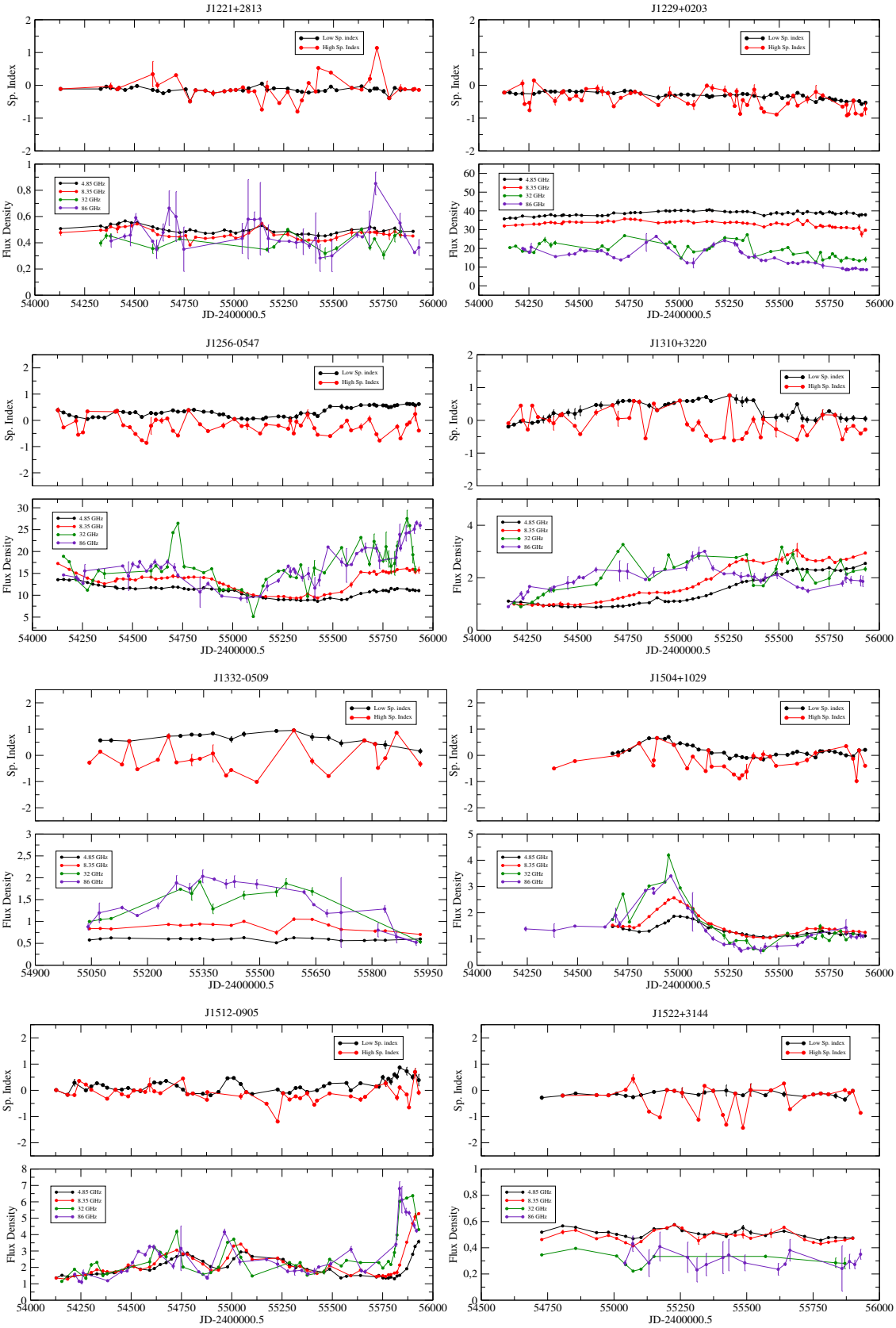

Figure A.16: Spectral indices plots (upper) Light curves for 4.85, 8.35, 32, 86 GHZ (lower). Sources from top to bottom: J1221+2813, J1229+0203, J1256-0547, J1310+3220, J1332-0509, J1504+1029, J1512-0905, J1522+3144

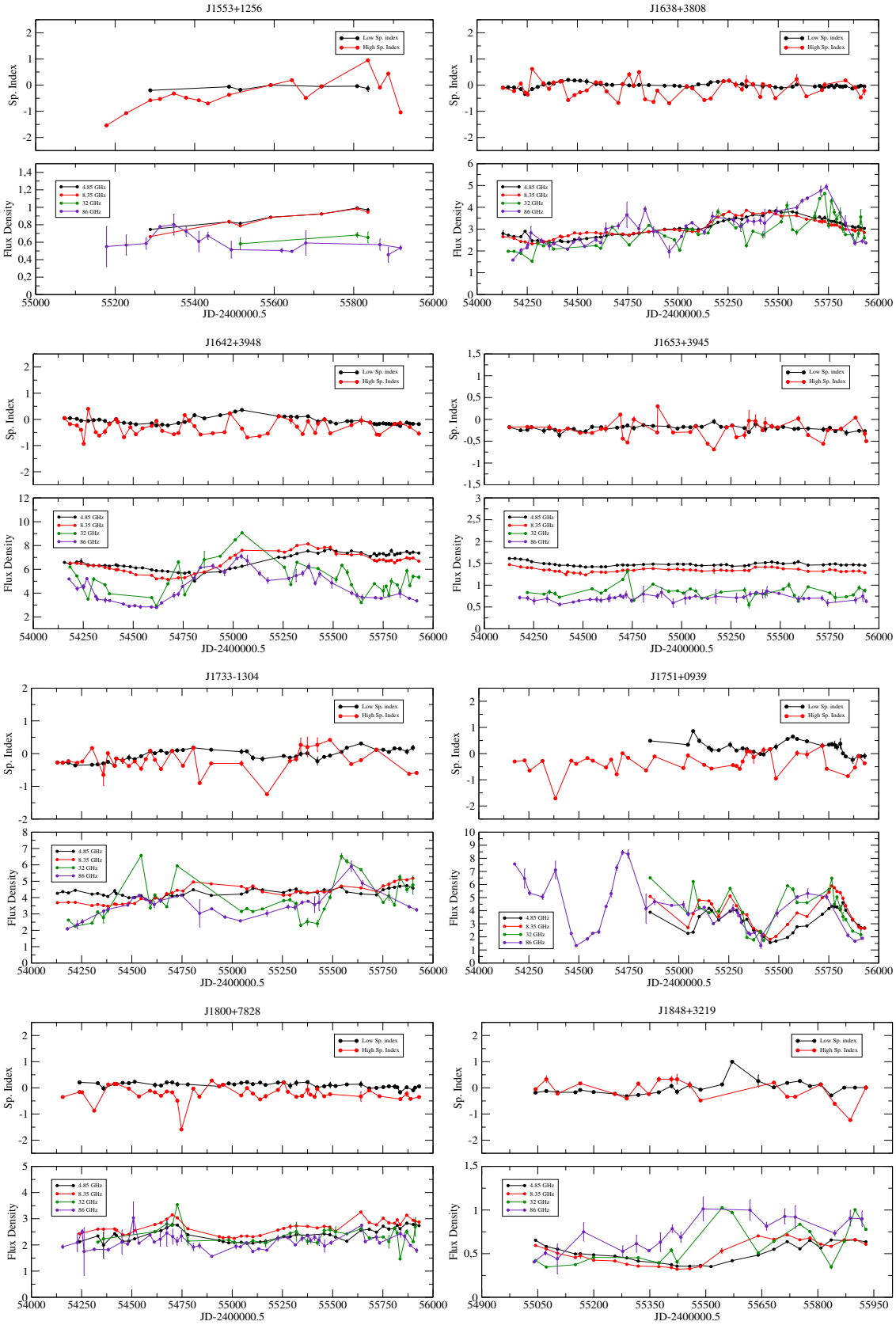

Figure A.17: Spectral indices plots (upper) Light curves for 4.85, 8.35, 32, 86 GHZ (lower). Sources from top to bottom: J1553+1256, J1635+3808, J1642+3948, J1653+3945, J1733-1304, J1751+0939, J1800+7828, J1848+3219

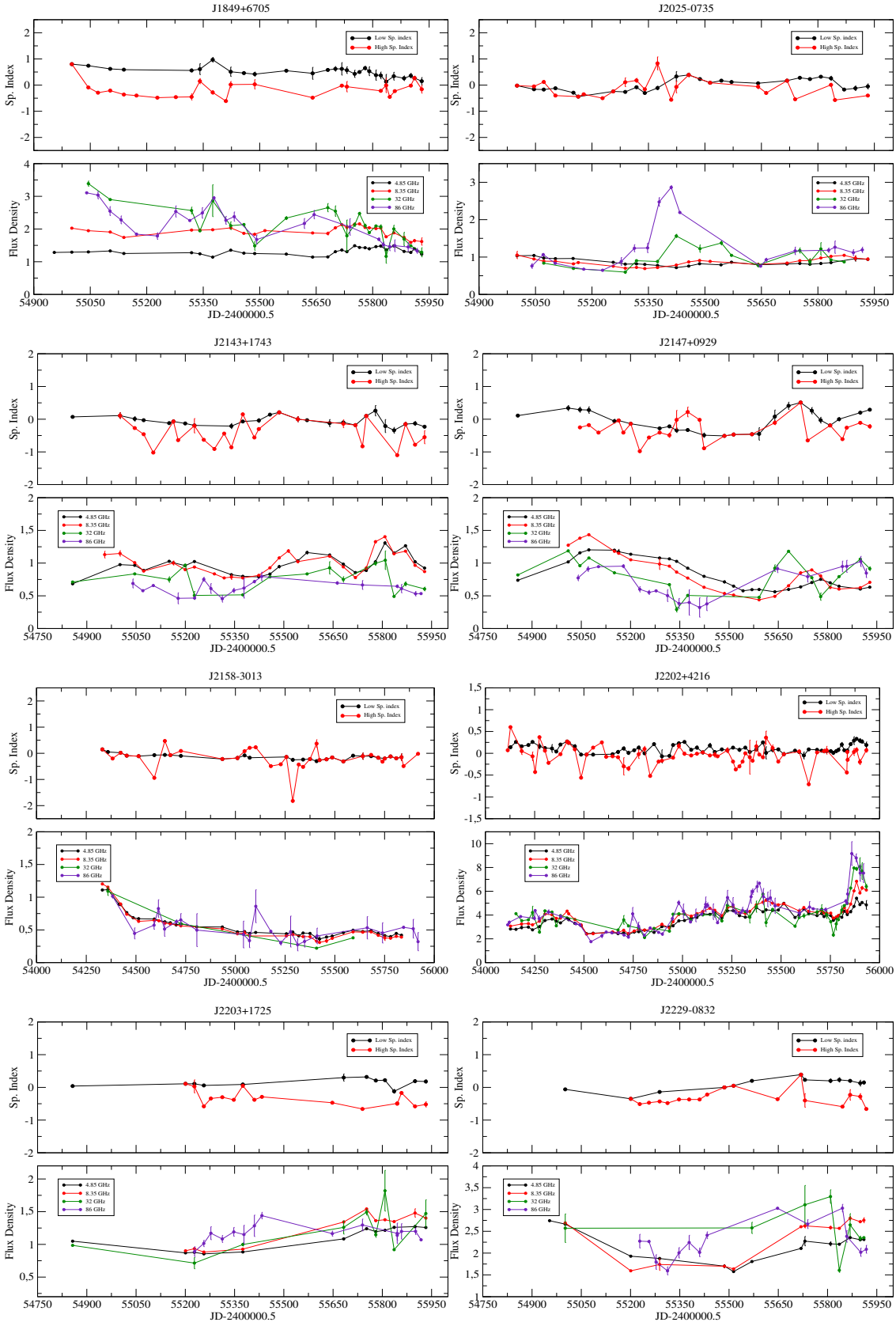

Figure A.18: Spectral indices plots (upper) Light curves for 4.85, 8.35, 32, 86 GHZ (lower). Sources from top to bottom: J1849+6705, J2025-0735, J2143+1743, J2147+0929, J2158-3013, J2202+4216, J2203+1725, J2229-0832

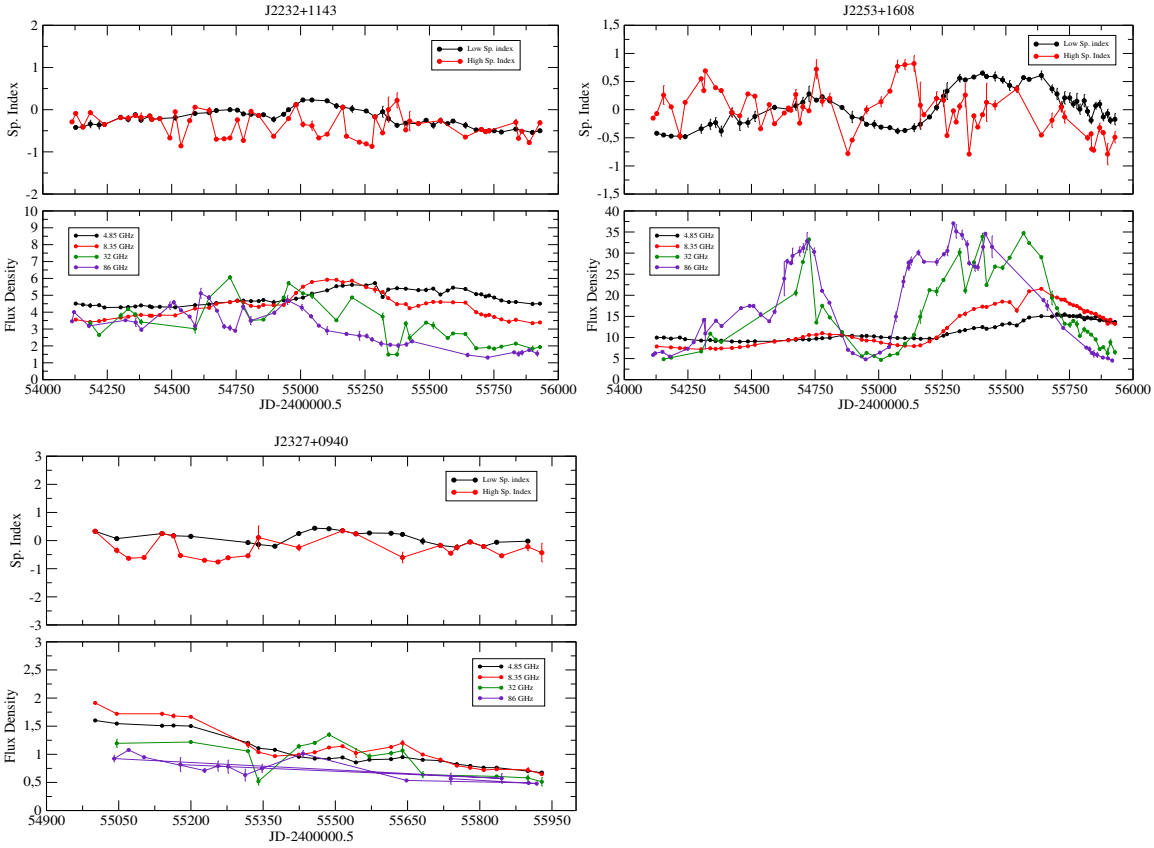

Figure A.19: Spectral indices plots (upper) Light curves for 4.85, 8.35, 32, 86 GHZ (lower). Sources from top to bottom: J2232+1143, J2253+1608, J2327+0940

A.3 Light Curves

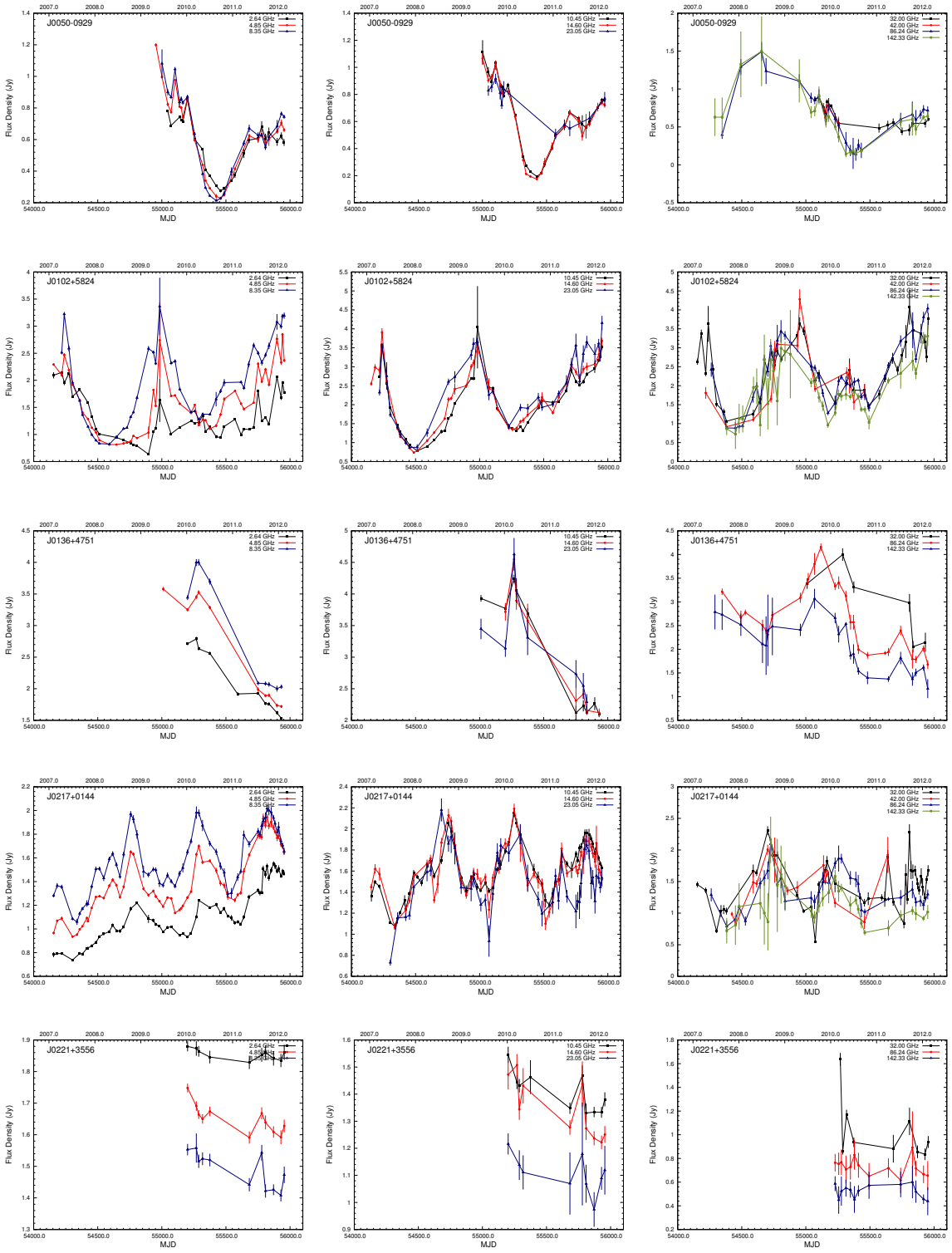

Figure A.20: Light curves of sources from top to bottom: J0050-0929, J0102+5824, J0136+4751, J0217+0144, J0221+3556. From left to right low (2.64, 4.85, 8.35 GHz), medium (10.45, 14.6, 23.05 GHz) and high (32, 42, 86.24, 142.32) GHz frequencies.

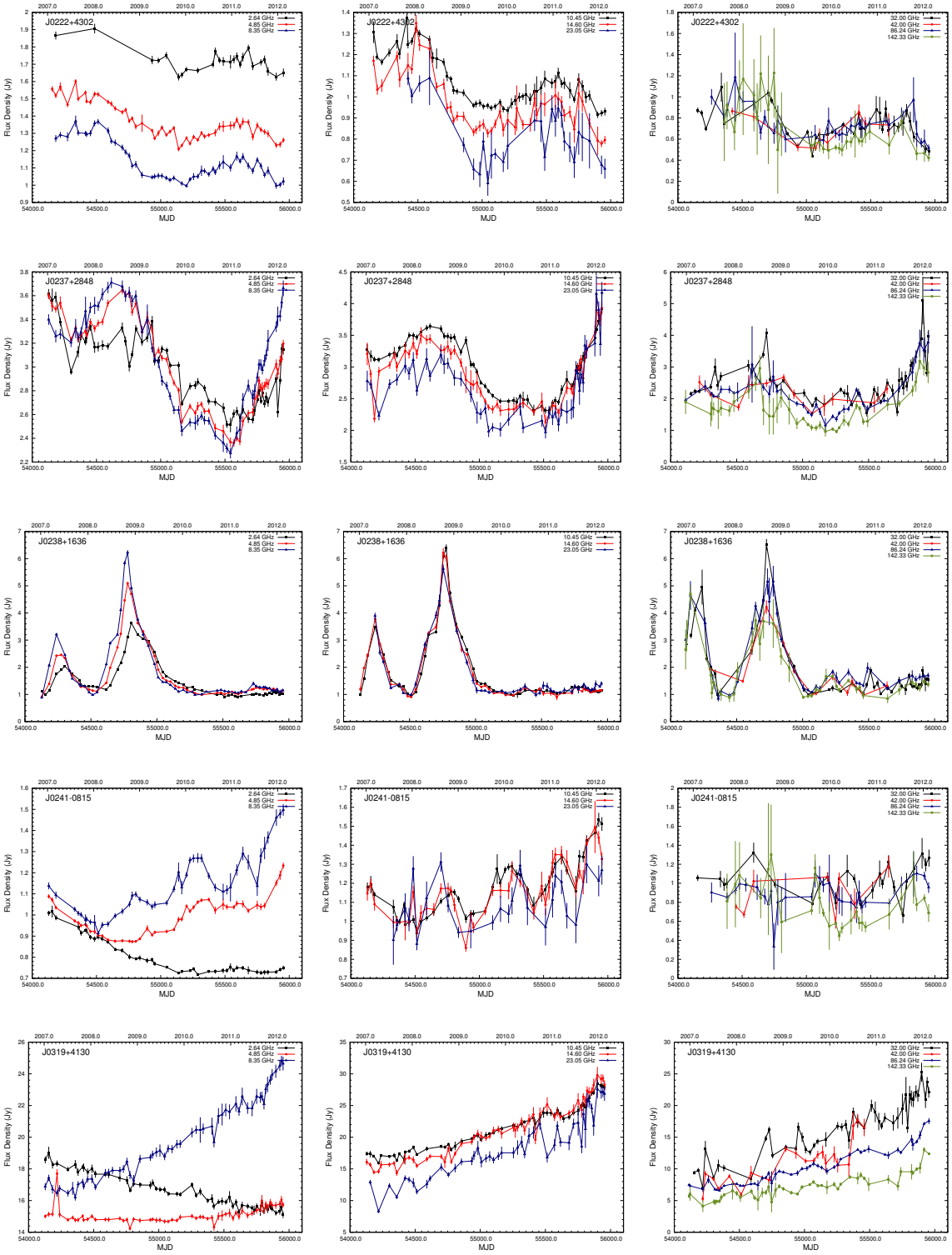

Figure A.21: Light curves of sources from top to bottom: J0222+4302, J0237+2848, J0238+1636, J0241-0815, J0319+4130. From left to right low (2.64, 4.85, 8.35 GHz), medium (10.45, 14.6, 23.05 GHz) and high (32, 42, 86.24, 142.32) GHz frequencies.

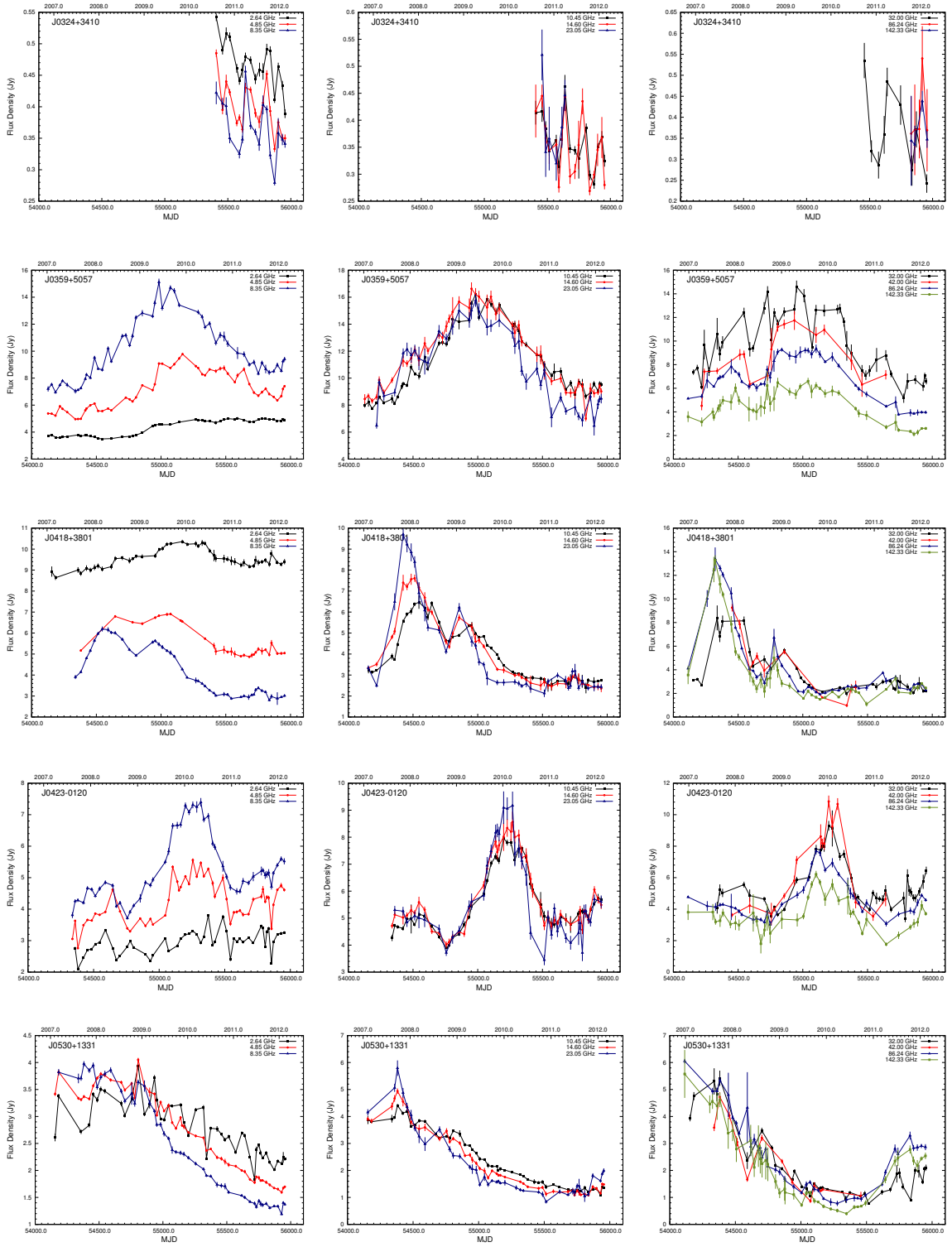

Figure A.22: Light curves of sources from top to bottom: J0324+3410, J0359+5057, J0418+1801, J0423-0120, J0530+1331. From left to right low (2.64, 4.85, 8.35 GHz), medium (10.45, 14.6, 23.05 GHz) and high (32, 42, 86.24, 142.32) GHz frequencies.

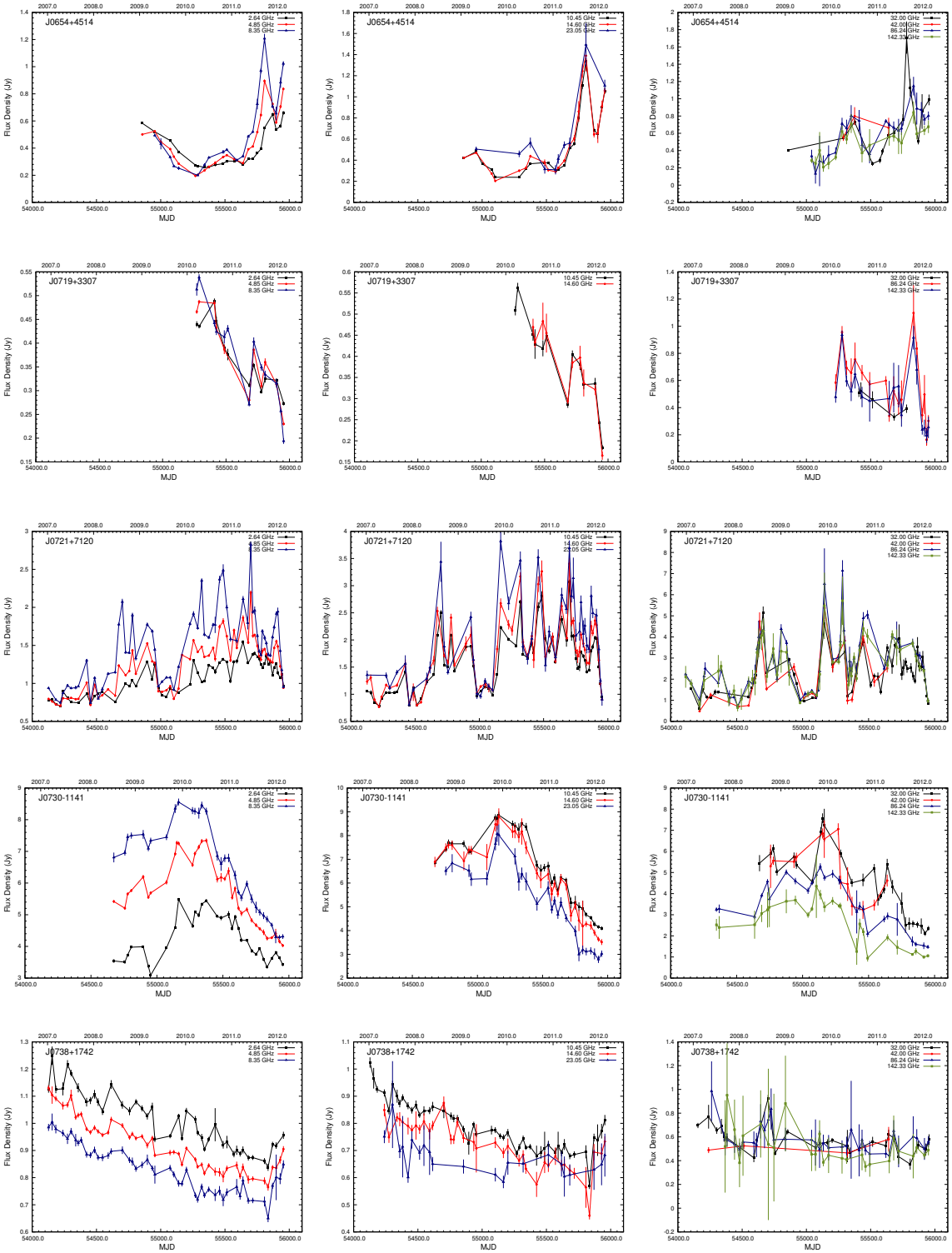

Figure A.23: Light curves of sources from top to bottom: J0654+4514, J0719+3307, J0721+7120, J0730-1141, J0738+1742. From left to right low (2.64, 4.85, 8.35 GHz), medium (10.45, 14.6, 23.05 GHz) and high (32, 42, 86.24, 142.32) GHz frequencies.

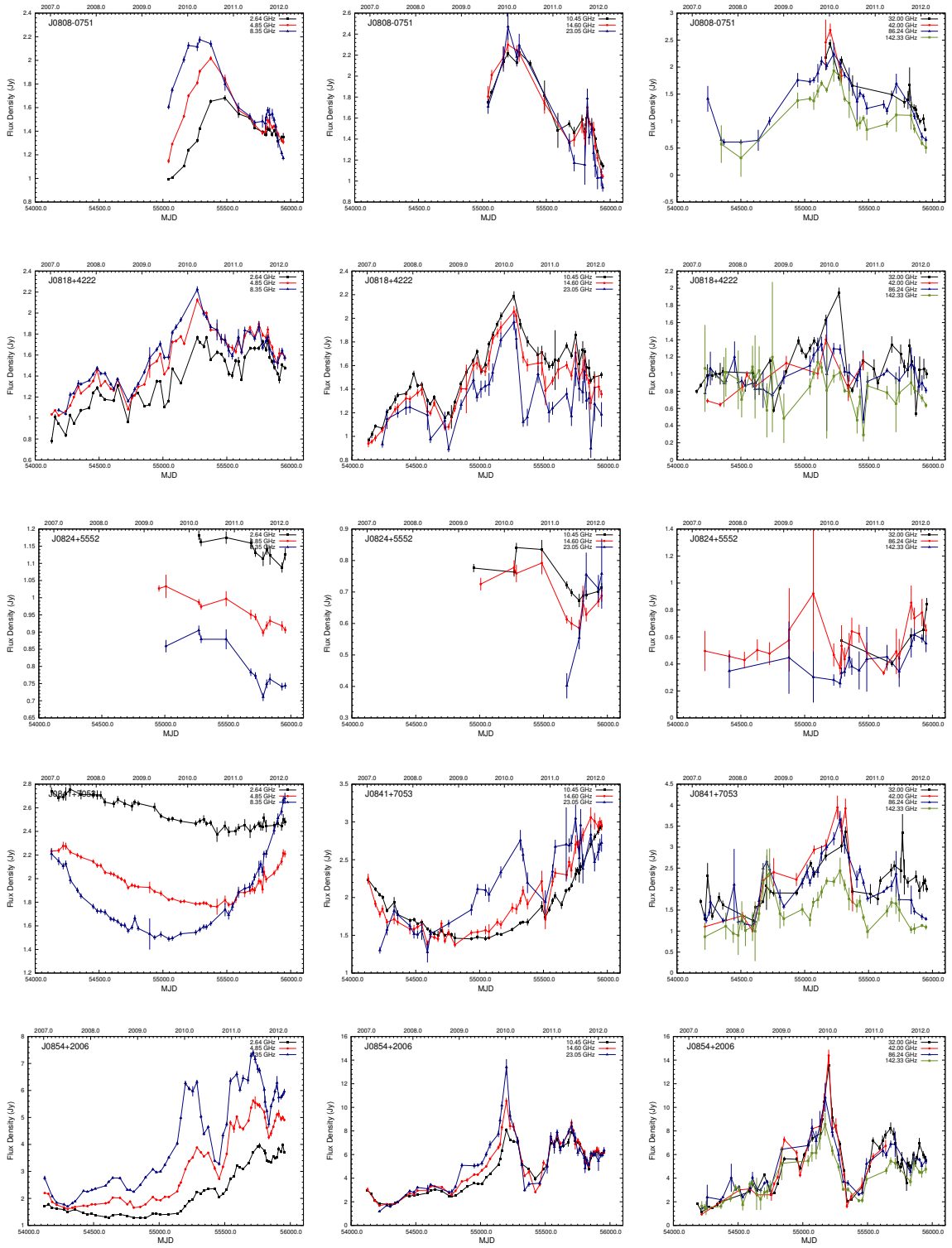

Figure A.24: Light curves of sources from top to bottom: J0808-0751, J0818+4222, J0824+5552, J0841+7053, J0854+2006. From left to right low (2.64, 4.85, 8.35 GHz), medium (10.45, 14.6, 23.05 GHz) and high (32, 42, 86.24, 142.32) GHz frequencies.

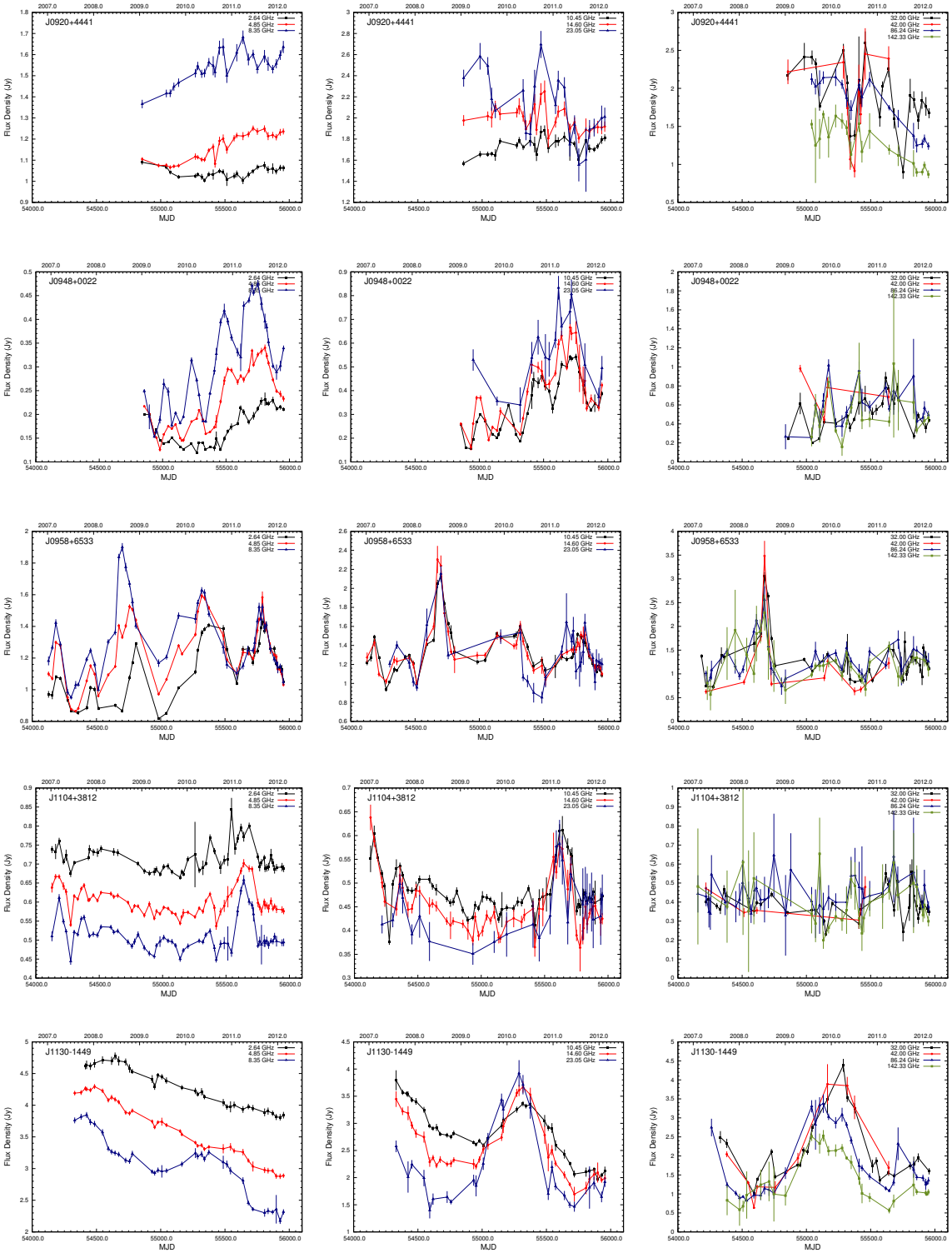

Figure A.25: Light curves of sources from top to bottom: J0920+4441, J0948+0022, J0958+6533, J1104+3812, J1130-1449. From left to right low (2.64, 4.85, 8.35 GHz), medium (10.45, 14.6, 23.05 GHz) and high (32, 42, 86.24, 142.32) GHz frequencies.

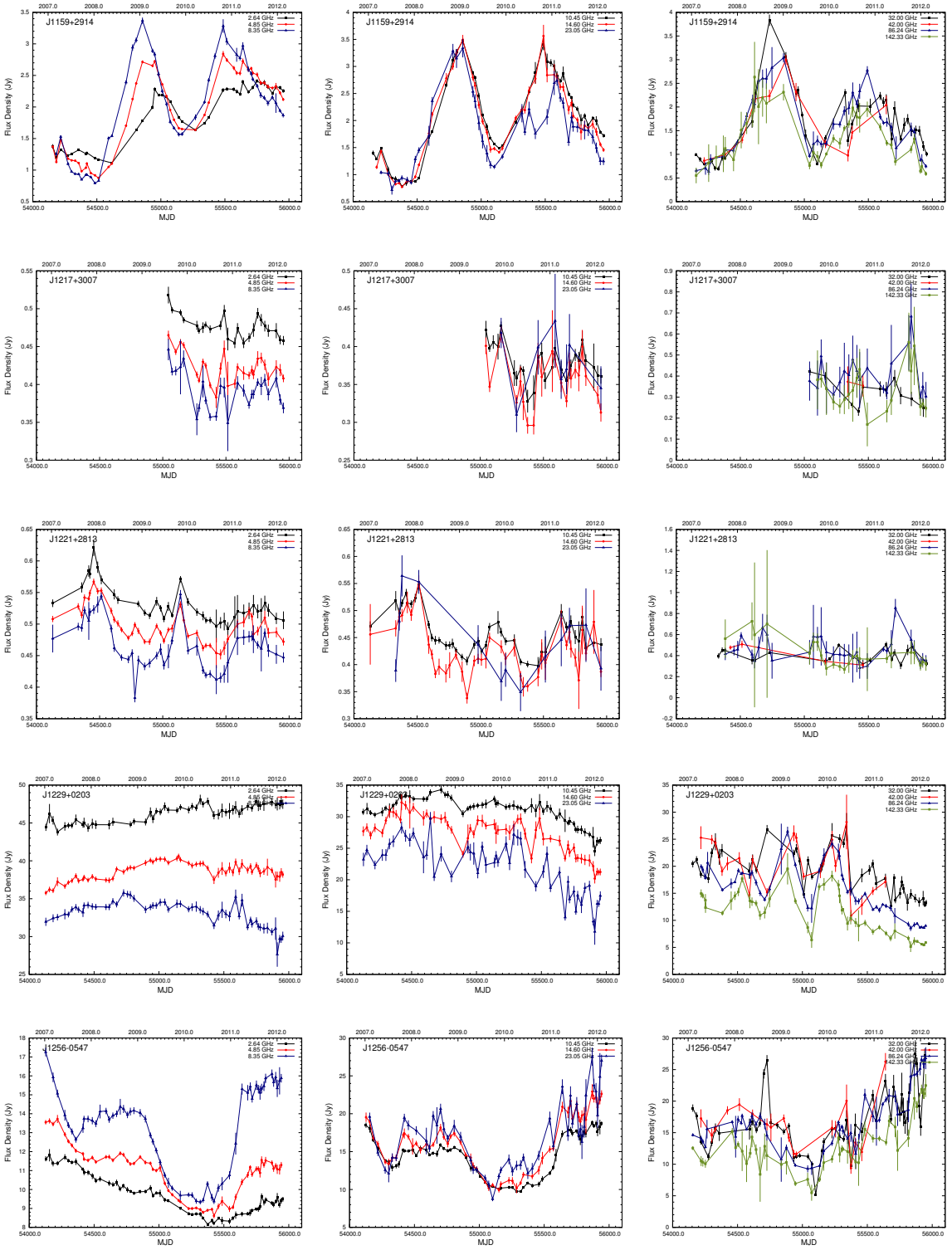

Figure A.26: Light curves of sources from top to bottom: J1159+2914, J1217+3007, J1221+2813, J1229+0203, J1256-054. From left to right low (2.64, 4.85, 8.35 GHz), medium (10.45, 14.6, 23.05 GHz) and high (32, 42, 86.24, 142.32) GHz frequencies.

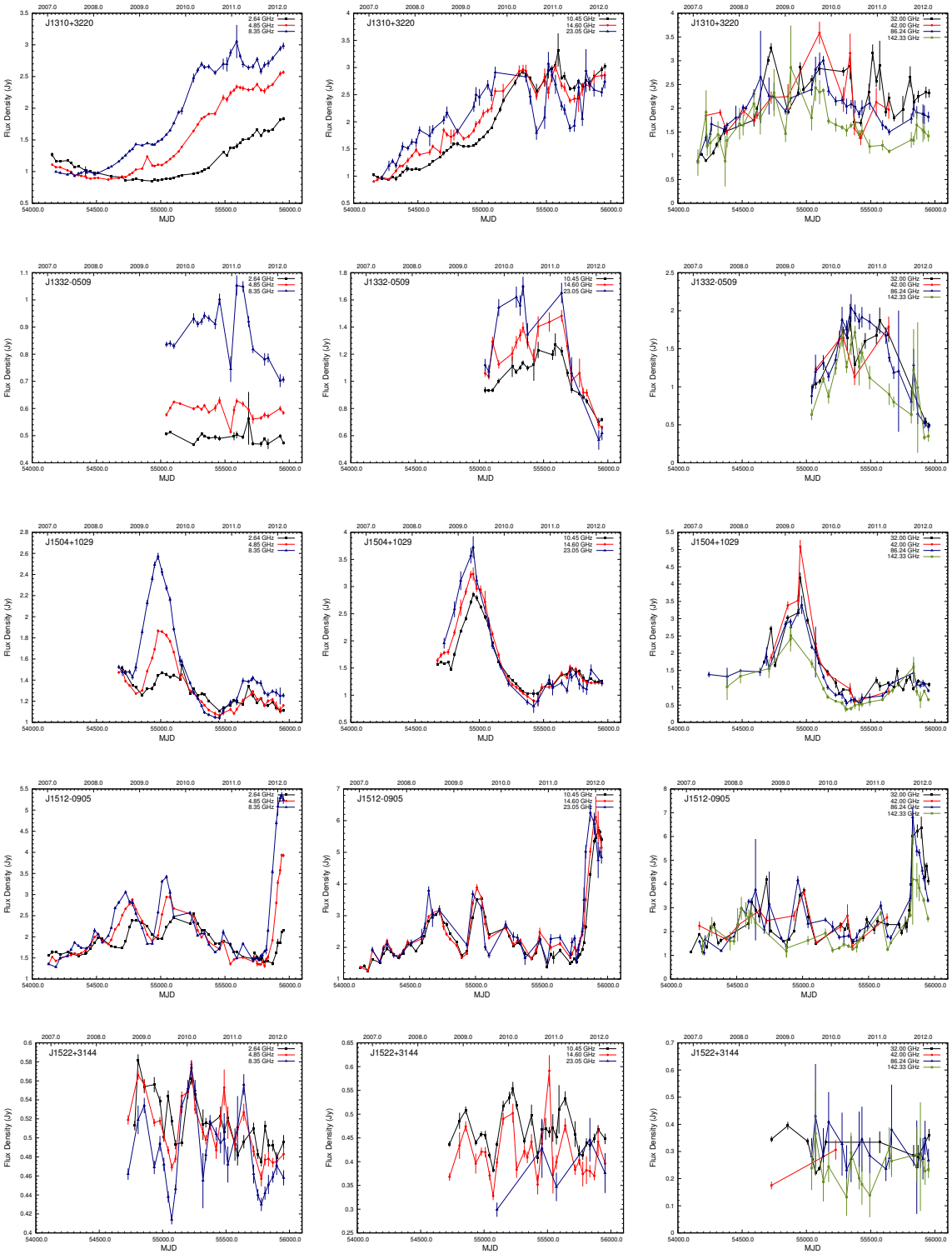

Figure A.27: Light curves of sources from top to bottom: J1310+3220, J1332-0509, J1504+1029, J1512-0905, J1522+3144. From left to right low (2.64, 4.85, 8.35 GHz), medium (10.45, 14.6, 23.05 GHz) and high (32, 42, 86.24, 142.32) GHz frequencies.

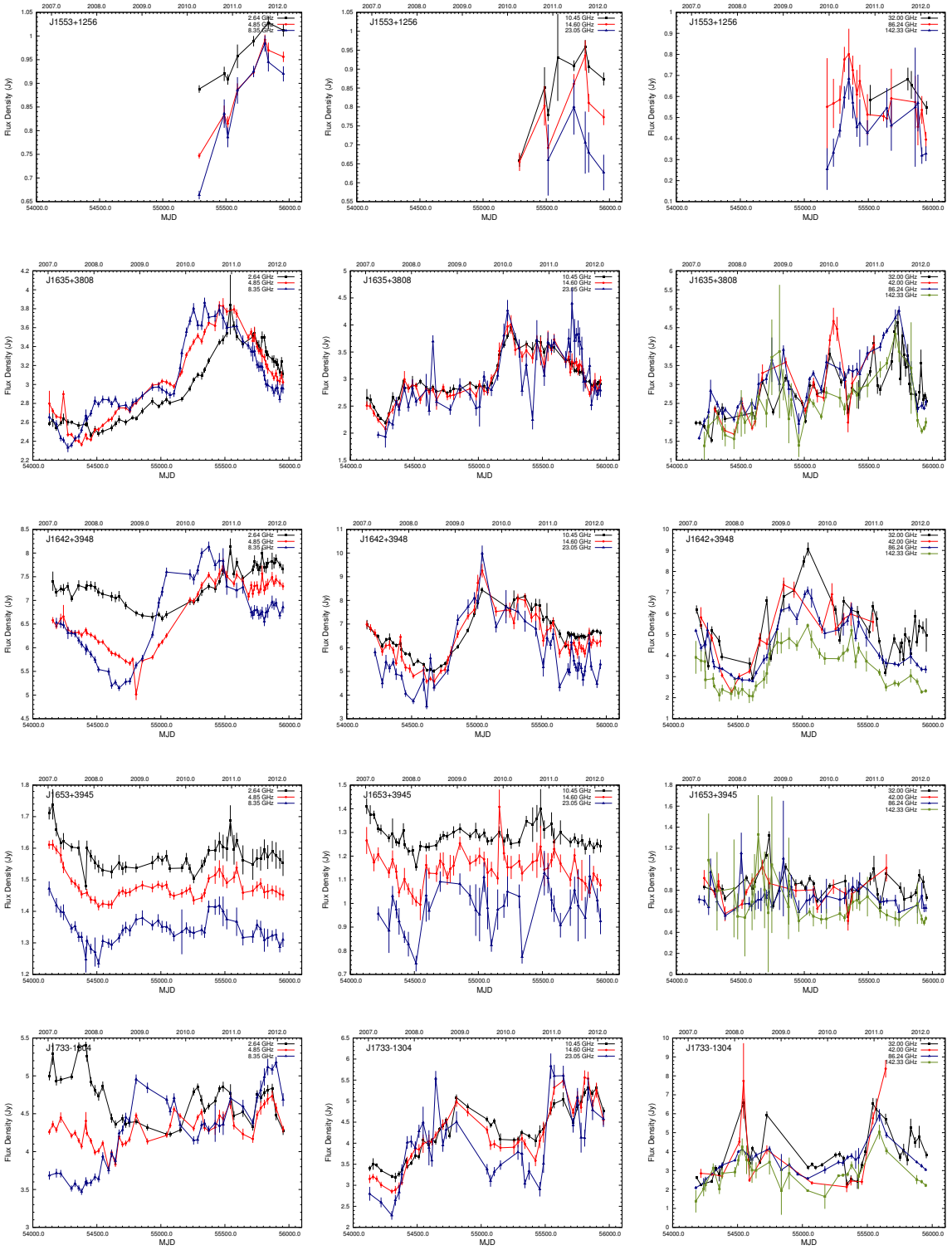

Figure A.28: Light curves of sources from top to bottom: J1553+1256, J1635+3808, J1642+3948, J1653+3945, J1733-1304. From left to right low (2.64, 4.85, 8.35 GHz), medium (10.45, 14.6, 23.05 GHz) and high (32, 42, 86.24, 142.32) GHz frequencies.

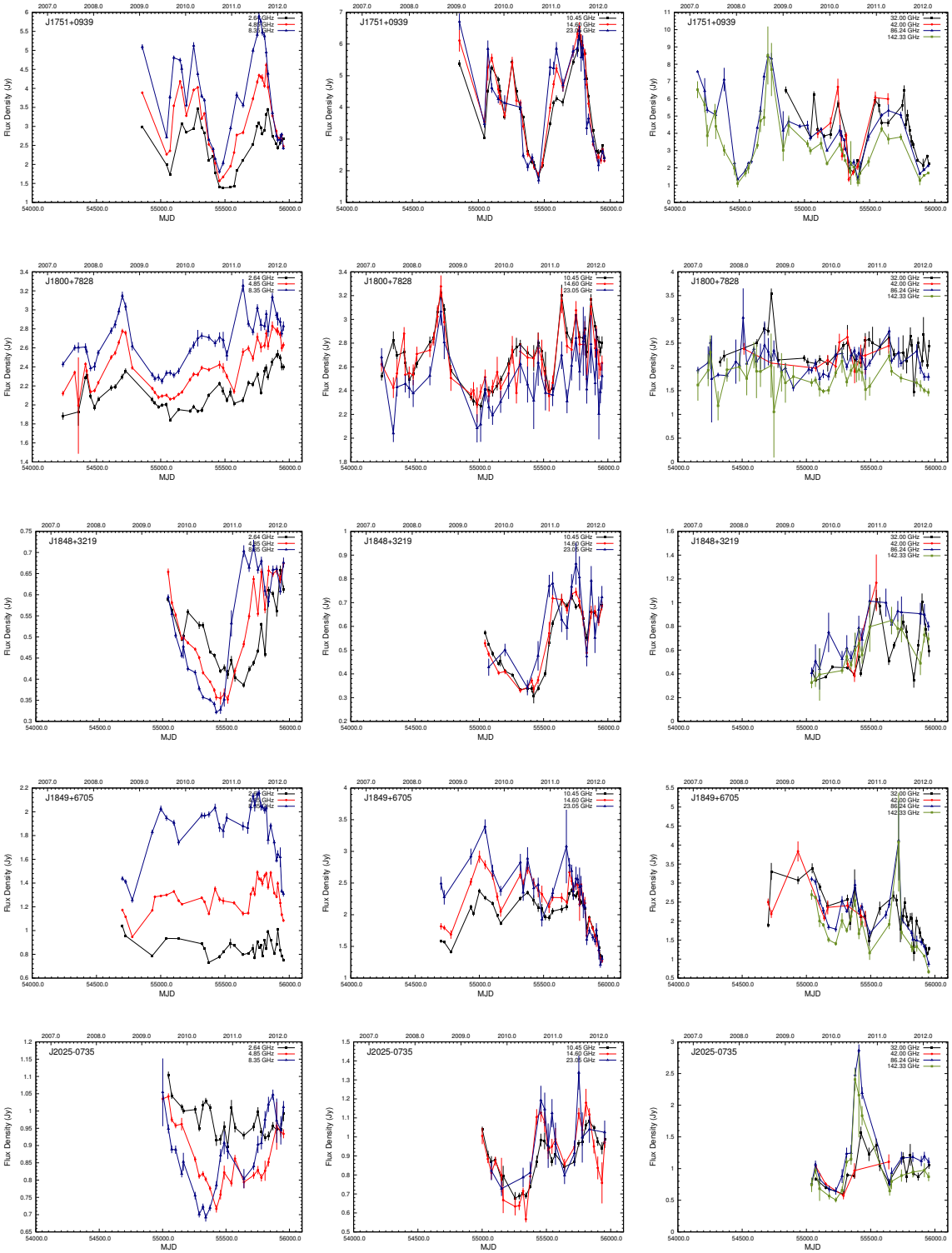

Figure A.29: Light curves of sources from top to bottom: J1751+0939, J1800+7828, J1848+3219, J1849+6705, J2025-0735. From left to right low (2.64, 4.85, 8.35 GHz), medium (10.45, 14.6, 23.05 GHz) and high (32, 42, 86.24, 142.32) GHz frequencies.

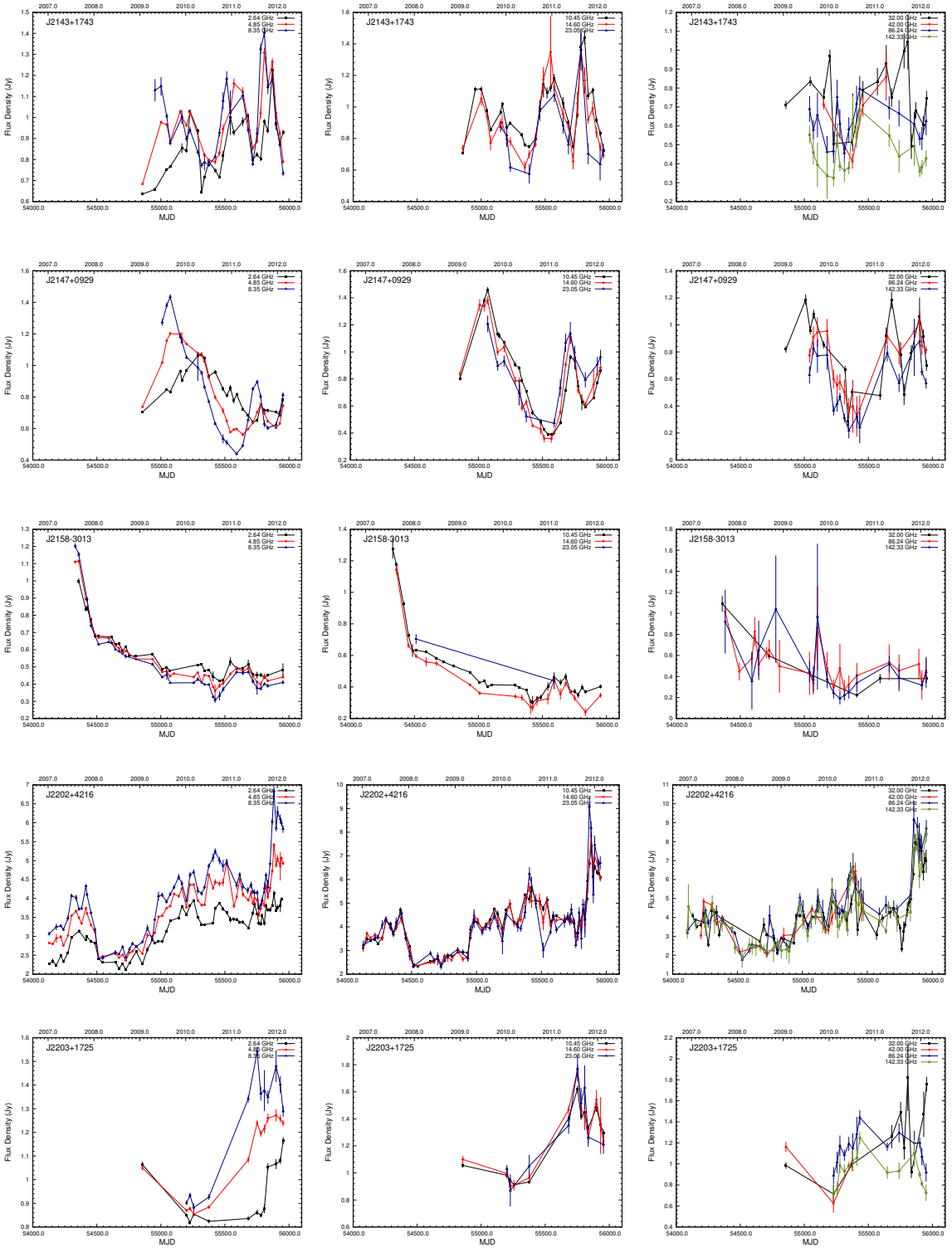

Figure A.30: Light curves of sources from top to bottom: J2143+1743, J2147+0929, J2158-3013, J2202+4216, J2203+1725. From left to right low (2.64, 4.85, 8.35 GHz), medium (10.45, 14.6, 23.05 GHz) and high (32, 42, 86.24, 142.32) GHz frequencies.

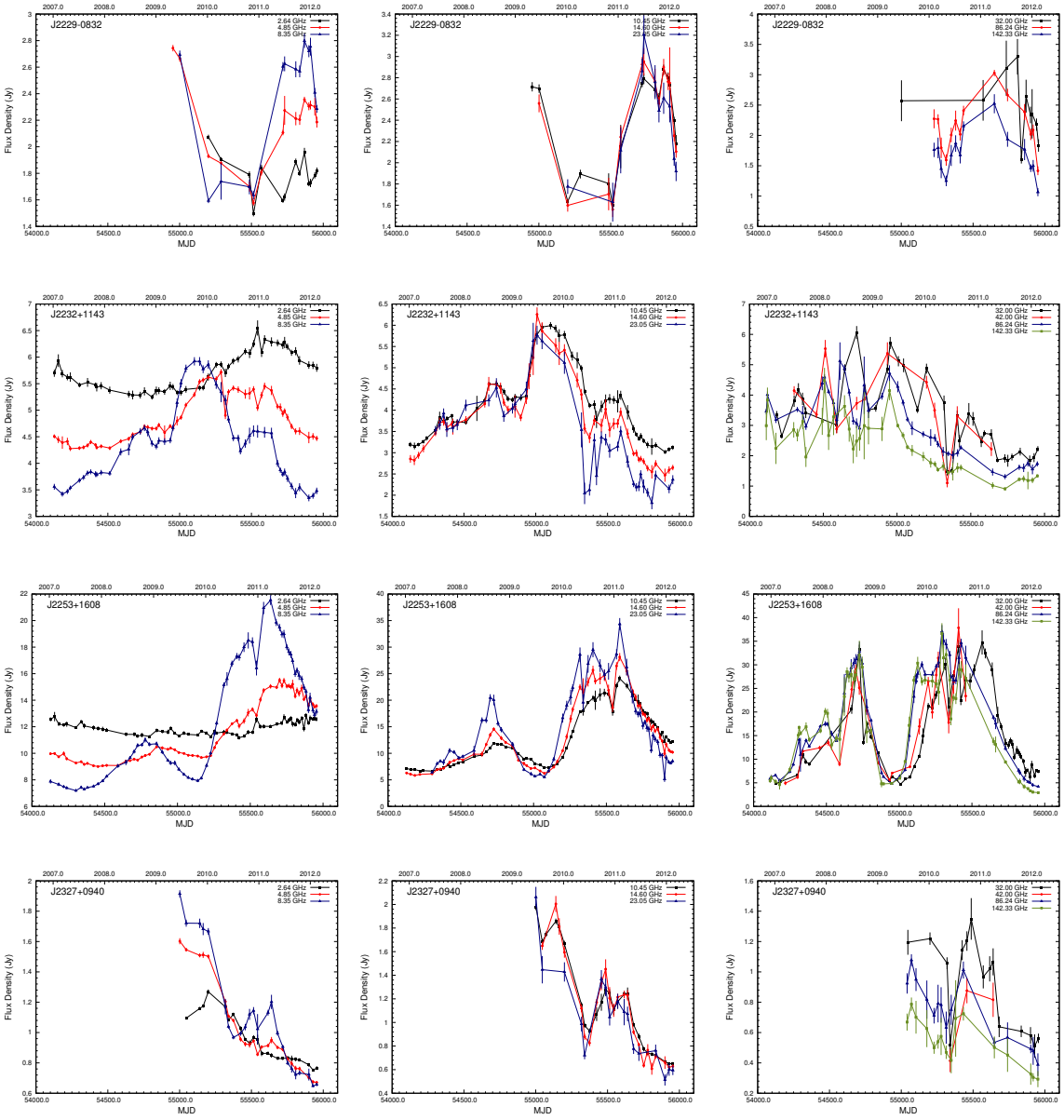

Figure A.31: Light curves of sources from top to bottom: J2229-0832, J2232+1143, J2253+1608, J2327+0940. From left to right low (2.64, 4.85, 8.35 GHz), medium (10.45, 14.6, 23.05 GHz) and high (32, 42, 86.24, 142.32) GHz frequencies.

A.4 $S_{max} - \nu_{max}$ plots

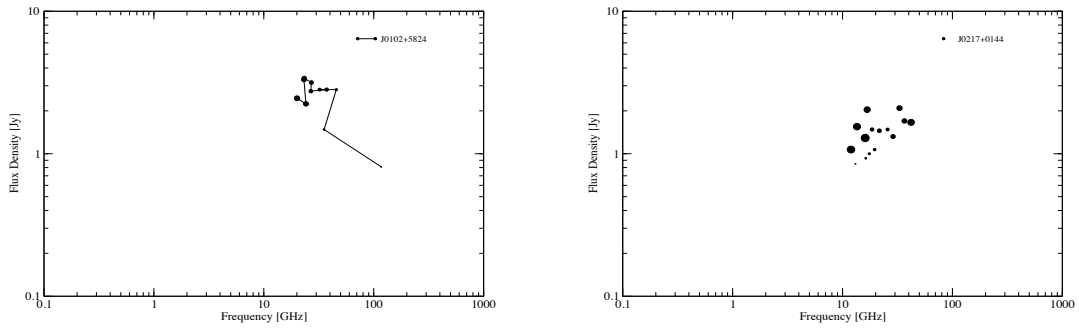

Figure A.32: Evolution of the spectral peak in the $S_{max} - \nu_{max}$ plane. Left panel is J0102+5824, right panel is J0217+0144. The size of symbols represents the time evolution. Time flows forward from smaller to larger symbols.

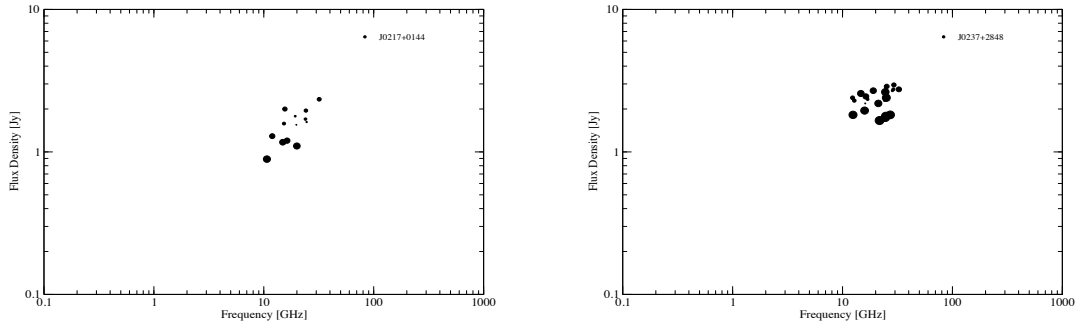

Figure A.33: Evolution of the spectral peak in the $S_{max} - \nu_{max}$ plane. Left panel is J0217+0144, right panel is J0237+2848. The size of symbols represents the time evolution. Time flows forward from smaller to larger symbols.

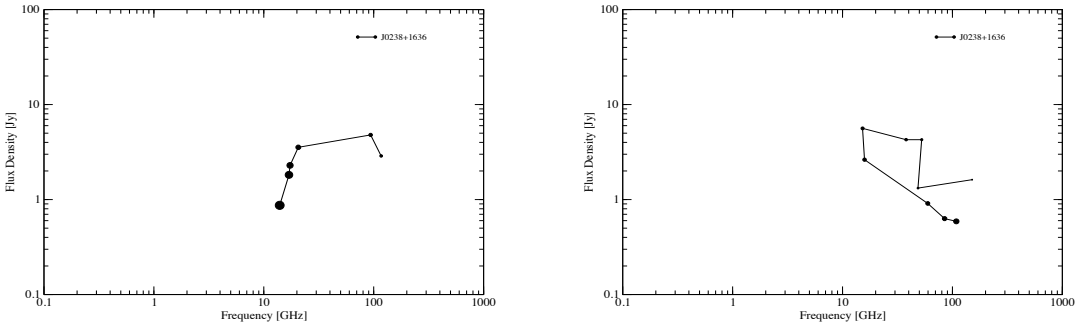

Figure A.34: Evolution of the spectral peak in the $S_{max} - \nu_{max}$ plane. Left and right panel is J0238+1636. The size of symbols represents the time evolution. Time flows forward from smaller to larger symbols.

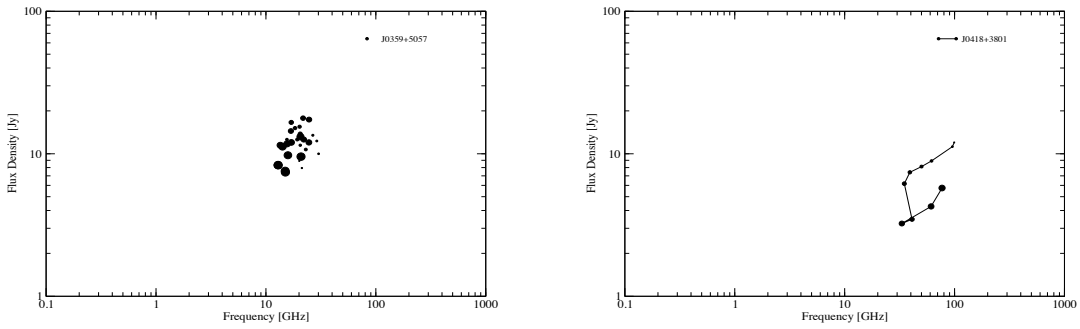

Figure A.35: Evolution of the spectral peak in the $S_{max} - \nu_{max}$ plane. Left panel is J0359+5057, right panel is J0418+3801. The size of symbols represents the time evolution. Time flows forward from smaller to larger symbols.

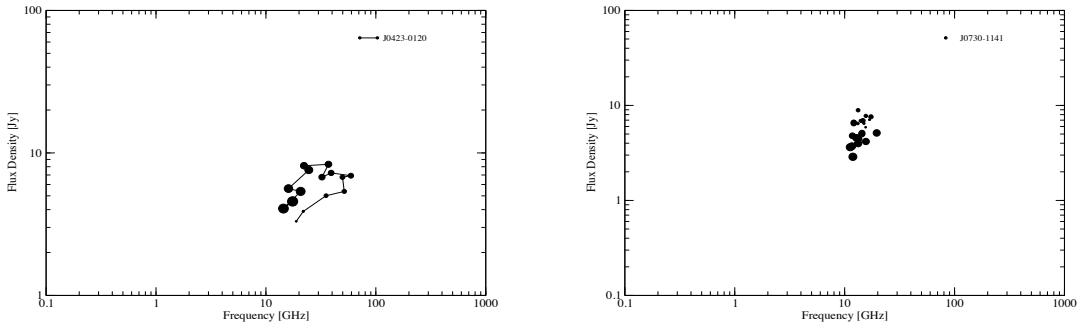

Figure A.36: Evolution of the spectral peak in the $S_{max} - \nu_{max}$ plane. Left panel is J0423-0120, right panel is J0730-1141. The size of symbols represents the time evolution. Time flows forward from smaller to larger symbols.

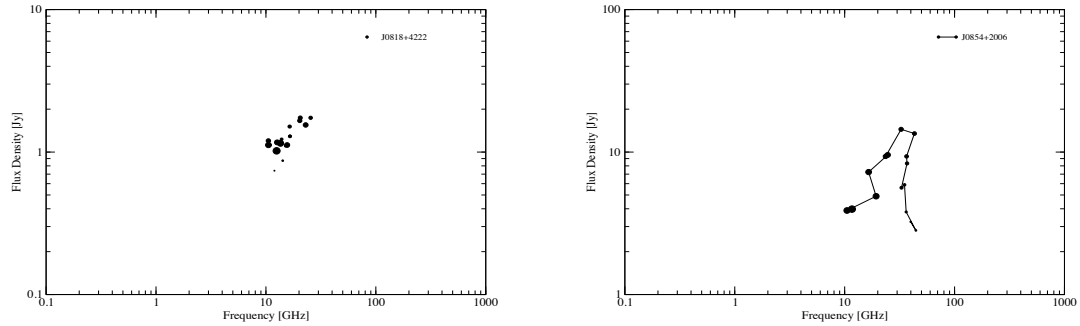

Figure A.37: Evolution of the spectral peak in the $S_{max} - \nu_{max}$ plane. Left panel is J0818+4222, right panel is J0854+2006. The size of symbols represents the time evolution. Time flows forward from smaller to larger symbols.

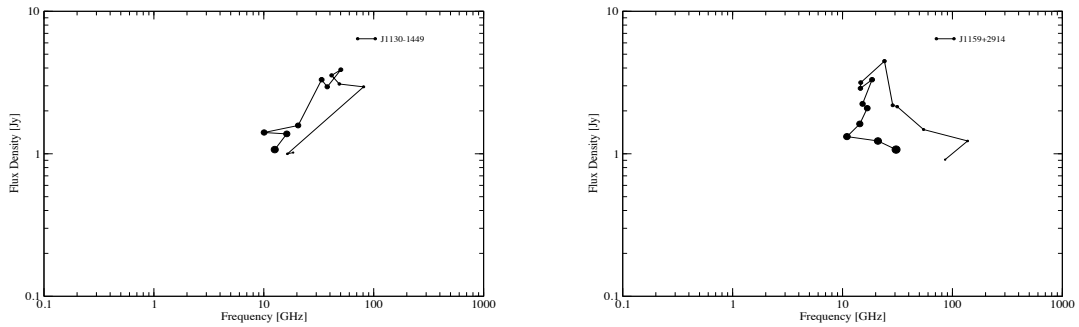

Figure A.38: Evolution of the spectral peak in the $S_{max} - \nu_{max}$ plane. Left panel is J1130-1449, right panel is J1159+2914. The size of symbols represents the time evolution. Time flows forward from smaller to larger symbols.

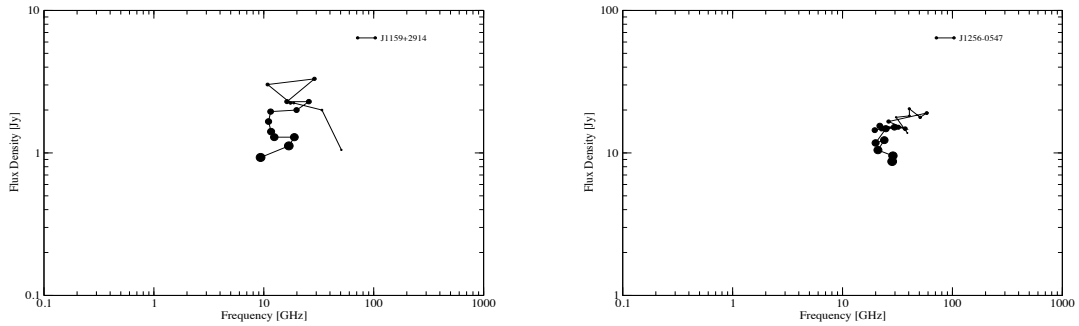

Figure A.39: Evolution of the spectral peak in the $S_{max} - \nu_{max}$ plane. Left panel is J1159+2914, right panel is J1256-0547. The size of symbols represents the time evolution. Time flows forward from smaller to larger symbols.

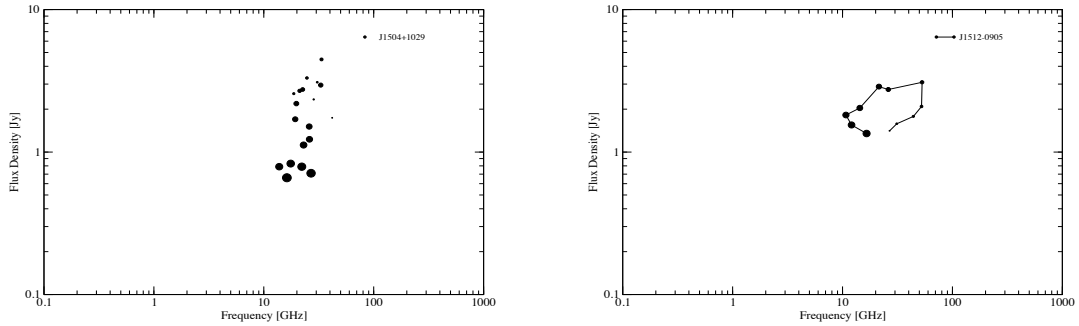

Figure A.40: Evolution of the spectral peak in the $S_{max} - \nu_{max}$ plane. Left panel is J1504+1029, right panel is J1512-0905. The size of symbols represents the time evolution. Time flows forward from smaller to larger symbols.

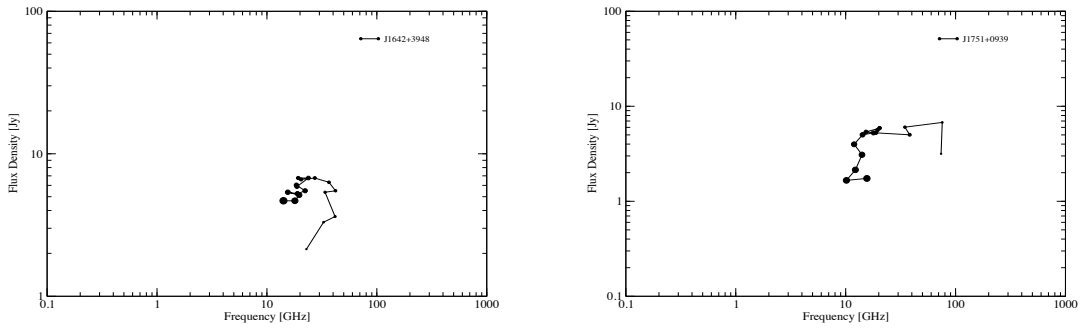

Figure A.41: Evolution of the spectral peak in the $S_{max} - \nu_{max}$ plane. Left panel is J1642+3948, right panel is J1751+0939. The size of symbols represents the time evolution. Time flows forward from smaller to larger symbols.

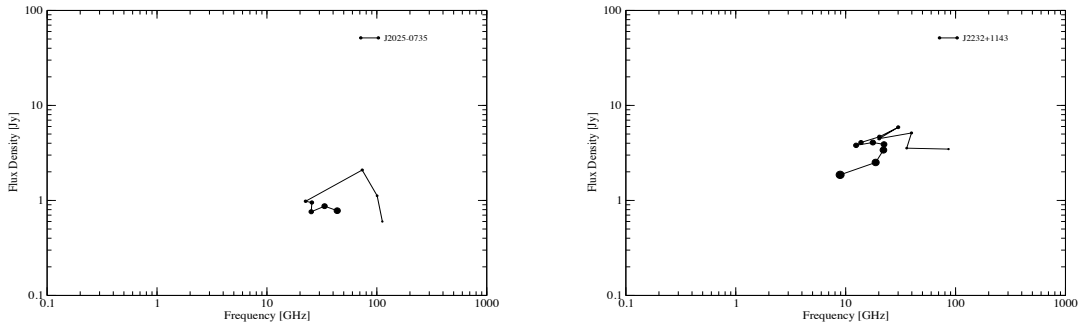

Figure A.42: Evolution of the spectral peak in the $S_{max} - \nu_{max}$ plane. Left panel is J2025-0735, right panel is J2232+1143. The size of symbols represents the time evolution. Time flows forward from smaller to larger symbols.

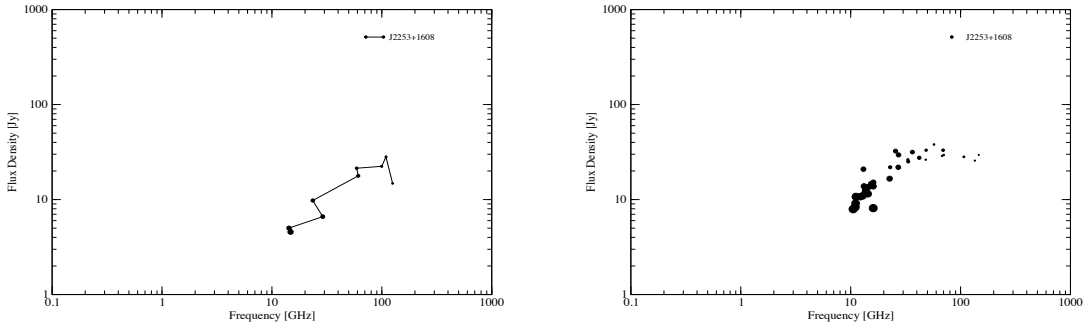

Figure A.43: Evolution of the spectral peak in the $S_{max} - \nu_{max}$ plane. Left and right panel is J2253+1608. The size of symbols represents the time evolution. Time flows forward from smaller to larger symbols.

A.5 Kolmogorov–Smirnov Test

The Kolmogorov—Smirnov test (K–S test) (Smirnov 1948; Press et al. 1992) is a non–parametric test i.e. makes no assumptions about the underlying distribution of data. The test is based on the K–S statistics that measures the supremum (greatest) distance between the empirical distribution function (EDF) of a univariate dataset and the comparison step function of a second dataset or it's cumulative distribution function (CDF). It can be used to compare a sample with a reference probability distribution (1–sample K–S test), or to compare if two underlying one dimensional probability distributions are sampled from the same parent population (2–sample K–S test). In both cases, the underlying population distribution is assumed to be continuous. The tests distribution-free character means that it can give valid probabilities for any underlying distribution of the original and comparison datasets. This is particularly valuable for astronomy, as the mathematical distributions of observed properties of astronomical phenomena are usually unknown. For the purposes of testing if various distributions differ in the current thesis, the 2–sample K–S test is used.

The Kolmogorov–Smirnov statistic is:

$$D_{n,n'} = \sup_x \mid F_{1,n}(x) - F_{2,n'}(x) \mid \tag{A.1}$$

where $F_{1,n}$ and $F_{2,n'}$ are the empirical distribution functions of the first and the second sample respectively and sup is the supremum function. The K–S statistic can be seen graphically in Fig. A.44.

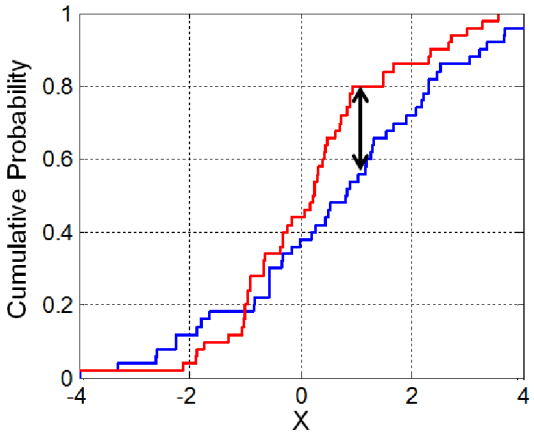

Figure A.44: Red and blue lines each correspond to an empirical distribution function, and the black arrow is the two-sample K–S statistic (image: Wikipedia).

The null and the alternative hypotheses are

- the two tested distributions are sampled from the same parent population
- the two tested distributions are not sampled from the same parent population.

The null hypothesis can be rejected at a "user" chosen significance level of α if the test

statistic $D_{n,n'}$ is greater than the critical value:

$$D_{n,n'} > c(\alpha)\sqrt{\frac{n+n'}{n \cdot n'}} \tag{A.2}$$

The value of $c(\alpha)$ for each level of α is given in Table A.4 (Smirnov 1948; Stephens 1974).

Table A.4: Values of $c(\alpha)$ for each significance level of α.

α	0.10 (90%)	0.05 (95%)	0.025 (97.5%)	0.01 (99%)	0.005 (99.5%)	0.001 (99.9%)
$c(\alpha)$	1.22	1.36	1.48	1.63	1.73	1.95

Throughout the current thesis the P–value is used. In contrast to comparing the K–S statistic with fixed values of α, the P–value is a probability and is calculated based on the $D_{n,n'}$ statistic. It denotes the threshold value of the significance level that the null hypothesis will be accepted for all values of α less than the calculated P–value. For example, if $P = 0.025$, the null hypothesis will be accepted for all significance levels of α less than P such as 0.01 (99%), and rejected at higher levels such as 0.05 and 0.1.

A.6 IDL Software description

The procedures for the reduction of PV data at the MPIFR institute that I developed are described. They were developed in the programming language of IDL, for its speed, ease of use with large tables and numerical accuracy. Bellow a short description is given alongside with the accepted parameters for each procedure.

Final calibration procedure This procedure is the center point of all the data reduction for the Pico Veleta telescope. It takes as input standard Mira files with lists of scans and calculated Gaussian peak values, pointing offsets and other information and performs all the corrections and error analysis described in Sect. 3.1.3. It outputs files with fully corrected values for all the scans and sources in the input along with control files for bad scans, calibration files etc. Bellow is a list with a short description of all the available options that can be called upon running the procedure.

- *source=['***','****','****', ...]*

  Defines the sources to be processed. Accepts an array of strings. If not defined then all the default sources for the monitoring program will be selected (original & revised samples).

- *calb=[***,***,***,***]*

  Defines the calibrations factors for each of the four receivers. Accepts a 4-element array representing the factors. If not defined then all factors are set to unity (1) and then are computed by the available calibrators and only if the /nocal keyword is not set.

- *file=['****','****','****', ...]*

  Defines an array of strings representing the input files to be processed. If it is not defined then all files in the working directory will be processed. Files that are accepted and that are found automatically are of type: "point_*-EDT.dat". The use of willcard characters is also possible and can be supplied like this: file=['*dat']

- *flux=[***,***,***,***,***,***]*

  Defines arbitrary reference flux densities to be used for the calibration of the data. Accepts a maximum of a 6–element array in Jy, with each entry being for the corresponding receiver that is to be reduced. Caution is necessary with this option if in the dataset are more than one calibrators. If a flux density is set to zero then the output of the corresponding frequencies will be '*******' meaning that data existed but no calibration is found and performed on them.

- *wdir=['*******/']*

  Defines the top directory that the output directory structure and files should be written. Accepts also a relative path. If not defined then the current directory is taken as the output directory.

- *dir_bin=['*****/']*

  Defines the directory with all the procedures and functions needed for the proper reduction of IRAM-PV data. If not defined then a default directory is taken. A relative path can also be entered. This default directory is: "/aux/zeall/lfuhrmann/GAMMA-project/IRAM/bin_idl/"

- */nocal*

  If the procedure is called with the /nocal keyword then no sensitivity correction will be performed and the output will be in Kelvins and not in Jy. If /nocal is called at the same time with calb or flux keywords then the last two are ignored. Default is to always perform the sensitivity correction.

- */nopc*

  If the procedure is called with the /nopc keyword, then no pointing correction will be performed. Default is to always perform pointing corrections.

- */nogain*

  If the procedure is called with the /nogain keyword then no gain correction is performed to the data. Default is to always perform gain–Elv corrections.

- */notau*

  If defined then the procedure does not perform a tau correction. Default is to always perform tau correction.

- */emir01* or */emir02*

  If defined then it is assumed that the data are in the standard emir format and contain two polarizations per scan. /emir01 is for 86 and 142 GHz set-up and /emir02 is for 86 and 230 GHz set-up. If not defined then it is assumed that the data are taken with the older ABCD receivers.

- */subscan*

  If defined then it is assumed that the structure of the input files are on the sub–scan level containing all the sub–scans of every scan.

- *gainratio=[**,**,**,**]*

  Defines an array of four numbers that represent the ratio between horizontal and vertical polarizations at 86, 142, 228 and 261 GHz respectively. In order for this to take effect on of the two emir set-ups must be also selected otherwise is ignored. This option corrects for any difference in the gain of the two polarizations. It is assumed that the gain ratio given here is Vertical/Horizontal with a default value for 86 GHz of V/H=1.02

- */nogratio*

  If defined then the default values for the ratio between the two polarizations are set to unity(1). So the effective gain ratio for 86 GHz will be in this case V/H=1.0 This option has effect only in the presence of EMIR data. It is a default option when the BBC backend is selected.

- */kalldir*

  If defined then no questions will be asked if an individual direction of Azi or Elv is found and any occurrence will be kept but with no pointing correction. Only valid when the input files is in the scan level and not in the sub–scan level.

- */skalldir*

  If defined then no questions will be asked if an individual direction of Azi or Elv is found and any occurrence will be skipped and logged in the file "bad_scans.dat". After that the user could flag the corresponding scans in order to re–run and finish the reduction. Only valid for input files that are in the scan level and not in the sub–scan level. */kalldir* and */skalldir* can not be called at the same time.

- */kcalibdir*

  By default if a measurement is from a calibrator (W3OH,K3–50A, MARS, URANUS, NGC 7027) and has only one direction recorded then it is skipped independent of what the user has chosen (y/n/yall/nall /kalldir /skalldir). To keep these measurements but with no pointing corrections set this keyword so the choice is done by what the user has selected.

- */ngc_time*

  If defined then a time depended correction for NGC 7027 calibrator scans is performed. The default is to make no such corrections. Such correction is only valid for 2 mm data currently. The correction applied is of the form $f(x) = \mathrm{a} + \mathrm{b}x$ where $x = \mathrm{JD} - 2439999.5$, $\mathrm{a} = -29.821$ and $\mathrm{b} = 0.0023408$.

- */delepochs*

  If defined then it deletes any epoch directories (Not the multiepoch directory) existing from previous runs. It deletes directories named EP* that they are in the current selected output directory.

- */effcomb*

  If defined then the directory structure in the output directory will be matched to the folder names of Effelsberg Epochs according to the database predefined in the code. If not defined then the folder names will be of type EP–**** according to the date of the observation of the input file.

- */allsource*

If defined then it processes all the available sources of the input files. If specific sources were selected with the "source" keyword then that selection is ignored.

- */no_astro_calib*

  If defined then the reference flux densities of the planets will be calculated with an older Fortran program. If there is already a file with predefined planet flux densities in the output directory then this has no effect. The default is to use the ASTRO program. The use of the default is recommended.

- */nbc* or */bbc*

  If defined then it selects the proper receiver list in each case correspondingly. If not defined then the default backend is "nbc". This is applicable only if one of the two emir set-ups are selected. When the bbc backend is selected then the list is: "reciever_list=[10,11,12,13,6,7]" When the nbc backend is selected then the list is: "reciever_list=[4,5,6,7]"

- *rxs_list=[*,*,*,*,*,*]*

  If defined it selects the receivers to be used. Any receiver can be entered. Max number of rxs accepted is six. The input is selected by a number code. Possible inputs are: 0=B100, 1=C150, 2=B230, 3=C270, 4=E0HL, 5=E0VL, 6=E1HL, 7=E1VL, 8=E2HL, 9=E2VL. For the bbc backend the receivers for the 3 mm band are: 10=E0HL, 11=E0VL, 12=E0HU, 13=E0VU. If not defined then the list of receivers is automatically selected according to other options (EMIR or ABC set-ups and backend combinations) It overrides the options */emir01* and */emir02* and the automatic selection of the parameter *beam_off* and gain ratio.

- *beam_off=[**]*

  It selects a beam offset value to be used when reducing data in the sub–scan level. Usually this value should be 0″but when the data are observed with the double beam technique this value becomes 30″. The selection of this value is done automatically according to the selection of receivers and backends. If a manual selection of receivers is done then the parameter *beam_off* must also be entered.

- *jd_offset=[*]*

  Accepts a floating number that is subtracted from the Julian date in order for example to convert it to MJD (Assuming the input date is JD). It does the operation "final_Date=input_Date - jd_offset". The default is to use a value of *jd_ offset*=2440000.0 to convert JD to (Alex) Julian Date (AJD = JD − 2440000.0). It should be noted that the actual used default is AJD = JD − 2439999.5 because the date of the output files from MIRA is actually JD − 0.5 instead of JD.

- *calibrator=['***','****','****',....]*

Defines the list of calibrators to be processed. Accepts an array of strings. If not defined then all the default calibrators for the IRAM monitoring program will be selected (NGC 7027, W3(OH), K3–50A, MARS and URANUS).

Flagging procedure This procedure edits the output files of MIRA and writes a new file with automatically flagged scans and sub–scans according to the criteria of Sect. 3.1.2. The output file is in the proper format that the final calibration procedure can read and perform the post–measurement corrections. Bellow a short description of the available options is presented.

- */emir_sub*

  If defined then it is assumed that the input file contains data taken with the EMIR receivers and are in the sub–scan level and sets a value of *point_val*=30 in order to compensate for the double beam offset. If not defined then it is assumed that the input files do not have this offset.

- */vlbi*

  If defined then a center frequency of $\sim$ 85 GHz for the E0 band is assumed and not the usual $\sim$ 86 GHz. The default is 86 GHz

- *file=['****','****','****',.....]*

  Defines an array of strings representing the files to be processed. If it is not defined then all files in working directory will be processed and selected automatically. Files that are automatically selected are of type: "point_*-EDT.dat". Also wildcard characters can be entered like this: file=['*dat']

Sub–Flagging procedure This procedure takes as input already flagged files created by the previous described flagging procedure and outputs a script file that can be run in Mira to flag subs–cans before fitting them. The available options are presented bellow.

- *file=['****','****','****',.....]*

  Defines an array of strings representing the files to be processed. If it is not defined then all files in the working directory will be processed and are found automatically. Files that are found is of type: "point_*-EDT.dat". Also wildcard characters can be entered like this: file=['*dat']

- *source=['**','**','**'....]*

  Defines an array of strings that specifies the source names to be processed. If nothing is given then all the available sources in the input file are processed.

- *out=['******']*

  Defines the output file that should be used. Accepts a string name.

- */emir01* or */emir02*

  If defined then it is assumed that the data are in the standard EMIR format and contain two polarizations per scan. */emir01* is for the 86 and 142 GHz set-up and */emir02* is for the 86 and 230 GHz set-up. If not defined then it is assumed that the data are taken with the older ABCD receivers.

- */subscan*

  If defined then the output format in Mira will be set to be in the sub–scan level.

- *mira_dir=['****/']*

  Defines the output directory that will be used in the Granada computer. The final directory with the averaged data after the run of Mira will be " /Mira/****/". The default directory is : "averaged_flagged/".

- */nbc*

  If defined then only scans from the NBC backend are selected.

- */bbc*

  If defined then only scans from the BBC backend are selected.

- */harcopy*

  If defined then Mira will produce postscript files. These files will be in the scan level. The result will be one file per input file.

List of Figures

List of Tables

Bibliography

Abdo, A. A., Ackermann, M., Agudo, I., Ajello, M., Aller, H. D., Aller, M. F., Angelakis, E., Arkharov, A. A., Axelsson, M., Bach, U., and et al. (2010a). The Spectral Energy Distribution of Fermi Bright Blazars. *ApJ*, 716:30–70, 0912.2040.

Abdo, A. A., Ackermann, M., Ajello, M., Allafort, A., Antolini, E., Atwood, W. B., Axelsson, M., Baldini, L., Ballet, J., Barbiellini, G., Bastieri, D., Baughman, B. M., Bechtol, K., Bellazzini, R., Berenji, B., Blandford, R. D., Bloom, E. D., Bogart, J. R., Bonamente, E., Borgland, A. W., Bouvier, A., Bregeon, J., Brez, A., Brigida, M., Bruel, P., Buehler, R., Burnett, T. H., Buson, S., Caliandro, G. A., Cameron, R. A., Cannon, A., Caraveo, P. A., Carrigan, S., Casandjian, J. M., Cavazzuti, E., Cecchi, C., Çelik, Ö., Celotti, A., Charles, E., Chekhtman, A., Chen, A. W., Cheung, C. C., Chiang, J., Ciprini, S., Claus, R., Cohen-Tanugi, J., Conrad, J., Costamante, L., Cotter, G., Cutini, S., D'Elia, V., Dermer, C. D., de Angelis, A., de Palma, F., De Rosa, A., Digel, S. W., Silva, E. d. C. e., Drell, P. S., Dubois, R., Dumora, D., Escande, L., Farnier, C., Favuzzi, C., Fegan, S. J., Ferrara, E. C., Focke, W. B., Fortin, P., Frailis, M., Fukazawa, Y., Funk, S., Fusco, P., Gargano, F., Gasparrini, D., Gehrels, N., Germani, S., Giebels, B., Giglietto, N., Giommi, P., Giordano, F., Giroletti, M., Glanzman, T., Godfrey, G., Grandi, P., Grenier, I. A., Grondin, M.-H., Grove, J. E., Guiriec, S., Hadasch, D., Harding, A. K., Hayashida, M., Hays, E., Healey, S. E., Hill, A. B., Horan, D., Hughes, R. E., Iafrate, G., Itoh, R., Jóhannesson, G., Johnson, A. S., Johnson, R. P., Johnson, T. J., Johnson, W. N., Kamae, T., Katagiri, H., Kataoka, J., Kawai, N., Kerr, M., Knödlseder, J., Kuss, M., Lande, J., Latronico, L., Lavalley, C., Lemoine-Goumard, M., Llena Garde, M., Longo, F., Loparco, F., Lott, B., Lovellette, M. N., Lubrano, P., Madejski, G. M., Makeev, A., Malaguti, G., Massaro, E., Mazziotta, M. N., McConville, W., McEnery, J. E., McGlynn, S., Michelson, P. F., Mitthumsiri, W., Mizuno, T., Moiseev, A. A., Monte, C., Monzani, M. E., Morselli, A., Moskalenko, I. V., Murgia, S., Nolan, P. L., Norris, J. P., Nuss, E., Ohno, M., Ohsugi, T., Omodei, N., Orlando, E., Ormes, J. F., Ozaki, M., Paneque, D., Panetta, J. H., Parent, D., Pelassa, V., Pepe, M., Pesce-Rollins, M., Piranomonte, S., Piron, F., Porter, T. A., Rainò, S., Rando, R., Razzano, M., Reimer, A., Reimer, O., Reposeur, T., Ripken, J., Ritz, S., Rodriguez, A. Y., Romani, R. W., Roth, M., Ryde, F., Sadrozinski, H. F.-W., Sanchez, D., Sander, A., Saz Parkinson, P. M., Scargle, J. D., Sgrò, C., Shaw, M. S., Siskind, E. J., Smith, P. D., Spandre, G., Spinelli, P., Starck, J.-L., Stawarz, Ł., Strickman, M. S., Suson, D. J., Tajima, H., Takahashi, H., Takahashi, T., Tanaka, T., Taylor, G. B., Thayer, J. B., Thayer, J. G., Thompson, D. J., Tibaldo, L., Torres, D. F., Tosti, G., Tramacere, A., Ubertini, P., Uchiyama, Y., Usher,

T. L., Vasileiou, V., Vilchez, N., Villata, M., Vitale, V., Waite, A. P., Wallace, E., Wang, P., Winer, B. L., Wood, K. S., Yang, Z., Ylinen, T., and Ziegler, M. (2010b). The First Catalog of Active Galactic Nuclei Detected by the Fermi Large Area Telescope. *ApJ*, 715:429–457, 1002.0150.

Abdo, A. A., Ackermann, M., Ajello, M., Allafort, A., Baldini, L., Ballet, J., Barbiellini, G., Baring, M. G., Bastieri, D., Bechtol, K., and et al. (2011a). Insights into the High-energy γ-ray Emission of Markarian 501 from Extensive Multifrequency Observations in the Fermi Era. *ApJ*, 727:129–+.

Abdo, A. A., Ackermann, M., Ajello, M., Antolini, E., Baldini, L., Ballet, J., Barbiellini, G., Baring, M. G., Bastieri, D., Bechtol, K., Bellazzini, R., Berenji, B., Blandford, R. D., Bloom, E. D., Bonamente, E., Borgland, A. W., Bregeon, J., Brez, A., Brigida, M., Bruel, P., Buehler, R., Buson, S., Caliandro, G. A., Cameron, R. A., Carrigan, S., Casandjian, J. M., Cavazzuti, E., Cecchi, C., Çelik, Ö., Chekhtman, A., Chen, A. W., Chiang, J., Ciprini, S., Claus, R., Cohen-Tanugi, J., Colafrancesco, S., Conrad, J., Cutini, S., Dermer, C. D., de Palma, F., Digel, S. W., Silva, E. d. C. e., Drell, P. S., Dubois, R., Dumora, D., Farnier, C., Favuzzi, C., Fegan, S. J., Ferrara, E. C., Focke, W. B., Frailis, M., Fukazawa, Y., Fusco, P., Gargano, F., Gasparrini, D., Gehrels, N., Giebels, B., Giglietto, N., Giommi, P., Giordano, F., Giroletti, M., Glanzman, T., Godfrey, G., Grandi, P., Grenier, I. A., Guillemot, L., Guiriec, S., Hadasch, D., Harding, A. K., Hayashida, M., Horan, D., Hughes, R. E., Itoh, R., Jackson, M. S., Jóhannesson, G., Johnson, A. S., Johnson, W. N., Kamae, T., Katagiri, H., Kataoka, J., Kawai, N., Knödlseder, J., Kuss, M., Lande, J., Latronico, L., Longo, F., Loparco, F., Lott, B., Lovellette, M. N., Lubrano, P., Madejski, G. M., Makeev, A., Mazziotta, M. N., McEnery, J. E., McGlynn, S., Meurer, C., Michelson, P. F., Mitthumsiri, W., Mizuno, T., Monte, C., Monzani, M. E., Morselli, A., Moskalenko, I. V., Murgia, S., Nestoras, I., Nolan, P. L., Norris, J. P., Nuss, E., Ohsugi, T., Okumura, A., Orlando, E., Ormes, J. F., Ozaki, M., Paneque, D., Panetta, J. H., Parent, D., Pelassa, V., Pepe, M., Pesce-Rollins, M., Piron, F., Porter, T. A., Rainò, S., Rando, R., Razzano, M., Reimer, A., Reimer, O., Reyes, L. C., Rodriguez, A. Y., Roth, M., Ryde, F., Sadrozinski, H. F.-W., Sambruna, R., Sander, A., Sato, R., Sgrò, C., Shaw, M. S., Siskind, E. J., Smith, P. D., Spandre, G., Spinelli, P., Stawarz, Ł., Stecker, F. W., Strickman, M. S., Suson, D. J., Takahashi, H., Takahashi, T., Tanaka, T., Thayer, J. B., Thayer, J. G., Thompson, D. J., Tibolla, O., Torres, D. F., Tosti, G., Tramacere, A., Uchiyama, Y., Usher, T. L., Vasileiou, V., Vilchez, N., Villata, M., Vitale, V., von Kienlin, A., Waite, A. P., Wang, P., Winer, B. L., Wood, K. S., Yang, Z., Ylinen, T., Ziegler, M., Tavecchio, F., Sikora, M., Schady, P., Roming, P., Chester, M. M., and Maraschi, L. (2010c). Suzaku Observations of Luminous Quasars: Revealing the Nature of High-energy Blazar Emission in Low-level Activity States. *ApJ*, 716:835–849.

Abdo, A. A., Ackermann, M., Ajello, M., Atwood, W. B., Axelsson, M., Baldini, L., Ballet, J., Band, D. L., Barbiellini, G., Bastieri, D., and et al. (2009a). Fermi/Large Area Telescope Bright Gamma-Ray Source List. *ApJS*, 183:46–66, 0902.1340.

Abdo, A. A., Ackermann, M., Ajello, M., Atwood, W. B., Axelsson, M., Baldini, L., Ballet, J., Barbiellini, G., Bastieri, D., Baughman, B. M., Bechtol, K., Bellazzini, R., Blandford, R. D., Bloom, E. D., Bonamente, E., Borgland, A. W., Bouvier, A., Bregeon, J., Brez, A., Brigida, M., Bruel, P., Burnett, T. H., Caliandro, G. A., Cameron, R. A., Caraveo, P. A., Casandjian, J. M., Cavazzuti, E., Cecchi, C., Charles, E., Chekhtman, A., Chen, A. W., Cheung, C. C., Chiang, J., Ciprini, S., Claus, R., Cohen-Tanugi, J., Colafrancesco, S., Collmar, W., Cominsky, L. R., Conrad, J., Costamante, L., Cutini, S., Dermer, C. D., de Angelis, A., de Palma, F., Digel, S. W., do Couto e Silva, E., Drell, P. S., Dubois, R., Dumora, D., Farnier, C., Favuzzi, C., Fegan, S. J., Ferrara, E. C., Finke, J., Focke, W. B., Foschini, L., Frailis, M., Fuhrmann, L., Fukazawa, Y., Funk, S., Fusco, P., Gargano, F., Gasparrini, D., Gehrels, N., Germani, S., Giebels, B., Giglietto, N., Giommi, P., Giordano, F., Giroletti, M., Glanzman, T., Godfrey, G., Grenier, I. A., Grondin, M.-H., Grove, J. E., Guillemot, L., Guiriec, S., Hanabata, Y., Harding, A. K., Hartman, R. C., Hayashida, M., Hays, E., Healey, S. E., Horan, D., Hughes, R. E., Jóhannesson, G., Johnson, A. S., Johnson, R. P., Johnson, T. J., Johnson, W. N., Kadler, M., Kamae, T., Katagiri, H., Kataoka, J., Kerr, M., Knödlseder, J., Kocian, M. L., Kuehn, F., Kuss, M., Lande, J., Latronico, L., Lemoine-Goumard, M., Longo, F., Loparco, F., Lott, B., Lovellette, M. N., Lubrano, P., Madejski, G. M., Makeev, A., Massaro, E., Mazziotta, M. N., McConville, W., McEnery, J. E., McGlynn, S., Meurer, C., Michelson, P. F., Mitthumsiri, W., Mizuno, T., Moiseev, A. A., Monte, C., Monzani, M. E., Moretti, E., Morselli, A., Moskalenko, I. V., Murgia, S., Nolan, P. L., Norris, J. P., Nuss, E., Ohsugi, T., Omodei, N., Orlando, E., Ormes, J. F., Ozaki, M., Paneque, D., Panetta, J. H., Parent, D., Pelassa, V., Pepe, M., Pesce-Rollins, M., Piron, F., Porter, T. A., Rainò, S., Rando, R., Razzano, M., Razzaque, S., Reimer, A., Reimer, O., Reposeur, T., Reyes, L. C., Ritz, S., Rochester, L. S., Rodriguez, A. Y., Romani, R. W., Ryde, F., Sadrozinski, H. F.-W., Sanchez, D., Sander, A., Saz Parkinson, P. M., Scargle, J. D., Schalk, T. L., Sellerholm, A., Sgrò, C., Shaw, M. S., Smith, D. A., Smith, P. D., Spandre, G., Spinelli, P., Starck, J.-L., Strickman, M. S., Suson, D. J., Tajima, H., Takahashi, H., Takahashi, T., Tanaka, T., Taylor, G. B., Thayer, J. B., Thayer, J. G., Thompson, D. J., Tibaldo, L., Torres, D. F., Tosti, G., Tramacere, A., Uchiyama, Y., Usher, T. L., Vilchez, N., Villata, M., Vitale, V., Waite, A. P., Winer, B. L., Wood, K. S., Ylinen, T., and Ziegler, M. (2009b). Bright Active Galactic Nuclei Source List from the First Three Months of the Fermi Large Area Telescope All-Sky Survey. *ApJ*, 700:597–622, 0902.1559.

Abdo, A. A., Ackermann, M., Ajello, M., Atwood, W. B., Baldini, L., Ballet, J., Barbiellini, G., Bastieri, D., Bechtol, K., Bellazzini, R., and et al. (2010d). Gamma-Ray Emission Concurrent with the Nova in the Symbiotic Binary V407 Cygni. *Science*, 329:817–821, 1008.3912.

Abdo, A. A., Ackermann, M., Ajello, M., Axelsson, M., Baldini, L., Ballet, J., Barbiellini, G., Bastieri, D., Baughman, B. M., Bechtol, K., and et al. (2009c). Multiwavelength Monitoring of the Enigmatic Narrow-Line Seyfert 1 PMN J0948+0022 in 2009 March-July. *ApJ*, 707:727–737, 0910.4540.

Abdo, A. A., Ackermann, M., Ajello, M., Axelsson, M., Baldini, L., Ballet, J., Barbiellini, G., Bastieri, D., Baughman, B. M., Bechtol, K., and et al. (2010e). A change in the optical polarization associated with a γ-ray flare in the blazar 3C279. *Nature*, 463:919–923, 1004.3828.

Abdo, A. A., Ackermann, M., Ajello, M., Baldini, L., Ballet, J., Barbiellini, G., Bastieri, D., Bechtol, K., Bellazzini, R., Berenji, B., Blandford, R. D., Bloom, E. D., Bonamente, E., Borgland, A. W., Bouvier, A., Brandt, T. J., Bregeon, J., Brez, A., Brigida, M., Bruel, P., Buehler, R., Burnett, T. H., Buson, S., Caliandro, G. A., Cameron, R. A., Cannon, A., Caraveo, P. A., Carrigan, S., Casandjian, J. M., Cavazzuti, E., Cecchi, C., Çelik, Ö., Celotti, A., Charles, E., Chekhtman, A., Chen, A. W., Cheung, C. C., Chiang, J., Ciprini, S., Claus, R., Cohen-Tanugi, J., Colafrancesco, S., Conrad, J., Davis, D. S., Dermer, C. D., de Angelis, A., de Palma, F., Silva, E. d. C. e., Drell, P. S., Dubois, R., Favuzzi, C., Fegan, S. J., Ferrara, E. C., Fortin, P., Frailis, M., Fukazawa, Y., Fusco, P., Gargano, F., Gasparrini, D., Gehrels, N., Germani, S., Giglietto, N., Giommi, P., Giordano, F., Giroletti, M., Glanzman, T., Godfrey, G., Grandi, P., Grenier, I. A., Grove, J. E., Guillemot, L., Guiriec, S., Hadasch, D., Hayashida, M., Hays, E., Horan, D., Hughes, R. E., Jackson, M. S., Jóhannesson, G., Johnson, A. S., Johnson, W. N., Kamae, T., Katagiri, H., Kataoka, J., Knödlseder, J., Kuss, M., Lande, J., Latronico, L., Lee, S.-H., Lemoine-Goumard, M., Llena Garde, M., Longo, F., Loparco, F., Lott, B., Lovellette, M. N., Lubrano, P., Madejski, G. M., Makeev, A., Malaguti, G., Mazziotta, M. N., McConville, W., McEnery, J. E., Michelson, P. F., Migliori, G., Mitthumsiri, W., Mizuno, T., Monte, C., Monzani, M. E., Morselli, A., Moskalenko, I. V., Murgia, S., Naumann-Godo, M., Nestoras, I., Nolan, P. L., Norris, J. P., Nuss, E., Ohsugi, T., Okumura, A., Omodei, N., Orlando, E., Ormes, J. F., Paneque, D., Panetta, J. H., Parent, D., Pelassa, V., Pepe, M., Persic, M., Pesce-Rollins, M., Piron, F., Porter, T. A., Rainò, S., Rando, R., Razzano, M., Razzaque, S., Reimer, A., Reimer, O., Reyes, L. C., Roth, M., Sadrozinski, H. F.-W., Sanchez, D., Sander, A., Scargle, J. D., Sgrò, C., Siskind, E. J., Smith, P. D., Spandre, G., Spinelli, P., Stawarz, Ł., Stecker, F. W., Strickman, M. S., Suson, D. J., Takahashi, H., Tanaka, T., Thayer, J. B., Thayer, J. G., Thompson, D. J., Tibaldo, L., Torres, D. F., Torresi, E., Tosti, G., Tramacere, A., Uchiyama, Y., Usher, T. L., Vandenbroucke, J., Vasileiou, V., Vilchez, N., Villata, M., Vitale, V., Waite, A. P., Wang, P., Winer, B. L., Wood, K. S., Yang, Z., Ylinen, T., and Ziegler, M. (2010f). Fermi Large Area Telescope Observations of Misaligned Active Galactic Nuclei. *ApJ*, 720:912–922.

Abdo, A. A., Ackermann, M., Ajello, M., Baldini, L., Ballet, J., Barbiellini, G., Bastieri, D., Bechtol, K., Bellazzini, R., Berenji, B., and et al. (2011b). Erratum: "Multi-wavelength Observations of the Flaring Gamma-ray Blazar 3C 66A in 2008 October". *ApJ*, 731:77.

Abdo, A. A., Ackermann, M., Ajello, M., Baldini, L., Ballet, J., Barbiellini, G., Bastieri, D., Bechtol, K., Bellazzini, R., Berenji, B., and et al. (2011c). Fermi Large Area Telescope Observations of Markarian 421: The Missing Piece of its Spectral Energy Distribution. *ApJ*, 736:131, 1106.1348.

Abdo, A. A., Ackermann, M., Ajello, M., Baldini, L., Ballet, J., Barbiellini, G., Bastieri, D., Bechtol, K., Bellazzini, R., Berenji, B., and et al. (2011d). Multi-wavelength Observations of the Flaring Gamma-ray Blazar 3C 66A in 2008 October. *ApJ*, 726:43–+.

Ackermann, M., Ajello, M., Allafort, A., Antolini, E., Atwood, W. B., Axelsson, M., Baldini, L., Ballet, J., Barbiellini, G., Bastieri, D., Bechtol, K., Bellazzini, R., Berenji, B., Blandford, R. D., Bloom, E. D., Bonamente, E., Borgland, A. W., Bottacini, E., Bouvier, A., Bregeon, J., Brigida, M., Bruel, P., Buehler, R., Burnett, T. H., Buson, S., Caliandro, G. A., Cameron, R. A., Caraveo, P. A., Casandjian, J. M., Cavazzuti, E., Cecchi, C., Charles, E., Cheung, C. C., Chiang, J., Ciprini, S., Claus, R., Cohen-Tanugi, J., Conrad, J., Costamante, L., Cutini, S., de Angelis, A., de Palma, F., Dermer, C. D., Digel, S. W., Silva, E. d. C. e., Drell, P. S., Dubois, R., Escande, L., Favuzzi, C., Fegan, S. J., Ferrara, E. C., Finke, J., Focke, W. B., Fortin, P., Frailis, M., Fukazawa, Y., Funk, S., Fusco, P., Gargano, F., Gasparrini, D., Gehrels, N., Germani, S., Giebels, B., Giglietto, N., Giommi, P., Giordano, F., Giroletti, M., Glanzman, T., Godfrey, G., Grenier, I. A., Grove, J. E., Guiriec, S., Gustafsson, M., Hadasch, D., Hayashida, M., Hays, E., Healey, S. E., Horan, D., Hou, X., Hughes, R. E., Iafrate, G., Jóhannesson, G., Johnson, A. S., Johnson, W. N., Kamae, T., Katagiri, H., Kataoka, J., Knödlseder, J., Kuss, M., Lande, J., Larsson, S., Latronico, L., Longo, F., Loparco, F., Lott, B., Lovellette, M. N., Lubrano, P., Madejski, G. M., Mazziotta, M. N., McConville, W., McEnery, J. E., Michelson, P. F., Mitthumsiri, W., Mizuno, T., Moiseev, A. A., Monte, C., Monzani, M. E., Moretti, E., Morselli, A., Moskalenko, I. V., Murgia, S., Nakamori, T., Naumann-Godo, M., Nolan, P. L., Norris, J. P., Nuss, E., Ohno, M., Ohsugi, T., Okumura, A., Omodei, N., Orienti, M., Orlando, E., Ormes, J. F., Ozaki, M., Paneque, D., Parent, D., Pesce-Rollins, M., Pierbattista, M., Piranomonte, S., Piron, F., Pivato, G., Porter, T. A., Rainò, S., Rando, R., Razzano, M., Razzaque, S., Reimer, A., Reimer, O., Ritz, S., Rochester, L. S., Romani, R. W., Roth, M., Sanchez, D. A., Sbarra, C., Scargle, J. D., Schalk, T. L., Sgrò, C., Shaw, M. S., Siskind, E. J., Spandre, G., Spinelli, P., Strong, A. W., Suson, D. J., Tajima, H., Takahashi, H., Takahashi, T., Tanaka, T., Thayer, J. G., Thayer, J. B., Thompson, D. J., Tibaldo, L., Tinivella, M., Torres, D. F., Tosti, G., Troja, E., Uchiyama, Y., Vandenbroucke, J., Vasileiou, V., Vianello, G., Vitale, V., Waite, A. P., Wallace, E., Wang, P., Winer, B. L., Wood, D. L., Wood, K. S., and Zimmer, S. (2011). The Second Catalog of Active Galactic Nuclei Detected by the Fermi Large Area Telescope. *ApJ*, 743:171, 1108.1420.

Ackermann, M., Ajello, M., Ballet, J., Barbiellini, G., Bastieri, D., Bellazzini, R., Blandford, R. D., Bloom, E. D., Bonamente, E., Borgland, A. W., and et al. (2012). Multi-wavelength Observations of Blazar AO 0235+164 in the 2008-2009 Flaring State. *ApJ*, 751:159, 1207.2932.

Agudo, I., Marscher, A. P., Jorstad, S. G., Gómez, J. L., Perucho, M., Piner, B. G., Rioja, M., and Dodson, R. (2012). Erratic Jet Wobbling in the BL Lacertae Object OJ287 Revealed by Sixteen Years of 7 mm VLBA Observations. *ApJ*, 747:63, 1112.4747.

Aleksić, J., Ansoldi, S., Antonelli, L. A., Antoranz, P., Babic, A., Bangale, P., Barres de Almeida, U., Barrio, J. A., Becerra González, J., Bednarek, W., and et al. (2014). MAGIC gamma-ray and multi-frequency observations of flat spectrum radio quasar PKS 1510-089 in early 2012. *A&A*, 569:A46, 1401.5646.

Aleksić, J., Antonelli, L. A., Antoranz, P., Asensio, M., Backes, M., Barres de Almeida, U., Barrio, J. A., Bednarek, W., Berger, K., Bernardini, E., Biland, A., Blanch, O., Bock, R. K., Boller, A., Bonnefoy, S., Bonnoli, G., Borla Tridon, D., Bretz, T., Carmona, E., Carosi, A., Carreto Fidalgo, D., Colin, P., Colombo, E., Contreras, J. L., Cortina, J., Cossio, L., Covino, S., Da Vela, P., Dazzi, F., De Angelis, A., De Caneva, G., De Lotto, B., Delgado Mendez, C., Doert, M., Domínguez, A., Dominis Prester, D., Dorner, D., Doro, M., Eisenacher, D., Elsaesser, D., Ferenc, D., Fonseca, M. V., Font, L., Fruck, C., García López, R. J., Garczarczyk, M., Garrido Terrats, D., Gaug, M., Giavitto, G., Godinović, N., González Muñoz, A., Gozzini, S. R., Hadamek, A., Hadasch, D., Herrero, A., Hose, J., Hrupec, D., Jankowski, F., Kadenius, V., Klepser, S., Knoetig, M. L., Krähenbühl, T., Krause, J., Kushida, J., La Barbera, A., Lelas, D., Leonardo, E., Lewandowska, N., Lindfors, E., Lombardi, S., López, M., López-Coto, R., López-Oramas, A., Lorenz, E., Lozano, I., Makariev, M., Mallot, K., Maneva, G., Mankuzhiyil, N., Mannheim, K., Maraschi, L., Marcote, B., Mariotti, M., Martínez, M., Masbou, J., Mazin, D., Meucci, M., Miranda, J. M., Mirzoyan, R., Moldón, J., Moralejo, A., Munar-Adrover, P., Nakajima, D., Niedzwiecki, A., Nieto, D., Nilsson, K., Nowak, N., Orito, R., Paiano, S., Palatiello, M., Paneque, D., Paoletti, R., Paredes, J. M., Partini, S., Persic, M., Pilia, M., Prada, F., Prada Moroni, P. G., Prandini, E., Puljak, I., Reichardt, I., Reinthal, R., Rhode, W., Ribó, M., Rico, J., Rügamer, S., Saggion, A., Saito, K., Saito, T. Y., Salvati, M., Satalecka, K., Scalzotto, V., Scapin, V., Schultz, C., Schweizer, T., Shore, S. N., Sillanpää, A., Sitarek, J., Snidaric, I., Sobczynska, D., Spanier, F., Spiro, S., Stamatescu, V., Stamerra, A., Steinke, B., Storz, J., Sun, S., Surić, T., Takalo, L., Takami, H., Tavecchio, F., Temnikov, P., Terzić, T., Tescaro, D., Teshima, M., Tibolla, O., Torres, D. F., Toyama, T., Treves, A., Uellenbeck, M., Vogler, P., Wagner, R. M., Weitzel, Q., Zandanel, F., Zanin, R., MAGIC Collaboration, Longo, F., Lucarelli, F., Pittori, C., Vercellone, S., AGILE Team, Bastieri, D., Sbarra, C., Fermi-LAT Collaboration, Angelakis, E., Fuhrmann, L., Nestoras, I., Krichbaum, T. P., Sievers, A., Zensus, J. A., F-GAMMA program, Antonyuk, K. A., Baumgartner, W., Berduygin, A., Carini, M., Cook, K., Gehrels, N., Kadler, M., Kovalev, Y. A., Kovalev, Y. Y., Krauss, F., Krimm, H. A., Lähteenmäki, A., Lister, M. L., Max-Moerbeck, W., Pasanen, M., Pushkarev, A. B., Readhead, A. C. S., Richards, J. L., Sainio, J., Shakhovskoy, D. N., Sokolovsky, K. V., Tornikoski, M., Tueller, J., Weidinger, M., and Wilms, J. (2013). The simultaneous low state spectral energy distribution of 1ES 2344+514 from radio to very high energies. *A&A*, 556:A67, 1211.2608.

Angelakis, E., Angelakis, E., Fuhrmann, L., Zensus, J. A., Nestoras, I., Marchili, N., Krichbaum, T. P., Ungerechts, H., Max-Moerbeck, W., Pavlidou, V., Pearson, T. J., Readhead, A. C. S., Richards, J. L., and Stevenson, M. A. (2010a). AGN Astrophysics via Multi-Frequency Monitoring of γ-ray Blazars in the Fermi-GST Era. In L. Maraschi, G. Ghis-

ellini, R. Della Ceca, & F. Tavecchio, editor, *Accretion and Ejection in AGN: a Global View*, volume 427 of *Astronomical Society of the Pacific Conference Series*, pages 289–+. 0910.0643.

Angelakis, E., Fuhrmann, L., Nestoras, I., Fromm, C. M., Perucho-Pla, M., Schmidt, R., Zensus, J. A., Marchili, N., Krichbaum, T. P., Ungerechts, H., Sievers, A., Riquelme, D., and Pavlidou, V. (2012a). F-GAMMA: On the phenomenological classification of continuum radio spectra variability patterns of Fermi blazars. *Journal of Physics Conference Series*, 372(1):012007, 1202.4242.

Angelakis, E., Fuhrmann, L., Nestoras, I., Fromm, C. M., Schmidt, R., Zensus, J. A., Marchili, N., Krichbaum, T. P., Perucho, M., Ungerechts, H., Sievers, A., Riquelme, D., and Foschini, L. (2012b). Unification and physical interpretation of the radio spectra variability patterns in Fermi blazars and jet emission from NLSy1s. *ArXiv e-prints*, 1205.1961.

Angelakis, E., Fuhrmann, L., Nestoras, I., Fromm, C. M., Schmidt, R., Zensus, J. A., Marchili, N., Krichbaum, T. P., Perucho-Pla, M., Ungerechts, H., Sievers, A., and Riquelme, D. (2011a). On the phenomenological classification of continuum radio spectra variability patterns of Fermi blazars. *ArXiv e-prints*, 1111.6992.

Angelakis, E., Fuhrmann, L., Nestoras, I., Schmidt, R., Zensus, J. A., Krichbaum, T. P., Ungerechts, H., Sievers, A., and Riquelme, D. (2011b). Broad-band radio behaviour of flaring BL Lac (J2202+4216). *The Astronomer's Telegram*, 3380:1.

Angelakis, E., Fuhrmann, L., Nestoras, I., Schmidt, R., Zensus, J. A., Krichbaum, T. P., Ungerechts, H., Sievers, A., and Riquelme, D. (2011c). Broad-band radio behaviour of flaring blazar 4C+38.41. *The Astronomer's Telegram*, 3360:1.

Angelakis, E., Fuhrmann, L., Nestoras, I., Schmidt, R., Zensus, J. A., Krichbaum, T. P., Ungerechts, H., Sievers, A., and Riquelme, D. (2011d). Millimeter radio event emerging in the gamma-ray flaring blazar PKS 0528+134. *The Astronomer's Telegram*, 3422:1.

Angelakis, E., Fuhrmann, L., Nestoras, I., Zensus, J. A., Marchili, N., Pavlidou, V., and Krichbaum, T. P. (2010b). The F-GAMMA program: multi-wavelength AGN studies in the Fermi-GST era. *ArXiv e-prints*, 1006.5610.

Angelakis, E., Fuhrmann, L., Marchili, N., Foschini, L., Myserlis, I., Karamanavis, V., Komossa, S., Blinov, D., Krichbaum, T. P., Sievers, A., Ungerechts, H., and Zensus, J. A. (2015). Radio jet emission from GeV-emitting narrow-line Seyfert 1 galaxies. *A&A*, 575:A55, 1501.02158.

Angelakis, E., Fuhrmann, L., and Myserlis, I. (2013). Properties of the radio jet emission of four gamma-ray Narrow Line Seyfert 1 galaxies. In *11th Hellenic Astronomical Conference*, pages 34–34. 1304.1706.

Angelakis, E., Fuhrmann, L., Myserlis, I., Nestoras, I., Karamanavis, V., Krichbaum, T. P., Zensus, A. J., Marchili, N., Foschini, L., Ungerechts, H., and Sievers, A. (2012c). Properties of the radio jet emission of gamma-ray Narrow Line Seyfert 1s. In *Proceedings of Nuclei of Seyfert galaxies and QSOs - Central engine conditions of star formation (Seyfert 2012). 6-8 November, 2012. Max-Planck-Insitut für Radioastronomie (MPIfR), Bonn, Germany. Online at, id.58*, page 58.

Angelakis, E., Kraus, A., Readhead, A. C. S., Zensus, J. A., Bustos, R., Krichbaum, T. P., Witzel, A., and Pearson, T. J. (2009). Multi-frequency measurements of the NVSS foreground sources in the cosmic background imager fields. I. Data release. *A&A*, 501:801–812, 0905.2660.

Atwood, W. B., Abdo, A. A., Ackermann, M., Althouse, W., Anderson, B., Axelsson, M., Baldini, L., Ballet, J., Band, D. L., Barbiellini, G., and et al. (2009). The Large Area Telescope on the Fermi Gamma-Ray Space Telescope Mission. *ApJ*, 697:1071–1102, 0902.1089.

Baars, J. W. M., Genzel, R., Pauliny-Toth, I. I. K., and Witzel, A. (1977). The absolute spectrum of CAS A - an accurate flux density scale and a set of secondary calibrators. *A&A*, 61:99–106.

Baars, J. W. M., Hooghoudt, B. G., Mezger, P. G., and de Jonge, M. J. (1987). The IRAM 30-m millimeter radio telescope on Pico Veleta, Spain. *A&A*, 175:319–326.

Backes, M., Uellenbeck, M., Hayashida, M., Satalecka, K., Tescaro, D., Terzić, T., MAGIC Collaboration, Fuhrmann, L., Nestoras, I., F-GAMMA project, Lähteenmäki, A., Tornikoski, M., Nieppola, E., Metsähovi, Böttcher, M., Collmar, W., and Weidinger, M. (2012). Long-term spectral and temporal behavior of the high-frequency peaked BL LAC object 1ES 1959+650. In Aharonian, F. A., Hofmann, W., and Rieger, F. M., editors, *American Institute of Physics Conference Series*, volume 1505 of *American Institute of Physics Conference Series*, pages 522–525.

Beckmann, V. and Shrader, C. R. (2013). The AGN phenomenon: open issues. *ArXiv e-prints*, 1302.1397.

Begelman, M. C., Blandford, R. D., and Rees, M. J. (1980). Massive black hole binaries in active galactic nuclei. *Nature*, 287:307–309.

Beuchert, T., Kadler, M., Wilms, J., Angelakis, E., Fuhrmann, L., Myserlis, I., Nestoras, I., Kraus, A., Bach, U., Ros, E., Grossberger, C., and Schulz, R. (2013). Single-Dish Radio Polarimetry in the F-GAMMA Program with the Effelsberg 100-m Radio Telescope. In *European Physical Journal Web of Conferences*, volume 61 of *European Physical Journal Web of Conferences*, page 6006.

Bevington, P. R. and Robinson, D. K. (1992). *Data reduction and error analysis for the physical sciences*.

Blandford, R. D. and Königl, A. (1979). Relativistic jets as compact radio sources. *ApJ*, 232:34–48.

Blandford, R. D., McKee, C. F., and Rees, M. J. (1977). Super-luminal expansion in extra-galactic radio sources. *Nature*, 267:211–216.

Błażejowski, M., Sikora, M., Moderski, R., and Madejski, G. M. (2000). Comptonization of Infrared Radiation from Hot Dust by Relativistic Jets in Quasars. *ApJ*, 545:107–116, arXiv:astro-ph/0008154.

Nestoras, I., Fuhrmann, L., Angelakis, E., Schmidt, R., Krichbaum, T. P., Zensus, J. A., Ungerechts, H., Sievers, A., and Riquelme, D. (2011a). Broad band radio outburst of gamma-ray flaring blazar 4C+28.07. *The Astronomer's Telegram*, 3674:1.

Nestoras, I., Fuhrmann, L., Angelakis, E., Schmidt, R., Krichbaum, T. P., Zensus, J. A., Ungerechts, H., Sievers, A., and Riquelme, D. (2011b). Record cm/mm-band radio flux levels of the gamma-ray flaring blazar PKS 1510-089. *The Astronomer's Telegram*, 3698:1.

Nestoras, I., Fuhrmann, L., Bach, U., Sokolovsky, K., Ungerechts, H., Riquelme, D., Sievers, A., Richards, J. L., Max-Moerbeck, W., Pearson, T. J., Readhead, A. C. S., and F-Gamma Team (2010). Radio detection of V407 Cyg - the possible counterpart of the new Fermi LAT Gamma-ray Transient J2102+4542 with the Effelsberg 100-m, OVRO 40-m and IRAM 30-m telescopes. *The Astronomer's Telegram*, 2506:1–+.

Nestoras, J. S., Mislis, D., Pyrzas, S., Tremou, E., Seiradakis, J. H., and Avgoloupis, S. I. (2006a). Seeing Measurements from Mt. Holomon. In Solomos, N., editor, *Recent Advances in Astronomy and Astrophysics*, volume 848 of *American Institute of Physics Conference Series*, pages 906–909.

Nestoras, J. S., Seiradakis, J. H., Harlaftis, E., Giannakis, O., and Kitsionas, S. (2006b). Fourier Analysis of SS433 - High Speed Photometry. In Solomos, N., editor, *Recent Advances in Astronomy and Astrophysics*, volume 848 of *American Institute of Physics Conference Series*, pages 427–431.

Böttcher, M. (2007). Broad-band Spectral Properties of Blazars. In Ho, L. C. and Wang, J.-W., editors, *The Central Engine of Active Galactic Nuclei*, volume 373 of *Astronomical Society of the Pacific Conference Series*, page 169.

Camenzind, M. and Krockenberger, M. (1992). The lighthouse effect of relativistic jets in blazars - A geometric origin of intraday variability. *A&A*, 255:59–62.

Carter, M., Lazareff, B., Maier, D., Chenu, J.-Y., Fontana, A.-L., Bortolotti, Y., Boucher, C., Navarrini, A., Blanchet, S., Greve, A., John, D., Kramer, C., Morel, F., Navarro, S., Peñalver, J., Schuster, K. F., and Thum, C. (2012). The EMIR multi-band mm-wave receiver for the IRAM 30-m telescope. *A&A*, 538:A89.

Chang, C. S., Ros, E., Kadler, M., Aller, M. F., Aller, H. D., Angelakis, E., Fuhrmann, L., Nestoras, I., and Ungerechts, H. (2010a). The Broadband Spectral Energy Distribution of the MOJAVE Sample. *ArXiv e-prints*, 1006.4777.

Chang, C. S., Ros, E., Kadler, M., Boeck, M., Wilms, J., Aller, M. F., Aller, H. D., Fuhrmann, L., Angelakis, E., and Nestoras, I. (2010b). The broadband emission properties of AGN jets. In *10th European VLBI Network Symposium and EVN Users Meeting: VLBI and the New Generation of Radio Arrays*, page 39.

Chang, C. S., Ros, E., Kadler, M., Boeck, M., Wilms, J., Aller, M. F., Aller, H. D., Fuhrmann, L., Angelakis, E., and Nestoras, I. (2011). The broadband emission properties of AGN jets. *ArXiv e-prints*, 1101.3284.

Chen, X., Rachen, J. P., Lopez-Caniego, M., Dickinson, C., Pearson, T. J., Fuhrmann, L., Krichbaum, T. P., and Partridge, B. (2013). Long-term variability of extragalactic radio sources in the Planck Early Release Compact Source Catalogue. *ArXiv e-prints*, 1302.2114.

Ciaramella, A., Bongardo, C., Aller, H. D., Aller, M. F., De Zotti, G., Lähteenmaki, A., Longo, G., Milano, L., Tagliaferri, R., Teräsranta, H., Tornikoski, M., and Urpo, S. (2004). A multifrequency analysis of radio variability of blazars. *A&A*, 419:485–500, arXiv:astro-ph/0401501.

Dermer, C. D. and Schlickeiser, R. (1993). Model for the High-Energy Emission from Blazars. *ApJ*, 416:458.

Fanti, C., Fanti, R., Dallacasa, D., Schilizzi, R. T., Spencer, R. E., and Stanghellini, C. (1995). Are compact steep-spectrum sources young? *A&A*, 302:317.

Fath, E. A. (1909). The Spectra of Some Spiral Nebulae and Globular Star Clusters. *Popular Astronomy*, 17:504–508.

Foschini, L., Angelakis, E., Fuhrmann, L., Ghisellini, G., Hovatta, T., Lahteenmaki, A., Lister, M. L., Braito, V., Gallo, L., Hamilton, T. S., Kino, M., Komossa, S., Pushkarev, A. B., Thompson, D. J., Tibolla, O., Tramacere, A., Carramiñana, A., Carrasco, L., Falcone, A., Giroletti, M., Grupe, D., Kovalev, Y. Y., Krichbaum, T. P., Max-Moerbeck, W., Nestoras, I., Pearson, T. J., Porras, A., Readhead, A. C. S., Recillas, E., Richards, J. L., Riquelme, D., Sievers, A., Tammi, J., Tornikoski, M., Ungerechts, H., Zensus, J. A., Celotti, A., Bonnoli, G., Doi, A., Maraschi, L., Tagliaferri, G., and Tavecchio, F. (2012a). Radio-to-γ-ray monitoring of the narrow-line Seyfert 1 galaxy PMN J0948 + 0022 from 2008 to 2011. *A&A*, 548:A106, 1209.5867.

Foschini, L., Angelakis, E., Fuhrmann, L., Ghisellini, G., Hovatta, T., Lahteenmaki, A., Lister, M. L., Braito, V., Gallo, L., Hamilton, T. S., Kino, M., Komossa, S., Pushkarev, A. B., Thompson, D. J., Tibolla, O., Tramacere, A., Carraminana, A., Carrasco, L., Falcone, A., Giroletti, M., Grupe, D., Kovalev, Y. Y., Krichbaum, T. P., Max-Moerbeck, W., Nestoras,

I., Pearson, T. J., Porras, A., Readhead, A. C. S., Recillas, E., Richards, J. L., Riquelme, D., Sievers, A., Tammi, J., Tornikoski, M., Ungerechts, H., Zensus, J. A., Celotti, A., Bonnoli, G., Doi, A., Maraschi, L., Tagliaferri, G., and Tavecchio, F. (2012b). VizieR Online Data Catalog: PMN J0948+0022 radio-to-gamma-ray monitoring (Foschini+, 2012). *VizieR Online Data Catalog*, 354:89106.

Foschini, L., Ghisellini, G., Kovalev, Y. Y., Lister, M. L., D'Ammando, F., Thompson, D. J., Tramacere, A., Angelakis, E., Donato, D., Falcone, A., Fuhrmann, L., Hauser, M., Kovalev, Y. A., Mannheim, K., Maraschi, L., Max-Moerbeck, W., Nestoras, I., Pavlidou, V., Pearson, T. J., Pushkarev, A. B., Readhead, A. C. S., Richards, J. L., Stevenson, M. A., Tagliaferri, G., Tibolla, O., Tavecchio, F., and Wagner, S. (2011a). The first gamma-ray outburst of a narrow-line Seyfert 1 galaxy: the case of PMN J0948+0022 in 2010 July. *MNRAS*, 413:1671–1677, 1010.4434.

Foschini, L., Ghisellini, G., Maraschi, L., Tagliaferri, G., Tavecchio, F., Kovalev, Y. Y., Kovalev, Y. A., Lister, M. L., Richards, J. L., D'Ammando, F., Thompson, D. J., Donato, D., Tramacere, A., Angelakis, E., Fuhrmann, L., Nestoras, I., Falcone, A., Hauser, M., Wagner, S., Mannheim, K., Tibolla, O., Max-Moerbeck, W., Pavlidou, V., Readhead, A. C. S., Stevenson, M. A., and Pushkarev, A. B. (2011b). The July 2010 outburst of the NLS1 PMN J0948+0022. *ArXiv e-prints*, 1110.5649.

Fromm, C. M., Fuhrmann, L., and Perucho, M. (2014). Multi-frequency properties of synthetic blazar radio light curves within the shock-in-jet scenario. *ArXiv e-prints*, 1412.7194.

Fromm, C. M., Perucho, M., Savolainen, T., Ros, E., Lobanov, A. P., Zensus, J. A., and Lähteenmäki, A. (2011). Evidence for shock-shock interaction in the jet of CTA 102. In Romero, G. E., Sunyaev, R. A., and Belloni, T., editors, *IAU Symposium*, volume 275 of *IAU Symposium*, pages 194–195. 1011.4837.

Fuhrmann, L., Angelakis, E., Nestoras, I., Krichbaum, T. P., Marchili, N., Schmidt, R., Zensus, J. A., Unberechts, H., Sievers, A., Riquelme, D., Foschini, L., Ghisellini, G., Ghirlanda, G., Tagliaferri, G., Tavecchio, F., Maraxchi, L., Giroletti, M., Calderone, G., Colpi, M., and Decarli, R. (2011a). Gamma-ray NLSy1s and 'classical' blazars: are they different at radio cm/mm bands? In *Narrow-Line Seyfert 1 Galaxies and their Place in the Universe*, page 26.

Fuhrmann, L., Angelakis, E., Nestoras, I., Schmidt, R., Krichbaum, T. P., Zensus, J. A., Ungerechts, H., Sievers, A., and Riquelme, D. (2011b). Radio re-brightening of the gamma-ray flaring blazar PKS 1510-089. *The Astronomer's Telegram*, 3500:1.

Fuhrmann, L., Bach, U., Nestoras, I., Krichbaum, T. P., and Angelakis, E. (2010). Radio follow-up of the Fermi-LAT Galactic Plane Transient J0109+6134 with the Effelsberg 100-m telescope. *The Astronomer's Telegram*, 2428:1–+.

Fuhrmann, L., Larsson, S., Chiang, J., Angelakis, E., Zensus, J. A., Nestoras, I., Krichbaum, T. P., Ungerechts, H., Sievers, A., Pavlidou, V., Readhead, A. C. S., Max-Moerbeck, W.,

and Pearson, T. J. (2014). Detection of significant cm to sub-mm band radio and γ-ray correlated variability in Fermi bright blazars. *MNRAS*, 441:1899–1909, 1403.4170.

Fuhrmann, L., Richards, J. L., Bach, U., Hovatta, T., Bremer, M., Nestoras, I., Karamanavis, V., Mooley, K., Myserlis, I., Readhead, A. C. S., Cheung, C. C., Pearson, T., and Angelakis, E. (2012). Follow-up radio observations of Nova Mon 2012 at 10 - 142 GHz. *The Astronomer's Telegram*, 4376:1.

Fuhrmann, L., Zensus, J. A., Krichbaum, T. P., Angelakis, E., and Readhead, A. C. S. (2007). Simultaneous Radio to (Sub-) mm-Monitoring of Variability and Spectral Shape Evolution of potential GLAST Blazars. In Ritz, S., Michelson, P., and Meegan, C. A., editors, *The First GLAST Symposium*, volume 921 of *American Institute of Physics Conference Series*, pages 249–251. 0704.3944.

Gänsicke, B. T., Rodríguez-Gil, P., Marsh, T. R., de Martino, D., Nestoras, J., Szkody, P., Aungwerojwit, A., Barros, S. C. C., Dillon, M., Araujo-Betancor, S., Arévalo, M. J., Casares, J., Groot, P. J., Kolb, U., Lázaro, C., Hakala, P., Martínez-Pais, I. G., Nelemans, G., Roelofs, G., Schreiber, M. R., van den Besselaar, E., and Zurita, C. (2006). A ZZCeti white dwarf in SDSSJ133941.11+484727.5. *MNRAS*, 365:969–976, astro-ph/0510712.

Ghisellini, G. (2012). Radiative Processes in High Energy Astrophysics. *ArXiv e-prints*, 1202.5949.

Giommi, P., Polenta, G., Laehteenmaeki, A., Thompson, D. J., Capalbi, M., Cutini, S., Gasparrini, D., Gonzalez-Nuevo, J., Leon-Tavares, J., Lopez-Caniego, M., Mazziotta, M. N., Monte, C., Perri, M., Raino, S., Tosti, G., Tramacere, A., Verrecchia, F., Aller, H. D., Aller, M. F., Angelakis, E., Bastieri, D., Berdyugin, A., Bonaldi, A., Bonavera, L., Burigana, C., Burrows, D. N., Buson, S., Cavazzuti, E., Chincarini, G., Colafrancesco, S., Costamante, L., Cuttaia, F., D'Ammando, F., de Zotti, G., Frailis, M., Fuhrmann, L., Galeotta, S., Gargano, F., Gehrels, N., Giglietto, N., Giordano, F., Giroletti, M., Keihaenen, E., King, O., Krichbaum, T. P., Lasenby, A., Lavonen, N., Lawrence, C. R., Leto, C., Lindfors, E., Mandolesi, N., Massardi, M., Max-Moerbeck, W., Michelson, P. F., Mingaliev, M., Natoli, P., Nestoras, I., Nieppola, E., Nilsson, K., Partridge, B., Pavlidou, V., Pearson, T. J., Procopio, P., Rachen, J. P., Readhead, A., Reeves, R., Reimer, A., Reinthal, R., Ricciardi, S., Richards, J., Riquelme, D., Saarinen, J., Sajina, A., Sandri, M., and Savolaine! n P., Sillanpaeae A., S. Y. S. M. T. G. T. L. T. J. T. D. T. L. T. L. T. M. T. C. T. M. U. G. U. H. V. F. W. J. Z. A. Z. J. Z. X. S. v. A. (2012a). VizieR Online Data Catalog: Planck + X/γ observations of blazars (Giommi+, 2012). *VizieR Online Data Catalog*, 354:19160.

Giommi, P., Polenta, G., Lähteenmäki, A., Thompson, D. J., Capalbi, M., Cutini, S., Gasparrini, D., González-Nuevo, J., León-Tavares, J., López-Caniego, M., Mazziotta, M. N., Monte, C., Perri, M., Rainò, S., Tosti, G., Tramacere, A., Verrecchia, F., Aller, H. D., Aller, M. F., Angelakis, E., Bastieri, D., Berdyugin, A., Bonaldi, A., Bonavera, L., Burigana, C., Burrows, D. N., Buson, S., Cavazzuti, E., Chincarini, G., Colafrancesco, S., Costamante, L., Cuttaia, F., D'Ammando, F., de Zotti, G., Frailis, M., Fuhrmann, L., Galeotta,

S., Gargano, F., Gehrels, N., Giglietto, N., Giordano, F., Giroletti, M., Keihänen, E., King, O., Krichbaum, T. P., Lasenby, A., Lavonen, N., Lawrence, C. R., Leto, C., Lindfors, E., Mandolesi, N., Massardi, M., Max-Moerbeck, W., Michelson, P. F., Mingaliev, M., Natoli, P., Nestoras, I., Nieppola, E., Nilsson, K., Partridge, B., Pavlidou, V., Pearson, T. J., Procopio, P., Rachen, J. P., Readhead, A., Reeves, R., Reimer, A., Reinthal, R., Ricciardi, S., Richards, J., Riquelme, D., Saarinen, J., Sajina, A., Sandri, M., Savolainen, P., Sievers, A., Sillanpää, A., Sotnikova, Y., Stevenson, M., Tagliaferri, G., Takalo, L., Tammi, J., Tavagnacco, D., Terenzi, L., Toffolatti, L., Tornikoski, M., Trigilio, C., Turunen, M., Umana, G., Ungerechts, H., Villa, F., Wu, J., Zacchei, A., Zensus, J. A., and Zhou, X. (2012b). Simultaneous Planck, Swift, and Fermi observations of X-ray and γ-ray selected blazars. *A&A*, 541:A160, 1108.1114.

Goss, W. M., Richards, A. M. S., Muxlow, T. W. B., and Thomasson, P. (2008). Galactic HI on the 50-au scale in the direction of three extragalactic sources observed with MERLIN. *MNRAS*, 388:165–175, 0804.0849.

Greenstein, J. L. and Matthews, T. A. (1963). Redshift of the Radio Source 3C 48. *AJ*, 68:279.

Greve, A., Neri, R., and Sievers, A. (1998). The gain-elevation correction of the IRAM 30-m telescope. *A&AS*, 132:413–416.

Griffin, M. J., Ade, P. A. R., Orton, G. S., Robson, E. I., Gear, W. K., Nolt, I. G., and Radostitz, J. V. (1986). Submillimeter and millimeter observations of Jupiter. *Icarus*, 65:244–256.

Grossberger, C., Kadler, M., Wilms, J., Müller, C., Beuchert, T., Ros, E., Ojha, R., Aller, M., Aller, H., Angelakis, E., Fuhrmann, L., Nestoras, I., Schmidt, R., Zensus, J. A., Krichbaum, T. P., Ungerechts, H., Sievers, A., and Riquelme, D. (2012). Structural Variability of 3C111 on Parsec Scales. *Acta Polytechnica*, 52(1):18, 1110.1197.

Guetta, D., Ghisellini, G., Lazzati, D., and Celotti, A. (2004). Internal shocks and the blazar sequence. Low and intermediate power BL Lac objects. *A&A*, 421:877–886, arXiv:astro-ph/0402164.

Gupta, A. C., Krichbaum, T. P., Wiita, P. J., Rani, B., Sokolovsky, K. V., Mohan, P., Mangalam, A., Marchili, N., Fuhrmann, L., Agudo, I., Bach, U., Bachev, R., Böttcher, M., Gabanyi, K. E., Gaur, H., Hawkins, K., Kimeridze, G. N., Kurtanidze, O. M., Kurtanidze, S. O., Lee, C.-U., Liu, X., McBreen, B., Nesci, R., Nestoras, G., Nikolashvili, M. G., Ohlert, J. M., Palma, N., Peneva, S., Pursimo, T., Semkov, E., Strigachev, A., Webb, J. R., Wiesemeyer, H., and Zensus, J. A. (2012). Multiwavelength intraday variability of the BL Lacertae S5 0716+714. *MNRAS*, 425:1357–1370, 1207.5942.

Hardee, P. E. (1987). Spatial stability of jets - The nonaxisymmetric fundamental and reflection modes. *ApJ*, 313:607–622.

Hartman, R. C., Bertsch, D. L., Fichtel, C. E., Hunter, S. D., Thompson, D. J., Kanbach, G., Mayer-Hasselwander, H. A., von Montigny, C., Pinkau, K., Kniffen, D. A., Lin, Y. C.,

Michelson, P. F., Nolan, P. L., Mattox, J. R., Piner, B. G., Schneid, E., Sreekumar, P., and Dingus, B. L. (1992). Unidentified High Energy Gamma Ray Sources Detected by EGRET at High Galactic Latitudes. In *American Astronomical Society Meeting Abstracts*, volume 24 of *Bulletin of the American Astronomical Society*, page 1155.

Hazard, C., Mackey, M. B., and Shimmins, A. J. (1963). Investigation of the Radio Source 3C 273 By The Method of Lunar Occultations. *Nature*, 197:1037–1039.

Healey, S. E., Romani, R. W., Cotter, G., Michelson, P. F., Schlafly, E. F., Readhead, A. C. S., Giommi, P., Chaty, S., Grenier, I. A., and Weintraub, L. C. (2008). CGRaBS: An All-Sky Survey of Gamma-Ray Blazar Candidates. *ApJS*, 175:97–104, 0709.1735.

Hovatta, T., Nieppola, E., Tornikoski, M., Valtaoja, E., Aller, M. F., and Aller, H. D. (2008). Long-term radio variability of AGN: flare characteristics. *A&A*, 485:51–61, 0805.1283.

Hovatta, T., Tornikoski, M., Lainela, M., Lehto, H. J., Valtaoja, E., Torniainen, I., Aller, M. F., and Aller, H. D. (2007). Statistical analyses of long-term variability of AGN at high radio frequencies. *A&A*, 469:899–912, 0705.3293.

Hovatta, T., Valtaoja, E., Tornikoski, M., and Lähteenmäki, A. (2009). Doppler factors, Lorentz factors and viewing angles for quasars, BL Lacertae objects and radio galaxies. *A&A*, 494:527–537, 0811.4278.

Hoyle, F. and Fowler, W. A. (1963a). Nature of Strong Radio Sources. *Nature*, 197:533–535.

Hoyle, F. and Fowler, W. A. (1963b). On the nature of strong radio sources. *MNRAS*, 125:169.

Karamanavis, V., Myserlis, I., Fuhrmann, L., Angelakis, E., Nestoras, I., Krichbaum, T. P., Zensus, J. A., Ungerechts, H., Sievers, A., and Riquelme, D. (2012). Gamma-ray blazar BL Lacertae: the highest recorded cm/mm radio flux over the past 30 years. *The Astronomer's Telegram*, 4349:1.

Kellermann, K. I. (1989). Compact Radio Sources and AGN's. In Hayakawa, S. and Sato, K., editors, *Big Bang, Active Galactic Nuclei and Supernovae*, page 239.

Kellermann, K. I. and Pauliny-Toth, I. I. K. (1969). The Spectra of Opaque Radio Sources. *ApJ*, 155:L71+.

Khachikyan, É. Y. and Weedman, D. W. (1971). A spectroscopic study of luminous galactic nuclei. *Astrophysics*, 7:231–240.

Konigl, A. and Choudhuri, A. R. (1985). A model of the polarization position-angle swings in BL Lacertae objects. *ApJ*, 289:188–192.

Krawczynski, H. (2004). TeV blazars - observations and models. *New A Rev.*, 48:367–373, astro-ph/0309443.

Kurtanidze, O. M., Tetradze, S. D., Richter, G. M., Nikolashvili, M. G., Kimeridze, G. N., and Sigua, L. A. (2009). Ten Years Optical Photometry of TeV BL Lacertae Objects. In Wang, W., Yang, Z., Luo, Z., and Chen, Z., editors, *The Starburst-AGN Connection*, volume 408 of *Astronomical Society of the Pacific Conference Series*, page 266.

Larsson, S., Fuhrmann, L., Weiss, A., Angelakis, E., Krichbaum, T. P., Nestoras, I., Zensus, J. A., Axelsson, M., Nilsson, D., Ryde, F., Hjalmarsdotter, L., Larsson, J., Lundgren, A., Mac-Auliffe, F., Parra, R., and Siringo, G. (2012). APEX sub-mm monitoring of gamma-ray blazars. *ArXiv e-prints*, 1206.3799.

Lobanov, A. P. and Zensus, J. A. (2001). A Cosmic Double Helix in the Archetypical Quasar 3C273. *Science*, 294:128–131.

Ly, C., Walker, R. C., and Junor, W. (2007). High-Frequency VLBI Imaging of the Jet Base of M87. *ApJ*, 660:200–205, astro-ph/0701511.

Lynden-Bell, D. (1969). Galactic Nuclei as Collapsed Old Quasars. *Nature*, 223:690–694.

MAGIC Collaboration, Aleksić, J., Ansoldi, S., Antonelli, L. A., Antoranz, P., Babic, A., Bangale, P., Barres de Almeida, U., Barrio, J. A., Becerra González, J., and et al. (2015). The 2009 multiwavelength campaign on Mrk 421: Variability and correlation studies. *ArXiv e-prints*, 1502.02650.

Mannheim, K. (1993). The proton blazar. *A&A*, 269:67–76, arXiv:astro-ph/9302006.

Marchili, N., Krichbaum, T. P., Liu, X., Song, H.-G., Gabányi, K. É., Fuhrmann, L., Witzel, A., and Zensus, J. A. (2012). A seasonal cycle and an abrupt change in the variability characteristics of the intraday variable source S4 0954+65. *A&A*, 542:A121, 1204.5012.

Marscher, A. P. and Gear, W. K. (1985). Models for high-frequency radio outbursts in extragalactic sources, with application to the early 1983 millimeter-to-infrared flare of 3C 273. *ApJ*, 298:114–127.

Massaro, E., Giommi, P., Leto, C., Marchegiani, P., Maselli, A., Perri, M., Piranomonte, S., and Sclavi, S. (2009). Roma-BZCAT: a multifrequency catalogue of blazars. *A&A*, 495:691–696, 0810.2206.

Matthews, T. A. and Sandage, A. R. (1963). Optical Identification of 3c 48, 3c 196, and 3c 286 with Stellar Objects. *ApJ*, 138:30.

Mauersberger, R., Guelin, M., Martin-Pintado, J., Thum, C., Cernicharo, J., Hein, H., and Navarro, S. (1989). Line calibrators at lambda = 1.3, 2, and 3 MM. *A&AS*, 79:217–261.

Michelson, P. F. (2008). GLAST: The Gamma-ray Large Area Space Telescope Mission. In *APS Meeting Abstracts*, page L2002.

Myserlis, I., Angelakis, E., Fuhrmann, L., Karamanavis, V., Nestoras, I., Krichbaum, T. P., Zensus, J. A., Ungerechts, H., and Sievers, A. (2012a). Recent radio activity of the Fermi blazar 4C +38.41. *The Astronomer's Telegram*, 4448:1.

Myserlis, I., Angelakis, E., Fuhrmann, L., Karamanavis, V., Nestoras, I., Krichbaum, T. P., Zensus, J. A., Ungerechts, H., and Sievers, A. (2012b). Recent radio activity of the Fermi blazar CTA 102. *The Astronomer's Telegram*, 4449:1.

Myserlis, I., Angelakis, E., Fuhrmann, L., Karamanavis, V., Nestoras, I., Krichbaum, T. P., Zensus, J. A., Ungerechts, H., and Sievers, A. (2012c). Recent radio activity of the Fermi blazar S5 0716+714. *The Astronomer's Telegram*, 4447:1.

Myserlis, I., Angelakis, E., Fuhrmann, L., Pavlidou, V., Nestoras, I., Karamanavis, V., Kraus, A., and Zensus, J. A. (2014). Multi-frequency linear and circular radio polarization monitoring of jet emission elements in $Fermi$ blazars. *ArXiv e-prints*, 1401.2072.

Oke, J. B. (1963). Absolute Energy Distribution in the Optical Spectrum of 3C 273. *Nature*, 197:1040–1041.

Orienti, M., Koyama, S., D'Ammando, F., Giroletti, M., Kino, M., Nagai, H., Venturi, T., Dallacasa, D., Giovannini, G., Angelakis, E., Fuhrmann, L., Hovatta, T., Max-Moerbeck, W., Schinzel, F. K., Akiyama, K., Hada, K., Honma, M., Niinuma, K., Gasparrini, D., Krichbaum, T. P., Nestoras, I., Readhead, A. C. S., Richards, J. L., Riquelme, D., Sievers, A., Ungerechts, H., and Zensus, J. A. (2013). Radio and γ-ray follow-up of the exceptionally high-activity state of PKS 1510-089 in 2011. *MNRAS*, 428:2418–2429, 1210.4319.

Ott, M., Witzel, A., Quirrenbach, A., Krichbaum, T. P., Standke, K. J., Schalinski, C. J., and Hummel, C. A. (1994). An updated list of radio flux density calibrators. *A&A*, 284:331–339.

Pasachoff, J. M., Babcock, B. A., Souza, S. P., Bruck, M. A., Hess, P. W., Kimmel, S. B., Levitt, J. S., Steele, A. S., Tsykalova, A. E., Rust, D. M., Noble, M. W., Wittenmyer, R., Kern, J., Hawkins, R. L., Seiradakis, J. H., Voulgaris, A., Pistikoudis, G., Nestoras, J., and Demianski, M. (2006). Coronal Observations at the 29 March 2006 Total Solar Eclipse. In *AAS/Solar Physics Division Meeting #37*, volume 38 of *Bulletin of the American Astronomical Society*, page 216.

Pavlidou, V., Richards, J. L., Max-Moerbeck, W., King, O. G., Pearson, T. J., Readhead, A. C. S., Reeves, R., Stevenson, M. A., Angelakis, E., Fuhrmann, L., Zensus, J. A., Giroletti, M., Reimer, A., Healey, S. E., Romani, R. W., and Shaw, M. S. (2012). Assessing the Significance of Apparent Correlations between Radio and Gamma-Ray Blazar Fluxes. *ApJ*, 751:149, 1204.0790.

Perley, R. A. and Butler, B. J. (2012). An Accurate Flux Density Scale from 1 to 50 GHz. *ArXiv e-prints*, 1211.1300.

Piner, B. G., Pant, N., and Edwards, P. G. (2010). The Jets of TeV Blazars at Higher Resolution: 43 GHz and Polarimetric VLBA Observations from 2005 to 2009. *ApJ*, 723:1150–1167, 1009.2269.

Piner, B. G., Pant, N., Edwards, P. G., and Wiik, K. (2009). Significant Limb-Brightening in the Inner Parsec of Markarian 501. *ApJ*, 690:L31–L34, 0812.3164.

Planck Collaboration, Aatrokoski, J., Ade, P. A. R., Aghanim, N., Aller, H. D., Aller, M. F., Angelakis, E., Arnaud, M., Ashdown, M., Aumont, J., and et al. (2011a). Planck early results. XV. Spectral energy distributions and radio continuum spectra of northern extragalactic radio sources. *A&A*, 536:A15, 1101.2047.

Planck Collaboration, Ade, P. A. R., Aghanim, N., Angelakis, E., Arnaud, M., Ashdown, M., Aumont, J., Baccigalupi, C., Balbi, A., Banday, A. J., and et al. (2011b). Planck early results. XIV. ERCSC validation and extreme radio sources. *A&A*, 536:A14, 1101.1721.

Press, W. H., Teukolsky, S. A., Vetterling, W. T., and Flannery, B. P. (1992). *Numerical recipes in FORTRAN. The art of scientific computing*.

Rani, B., Krichbaum, T. P., Fuhrmann, L., Böttcher, M., Lott, B., Aller, H. D., Aller, M. F., Angelakis, E., Bach, U., Bastieri, D., Falcone, A. D., Fukazawa, Y., Gabanyi, K. E., Gupta, A. C., Gurwell, M., Itoh, R., Kawabata, K. S., Krips, M., Lähteenmäki, A. A., Liu, X., Marchili, N., Max-Moerbeck, W., Nestoras, I., Nieppola, E., Quintana-Lacaci, G., Readhead, A. C. S., Richards, J. L., Sasada, M., Sievers, A., Sokolovsky, K., Stroh, M., Tammi, J., Tornikoski, M., Uemura, M., Ungerechts, H., Urano, T., and Zensus, J. A. (2013). Radio to gamma-ray variability study of blazar S5 0716+714. *A&A*, 552:A11, 1301.7087.

Readhead, A. C. S. (1994). Equipartition brightness temperature and the inverse Compton catastrophe. *ApJ*, 426:51–59.

Rees, M. J. (1966). Appearance of Relativistically Expanding Radio Sources. *Nature*, 211:468–470.

Reuter, H.-P. and Kramer, C. (1998). The mm-to-submm continuum spectra of W 3(OH) and K 3-50A. *A&A*, 339:183–186.

Reuter, H.-P., Kramer, C., Sievers, A., Paubert, G., Moreno, R., Greve, A., Leon, S., Panis, J. F., Ruiz-Moreno, M., Ungerechts, H., and Wild, W. (1997). Millimetre continuum measurements of extragalactic radio sources. IV. Data from 1993-1994. *A&AS*, 122:271–276.

Richards, J., Max-Moerbeck, W., Pavlidou, V., Pearson, T. J., Readhead, A. C. S., Stevenson, M. A., Healey, S. E., Romani, R. W., Shaw, M., Angelakis, E., Fuhrmann, L., Zensus, J. A., Grainge, K., and Taylor, G. B. (2009). 15 GHz Monitoring Of Gamma-ray Blazars With The OVRO 40 Meter Telescope In Support Of Fermi-GST. In *American Astronomical Society Meeting Abstracts #214*, volume 214 of *American Astronomical Society Meeting Abstracts*, page 303.08.

Richards, J. L., Max-Moerbeck, W., Pavlidou, V., Readhead, A. C. S., Pearson, T. J., King, O. G., Reeves, R., Stevenson, M. A., and Shepherd, M. C. (2011). Radio Variability Studies of Gamma-Ray Blazars with the OVRO 40 m Telescope. *ArXiv e-prints*, 1111.0318.

Salpeter, E. E. (1964). Accretion of Interstellar Matter by Massive Objects. *ApJ*, 140:796–800.

Schmidt, M. (1963). 3C 273 : A Star-Like Object with Large Red-Shift. *Nature*, 197:1040.

Schmidt, R., Fuhrmann, L., Angelakis, E., Nestoras, I., Krichbaum, T. P., Zensus, J. A., Ungerechts, H., Sievers, A., and Riquelme, D. (2011). Broad-band radio activity of gamma-ray flaring FSRQ B3 0650+453. *The Astronomer's Telegram*, 3596:1.

Scott, M. A. and Readhead, A. C. S. (1977). The low-frequency structure of powerful radio sources and limits to departures from equipartition. *MNRAS*, 180:539–550.

Seyfert, C. K. (1943). Nuclear Emission in Spiral Nebulae. *ApJ*, 97:28.

Shakura, N. I. and Sunyaev, R. A. (1973). Black holes in binary systems. Observational appearance. *A&A*, 24:337–355.

Sikora, M., Begelman, M. C., and Rees, M. J. (1994). Comptonization of diffuse ambient radiation by a relativistic jet: The source of gamma rays from blazars? *ApJ*, 421:153–162.

Sikora, M. and Madejski, G. (2001). On pair content of quasar jets. *X-ray Astronomy: Stellar Endpoints, AGN, and the Diffuse X-ray Background*, 599:935–938.

Simonetti, J. H., Cordes, J. M., and Heeschen, D. S. (1985). Flicker of extragalactic radio sources at two frequencies. *ApJ*, 296:46–59.

Siringo, G., Kreysa, E., Kovacs, A., Schuller, F., Weiß, A., Esch, W., Gemünd, H.-P., Jethava, N., Lundershausen, G., Güsten, R., Menten, K. M., Beelen, A., Bertoldi, F., Beeman, J. W., Haller, E. E., and Colin, A. (2008). The large APEX bolometer camera LABOCA. In *Society of Photo-Optical Instrumentation Engineers (SPIE) Conference Series*, volume 7020 of *Society of Photo-Optical Instrumentation Engineers (SPIE) Conference Series*.

Smirnov, N. (1948). Table for estimating the goodness of fit of empirical distributions. *Ann. Math. Statist.*, 19(2):279–281.

Sokolovsky, K. V., Schinzel, F. K., Tanaka, Y. T., Abolmasov, P. K., Angelakis, E., Bulgarelli, A., Carrasco, L., Cenko, S. B., Cheung, C. C., Clubb, K. I., D'Ammando, F., Escande, L., Fegan, S. J., Filippenko, A. V., Finke, J. D., Fuhrmann, L., Fukazawa, Y., Hays, E., Healey, S. E., Ikejiri, Y., Itoh, R., Kawabata, K. S., Komatsu, T., Kovalev, Y. A., Kovalev, Y. Y., Krichbaum, T. P., Larsson, S., Lister, M. L., Lott, B., Max-Moerbeck, W., Nestoras, I., Pittori, C., Pursimo, T., Pushkarev, A. B., Readhead, A. C. S., Recillas, E., Richards, J. L., Riquelme, D., Romani, R. W., Sakimoto, K., Sasada, M., Schmidt, R., Shaw, M. S., Sievers, A., Thompson, D. J., Uemura, M., Ungerechts, H., Vercellone, S., Verrecchia, F., Yamanaka, M., Yoshida, M., and Zensus, J. A. (2014). Two active states of the narrow-line gamma-ray-loud AGN GB 1310+487. *A&A*, 565:A26, 1401.2151.

Spada, M., Ghisellini, G., Lazzati, D., and Celotti, A. (2001). Internal shocks in the jets of radio-loud quasars. *MNRAS*, 325:1559–1570, arXiv:astro-ph/0103424.

Stephens, M. A. (1974). Edf statistics for goodness of fit and some comparisons. *Journal of the American Statistical Association*, 69(347):pp. 730–737.

Steppe, H., Liechti, S., Mauersberger, R., Koempe, C., Brunswig, W., and Ruiz-Moreno, M. (1992). Millimeter continuum measurements of extragalactic radio sources. II. *A&AS*, 96:441–475.

Steppe, H., Paubert, G., Sievers, A., Reuter, H. P., Greve, A., Liechti, S., Le Floch, B., Brunswig, W., Menendez, C., and Sanchez, S. (1993). Millimeter Continuum Measurements of Extragalactic Radio Sources - Part Three. *A&AS*, 102:611.

Steppe, H., Salter, C. J., Chini, R., Kreysa, E., Brunswig, W., and Lobato Perez, J. (1988). Millimeter continuum measurements of extragalactic radio sources. *A&AS*, 75:317–351.

Stevens, J. A., Litchfield, S. J., Robson, E. I., Hughes, D. H., Gear, W. K., Terasranta, H., Valtaoja, E., and Tornikoski, M. (1994). Multifrequency observations of blazars. 5: Long-term millimeter, submillimeter, and infrared monitoring. *ApJ*, 437:91–107.

Taylor, G. B. and Perley, R. A. (1992). The structure of the hot spots in 3C 295. *A&A*, 262:417–423.

Trippe, S., Krips, M., Piétu, V., Neri, R., Winters, J. M., Gueth, F., Bremer, M., Salome, P., Moreno, R., Boissier, J., and Fontani, F. (2011). The long-term millimeter activity of active galactic nuclei. *A&A*, 533:A97, 1107.5456.

Türler, M. (2011). Shock-in-jet model for quasars and microquasars. *Mem. Soc. Astron. Italiana*, 82:104, 1010.0907.

Türler, M., Courvoisier, T. J.-L., and Paltani, S. (2000). Modelling 20 years of synchrotron flaring in the jet of 3C 273. *A&A*, 361:850–862, arXiv:astro-ph/0008480.

Ulich, B. L. (1980). Improved correction for millimeter-wavelength atmospheric attenuation. *Astrophys. Lett.*, 21:21–28.

Ulich, B. L. (1981). Millimeter-wavelength continuum calibration sources. *AJ*, 86:1619–1626.

Ulich, B. L., Davis, J. H., Rhodes, P. J., and Hollis, J. M. (1980). Absolute brightness temperature measurements at 3.5-mm wavelength. *IEEE Transactions on Antennas and Propagation*, 28:367–377.

Ungerechts, H., Kramer, C., Lefloch, B., Leon, S., Masset, F., Moreno, R., Paubert, G., Reynaud, D., Sievers, A., and Wild, W. (1998). Millimeter Continuum Monitoring of Extragalactic Radio Sources with the IRAM 30m Telescope. In J. A. Zensus, G. B. Taylor, & J. M. Wrobel, editor, *IAU Colloq. 164: Radio Emission from Galactic and Extragalactic Compact Sources*, volume 144 of *Astronomical Society of the Pacific Conference Series*, page 149.

Urry, M. (1999). BL Lac Objects and Blazars: Past, Present and Future. In Takalo, L. O. and Sillanpää, A., editors, *BL Lac Phenomenon*, volume 159 of *Astronomical Society of the Pacific Conference Series*, page 3.

Valtaoja, E., Terasranta, H., Urpo, S., Nesterov, N. S., Lainela, M., and Valtonen, M. (1992a). Five Years Monitoring of Extragalactic Radio Sources - Part Four - Variability Statistics and the Unified Models for AGN / Active Galactic Nuclei. *A&A*, 254:80.

Valtaoja, E., Terasranta, H., Urpo, S., Nesterov, N. S., Lainela, M., and Valtonen, M. (1992b). Five Years Monitoring of Extragalactic Radio Sources - Part Three - Generalized Shock Models and the Dependence of Variability on Frequency. *A&A*, 254:71.

Vermeulen, R. C. and Cohen, M. H. (1994). Superluminal motion statistics and cosmology. *ApJ*, 430:467–494.

Villata, M. and Raiteri, C. M. (1999). Helical jets in blazars. I. The case of MKN 501. *A&A*, 347:30–36.

Vourlidas, A., Sanchez Andrade-Nuño, B., Landi, E., Patsourakos, S., Teriaca, L., Schühle, U., Korendyke, C. M., and Nestoras, I. (2010). The Structure and Dynamics of the Upper Chromosphere and Lower Transition Region as Revealed by the Subarcsecond VAULT Observations. *Sol. Phys.*, 261:53–75, 0912.2272.

Wilson, T. L., Rohlfs, K., and Hüttemeister, S. (2009). *Tools of Radio Astronomy*. Springer-Verlag.

Zel'dovich, Y. B. (1964). The Fate of a Star and the Evolution of Gravitational Energy Upon Accretion. *Soviet Physics Doklady*, 9:195.

Zijlstra, A. A., van Hoof, P. A. M., and Perley, R. A. (2008). The Evolution of NGC 7027 at Radio Frequencies: A New Determination of the Distance and Core Mass. *ApJ*, 681:1296–1309, 0801.3327.

Erklärung

Ich versichere, dass ich die von mir vorgelegte Dissertation selbständig angefertigt, die benutzten Quellen und Hilfsmittel vollständig angegeben und die Stellen der Arbeit, einschließlich Tabellen, Karten und Abbildungen, die anderen Werken im Wortlaut oder dem Sinn nach entnommen sind, in jedem Einzelfall als Entlehnung kenntlich gemacht habe; dass diese Dissertation noch keiner anderen Fakultät oder Universität zur Prüfung vorgelegen hat; dass sie, abgesehen von unten angegebenen Teilpublikationen – noch nicht veröffentlicht worden ist sowie, dass ich eine solche Veröffentlichung vor Abschluss des Promotionsverfahrens nicht vornehmen werde. Die Bestimmungen der Promotionsordnung sind mir bekannt. Die von mir vorgelegte Dissertation ist von Prof. Dr. J. Anton Zensus und Prof. Dr. Andreas Eckart betreut worden.

Köln, den 01.04.2015

Teilpublikationen

1. Nestoras, I., Fuhrmann, L., Angelakis, E., Schmidt, R., Krichbaum, T. P., Zensus, J. A., Ungerechts, H., Sievers, A., and Riquelme, D. (2011b). Record cm/mm-band radio flux levels of the gamma-ray flaring blazar PKS 1510-089. *The Astronomer's Telegram*, 3698:1

2. Nestoras, I., Fuhrmann, L., Angelakis, E., Schmidt, R., Krichbaum, T. P., Zensus, J. A., Ungerechts, H., Sievers, A., and Riquelme, D. (2011a). Broad band radio outburst of gamma-ray flaring blazar 4C+28.07. *The Astronomer's Telegram*, 3674:1

3. Nestoras, I., Fuhrmann, L., Bach, U., Sokolovsky, K., Ungerechts, H., Riquelme, D., Sievers, A., Richards, J. L., Max-Moerbeck, W., Pearson, T. J., Readhead, A. C. S., and F-Gamma Team (2010). Radio detection of V407 Cyg - the possible counterpart of the new Fermi LAT Gamma-ray Transient J2102+4542 with the Effelsberg 100-m, OVRO 40-m and IRAM 30-m telescopes. *The Astronomer's Telegram*, 2506:1–+

4. Nestoras, J. S., Mislis, D., Pyrzas, S., Tremou, E., Seiradakis, J. H., and Avgoloupis, S. I. (2006a). Seeing Measurements from Mt. Holomon. In Solomos, N., editor, *Recent Advances in Astronomy and Astrophysics*, volume 848 of *American Institute of Physics Conference Series*, pages 906–909

5. Nestoras, J. S., Seiradakis, J. H., Harlaftis, E., Giannakis, O., and Kitsionas, S. (2006b). Fourier Analysis of SS433 - High Speed Photometry. In Solomos, N., editor, *Recent Advances in Astronomy and Astrophysics*, volume 848 of *American Institute of Physics Conference Series*, pages 427–431

Ioannis Nestoras

Lebenslauf

Xasioti 6
Larissa, Greece 41335
(+30) 6944701695
inestoras@gmail.com
Date of birth: 08/11/1982

Ausbildung

2008–2015 **PhD in Astrophysics/Radioastronomy**, *Max-Planck-Institut für Radioastronomie*, Bonn, Germany.
Pending final presentation

2000–2007 **BSc in Physics**, *Aristotle University*, Thessaloniki, Greece, *GPA – 7.0/10 (Top 35%)*.
Major: Astronomy

1996–1999 **High school**, Larissa, Greece, *GPA – 17.2/20*.

Diplomarbeiten

Titel *Photometric observations and Data Reduction of Contact Binary Systems and of SS433. Long Term Study of the Astronomical Seeing in Mount Xolomon Chalkidikis.*

Supervisor Professor J. Seiradakis

PhD Thesis

Titel *Broad-band jet emission and variability of γ – ray Blazars.*

Supervisor Dr. L. Fuhrmann

Arbeit & Lehrerfahrung

2008–2013 **MPIFR**, *Max-Planck-Institut für Radioastronomie*, Bonn, Germany.

2007–2008 **NRL**, *Naval Research Laboratory*, Washington DC, USA.

EDV-Kenntnisse

Betriebssysteme Mac OS X, Microsoft Windows, Linux

Programmierung IDL, C– shell, LaTeX, Fortran 77/95, Visual Basic, AWK , Basics of: SQL, C, C++, PYTHON, HTML

Sonstige Software Adobe Photoshop, Microsoft Office, OpenOffice, Apple Logic Pro

Gesprochene Sprachen

Greek **Muttersprachler**

English **Fortgeschritten** *Fliessend in Wort und Schrift)*

Deutsch **Basic** *Grund Wörter und Sätze nur*

Persönliche Interessen

- Photography (my portfolio is here)
- Mountain hiking
- Reading books
- Electroacoustics
- Astrophotography
- Running
- Music (listening & composing)
- Amateur radio producer

Veröffentlichungen

1. MAGIC Collaboration, Aleksić, J., Ansoldi, S., Antonelli, L. A., Antoranz, P., Babic, A., Bangale, P., Barres de Almeida, U., Barrio, J. A., Becerra González, J., and et al. (2015). The 2009 multiwavelength campaign on Mrk 421: Variability and correlation studies. *ArXiv e-prints*, 1502.02650

2. Aleksić, J., Ansoldi, S., Antonelli, L. A., Antoranz, P., Babic, A., Bangale, P., Barres de Almeida, U., Barrio, J. A., Becerra González, J., Bednarek, W., and et al. (2014). MAGIC gamma-ray and multi-frequency observations of flat spectrum radio quasar PKS 1510-089 in early 2012. *A&A*, 569:A46, 1401.5646

3. Fuhrmann, L., Larsson, S., Chiang, J., Angelakis, E., Zensus, J. A., Nestoras, I., Krichbaum, T. P., Ungerechts, H., Sievers, A., Pavlidou, V., Readhead, A. C. S., Max-Moerbeck, W., and Pearson, T. J. (2014). Detection of significant cm to sub-mm band radio and γ-ray correlated variability in Fermi bright blazars. *MNRAS*, 441:1899–1909, 1403.4170

4. Sokolovsky, K. V., Schinzel, F. K., Tanaka, Y. T., Abolmasov, P. K., Angelakis, E., Bulgarelli, A., Carrasco, L., Cenko, S. B., Cheung, C. C., Clubb, K. I., D'Ammando, F., Escande, L., Fegan, S. J., Filippenko, A. V., Finke, J. D., Fuhrmann, L., Fukazawa, Y., Hays, E., Healey, S. E., Ikejiri, Y., Itoh, R., Kawabata, K. S., Komatsu, T., Kovalev, Y. A., Kovalev, Y. Y., Krichbaum, T. P., Larsson, S., Lister, M. L., Lott, B., Max-Moerbeck, W., Nestoras, I., Pittori, C., Pursimo, T., Pushkarev, A. B., Readhead, A. C. S., Recillas, E., Richards, J. L., Riquelme, D., Romani, R. W., Sakimoto, K., Sasada, M., Schmidt, R., Shaw, M. S., Sievers, A., Thompson, D. J., Uemura, M., Ungerechts, H., Vercellone, S., Verrecchia, F., Yamanaka, M., Yoshida, M., and Zensus, J. A. (2014). Two active states of the narrow-line gamma-ray-loud AGN GB 1310+487. *A&A*, 565:A26, 1401.2151

5. Myserlis, I., Angelakis, E., Fuhrmann, L., Pavlidou, V., Nestoras, I., Karamanavis, V., Kraus, A., and Zensus, J. A. (2014). Multi-frequency linear and circular radio polarization monitoring of jet emission elements in $Fermi$ blazars. *ArXiv e-prints*, 1401.2072

6. Beuchert, T., Kadler, M., Wilms, J., Angelakis, E., Fuhrmann, L., Myserlis, I., Nestoras, I., Kraus, A., Bach, U., Ros, E., Grossberger, C., and Schulz, R. (2013). Single-Dish Radio Polarimetry in the F-GAMMA Program with the Effelsberg 100-m Radio Telescope. In *European Physical Journal Web of Conferences*, volume 61 of *European Physical Journal Web of Conferences*, page 6006

7. Angelakis, E., Fuhrmann, L., and Myserlis, I. (2013). Properties of the radio jet emission of four gamma-ray Narrow Line Seyfert 1 galaxies. In *11th Hellenic Astronomical Conference*, pages 34–34. 1304.1706

8. Aleksić, J., Antonelli, L. A., Antoranz, P., Asensio, M., Backes, M., Barres de Almeida, U., Barrio, J. A., Bednarek, W., Berger, K., Bernardini, E., Biland, A., Blanch, O.,

Bock, R. K., Boller, A., Bonnefoy, S., Bonnoli, G., Borla Tridon, D., Bretz, T., Carmona, E., Carosi, A., Carreto Fidalgo, D., Colin, P., Colombo, E., Contreras, J. L., Cortina, J., Cossio, L., Covino, S., Da Vela, P., Dazzi, F., De Angelis, A., De Caneva, G., De Lotto, B., Delgado Mendez, C., Doert, M., Domínguez, A., Dominis Prester, D., Dorner, D., Doro, M., Eisenacher, D., Elsaesser, D., Ferenc, D., Fonseca, M. V., Font, L., Fruck, C., García López, R. J., Garczarczyk, M., Garrido Terrats, D., Gaug, M., Giavitto, G., Godinović, N., González Muñoz, A., Gozzini, S. R., Hadamek, A., Hadasch, D., Herrero, A., Hose, J., Hrupec, D., Jankowski, F., Kadenius, V., Klepser, S., Knoetig, M. L., Krähenbühl, T., Krause, J., Kushida, J., La Barbera, A., Lelas, D., Leonardo, E., Lewandowska, N., Lindfors, E., Lombardi, S., López, M., López-Coto, R., López-Oramas, A., Lorenz, E., Lozano, I., Makariev, M., Mallot, K., Maneva, G., Mankuzhiyil, N., Mannheim, K., Maraschi, L., Marcote, B., Mariotti, M., Martínez, M., Masbou, J., Mazin, D., Meucci, M., Miranda, J. M., Mirzoyan, R., Moldón, J., Moralejo, A., Munar-Adrover, P., Nakajima, D., Niedzwiecki, A., Nieto, D., Nilsson, K., Nowak, N., Orito, R., Paiano, S., Palatiello, M., Paneque, D., Paoletti, R., Paredes, J. M., Partini, S., Persic, M., Pilia, M., Prada, F., Prada Moroni, P. G., Prandini, E., Puljak, I., Reichardt, I., Reinthal, R., Rhode, W., Ribó, M., Rico, J., Rügamer, S., Saggion, A., Saito, K., Saito, T. Y., Salvati, M., Satalecka, K., Scalzotto, V., Scapin, V., Schultz, C., Schweizer, T., Shore, S. N., Sillanpää, A., Sitarek, J., Snidaric, I., Sobczynska, D., Spanier, F., Spiro, S., Stamatescu, V., Stamerra, A., Steinke, B., Storz, J., Sun, S., Surić, T., Takalo, L., Takami, H., Tavecchio, F., Temnikov, P., Terzić, T., Tescaro, D., Teshima, M., Tibolla, O., Torres, D. F., Toyama, T., Treves, A., Uellenbeck, M., Vogler, P., Wagner, R. M., Weitzel, Q., Zandanel, F., Zanin, R., MAGIC Collaboration, Longo, F., Lucarelli, F., Pittori, C., Vercellone, S., AGILE Team, Bastieri, D., Sbarra, C., Fermi-LAT Collaboration, Angelakis, E., Fuhrmann, L., Nestoras, I., Krichbaum, T. P., Sievers, A., Zensus, J. A., F-GAMMA program, Antonyuk, K. A., Baumgartner, W., Berduygin, A., Carini, M., Cook, K., Gehrels, N., Kadler, M., Kovalev, Y. A., Kovalev, Y. Y., Krauss, F., Krimm, H. A., Lähteenmäki, A., Lister, M. L., Max-Moerbeck, W., Pasanen, M., Pushkarev, A. B., Readhead, A. C. S., Richards, J. L., Sainio, J., Shakhovskoy, D. N., Sokolovsky, K. V., Tornikoski, M., Tueller, J., Weidinger, M., and Wilms, J. (2013). The simultaneous low state spectral energy distribution of 1ES 2344+514 from radio to very high energies. *A&A*, 556:A67, 1211.2608

9. Rani, B., Krichbaum, T. P., Fuhrmann, L., Böttcher, M., Lott, B., Aller, H. D., Aller, M. F., Angelakis, E., Bach, U., Bastieri, D., Falcone, A. D., Fukazawa, Y., Gabanyi, K. E., Gupta, A. C., Gurwell, M., Itoh, R., Kawabata, K. S., Krips, M., Lähteenmäki, A. A., Liu, X., Marchili, N., Max-Moerbeck, W., Nestoras, I., Nieppola, E., Quintana-Lacaci, G., Readhead, A. C. S., Richards, J. L., Sasada, M., Sievers, A., Sokolovsky, K., Stroh, M., Tammi, J., Tornikoski, M., Uemura, M., Ungerechts, H., Urano, T., and Zensus, J. A. (2013). Radio to gamma-ray variability study of blazar S5 0716+714. *A&A*, 552:A11, 1301.7087

10. Orienti, M., Koyama, S., D'Ammando, F., Giroletti, M., Kino, M., Nagai, H., Venturi, T., Dallacasa, D., Giovannini, G., Angelakis, E., Fuhrmann, L., Hovatta, T., Max-Moerbeck, W., Schinzel, F. K., Akiyama, K., Hada, K., Honma, M., Niinuma, K., Gasparrini, D., Krichbaum, T. P., Nestoras, I., Readhead, A. C. S., Richards, J. L., Riquelme, D., Sievers, A., Ungerechts, H., and Zensus, J. A. (2013). Radio and γ-ray follow-up of the exceptionally high-activity state of PKS 1510-089 in 2011. *MNRAS*, 428:2418–2429, 1210.4319

11. Backes, M., Uellenbeck, M., Hayashida, M., Satalecka, K., Tescaro, D., Terzić, T., MAGIC Collaboration, Fuhrmann, L., Nestoras, I., F-GAMMA project, Lähteenmäki, A., Tornikoski, M., Nieppola, E., Metsähovi, Böttcher, M., Collmar, W., and Weidinger, M. (2012). Long-term spectral and temporal behavior of the high-frequency peaked BL LAC object 1ES 1959+650. In Aharonian, F. A., Hofmann, W., and Rieger, F. M., editors, *American Institute of Physics Conference Series*, volume 1505 of *American Institute of Physics Conference Series*, pages 522–525

12. Foschini, L., Angelakis, E., Fuhrmann, L., Ghisellini, G., Hovatta, T., Lahteenmaki, A., Lister, M. L., Braito, V., Gallo, L., Hamilton, T. S., Kino, M., Komossa, S., Pushkarev, A. B., Thompson, D. J., Tibolla, O., Tramacere, A., Carramiñana, A., Carrasco, L., Falcone, A., Giroletti, M., Grupe, D., Kovalev, Y. Y., Krichbaum, T. P., Max-Moerbeck, W., Nestoras, I., Pearson, T. J., Porras, A., Readhead, A. C. S., Recillas, E., Richards, J. L., Riquelme, D., Sievers, A., Tammi, J., Tornikoski, M., Ungerechts, H., Zensus, J. A., Celotti, A., Bonnoli, G., Doi, A., Maraschi, L., Tagliaferri, G., and Tavecchio, F. (2012a). Radio-to-γ-ray monitoring of the narrow-line Seyfert 1 galaxy PMN J0948 + 0022 from 2008 to 2011. *A&A*, 548:A106, 1209.5867

13. Foschini, L., Angelakis, E., Fuhrmann, L., Ghisellini, G., Hovatta, T., Lahteenmaki, A., Lister, M. L., Braito, V., Gallo, L., Hamilton, T. S., Kino, M., Komossa, S., Pushkarev, A. B., Thompson, D. J., Tibolla, O., Tramacere, A., Carraminana, A., Carrasco, L., Falcone, A., Giroletti, M., Grupe, D., Kovalev, Y. Y., Krichbaum, T. P., Max-Moerbeck, W., Nestoras, I., Pearson, T. J., Porras, A., Readhead, A. C. S., Recillas, E., Richards, J. L., Riquelme, D., Sievers, A., Tammi, J., Tornikoski, M., Ungerechts, H., Zensus, J. A., Celotti, A., Bonnoli, G., Doi, A., Maraschi, L., Tagliaferri, G., and Tavecchio, F. (2012b). VizieR Online Data Catalog: PMN J0948+0022 radio-to-gamma-ray monitoring (Foschini+, 2012). *VizieR Online Data Catalog*, 354:89106

14. Myserlis, I., Angelakis, E., Fuhrmann, L., Karamanavis, V., Nestoras, I., Krichbaum, T. P., Zensus, J. A., Ungerechts, H., and Sievers, A. (2012b). Recent radio activity of the Fermi blazar CTA 102. *The Astronomer's Telegram*, 4449:1

15. Myserlis, I., Angelakis, E., Fuhrmann, L., Karamanavis, V., Nestoras, I., Krichbaum, T. P., Zensus, J. A., Ungerechts, H., and Sievers, A. (2012a). Recent radio activity of the Fermi blazar 4C +38.41. *The Astronomer's Telegram*, 4448:1

16. Myserlis, I., Angelakis, E., Fuhrmann, L., Karamanavis, V., Nestoras, I., Krichbaum, T. P., Zensus, J. A., Ungerechts, H., and Sievers, A. (2012c). Recent radio activity of the Fermi blazar S5 0716+714. *The Astronomer's Telegram*, 4447:1

17. Gupta, A. C., Krichbaum, T. P., Wiita, P. J., Rani, B., Sokolovsky, K. V., Mohan, P., Mangalam, A., Marchili, N., Fuhrmann, L., Agudo, I., Bach, U., Bachev, R., Böttcher, M., Gabanyi, K. E., Gaur, H., Hawkins, K., Kimeridze, G. N., Kurtanidze, O. M., Kurtanidze, S. O., Lee, C.-U., Liu, X., McBreen, B., Nesci, R., Nestoras, G., Nikolashvili, M. G., Ohlert, J. M., Palma, N., Peneva, S., Pursimo, T., Semkov, E., Strigachev, A., Webb, J. R., Wiesemeyer, H., and Zensus, J. A. (2012). Multiwavelength intraday variability of the BL Lacertae S5 0716+714. *MNRAS*, 425:1357–1370, 1207.5942

18. Fuhrmann, L., Richards, J. L., Bach, U., Hovatta, T., Bremer, M., Nestoras, I., Karamanavis, V., Mooley, K., Myserlis, I., Readhead, A. C. S., Cheung, C. C., Pearson, T., and Angelakis, E. (2012). Follow-up radio observations of Nova Mon 2012 at 10 - 142 GHz. *The Astronomer's Telegram*, 4376:1

19. Karamanavis, V., Myserlis, I., Fuhrmann, L., Angelakis, E., Nestoras, I., Krichbaum, T. P., Zensus, J. A., Ungerechts, H., Sievers, A., and Riquelme, D. (2012). Gamma-ray blazar BL Lacertae: the highest recorded cm/mm radio flux over the past 30 years. *The Astronomer's Telegram*, 4349:1

20. Giommi, P., Polenta, G., Laehteenmaeki, A., Thompson, D. J., Capalbi, M., Cutini, S., Gasparrini, D., Gonzalez-Nuevo, J., Leon-Tavares, J., Lopez-Caniego, M., Mazziotta, M. N., Monte, C., Perri, M., Raino, S., Tosti, G., Tramacere, A., Verrecchia, F., Aller, H. D., Aller, M. F., Angelakis, E., Bastieri, D., Berdyugin, A., Bonaldi, A., Bonavera, L., Burigana, C., Burrows, D. N., Buson, S., Cavazzuti, E., Chincarini, G., Colafrancesco, S., Costamante, L., Cuttaia, F., D'Ammando, F., de Zotti, G., Frailis, M., Fuhrmann, L., Galeotta, S., Gargano, F., Gehrels, N., Giglietto, N., Giordano, F., Giroletti, M., Keihaenen, E., King, O., Krichbaum, T. P., Lasenby, A., Lavonen, N., Lawrence, C. R., Leto, C., Lindfors, E., Mandolesi, N., Massardi, M., Max-Moerbeck, W., Michelson, P. F., Mingaliev, M., Natoli, P., Nestoras, I., Nieppola, E., Nilsson, K., Partridge, B., Pavlidou, V., Pearson, T. J., Procopio, P., Rachen, J. P., Readhead, A., Reeves, R., Reimer, A., Reinthal, R., Ricciardi, S., Richards, J., Riquelme, D., Saarinen, J., Sajina, A., Sandri, M., and Savolaine! n P., Sillanpaeae A., S. Y. S. M. T. G. T. L. T. J. T. D. T. L. T. L. T. M. T. C. T. M. U. G. U. H. V. F. W. J. Z. A. Z. J. Z. X. S. v. A. (2012a). VizieR Online Data Catalog: Planck + X/γ observations of blazars (Giommi+, 2012). *VizieR Online Data Catalog*, 354:19160

21. Angelakis, E., Fuhrmann, L., Nestoras, I., Fromm, C. M., Perucho-Pla, M., Schmidt, R., Zensus, J. A., Marchili, N., Krichbaum, T. P., Ungerechts, H., Sievers, A., Riquelme, D., and Pavlidou, V. (2012a). F-GAMMA: On the phenomenological classification of continuum radio spectra variability patterns of Fermi blazars. *Journal of Physics Conference Series*, 372(1):012007, 1202.4242

22. Larsson, S., Fuhrmann, L., Weiss, A., Angelakis, E., Krichbaum, T. P., Nestoras, I., Zensus, J. A., Axelsson, M., Nilsson, D., Ryde, F., Hjalmarsdotter, L., Larsson, J., Lundgren, A., Mac-Auliffe, F., Parra, R., and Siringo, G. (2012). APEX sub-mm monitoring of gamma-ray blazars. *ArXiv e-prints*, 1206.3799

23. Ackermann, M., Ajello, M., Ballet, J., Barbiellini, G., Bastieri, D., Bellazzini, R., Blandford, R. D., Bloom, E. D., Bonamente, E., Borgland, A. W., and et al. (2012). Multiwavelength Observations of Blazar AO 0235+164 in the 2008-2009 Flaring State. *ApJ*, 751:159, 1207.2932

24. Angelakis, E., Fuhrmann, L., Nestoras, I., Fromm, C. M., Schmidt, R., Zensus, J. A., Marchili, N., Krichbaum, T. P., Perucho, M., Ungerechts, H., Sievers, A., Riquelme, D., and Foschini, L. (2012b). Unification and physical interpretation of the radio spectra variability patterns in Fermi blazars and jet emission from NLSy1s. *ArXiv e-prints*, 1205.1961

25. Giommi, P., Polenta, G., Lähteenmäki, A., Thompson, D. J., Capalbi, M., Cutini, S., Gasparrini, D., González-Nuevo, J., León-Tavares, J., López-Caniego, M., Mazziotta, M. N., Monte, C., Perri, M., Rainò, S., Tosti, G., Tramacere, A., Verrecchia, F., Aller, H. D., Aller, M. F., Angelakis, E., Bastieri, D., Berdyugin, A., Bonaldi, A., Bonavera, L., Burigana, C., Burrows, D. N., Buson, S., Cavazzuti, E., Chincarini, G., Colafrancesco, S., Costamante, L., Cuttaia, F., D'Ammando, F., de Zotti, G., Frailis, M., Fuhrmann, L., Galeotta, S., Gargano, F., Gehrels, N., Giglietto, N., Giordano, F., Giroletti, M., Keihänen, E., King, O., Krichbaum, T. P., Lasenby, A., Lavonen, N., Lawrence, C. R., Leto, C., Lindfors, E., Mandolesi, N., Massardi, M., Max-Moerbeck, W., Michelson, P. F., Mingaliev, M., Natoli, P., Nestoras, I., Nieppola, E., Nilsson, K., Partridge, B., Pavlidou, V., Pearson, T. J., Procopio, P., Rachen, J. P., Readhead, A., Reeves, R., Reimer, A., Reinthal, R., Ricciardi, S., Richards, J., Riquelme, D., Saarinen, J., Sajina, A., Sandri, M., Savolainen, P., Sievers, A., Sillanpää, A., Sotnikova, Y., Stevenson, M., Tagliaferri, G., Takalo, L., Tammi, J., Tavagnacco, D., Terenzi, L., Toffolatti, L., Tornikoski, M., Trigilio, C., Turunen, M., Umana, G., Ungerechts, H., Villa, F., Wu, J., Zacchei, A., Zensus, J. A., and Zhou, X. (2012b). Simultaneous Planck, Swift, and Fermi observations of X-ray and γ-ray selected blazars. *A&A*, 541:A160, 1108.1114

26. Angelakis, E., Fuhrmann, L., Myserlis, I., Nestoras, I., Karamanavis, V., Krichbaum, T. P., Zensus, A. J., Marchili, N., Foschini, L., Ungerechts, H., and Sievers, A. (2012c). Properties of the radio jet emission of gamma-ray Narrow Line Seyfert 1s. In *Proceedings of Nuclei of Seyfert galaxies and QSOs - Central engine conditions of star formation (Seyfert 2012). 6-8 November, 2012. Max-Planck-Insitut für Radioastronomie (MPIfR), Bonn, Germany. Online at, id.58*, page 58

27. Grossberger, C., Kadler, M., Wilms, J., Müller, C., Beuchert, T., Ros, E., Ojha, R., Aller, M., Aller, H., Angelakis, E., Fuhrmann, L., Nestoras, I., Schmidt, R., Zensus, J. A., Krichbaum, T. P., Ungerechts, H., Sievers, A., and Riquelme, D. (2012). Structural Variability of 3C111 on Parsec Scales. *Acta Polytechnica*, 52(1):18, 1110.1197

28. Planck Collaboration, Aatrokoski, J., Ade, P. A. R., Aghanim, N., Aller, H. D., Aller, M. F., Angelakis, E., Arnaud, M., Ashdown, M., Aumont, J., and et al. (2011a). Planck early results. XV. Spectral energy distributions and radio continuum spectra of northern extragalactic radio sources. *A&A*, 536:A15, 1101.2047

29. Planck Collaboration, Ade, P. A. R., Aghanim, N., Angelakis, E., Arnaud, M., Ashdown, M., Aumont, J., Baccigalupi, C., Balbi, A., Banday, A. J., and et al. (2011b). Planck early results. XIV. ERCSC validation and extreme radio sources. *A&A*, 536:A14, 1101.1721

30. Angelakis, E., Fuhrmann, L., Nestoras, I., Fromm, C. M., Schmidt, R., Zensus, J. A., Marchili, N., Krichbaum, T. P., Perucho-Pla, M., Ungerechts, H., Sievers, A., and Riquelme, D. (2011a). On the phenomenological classification of continuum radio spectra variability patterns of Fermi blazars. *ArXiv e-prints*, 1111.6992

31. Foschini, L., Ghisellini, G., Maraschi, L., Tagliaferri, G., Tavecchio, F., Kovalev, Y. Y., Kovalev, Y. A., Lister, M. L., Richards, J. L., D'Ammando, F., Thompson, D. J., Donato, D., Tramacere, A., Angelakis, E., Fuhrmann, L., Nestoras, I., Falcone, A., Hauser, M., Wagner, S., Mannheim, K., Tibolla, O., Max-Moerbeck, W., Pavlidou, V., Readhead, A. C. S., Stevenson, M. A., and Pushkarev, A. B. (2011b). The July 2010 outburst of the NLS1 PMN J0948+0022. *ArXiv e-prints*, 1110.5649

32. Schmidt, R., Fuhrmann, L., Angelakis, E., Nestoras, I., Krichbaum, T. P., Zensus, J. A., Ungerechts, H., Sievers, A., and Riquelme, D. (2011). Broad-band radio activity of gamma-ray flaring FSRQ B3 0650+453. *The Astronomer's Telegram*, 3596:1

33. Abdo, A. A., Ackermann, M., Ajello, M., Baldini, L., Ballet, J., Barbiellini, G., Bastieri, D., Bechtol, K., Bellazzini, R., Berenji, B., and et al. (2011c). Fermi Large Area Telescope Observations of Markarian 421: The Missing Piece of its Spectral Energy Distribution. *ApJ*, 736:131, 1106.1348

34. Fuhrmann, L., Angelakis, E., Nestoras, I., Schmidt, R., Krichbaum, T. P., Zensus, J. A., Ungerechts, H., Sievers, A., and Riquelme, D. (2011b). Radio re-brightening of the gamma-ray flaring blazar PKS 1510-089. *The Astronomer's Telegram*, 3500:1

35. Angelakis, E., Fuhrmann, L., Nestoras, I., Schmidt, R., Zensus, J. A., Krichbaum, T. P., Ungerechts, H., Sievers, A., and Riquelme, D. (2011d). Millimeter radio event emerging in the gamma-ray flaring blazar PKS 0528+134. *The Astronomer's Telegram*, 3422:1

36. Foschini, L., Ghisellini, G., Kovalev, Y. Y., Lister, M. L., D'Ammando, F., Thompson, D. J., Tramacere, A., Angelakis, E., Donato, D., Falcone, A., Fuhrmann, L., Hauser, M., Kovalev, Y. A., Mannheim, K., Maraschi, L., Max-Moerbeck, W., Nestoras, I., Pavlidou, V., Pearson, T. J., Pushkarev, A. B., Readhead, A. C. S., Richards, J. L., Stevenson, M. A., Tagliaferri, G., Tibolla, O., Tavecchio, F., and Wagner, S. (2011a). The first gamma-ray outburst of a narrow-line Seyfert 1 galaxy: the case of PMN J0948+0022 in 2010 July. *MNRAS*, 413:1671–1677, 1010.4434

37. Angelakis, E., Fuhrmann, L., Nestoras, I., Schmidt, R., Zensus, J. A., Krichbaum, T. P., Ungerechts, H., Sievers, A., and Riquelme, D. (2011b). Broad-band radio behaviour of flaring BL Lac (J2202+4216). *The Astronomer's Telegram*, 3380:1

38. Angelakis, E., Fuhrmann, L., Nestoras, I., Schmidt, R., Zensus, J. A., Krichbaum, T. P., Ungerechts, H., Sievers, A., and Riquelme, D. (2011c). Broad-band radio behaviour of flaring blazar 4C+38.41. *The Astronomer's Telegram*, 3360:1

39. Abdo, A. A., Ackermann, M., Ajello, M., Baldini, L., Ballet, J., Barbiellini, G., Bastieri, D., Bechtol, K., Bellazzini, R., Berenji, B., and et al. (2011b). Erratum: "Multi-wavelength Observations of the Flaring Gamma-ray Blazar 3C 66A in 2008 October". *ApJ*, 731:77

40. Abdo, A. A., Ackermann, M., Ajello, M., Allafort, A., Baldini, L., Ballet, J., Barbiellini, G., Baring, M. G., Bastieri, D., Bechtol, K., and et al. (2011a). Insights into the High-energy γ-ray Emission of Markarian 501 from Extensive Multifrequency Observations in the Fermi Era. *ApJ*, 727:129–+

41. Chang, C. S., Ros, E., Kadler, M., Boeck, M., Wilms, J., Aller, M. F., Aller, H. D., Fuhrmann, L., Angelakis, E., and Nestoras, I. (2011). The broadband emission properties of AGN jets. *ArXiv e-prints*, 1101.3284

42. Abdo, A. A., Ackermann, M., Ajello, M., Baldini, L., Ballet, J., Barbiellini, G., Bastieri, D., Bechtol, K., Bellazzini, R., Berenji, B., and et al. (2011d). Multi-wavelength Observations of the Flaring Gamma-ray Blazar 3C 66A in 2008 October. *ApJ*, 726:43–+

43. Fuhrmann, L., Angelakis, E., Nestoras, I., Krichbaum, T. P., Marchili, N., Schmidt, R., Zensus, J. A., Unberechts, H., Sievers, A., Riquelme, D., Foschini, L., Ghisellini, G., Ghirlanda, G., Tagliaferri, G., Tavecchio, F., Maraxchi, L., Giroletti, M., Calderone, G., Colpi, M., and Decarli, R. (2011a). Gamma-ray NLSy1s and 'classical' blazars: are they different at radio cm/mm bands? In *Narrow-Line Seyfert 1 Galaxies and their Place in the Universe*, page 26

44. Angelakis, E., Angelakis, E., Fuhrmann, L., Zensus, J. A., Nestoras, I., Marchili, N., Krichbaum, T. P., Ungerechts, H., Max-Moerbeck, W., Pavlidou, V., Pearson, T. J., Readhead, A. C. S., Richards, J. L., and Stevenson, M. A. (2010a). AGN Astrophysics via Multi-Frequency Monitoring of γ-ray Blazars in the Fermi-GST Era. In L. Maraschi, G. Ghisellini, R. Della Ceca, & F. Tavecchio, editor, *Accretion and Ejection in AGN: a Global View*, volume 427 of *Astronomical Society of the Pacific Conference Series*, pages 289–+. 0910.0643

45. Abdo, A. A., Ackermann, M., Ajello, M., Baldini, L., Ballet, J., Barbiellini, G., Bastieri, D., Bechtol, K., Bellazzini, R., Berenji, B., Blandford, R. D., Bloom, E. D., Bonamente, E., Borgland, A. W., Bouvier, A., Brandt, T. J., Bregeon, J., Brez, A., Brigida, M., Bruel, P., Buehler, R., Burnett, T. H., Buson, S., Caliandro, G. A., Cameron, R. A., Cannon, A., Caraveo, P. A., Carrigan, S., Casandjian, J. M., Cavazzuti, E., Cecchi, C., Çelik, Ö., Celotti, A., Charles, E., Chekhtman, A., Chen, A. W., Cheung, C. C., Chiang, J.,

Ciprini, S., Claus, R., Cohen-Tanugi, J., Colafrancesco, S., Conrad, J., Davis, D. S., Dermer, C. D., de Angelis, A., de Palma, F., Silva, E. d. C. e., Drell, P. S., Dubois, R., Favuzzi, C., Fegan, S. J., Ferrara, E. C., Fortin, P., Frailis, M., Fukazawa, Y., Fusco, P., Gargano, F., Gasparrini, D., Gehrels, N., Germani, S., Giglietto, N., Giommi, P., Giordano, F., Giroletti, M., Glanzman, T., Godfrey, G., Grandi, P., Grenier, I. A., Grove, J. E., Guillemot, L., Guiriec, S., Hadasch, D., Hayashida, M., Hays, E., Horan, D., Hughes, R. E., Jackson, M. S., Jóhannesson, G., Johnson, A. S., Johnson, W. N., Kamae, T., Katagiri, H., Kataoka, J., Knödlseder, J., Kuss, M., Lande, J., Latronico, L., Lee, S.-H., Lemoine-Goumard, M., Llena Garde, M., Longo, F., Loparco, F., Lott, B., Lovellette, M. N., Lubrano, P., Madejski, G. M., Makeev, A., Malaguti, G., Mazziotta, M. N., McConville, W., McEnery, J. E., Michelson, P. F., Migliori, G., Mitthumsiri, W., Mizuno, T., Monte, C., Monzani, M. E., Morselli, A., Moskalenko, I. V., Murgia, S., Naumann-Godo, M., Nestoras, I., Nolan, P. L., Norris, J. P., Nuss, E., Ohsugi, T., Okumura, A., Omodei, N., Orlando, E., Ormes, J. F., Paneque, D., Panetta, J. H., Parent, D., Pelassa, V., Pepe, M., Persic, M., Pesce-Rollins, M., Piron, F., Porter, T. A., Rainò, S., Rando, R., Razzano, M., Razzaque, S., Reimer, A., Reimer, O., Reyes, L. C., Roth, M., Sadrozinski, H. F.-W., Sanchez, D., Sander, A., Scargle, J. D., Sgrò, C., Siskind, E. J., Smith, P. D., Spandre, G., Spinelli, P., Stawarz, Ł., Stecker, F. W., Strickman, M. S., Suson, D. J., Takahashi, H., Tanaka, T., Thayer, J. B., Thayer, J. G., Thompson, D. J., Tibaldo, L., Torres, D. F., Torresi, E., Tosti, G., Tramacere, A., Uchiyama, Y., Usher, T. L., Vandenbroucke, J., Vasileiou, V., Vilchez, N., Villata, M., Vitale, V., Waite, A. P., Wang, P., Winer, B. L., Wood, K. S., Yang, Z., Ylinen, T., and Ziegler, M. (2010f). Fermi Large Area Telescope Observations of Misaligned Active Galactic Nuclei. *ApJ*, 720:912–922

46. Abdo, A. A., Ackermann, M., Ajello, M., Atwood, W. B., Baldini, L., Ballet, J., Barbiellini, G., Bastieri, D., Bechtol, K., Bellazzini, R., and et al. (2010d). Gamma-Ray Emission Concurrent with the Nova in the Symbiotic Binary V407 Cygni. *Science*, 329:817–821, 1008.3912

47. Angelakis, E., Fuhrmann, L., Nestoras, I., Zensus, J. A., Marchili, N., Pavlidou, V., and Krichbaum, T. P. (2010b). The F-GAMMA program: multi-wavelength AGN studies in the Fermi-GST era. *ArXiv e-prints*, 1006.5610

48. Chang, C. S., Ros, E., Kadler, M., Aller, M. F., Aller, H. D., Angelakis, E., Fuhrmann, L., Nestoras, I., and Ungerechts, H. (2010a). The Broadband Spectral Energy Distribution of the MOJAVE Sample. *ArXiv e-prints*, 1006.4777

49. Abdo, A. A., Ackermann, M., Ajello, M., Antolini, E., Baldini, L., Ballet, J., Barbiellini, G., Baring, M. G., Bastieri, D., Bechtol, K., Bellazzini, R., Berenji, B., Blandford, R. D., Bloom, E. D., Bonamente, E., Borgland, A. W., Bregeon, J., Brez, A., Brigida, M., Bruel, P., Buehler, R., Buson, S., Caliandro, G. A., Cameron, R. A., Carrigan, S., Casandjian, J. M., Cavazzuti, E., Cecchi, C., Çelik, Ö., Chekhtman, A., Chen, A. W., Chiang, J., Ciprini, S., Claus, R., Cohen-Tanugi, J., Colafrancesco, S., Conrad, J., Cutini, S.,

Dermer, C. D., de Palma, F., Digel, S. W., Silva, E. d. C. e., Drell, P. S., Dubois, R., Dumora, D., Farnier, C., Favuzzi, C., Fegan, S. J., Ferrara, E. C., Focke, W. B., Frailis, M., Fukazawa, Y., Fusco, P., Gargano, F., Gasparrini, D., Gehrels, N., Giebels, B., Giglietto, N., Giommi, P., Giordano, F., Giroletti, M., Glanzman, T., Godfrey, G., Grandi, P., Grenier, I. A., Guillemot, L., Guiriec, S., Hadasch, D., Harding, A. K., Hayashida, M., Horan, D., Hughes, R. E., Itoh, R., Jackson, M. S., Jóhannesson, G., Johnson, A. S., Johnson, W. N., Kamae, T., Katagiri, H., Kataoka, J., Kawai, N., Knödlseder, J., Kuss, M., Lande, J., Latronico, L., Longo, F., Loparco, F., Lott, B., Lovellette, M. N., Lubrano, P., Madejski, G. M., Makeev, A., Mazziotta, M. N., McEnery, J. E., McGlynn, S., Meurer, C., Michelson, P. F., Mitthumsiri, W., Mizuno, T., Monte, C., Monzani, M. E., Morselli, A., Moskalenko, I. V., Murgia, S., Nestoras, I., Nolan, P. L., Norris, J. P., Nuss, E., Ohsugi, T., Okumura, A., Orlando, E., Ormes, J. F., Ozaki, M., Paneque, D., Panetta, J. H., Parent, D., Pelassa, V., Pepe, M., Pesce-Rollins, M., Piron, F., Porter, T. A., Rainò, S., Rando, R., Razzano, M., Reimer, A., Reimer, O., Reyes, L. C., Rodriguez, A. Y., Roth, M., Ryde, F., Sadrozinski, H. F.-W., Sambruna, R., Sander, A., Sato, R., Sgrò, C., Shaw, M. S., Siskind, E. J., Smith, P. D., Spandre, G., Spinelli, P., Stawarz, Ł., Stecker, F. W., Strickman, M. S., Suson, D. J., Takahashi, H., Takahashi, T., Tanaka, T., Thayer, J. B., Thayer, J. G., Thompson, D. J., Tibolla, O., Torres, D. F., Tosti, G., Tramacere, A., Uchiyama, Y., Usher, T. L., Vasileiou, V., Vilchez, N., Villata, M., Vitale, V., von Kienlin, A., Waite, A. P., Wang, P., Winer, B. L., Wood, K. S., Yang, Z., Ylinen, T., Ziegler, M., Tavecchio, F., Sikora, M., Schady, P., Roming, P., Chester, M. M., and Maraschi, L. (2010c). Suzaku Observations of Luminous Quasars: Revealing the Nature of High-energy Blazar Emission in Low-level Activity States. *ApJ*, 716:835–849

50. Abdo, A. A., Ackermann, M., Agudo, I., Ajello, M., Aller, H. D., Aller, M. F., Angelakis, E., Arkharov, A. A., Axelsson, M., Bach, U., and et al. (2010a). The Spectral Energy Distribution of Fermi Bright Blazars. *ApJ*, 716:30–70, 0912.2040

51. Abdo, A. A., Ackermann, M., Ajello, M., Axelsson, M., Baldini, L., Ballet, J., Barbiellini, G., Bastieri, D., Baughman, B. M., Bechtol, K., and et al. (2010e). A change in the optical polarization associated with a γ-ray flare in the blazar 3C279. *Nature*, 463:919–923, 1004.3828

52. Fuhrmann, L., Bach, U., Nestoras, I., Krichbaum, T. P., and Angelakis, E. (2010). Radio follow-up of the Fermi-LAT Galactic Plane Transient J0109+6134 with the Effelsberg 100-m telescope. *The Astronomer's Telegram*, 2428:1–+

53. Vourlidas, A., Sanchez Andrade-Nuño, B., Landi, E., Patsourakos, S., Teriaca, L., Schühle, U., Korendyke, C. M., and Nestoras, I. (2010). The Structure and Dynamics of the Upper Chromosphere and Lower Transition Region as Revealed by the Subarcsecond VAULT Observations. *Sol. Phys.*, 261:53–75, 0912.2272

54. Chang, C. S., Ros, E., Kadler, M., Boeck, M., Wilms, J., Aller, M. F., Aller, H. D., Fuhrmann, L., Angelakis, E., and Nestoras, I. (2010b). The broadband emission prop-

erties of AGN jets. In *10th European VLBI Network Symposium and EVN Users Meeting: VLBI and the New Generation of Radio Arrays*, page 39

55. Abdo, A. A., Ackermann, M., Ajello, M., Axelsson, M., Baldini, L., Ballet, J., Barbiellini, G., Bastieri, D., Baughman, B. M., Bechtol, K., and et al. (2009c). Multiwavelength Monitoring of the Enigmatic Narrow-Line Seyfert 1 PMN J0948+0022 in 2009 March-July. *ApJ*, 707:727–737, 0910.4540

56. Pasachoff, J. M., Babcock, B. A., Souza, S. P., Bruck, M. A., Hess, P. W., Kimmel, S. B., Levitt, J. S., Steele, A. S., Tsykalova, A. E., Rust, D. M., Noble, M. W., Wittenmyer, R., Kern, J., Hawkins, R. L., Seiradakis, J. H., Voulgaris, A., Pistikoudis, G., Nestoras, J., and Demianski, M. (2006). Coronal Observations at the 29 March 2006 Total Solar Eclipse. In *AAS/Solar Physics Division Meeting #37*, volume 38 of *Bulletin of the American Astronomical Society*, page 216

57. Gänsicke, B. T., Rodríguez-Gil, P., Marsh, T. R., de Martino, D., Nestoras, J., Szkody, P., Aungwerojwit, A., Barros, S. C. C., Dillon, M., Araujo-Betancor, S., Arévalo, M. J., Casares, J., Groot, P. J., Kolb, U., Lázaro, C., Hakala, P., Martínez-Pais, I. G., Nelemans, G., Roelofs, G., Schreiber, M. R., van den Besselaar, E., and Zurita, C. (2006). A ZZCeti white dwarf in SDSSJ133941.11+484727.5. *MNRAS*, 365:969–976, astro-ph/0510712